Instituto de Ciencia de Materiales de Madrid (CSIC)

Departamento de Física Aplicada, Universidad Autónoma de Madrid.

Ignacio Mínguez Bacho

"Nanostructures Fabrication: Porous Anodic Alumina and ZnO Nanorods"

Supervisor: Manuel Hernández Vélez.

Co-Supervisor: Manuel Vázquez Villalabeitia.

A thesis submitted to apply for the degree of Doctor of Philosophy in Physics Sciences.

May, 2012.

Summary.

Through the following report it is going to be presented and discussed the results obtained from the investigation carried out for during the development of the doctoral thesis. This work is based fundamentally on the development and fabrication of Nanoporous Anodic Alumina Films, (NAAF), and Zinc Oxide nanostructures. These materials have been widely and systematically charecterised based on the use of different techniques in order to conveniently study their composition, structure and properties.

Firstly, it is explained the fabrication process of NAAF grown with the objective of reducing geometric parameters (i.e. pore diameter and interpore distance) of such. With this purpose, double anodization process have been carried out, using aqueous electrolytes based on sulphuric acid with three distinct concentrations, being 3, 10 and 20wt%. In addition, the voltage applied during the process of anodization varied between 28 and 5 volts for each one of the used electrolytes. The NAAFs obtained have certain geometric characteristics that vary based on the parameters used to fabricate them. These variations in their geometry can be small between each other, for which a methodology for their study was carried out which allows for differentiation. This method is based on the application of the self-correlation function (SCF) on surface micrographs of NAAF obtained by high resolution scanning electron microscope (HR-SEM). The process of transforming micrographs in self-correlation images, allows us to obtain precise measurements of the geometric parameters of each one of the NAAFs, which in turn gives is the possibility to carry out a qualitative and quantitative study of the hexagonal ordering degree which was generated among the nanopores.

On the other hand, on the same samples, a compositional and structural study has been carried out using the combination of techniques as Rutherford and Backscattering Spectronemetry (RBS), thermo-gravimetry (TG), Infrared spectrometry IR) and the diffraction of X-rays and the complementation among them.

Another study carried out was their growth-rate, volume expansion and the efficiency of anodisation depending on their experimental parameters. Starting from the reflectance spectra, we were also able to calculate the refraction index based on a mathematic algorithm based on Snell's law and Bragg's equation. Also, the samples thickness was estimated with great precision through a non-destructive method based on Maxwell-Garnett's effective model.

Finally, the above lead us to the fabrication and morphology and magnetic characterization of Co nanowires by using these NAAFs as templates.

Other subject of interest in the scientific community discussed in this thesis has been the growth of anodic alumina through a process so called hard anodization (HA). In this case, it was studied in two ways, both potentiostatic processes. In one of the experimental procedures the voltage rate applied increased between 25 and 60V, stopping the process at various distinct moments. After the analysis of the morphology characterization, it has been possible to observe a high degree of ordering achieved within short times and a dependence on the time with the centre to centre distance of the anodic alumina cells.

In the second study, aluminum anodization was carried out by pulsed anodization (PA). This method is based on alternating periodic HA and mild anodization (MA) (i.e., the more typical). The alternation of these two modes of anodization provokes a variation in diameter and structure on the lengths of the nano-channels of anodic alumina. During the length of both types of segments can be controlled by the duration of these pulses. Also, we were able to control the shape of the HA pulses, between squares, exponentials and triangles signals. The structures obtained were used as a template for the fabrication of modulated Co nanowires with high aspect ratio.

Finally, some studies have been presented investigating the obtention of ZnO nanowires within NAAF templates; however the results were not the expected. One simple and low-cost alternative for obtaining nanostructures of ZnO has been the hydrothermal method. This chemical method is based on the chemical reaction that is produced based on the aqueous solution through which length and diameter of the remaining nanorods can be controlled by varying the concentration of ZnO precursor and growth time. The lengths obtained vary approximately between 1 and 4μm and its diameters between 40 and 600nm, being greater due to the distribution in size. These ZnO nanorods have been grown in a substrate of Fluor doped Tin oxide, which is a transparent conductor oxide.

This transparent substrate, along with the photo-catalytic properties of ZnO improved due to the deposit of CdS, allows for the development of a device capable of producing Hydrogen starting from solar light by dissociation of water molecules thanks to the photo-current generated by carriers of the semi-conductors in question.

Resumen

A lo largo de la presente memoria se van a presentar y discutir los resultados obtenidos del trabajo desarrollado durante el periodo de elaboración de la tesis doctoral. Este trabajo se ha basado fundamentalmente en el desarrollo y fabricación de películas nanoporosas de oxido de aluminio anódico y nanoestructuras de óxido de zinc. Estos materiales han sido amplia y sistemáticamente caracterizados mediante el uso de diferentes técnicas para el conveniente estudio de sus composiciones, estructuras y propiedades.

En primer lugar, se expone el proceso de fabricación las películas de alúmina anódica nanoporosas (PAAN) crecidas con el objetivo de reducir los parámetros geométricos (es decir, diámetro de poro y distancia interporo) de las mismas. Para ello se han realizado procesos de doble anodización, utilizando electrolitos acuosos basados en ácido sulfúrico con tres concentraciones distintas, siendo éstas del 3, 10 y 20% en peso. Además, el voltaje aplicado durante el proceso de anodización se ha variado entre 28 y 5 voltios para cada una de los electrolitos utilizados. Las PAAN obtenidas poseen unas características geométricas que van variando en función de los parámetros de fabricación utilizados. Estas variaciones en sus geometrías pueden ser pequeñas de una a otra y para su estudio se elaboró una metodología que permitiera su diferenciación. Este método está basado en la aplicación de la función de autocorrelación a micrografías de la superficie de las PAAN obtenidas mediante microscopía de alta resolución por barrido de electrones (HR-SEM). El procesamiento de las micrografías transformándolas en imágenes de autocorrelación, nos permite obtener medidas precisas de los parámetros geométricos de cada una de las PAAN, así como la posibilidad de realizar un estudio cualitativo y cuantitativo del grado de ordenamiento hexagonal que se haya producido en los nanoporos.

Por otro lado, sobre estas mismas muestras se ha realizado un estudio composicional y estructural mediante la combinación de técnicas como Rutherford Backscattering Spectrometry (RBS), termo-gravimetría (TG), espectrometría infrarroja (IR) y difracción de rayos-X (DRX) y su complementación entre ellas.

También se llevó a cabo un estudio sobre sus tasas de crecimiento, el volumen de expansión y la eficiencia de anodización en función de los parámetros experimentales. A partir de sus espectros de reflectancia se pudo calcular el índice de refracción mediante un algoritmo matemático basado en la Ley de Snell y la ecuación de Bragg. Además, también se estimó con

bastante precisión el espesor de las muestras mediante un método no destructivo basado en el modelo efectivo de Maxwell-Garnett.

Finalmente, se procedió a la fabricación y caracterización morfológica y magnética de nanohilos de Co utilizando estas PAAN como plantillas.

Otro importante tema de interés en la comunidad científica tratado en esta tesis ha sido la fabricación de alúmina anódica mediante procesos de la llamada anodización dura (AD). Aquí se ha procedido de dos formas, ambos han sido procesos potenciostáticos. En uno de los procedimientos experimentales se aplicó una rampa de voltaje aumentándolo de 25 a 60V, deteniendo el proceso a distintos tiempos. En la caracterización morfológica se ha podido observar un altísimo grado de ordenamiento conseguido en tiempos muy reducidos y una dependencia con el tiempo en la distancia centro a centro de las celdas de alúmina anódica.

Por otro lado, se realizado anodización de aluminio mediante anodización pulsada. Este método está basado en la alternancia periódica de pulsos de anodización dura y anodización suave, (la típica). La alternancia de estos dos modos de anodización provoca la variación del diámetro y de la estructura a lo largo de los nano-canales de alúmina anódica. Mediante la duración de estos pulsos se puede controlar la longitud de los dos tipos de segmentos. Además de la duración de éstos también hemos podido controlar la forma de los pulsos de anodización dura variando entre cuadrados, exponenciales y triangulares. Las estructuras obtenidas se han utilizado como plantilla para la fabricación de nanohilos modulados de Co con una alta relación de aspecto.

Para terminar, se han presentado distintos trabajos en los que se ha buscado la obtención de nanohilos de ZnO en las plantillas de PAAN, sin embargo los resultados no fueron los esperados. Una vía alternativa para la obtención de nanoestructuras de ZnO por un método sencillo y de bajo coste, ha sido el método hidrotermal. Este método químico está basado en una reacción química que se produce a partir de una solución acuosa mediante la cual, variando la concentración del precursor del ZnO y el tiempo de crecimiento se controla la longitud y diámetro de los resultantes nanorods. Las longitudes obtenidas varían aproximadamente entre 1 y 4µm y sus diámetros entre 40 y 600nm llegando a ser mayores debido a la distribución de tamaños. Estos nanorods de ZnO se han crecido en un substrato de óxido de estaño dopado con Flúor que es un oxido transparente y conductor. Este substrato transparente junto con las propiedades fotocatalizadoras del ZnO aumentadas mediante la deposición de CdS ha permitido el desarrollo de un dispositivo capaz de producir Hidrógeno a

partir de luz solar por disociación de moléculas de agua gracias a la fotocorriente generada por los portadores de los semiconductores en cuestión.

Contents.

Introduction.

Since the last quarter of the past century, Nanoscience and Nanotechnology began to be among the most relevant scientific research areas and in few years they also started to form part of the common vocabulary in worldwide societies. The scientific and technical background of this Thesis has its origin in the advances of science and technology along 20^{th} century for understanding and controlling materials properties when their characteristic dimensions continuously decrease.

The evolution of Nanoscience and Nanotechnology in the different disciplines of research gives rise to new sectors such as Nanobiotechnology (drug delivery as example), Nanoelectronics (quantum computing, photonics, spintronics), Nanomaterials (nanowires, nanorods, nanotubes, …), etc., e.g., for energetic applications, some of which are broached in this manuscript.

In general, there are two approaches for fabrication and synthesis in the field of Nanotechnology, i.e., the so called "top- down" and "bottom-up" strategies. "Top- down" approaches are based on the search of small dimensions starting from bulky samples. These methods are already installed in industrial productions. Usually, some of them come together with others like laser interference lithography, focused ion beam or electron beam lithography which are too expensive for industrial applications, and have serious limitations in the design and fabrication of reduced dimension devices, below 10 nanometers. Nowadays, the big challenge lays on the "bottom-up" techniques which foundation is the achievement of complex systems starting form atomic or molecular functional elements. Recently it has been demonstrated the high importance of bottom – up techniques to get devices for important applications in the field of energy generation and storage.

The experimental work presented in this thesis has been oriented towards the fabrication and characterization of nanostructures obtained by mean of "bottom-up" techniques being the main materials grown in this work: Nanoporous Anodic Alumina Films (NAAF) and Nanostructured Zinc Oxide.

The formation and understanding of the growth mechanisms of NAAF have attracted great interest of researchers since several decades ago. The most important factor determining the type of anodic Alumina film formed is the acid character on which is based the working electrolyte. Depending on the acid strength or weakness, the electrolytes have the ability or not of dissolving anodic aluminium oxide. It is also possible to fabricate porous anodic aluminium oxide with organic acid under certain condition in self-ordering regimes. The electrolytes which produce porous type oxide films are those which slightly dissolve the alumina. These electrolytes are based on strong acid as phosphoric, oxalic or sulphuric acid. The most common acids for growing porous type anodic alumina are sulphuric, oxalic and phosphoric acid. Aluminium anodization has achieved a renewed interest for Nanotechnology applications. During the last decade, the fabrication of NAAF and their use as template for subsequent synthesis of functional nanomateriales such as, nanowires, nanotubes, nanodots nanocones or nanorings have had a huge increase.

On the other hand, there are several theories dealing with pore formation in NAAF. The most of these theories are based on the concept introduced by Hoar and Mott at the end of the 50's of "field-assisted dissolution", (FAD) i.e., dissolution of aluminium oxide assisted by electric field. According to this theory, pure anodic Alumina is formed at the metal/oxide interface, while in the oxide/electrolyte interface, migrant ions coming from the electrolyte are incorporated into the anodic alumina matrix, resulting in a pure alumina inner layer and an anion contaminated anodic alumina outer layer. This model faced up some difficulties to explain the alumina growth process and particularly conflictive was that following the FAD model, no cells should appear, the FAD model cannot explain the hexagonal cell boundaries.

Several years later, after the achievement of hexagonally self-ordered pores by Masuda et al., some others models and explanations accompanied by experimental evidences about pore formation, growth and ordering have arisen. In the last five years a a new wave of models has been mainly based on the study of aluminium flow and anionic species, electric field and current densities giving rise to the field-induced plasticity (FIP) also called field-assisted flow (FAF) which takes places within the barrier layer during the film growth. Highly significant are recent reports of García-Vergara et al. Borne out by a wide experimental work in the frame of alumina formation research. From their results it is observed that the dissolution of alumina, does not play an important role as a mechanism of dissolution during aluminium anodization and there is a flow of material toward the cell walls.

Therefore, it can be concluded that after decades of studies the mechanism of formation and growth and even less the self-ordering conditions for NAAF growth are still not clear. From my point of view there are two ways of thinking; the most accepted during the last decades, the FAD model, related to the equilibrium between the aluminium oxide growth and the chemical dissolution assisted by the electric field, and the another one, the more recent FIP model, related with the plastic flow of the alumina generated towards the cell walls. This model is able to explain some important questions that FAD cannot.

Other functional material on which we have worked in this Thesis has been ZnO. 1D ZnO nanostructures are very versatile systems, with a lot of practical applications. ZnO nanowire arrays have shown promising photoluminescence properties for UV lasing optical waveguides and UV photodetectors. In general, ZnO show n-type semiconductor behaviour, and becoming p-type is not an easy task Nevertheless, by junction both n and p type ZnO it can be also used for the fabrication of Light Emitting Diodes. Recently, the main practical applications of ZnO nanostructures are addressed to the solar energy field. One of the most important applications is as fundamental part for fabrication of Dye-sensitized solar cells (DSSCs) and photovoltaic. Specially the recent development of photoelectrochemical cells (PECs) has renewed the interest on this material for solar cells applications [42]. Thus one chapters in our work deal with these nanostructures and their relevant application.

Among the main general objectives of this thesis are: the fabrication and optimization of NAAF with small pore diameters, a systematic study of the self-ordering regimes and their characterization and the use of NAAF as templates for the growth of functional one-dimensional arrays. From the design and fabrication of ordered porous anodic alumina nanostructures, we have managed a broad range of geometrical parameters, such as, reduced

pore diameters, highly ordered nanopores under hard anodization conditions and modulation of nano-channels along the pore walls of anodic alumina.

Other specific objectives reached have been the fabrication of Co nanowires with around 20nm diameters and modulated nanowires. After the study on the ZnO nanowires growth by mean of electrochemical processes, we also explore the growth of ZnO nanorods with diameters between 50 and 600nm and their use in a PECs for solar energy application.

The Thesis is structured in four chapters dealing with the topics describing briefly as follows:

Chapter 1: Here, the starting materials, developed experimental methods and the characterization techniques used in our research work are presented.

Chapter 2: This consists in the presentation of the results obtained from the anodization at different applied voltages and acid concentration in different electrolytes basically sulphuric acid based. Morphology, compositional and structural analyses of the samples is discussed, as well their physical and optical properties. At the end an example of their application as template for magnetic nanowires is also shown.

Chapter3: This chapter deals with the results obtained from aluminum anodization at high electric fields. Exhaustive morphological analyses of samples grown by two different methods are discussed. Here it is also presented the fabrication and characterization of magnetic nanowires with novel geometric features.

Chapter 4: In this chapter the presentation of the results obtained from the fabrication of ZnO nanostructures are presented, particularly, morphological and structural characterization and photoluminescent and photoelectrochemical properties of ZnO nanorods sensitized with CdS nanoparticles looking for solar energy applications.

Finally, general conclusions of the work are presented.

Relevant Bibliography related with Thesis subjects

Feigel, A., Z. Kotler, and B. Sfez, *Scalable interference lithography alignment for fabrication of three-dimensional photonic crystals.* Optics Letters, 2002. 27(9): p. 746-748.

Lo, C.J., T. Aref, and A. Bezryadin, *Fabrication of symmetric sub-5 nm nanopores using focused ion and electron beams.* Nanotechnology, 2006. 17(13): p. 3264-3267.

Lu, W. and C.M. Lieber, *Nanoelectronics from the bottom up.* Nat Mater, 2007. 6(11): p. 841-850.

Magasinski, A., et al., *High-performance lithium-ion anodes using a hierarchical bottom-up approach.* Nat Mater, 2010. 9(4): p. 353-358.

Masuda, H. and K. Fukuda, *ORDERED METAL NANOHOLE ARRAYS MADE BY A 2-STEP REPLICATION OF HONEYCOMB STRUCTURES OF ANODIC ALUMINA.* Science, 1995. 268(5216): p. 1466-1468.

Lee, W., *The Anodization of Aluminum for Nanotechnology Applications.* Jom, 2010. 62(6): p. 57-63.

Nielsch, K., et al., *High density hexagonal nickel nanowire array.* Journal of Magnetism and Magnetic Materials, 2002. 249(1-2): p. 234-240.

Lee, W., et al., *Metal membranes with hierarchically organized nanotube arrays.* Chemistry of Materials, 2005. 17(13): p. 3325-3327.

Zhao, S., et al., *New application of AAO template: A mold for nanoring and nanocone arrays.* Journal of the American Chemical Society, 2006. 128(38): p. 12352-12353.

Hoar, T.P. and N.F. Mott, *A MECHANISM FOR THE FORMATION OF POROUS ANODIC OXIDE FILMS ON ALUMINIUM.* Journal of Physics and Chemistry of Solids, 1959. 9(2): p. 97-99.

Thompson, G.E. and G.C. Wood, *Porous anodic film formation on aluminium.* Nature, 1981. 290(5803): p. 230-232.

Masuda, H., F. Hasegwa, and S. Ono, *Self-ordering of cell arrangement of anodic porous alumina formed in sulfuric acid solution.* Journal of the Electrochemical Society, 1997. 144(5): p. L127-L130.

Houser, J.E. and K.R. Hebert, *The role of viscous flow of oxide in the growth of self-ordered porous anodic alumina films.* Nature Materials, 2009. 8(5): p. 415-420.

Su, Z., G. Haehner, and W. Zhou, *Investigation of the pore formation in anodic aluminium oxide.* Journal of Materials Chemistry, 2008. 18(47): p. 5787-5795.

Oh, J. and C.V. Thompson, *The role of electric field in pore formation during aluminum anodization.* Electrochimica Acta, 2011. 56(11): p. 4044-4051.

Garcia-Vergara, S.J., et al., *Tracer studies relating to alloying element behaviour in porous anodic alumina formed in phosphoric acid.* Electrochimica Acta, 2010. 55(9): p. 3175-3184.

Wu, Z., C. Richter, and L. Menon, *A study of anodization process during pore formation in nanoporous alumina templates.* Journal of the Electrochemical Society, 2007. 154(1): p. E8-E12.

Martinson, A.B.F., et al., *ZnO nanotube based dye-sensitized solar cells.* Nano Letters, 2007. 7(8): p. 2183-2187.

Greene, L.E., et al., *General route to vertical ZnO nanowire arrays using textured ZnO seeds.* Nano Letters, 2005. 5(7): p. 1231-1236.

Gratzel, M., *Photoelectrochemical cells.* Nature, 2001. 414(6861): p. 338-344.

Chapter 1. Experimental techniques and characterization methods.

In this chapter we are going to describe briefly the fundamentals of the fabrication methods and also the characterization techniques used during the development of this work.

1.1. Preparation and fabrication processes for NAAF.

1.1.1. Starting material and preparation process.

Aluminium disks

High purity (99.999%; Goodfellow) Aluminium (Al) disks have been used as starting material. The use of Aluminium with lower purity can modify the structure and composition of NAAF [1]. From the manufacturer's website [2] is possible to find technical information of the Aluminium used in this work. In Table 1.1 are presented some of the main characteristics of our interest.

Table 1.1: Structural, physical and electrical properties of Aluminium Goodfellow.

Crystalline Structure	Density (gr/cm^3)	Melting Point (°C)	Electrical Resistivity (ρ) @20°C (μΩ·cm)	Temperature Coefficient of resistance (α) @0-100°C (K^{-1})
FCC	2.70	660.4	2.67	0.0045

It is worth to mention that, since the anodization processes are carried out at 0°C, the electrical resistivity will be different than that at 20°C. It can be easily calculated from **¡Error! No se encuentra el origen de la referencia.**:

$$\textbf{Eq. 1.1:}\quad \int_{\rho_{20^\circ C}}^{\rho_{0^\circ C}} \frac{d\rho}{\rho_s} = \int_{T=20^\circ C}^{T=0^\circ C} \alpha \cdot dT$$

Where ρ_s denotes the electrical resistivity according tabulated standards, $d\rho$ the differential in electrical resistivity, α is the temperature coefficient of resistance, T the temperature and dT the change in temperature.

So, $\rho_{0^\circ C}$ = 2.43 μΩ·cm. Aluminium metal is also a remarkable thermal conductor which is a very suitable property in order to remove the heating generated during the anodization process.

The diameters of the Al disks used are 25±0.5 and 15±0.5 cm and the thickness is 0.5±0.05 mm.

Cleaning process

Cleanness and purity of all involved elements in the preparation process are of crucial importance on the good development of the experiments and also into the final results.

In order to avoid possible contamination, Al disks have to be degreased. To do that, Al disks are ultrasonicated during 5 minutes into both Acetone and Ethanol, in this order, having into account the polarity of these liquids [3]. After that, Al disks can be rinsed with ultrapure water and stored or, rinsed with Ethanol if they are going to be electrochemically polished just next.

Electrochemical polishing

It is necessary to have a smooth surface in order to enhance the mechanical stability and the quality of the NAAF.

In this process, the sample is immersed into an acidic electrolyte highly stirred under certain applied voltage. The Al disk is connected as the anode and a Platinum (Pt) mesh as the cathode. More specifically, the electrolyte consists of a mixture of 75% ethanol (C_2H_5OH) and 25% perchloric acid ($HClO_4$) [4, 5] under 20 V at temperatures between 5–10°C during 150s. Previous studies in this researching group concluded that these conditions are the optimum to get the smoother surface possible by using this method, becoming a mirror like surface with a roughness below 1.5 nm [6]. Under these conditions the current density is around 250 mA/cm^2. Since this electrolyte is based on ethanol, which is highly flammable, the storing and working temperature must not be higher than 15°C. This is of vital importance mostly under working conditions; otherwise, the solution could explode. The recipient which contains the electrolyte is immersed into a cooling liquid (ice and water) in order to remain the temperature in the range of temperatures mentioned above. It is also recommended not to use it with temperatures below 0°C since the current density would be low and the roughness will be higher, so the surface will not be perceived as a mirror like surface.

Immediately after electrochemical polishing, the Al disks are vigorous rinsed, first with ethanol and second with ultrapure water in order to remove any remainder of electrolyte. Next, the Al disks are dried with compressed air and then they are ready to be stored or anodized.

1.1.2. Electrochemical cell and anodization experimental set-up.

Electrochemical cell

A typical electrochemical cell used for Aluminium anodization basically is composed of a Cooper plate which in contact with the Al disks takes the role of anode, a Teflon piece with a 2 centimetres diameter hole where the Al disks are placed and sealed by a rubber o-ring being one side exposed to the electrolyte, and another Teflon piece which support the Platinum electrode acting as cathode. At the same time, the electrochemical cell is placed on a cooling surface in order to reach and keep the adequate temperature for the system (Figure 1.1).

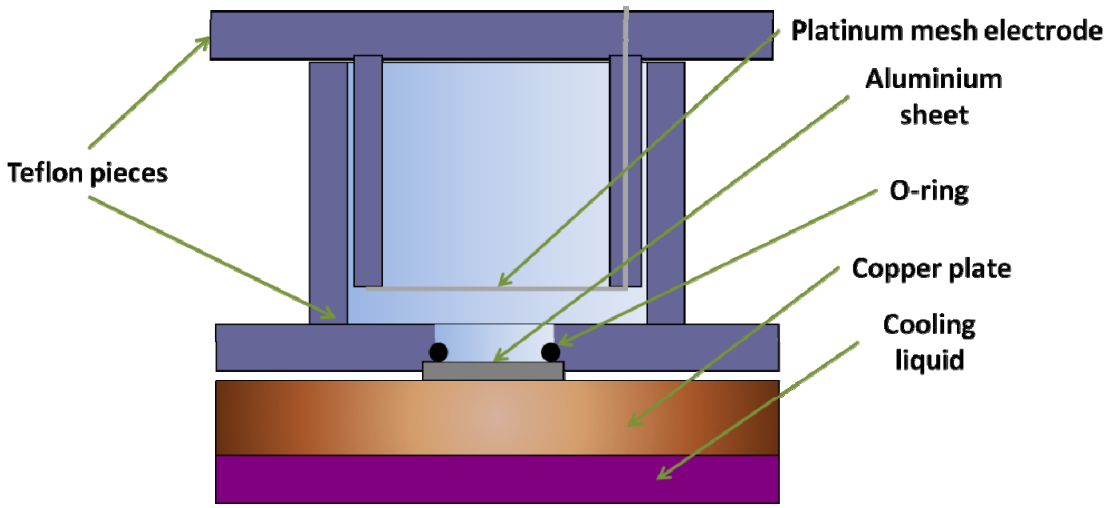

Figure 1.1: Typical electrochemical cell for Aluminium anodization.

But this typical set up do not guaranties maintaining the initial temperature of the electrolyte during the anodization process for a great part of the experiments carried out in the development of this work. Temperature is a parameter which plays a crucial role during anodization of aluminium, as we will see later on. That is the reason why it is very important trying to remain stable the temperature of the system while the process is running. Experiments which generate high current densities are accompanied by a significant evolution of the Joule heating which may raises the temperature of the system, and in the typical cell, the only refrigerating area is the exposed part of the aluminium disk. For this reason, we have used a set-up which improves significantly the cooling system of a typical cell.

The anodization processes were performed using a homemade electrochemical cell made with Teflon, with an inner chamber surrounding its walls. A cooling liquid is continuously

flowing within the chamber (Figure 1.2). This cooling system provides a high thermal stability to the process.

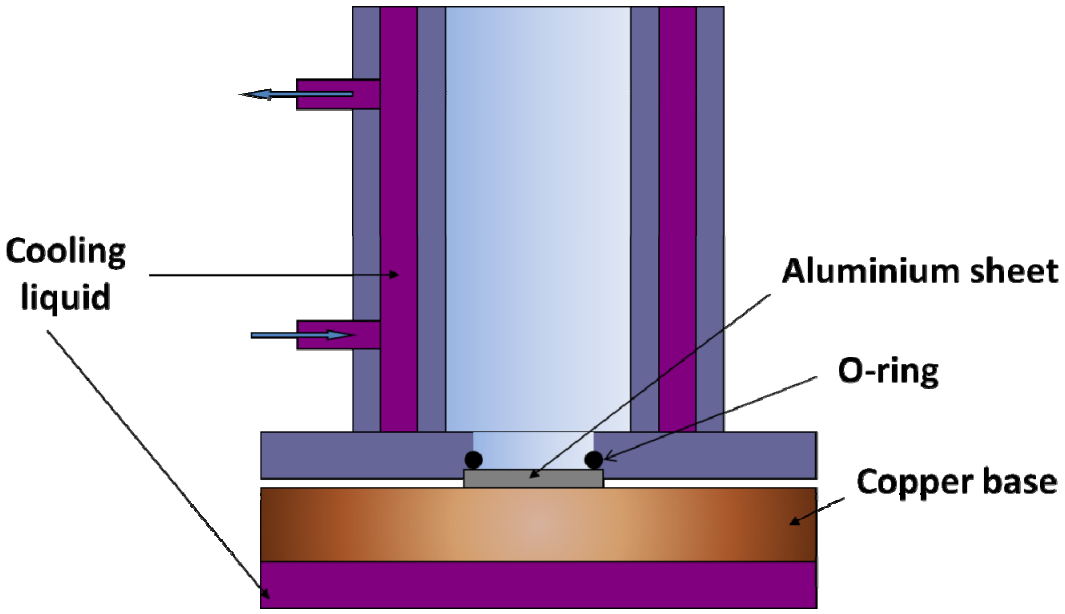

Figure 1.2: Improved electrochemical cell with enhanced cooling system.

Experimental set-up for Al anodization

The anodization process is controlled by a Keithley 2400 Source-meter connected by a National Instruments GPIB-USB controller to a computer which drives the source-meter by programs based on Labview.

The Keithley 2400 Source-meter works within two different ranges as showed in Figure 1.3.

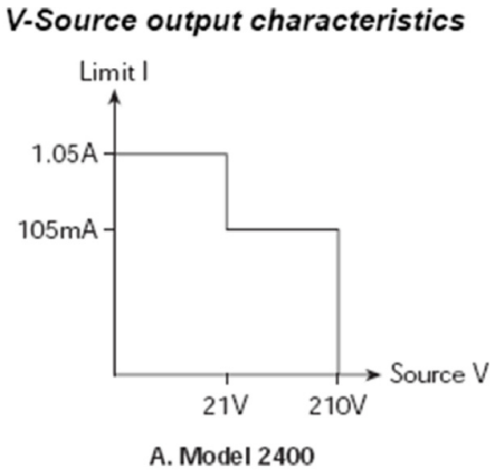

Figure 1.3: Operating boundaries for the V-Source. Only the first quadrant of operation is covered since operation in the other three quadrants is similar [7].

So, if we apply voltages above 21 V the maximum current that can be measured is 105 mA, and in the cases when we apply voltages below 21 V it is possible to register current up to 1.05 A. This is factor to take into account for our experiments since some of them are out of these boundaries.

The temperature of the cooling liquid is controlled by a cooler, model Haake Phoenix II C25P. For the anodization experiments this temperature is fixed at -2.0˚C. The cooling liquid circulates from the cooler to the Cooper plate and also into the inner chamber inside the walls of the electrochemical cell. In this way, both Aluminium disk and electrolyte are cooled at the same time.

Other important parameter is the stirring. It is necessary to continuously stir the electrolyte in order to maintain a homogenous temperature and refresh the solution at the pore bottom to avoid ionic gradients on the electrolyte/oxide interface and remove the Oxygen bubbles from the surface. We stir mechanically with a propeller from IKA RW-11.

A schematic diagram of the experimental set-up for Aluminium anodization used in our laboratory is represented in Figure 1.4:

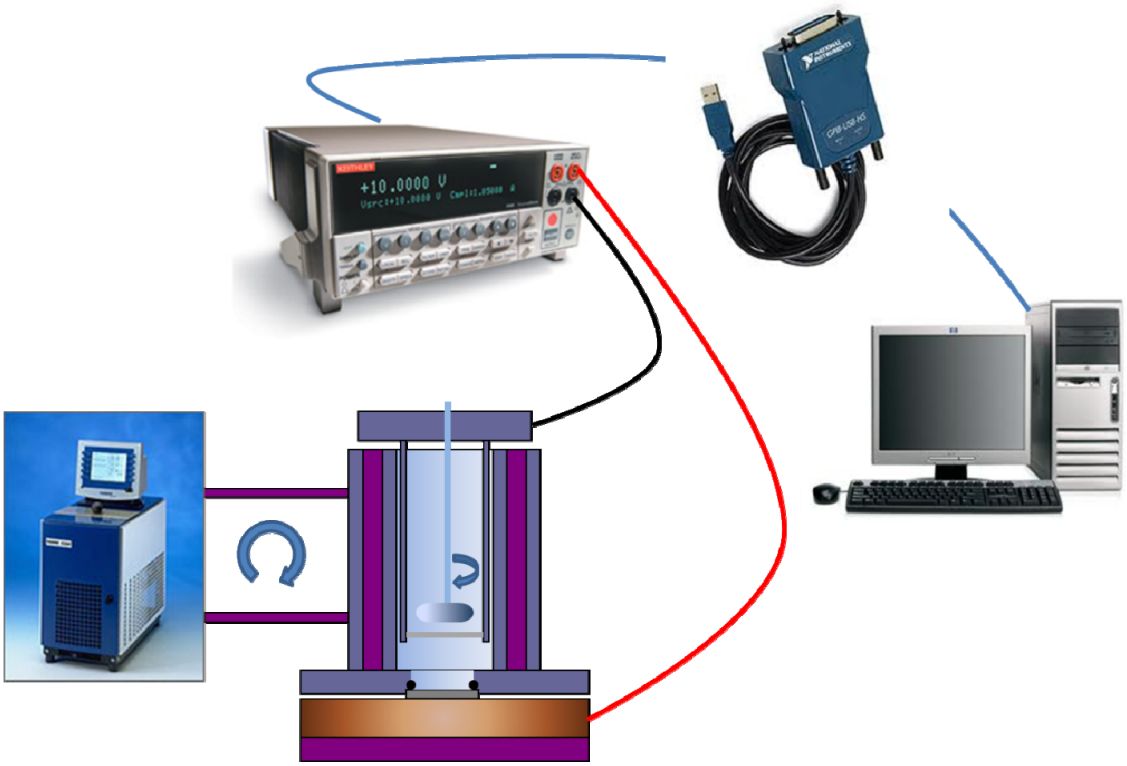

Figure 1.4: Schematic diagram of the experimental set-up for Aluminium anodization.

1.1.3. Two step anodization process.

The two step anodization process was developed the first time by Masuda et al. [8]. This method opened a new way for the fabrication of nanostructured materials by using anodic alumina as a template. A schematic diagram of the two step anodization process is showed in Figure 1.5.

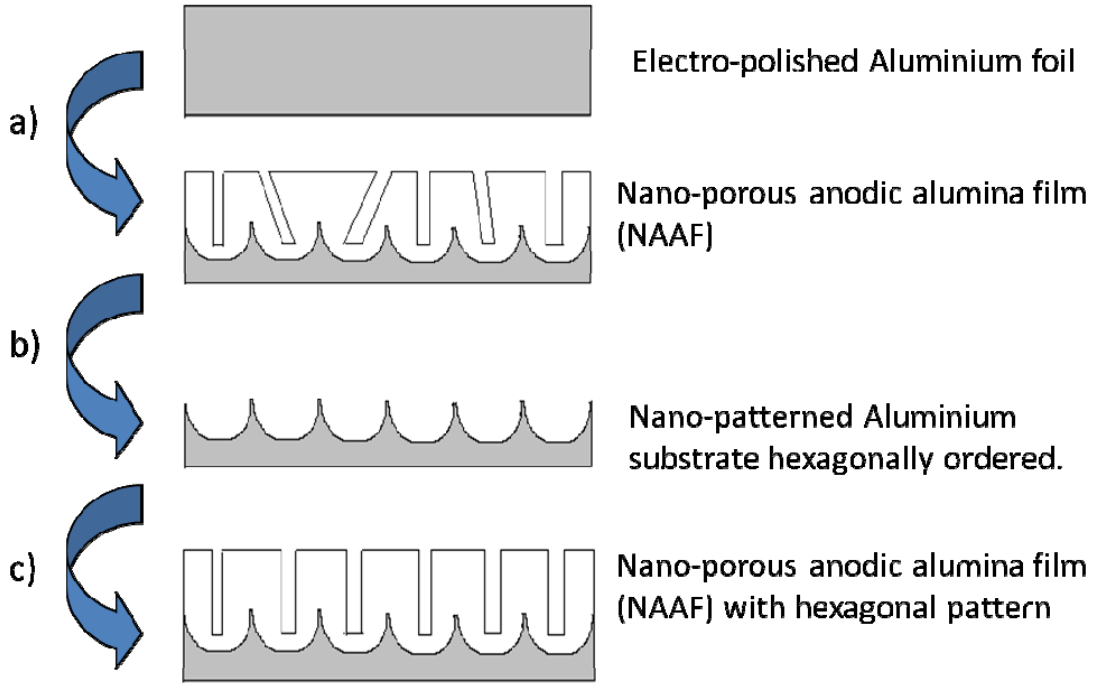

Figure 1.5: Schematic diagram of the experimental process. a) First anodization, b) Dissolution of the anodic alumina film, c) Second anodization.

During the first step, (Figure 1.5a) the electro-polished aluminium foil is anodized with the set-up showed in Figure 1.4, following the required experimental conditions (acid concentration, applied voltage, temperature, stirring) for reaching a self-ordered pattern on the aluminium surface [9-12]. These conditions vary from one acid based electrolyte to other as we will see more detailed in the chapter 2 and 3.

After the first step, a thick film of nanoporous anodic alumina remains on the surface of the aluminium. This film presents disordered pores on the surface which slightly are getting order along the nano-channels till, finally, at the base of the film, where the oxide is in contact with the aluminium, the nano-channels have hexagonal order and subsequently, the Aluminium substrate.

Since, our interest is on the formed pattern on the Aluminium substrate and not on the NAAF grown, we can remove the anodic alumina but without affect the substrate. For this, we

use a selective chemical etching which dissolves the alumina without etching the Aluminium substrate. The aqueous solution is composed by 0.18 M Chromic oxide (CrO_3), and 0.72 M Phosphoric acid. After immersing the samples for 24 hours in this solution at a temperature ranging between 20°C to 23°C, the anodic alumina has been dissolved and the hexagonally patterned Al substrate is exposed (Figure 1.5b). This process is faster if we increase the temperature of the solution up to 40°C. After this selective etching, the sample has to be thoroughly rinsed with ultrapure water in order to remove the acidic species on the sample which could be cause of undesirable contamination in the alumina structure.

During the second anodization (Figure 1.5c), we apply the same experimental parameters, in order to grow a NAAF which reproduces the pattern of the Aluminium substrate from the surface to the pore bottom with straight nano-channels.

1.1.4. Barrier Layer reduction.

The barrier layer reduction is an anodization process which is only necessary if the experiment requires that the barrier layer allow charge transfer, i.e. electrodeposition (see Secction 1.2.1). This process also allows growing relatively thin NAAFs (from few hundred of nanometers) and electrodepositing inside the pores without removing the aluminium substrate, which is very desirable since the huge difficulty of handling free-standing NAAF with so thin thickness.

The aim of this process is thinning the pore base till the thickness become less than 10nm. This experimental process is carried out inside the same electrochemical cell, just after finishing the second anodization with the same experimental conditions, except the applied voltage which is the key parameter for the barrier layer reduction. In order to carry out this modification in the NAAF it is necessary to apply an anodizing voltage signal stepwise reduced so that, a progressive thinning of the pore base take place [13]. Since the relation between the applied voltage and the thickness of the barrier layer [14], we know that by decreasing the applied voltage, the thickness of the barrier layer is also reduced (Eq. 1.2):

$$\text{Eq. 1.2:} \quad 2D_{BL} \approx D_{int} = k \cdot U$$

Where D_{BL} is the thickness of the barrier layer, D_{int} is the interpore distance, U is the applied voltage and k is a factor which value is around 2,5 nm/V.

Each applied voltage reduction step comes with an increase of the current density, which indicates that the resistance decrease. That means that the barrier layer is getting thinner. This

thinning takes place at the base of each pore where branched pores, also known as dendrites, appear with diameters accordingly to the applied voltages. When the thickness of the barrier layer has reached the corresponding to the applied voltage, the current density reaches the maximum and the anodization would continue it a steady-state.

In order to do this, we use an exponential decrease function following the Eq. 1.3:

$$\text{Eq. 1.3: } V_i = V_0 \cdot e^{-i/\tau} \text{ where, } i = 1,..,\ {}^{t_{BLR}}/_{t_{step}}$$

Where i is the step number, τ is a constant dependent on the acid solution, V_0 is the starting voltage, V_i is the voltage after each step, t_{BLR} is the time which takes the barrier layer reduction and t_{step} is the length time of each step. In Figure 1.6 is represented the barrier layer after the applying the exponential voltage reduction of Eq.1.3.

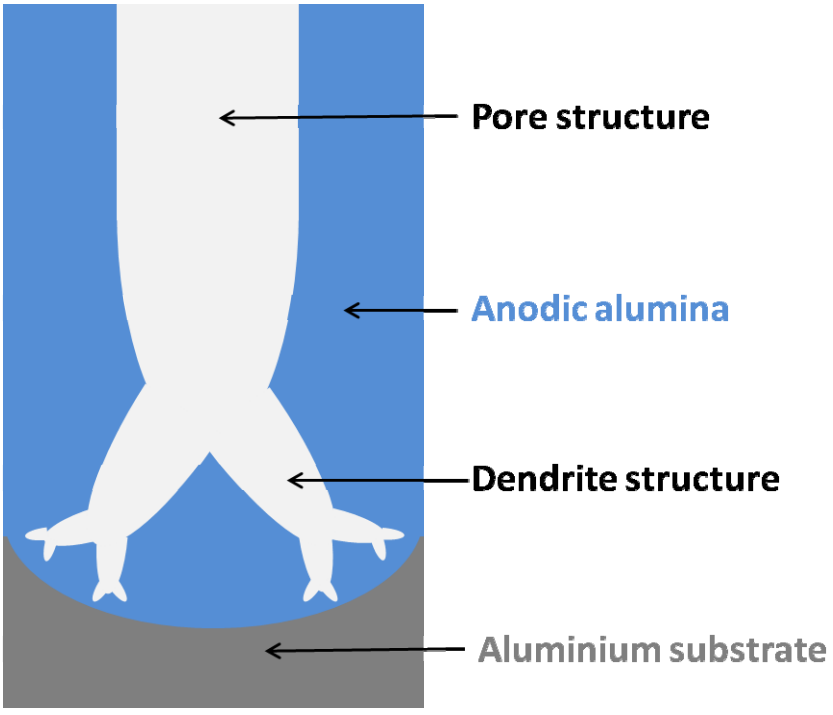

Figure 1.6: Schematic representation of the barrier layer reduction on the aluminium substrate with the dendrite structures.

1.1.5. Preparation of Nano-Porous Anodic Alumina Membranes (NAAM).

There are several ways to prepare NAAM's. All of them require chemical or electrochemical etching.

In this work, we have used a method based on another previously used in our laboratory [6]. A schematic diagram is presented in Figure 1.7.

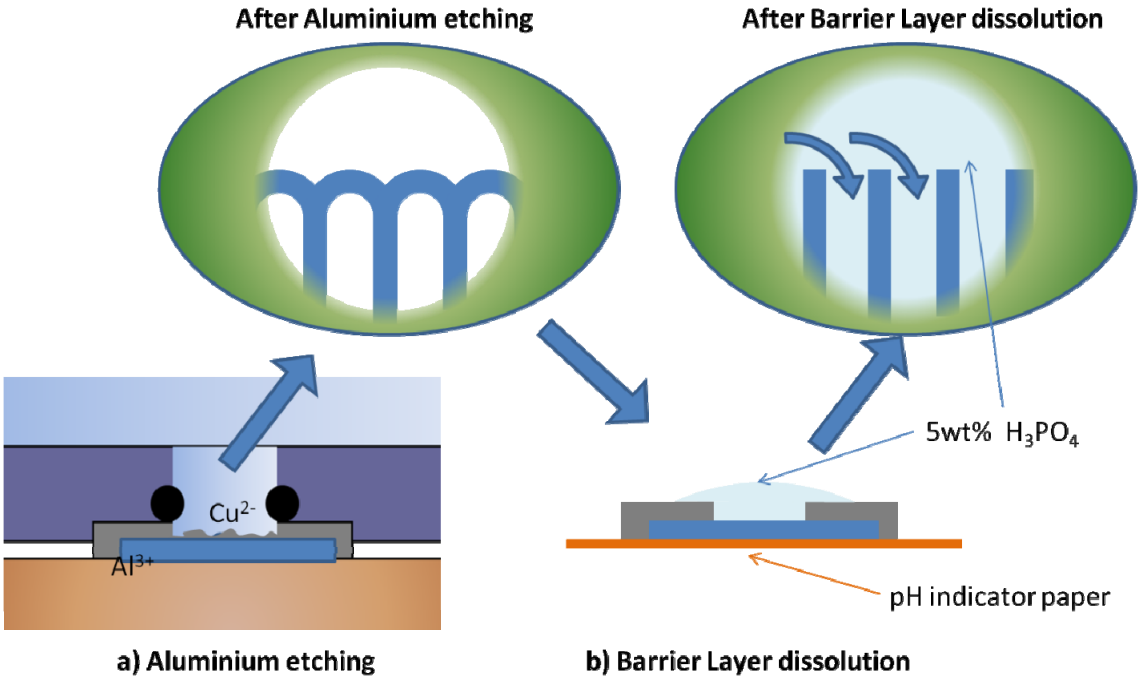

Figure 1.7: Method for the preparation of NAAM. a) Chemical etching of Aluminium in order to remove it; b) Chemical etching of the barrier layer in order to open the bottom part of the pore.

The preparation of the membrane takes two steps:

Removal of the Aluminium substrate.

In the first step we have to remove the Aluminium under the NAAF (Figure 1.7a). We do this by chemical reaction. This method is based on the chemical reaction between the aluminium and aqueous solution composed by 0.1 M of Copper chloride ($CuCl_2$) and 3 M of Hydrochloric acid (HCl). The Copper salt oxides the aluminium foil following the next reaction:

$$Cu^{+2}(aq) + 2e^- \rightarrow Cu^0(s) \qquad E^0 = 0.34\,V$$

$$Al^0(s) - 3e^- \rightarrow Al^{+3}(aq) \qquad E^0 = -1.68\,V$$

$$3Cu^{+2}(aq) + 2Al^0(s) \rightarrow 3Cu^0(s) + 2Al^{+3}(aq)$$

$$E^0{}_{redox} = E^0{}_{redution} - E^0{}_{oxidation} = 0.34V - (-1.68V) = 2.02V$$

As we can see in previous equation the potential reaction is positive, this means that the process has a negative Gibbs energy (ΔG^0) and therefore is spontaneous and exothermic.

Since although alumina is mechanically hard material, it is also a very fragile, so it is quite difficult handle it free-standing. Preparing NAAMs by this method requires NAAFs with thicknesses of tens of microns in order to avoid mechanical breaking the alumina layer since the chemical reaction is strong enough to break the anodic alumina film causing a risky situation. This chemical etching is not as selective as the previous one, since once the metallic Aluminium is consumed, the solution keep on etching the Aluminium atoms of the NAAF, so we must be very careful when the remaining Aluminium is nearly consumed. This is a very exo-thermal reaction, so the temperature will increase during the process, accelerating the reaction at the same time. This is an undesirable fact which can damage the mechanical structure of the NAAF making it unusable or even could lead to the complete dissolution of the anodic alumina, provoking an acidic leak. In order to control the temperature and hence the etching strength, the solution concentration can be reduced by adding ultrapure water. In this way we can refrigerate and dilute the solution.

When the base of the NAAF is exposed, we have to remove the etching solution and the sample from the Teflon cell and rinse it with ultrapure water in order to avoid contamination which could damage the sample.

Removal of the barrier layer.

Once the Aluminium substrate has been removed, the anodic alumina barrier layer is uncovered and it can be etched. The etching is carried out by using a Phosphoric acid based solution with a 5wt% concentration at room temperature. This process is extremely sensitive to some parameters as the concentration or temperature, and small changes of them varies significantly the etching rate, so it is no advisable fixing a etching time since it could be different from one to another sample.

Our method is simple and obviates small changes on the etching conditions (Figure 1.7b). We face down the sample on a pH indicator paper and put a drop of phosphoric acid solution on the top of the barrier layer. When the barrier layer begins to disappear the acidic solution goes through the nano-channels and reaches the pH indicator paper changing its colour. After that, the membrane is immersed into ultrapure water for several minutes in order to rinse it. Then the sample is dried. We repeat the process a second time to be sure that the most of the pores are open. Then, rinsed thoroughly with ultrapure water and dry it again.

This method optimizes the etching time and reduce significantly the pore widening compared to other methods which involves immerse the whole sample into the phosphoric acid solution.

1.2. Electrodeposition processes for synthesis of nanowires.

1.2.1. Pulsed electrodeposition.

Electrodepositing with the Aluminium substrate as electrode, we need to reduce the barrier layer as explained in section 1.1.4. After this step the sample is ready to be electrodeposited by this technique.

This kind of electrodeposition is composed by the combination of galvanostatic, potentiostatic and recovering pulses repeated successively.

The first pulse is the galvanostatic pulse during which the deposition of the metal takes place. The magnitude of this pulse depends on the material which is going to be electrodeposited, but the length will be always around 12 ms. The metallic ions go through the pore till the pore base which acts as cathode and get reduce obtaining the necessary electrons becoming metallic material.

The second pulse is the potentiostatic pulse. The magnitude of this pulse has to be the same as the last potential applied during the barrier layer reduction procedure and its length is about 4ms. Its function is discharging the remaining barrier layer since acts as a capacitor. This pulse also can repair possible alumina cracks and homogenise the barrier layer after the previous deposition pulse.

The third part of the cycle is a period during which no voltage or current is applied. The aim of this pulse is to maintain constant both ion concentration and pH of the electrolyte at the interface where the deposition takes place. So by increasing this time, more homogeneous will be the electrodeposition.

Due to the geometry of the system this is a bottom up technique, so the filling of the pores takes place from the dendrite structure upwards as is shown in Figure 1.8 :

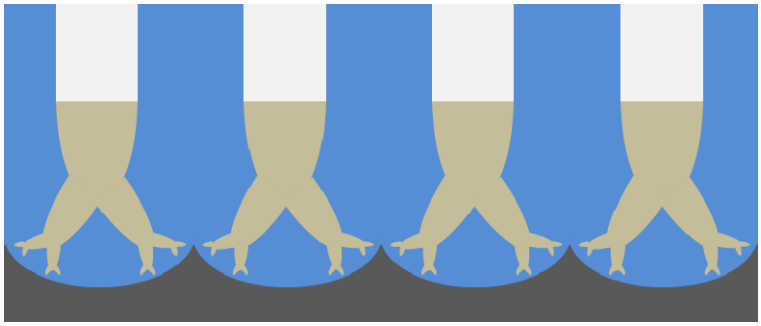

Figure 1.8: Schematic representation of electrodeposited metal filling the dendrite structure after barrier layer reduction.

1.2.2. Potentiostatic electrochemical deposition.

The experimental set-up for potentiostatic electrochemical deposition (PECD) requires a three electrode configuration which consists of one working electrode, one counter electrode and one reference electrode.

There are different types of reference electrodes.

After finishing the process depicted in section 1.1.5, a metallic layer must be grown on one of the sides. This metallic layer will act as the working electrode where the electrodeposition takes place. The thickness of the metallic layer must be thick enough to close the nanopores again. In our case, we have used a rotary-pumped sputter coater model Quorum Q150R to sputter a Gold layer of 150 nm thickness (Quorum). The counter electrode is the Platinum electrode.

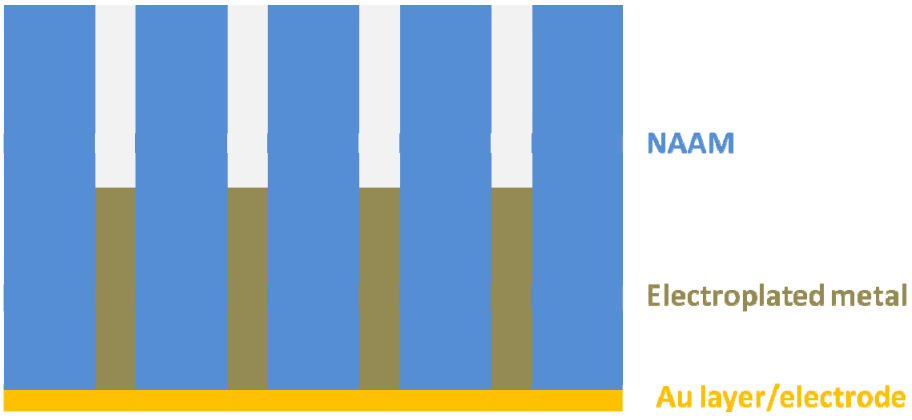

Figure 1.9: Schematic representation of the NAAM prepared for metal electroplating.

The sample is placed into an electrochemical cell as shown in Figure 1.1. After that, the electrolyte containing the metallic ions covers the three electrodes being slowly stirred in

order to renew the solution at the electrolyte/metal interface. During this process the source act as voltage supply and applies a constant voltage.

1.3. Hydrothermal process for nanostructured materials.

1.3.1. Preparation and fabrication of Zinc Oxide nanorods.

The hydrothermal growth process of Zinc Oxide (ZnO) involves three phases which are represented in Figure 1.10 :

- Growth promoting solution: This is an aqueous solution based on Zinc Nitrate Hexahydrate, $Zn(NO_3)_2 \cdot 6H_2O$ (99.999%) and Hexamethylenetetramine (HMT), $(CH_2)_6N_4$.
- Catalyst layer: or seed layer, which has a double role; as precursor adsorbed-decomposer and as crystal lattice supporting the crystallization of ZnO nanorods.
- Solid crystalline product: ZnO nanorods.

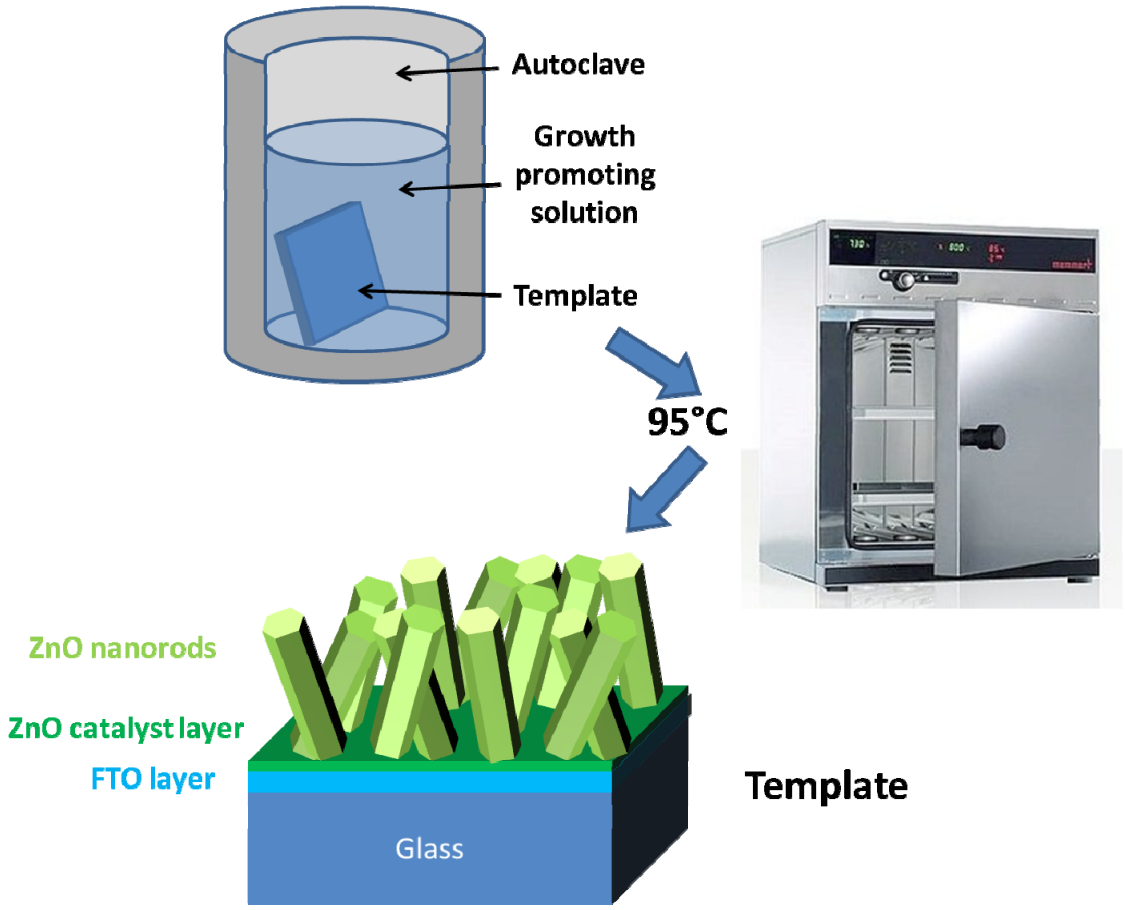

Figure 1.10: Schematic representation of the experimental set-up for hydrothermal growth and the template structure after the process.

The template is a Fluorine-doped tin oxide film, (SnO_2:F), also called FTO, covering a glass substrate. The template is previously cleaned by ultrasounds first with ethanol, second, with acetone and finally, rinsed with ultrapure water in order to remove organic impurities on the transparent conductive surface. This kind of substrate is very convenient for our purpose since both glass and FTO are transparent to the visible range of the light spectrum, in addition of the fact the FTO is a high conductive material.

On the other hand, since FTO has a tetragonal structure it is necessary a second layer which matches with the ZnO lattice. That is the reason why we have to deposit a ZnO thin layer (10nm). In our case, we perform the deposit by Atomic Layer Deposition (ALD) technique. This method allows the deposition monolayer by monolayer resulting in a very homogeneous layer which thickness can be controlled with high accuracy. The metal precursor is Di-ethyl Zinc (DEZ), $Zn(C_2H_5)_2$, and the Oxygen precursor is water. The substrate is placed into a chamber at 200°C where is alternatively exposed to the precursors. The chamber is purged with Argon gas between exposure and exposure. The deposition rate is 0.7 Å/cycle, so we perform 70 cycles in order to obtain a 10 nm film thickness. After the ALD process the substrate is annealed at 400°C by applying a rate of 30°C/min, in air atmosphere to improve the crystal quality of the ZnO layer.

An alternative procedure to obtain a catalyst layer is dipping the substrate into other solution with the finality of depositing a ZnO layer of particles. The substrate is dipped into an organic solution formed by Ethanol, 0.005M Zinc Acetate, $Zn(O_2CCH_3)_2$, and 0.005M Diethilamine, $(C_2H_5)_2NH$,. This solution is heated up to 60°C so that after the substrate is immersed, slowly removed and quickly evaporated 5 to 6 times, remains a ZnOH sol-gel layer. The substrate with the ZnOH sol-gel layer is annealed up to 450°C at 30°C/min during 1 hour. The reaction process is as follows:

$$Zn(Ac)_2 \rightarrow Zn^{2+} + 2Ac^-$$

$$(Et)_2NH + H_2O \rightarrow (Et)_2NH^+ + OH^-$$

$$2OH^- + Zn^{2+} \rightarrow Zn(OH)_2$$

$$Zn(OH)_2 \rightarrow ZnO + H_2O$$

This method, although is cheaper, results in a more inhomogeneous catalyst layer and less reproducible results. As consequence, the subsequent nanorods growth is less uniform.

The FTO templates are placed in oblique position into a Teflon autoclave in order to avoid precipitation on the catalyst layer. This autoclave is filled with growth-promoting solution covering the FTO template and then hermetically closed. The container is placed into a Memmert oven which is heated at a rate of 3°C/min up to 95°C in order to activate the chemical reaction for growing the ZnO nanorods.

We can control the diameter of the resultant nanorods by varying at par the molar concentration of the precursors. On the other hand, the length can also be controlled by the time of the growing process, but after 12 hours the reaction slow down and the nanorods will not grow anymore.

After the hydrothermal growth the sample is removed from the autoclave, rinsed with ultrapure water and dried with Nitrogen gas.

1.3.2. Deposition of semiconductor quantum dots.

The deposit of CdS quantum dots is based on a method know as successive ionic layer absorption and reaction (SILAR) [15]. This method consists of several cycles of two dip-coating steps of the ZnO nanorods on the template into the precursor solutions during 10 to 15 seconds each, before rinse with water. A schematic diagram is presented in Figure 1.11.

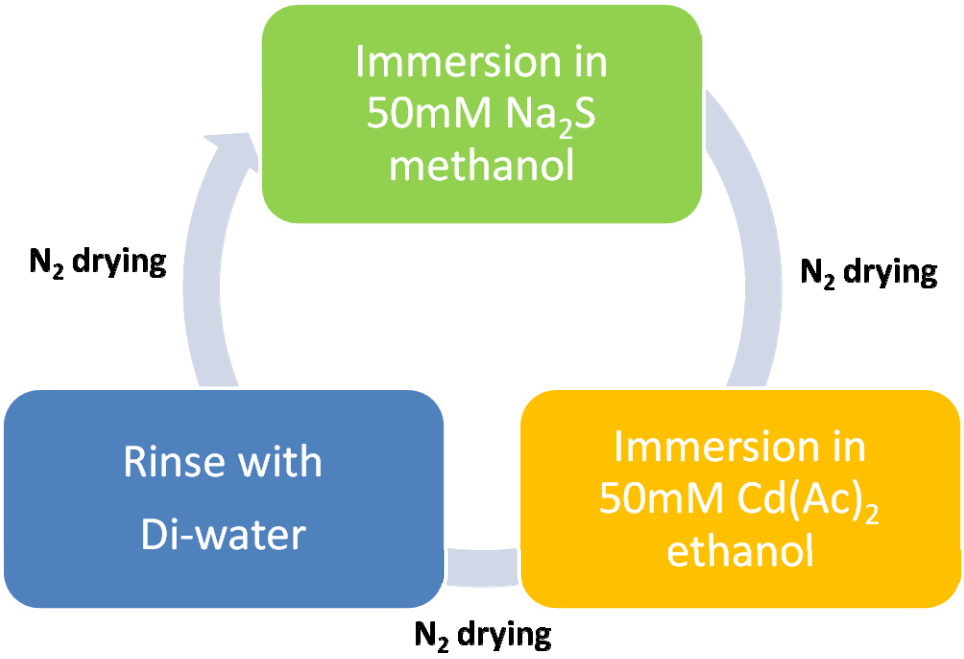

Figure 1.11: Schematic diagram of the SILAR process for CdS coating.

The S^- solution precursor consists of Sodium sulphide, Na_2S (98%), dissolved into methanol to form a 50mM solution. On the other hand, the Cd^+ solution precursor consists of Cadmium acetate dehydrate, $Cd(CH_3CO_2)_2$ (98%), dissolved into ethanol to form a 50 mM solution.

1.4. Characterization techniques.

1.4.1. Scanning Electron Microscopy (SEM).

This technique allows us to obtain micrographs at high resolution of organic and inorganic materials. In comparison with the optic microscopy, the light is replaced by the electron beam, and the optical lenses by electromagnets. The samples need to be conductive enough to transport the electrons, so in case it would be necessary, the samples must be coated by a conductive layer, usually, Gold or Chromium.

The selected surface of the sample is scanned with a highly concentrated electron beam. The electrons can be dispersed by the sample or can induce the generation of secondary electrons. The dispersed electrons or secondary electrons are collected and counted by a detector, which is an electronic device suited close to the sample stage. There are also several types of dectectors vCD, TLD...

The software becomes the electric signal into a micrograph composed by pixels. As the electron beam scans the surface of the sample and the electrons collected by the detector, the micrograph is presented on the screen. The scanning electron microscopes can reach magnifications up to 500kx or ever higher as we will see in this manuscript. These kinds of microscopes also provides images with high focus depth which means that it is possible to obtain more realistic micrographs making easily the interpretation of the scanned surface.

These measurements were carried out at the Interdepartamental Service for Research (SiDI, Spanish abbreviation) from the Automomous University of Madrid (UAM, Spanish abbvervitation) with a Philips XL30 SFEG and at the electronic microscopy services of the Materials Sciences Institute of Madrid (ICMM, Spanish abbreviation)

1.4.2. X-ray diffraction spectrometry.

X-ray diffraction technique provides us information about the structure of the material. It is possible if a given material is amorphous or crystalline starting from the diffractograms. In case

of a crystalline material it is also possible determining the existing crystalline phases and the crystalline grain sizes [16].

The diffraction phenomenon comes described by the Bragg equation (Eq.1.4).

$$\text{Eq. 1.4:}\quad n\lambda = 2d_{hkl}\sin\theta$$

Where λ is the wavelength of the incident wave, d_{hkl} is the distance between the planes with the miller indexes (hkl), and θ the angle formed by the propagating vectors of the incident and scattered waves.

Since we do not work in ideal conditions the diffraction peaks are enlarged. The widening of the peaks is attributed to several reasons, which we could summarize in two:

- Widening due to the measurement instrument, due to the lack of radiation monochromaticity and the divergence of the incident beam.
- Widening due to the material itself, since we do not work with monocrystals.

From this widening it is possible determining the average crystal grain size by Debye-Scherrer formula (Eq. 1.5):

$$\text{Eq. 1.5}\quad Grain\ Size_{hkl} = \frac{k\cdot\lambda}{\beta\cdot\cos\theta}$$

Where we took k = 0.9, λ the wavelength of the radiation λ_{Cu} = 1.54060 Å, β is the full width at half maximum, or half-width in radians and θ is the position of the maximum of diffraction.

The orientation parameter is given by Eq. 1.6:

$$\text{Eq. 1.6:}\quad Orientation\ parameter = \frac{\frac{I_m}{I_p}}{\sum_{n=1}^{n^{\circ}of\ peaks}\frac{I_m}{I_p}}$$

Where I_m is the measured intensity of the peaks on the diffractograms and I_p is the standard powder intensity from the data base form the International Center for Diffraction Data (ICDD).

The measurements have been performed in a diffractometer Siemens D-5000, employing radiation CuKα (λ = 1.54060 Å) in configuration $\theta - 2\theta$, with an angle resolution of 0.016 ^{o}.

The resolution of the equipment is around of 1%, this means that if you have a phase with a concentration of this order, it could not appear in the XRD spectra. Also, if we are working near of that limit, the quantitative results (i.e., the proportional relation between the maximum

intensity and the relative concentration of the compound which belongs to the maximum) begin to not be reliable.

This equipment belongs to Interdepartmental Research Service (SIdI) from Autonomous University of Madrid (UAM).

1.4.3. Rutherford Backscattering Spectrometry (RBS).

Accelerator.

The facility where the experiments were carried out at the Centre for Micro Analysis of Materials, (CMAM), is a 5 MV terminal voltage tandem accelerator [17]. A scheme of the tandem accelerator is presented in Figure 1.12:

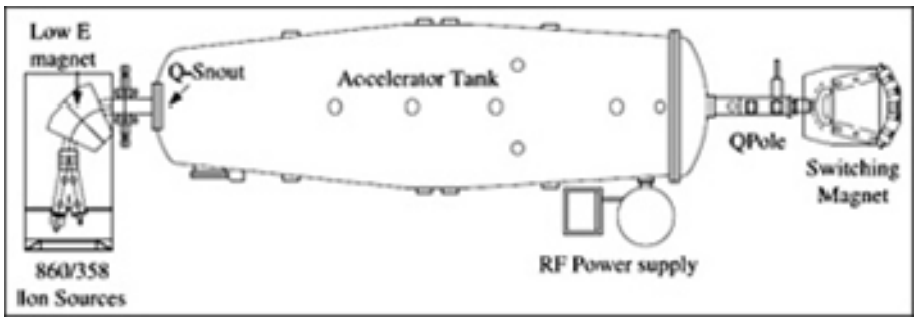

Figure 1.12: Scheme of the tandem accelerator at the CMAM [17].

On the first stage of the facility is placed the ion source, which is able to produce any ion from Hydrogen even to Uranium. Actually is two ion sources, one for H and He and the other for the rest of the elements. We are going to focus on the model HVEE-358 Duoplasmatron ion source which is purpose is producing H and He.

In this model, a two-stage discharge is involved in the generation of the ion beam. The first discharge is sustained by the thermionic electron emission from a filament (cathode). An intermediate electrode acts as the anode for the first discharge and is equipped with an aperture in its centre. The discharge is guided through the axial magnetic field in the aperture into the second discharge chamber. The second discharge is maintained between the intermediate electrode, which now acts as a cathode, and the main anode. The strong axial magnetic field generated in this region confines the plasma into a small volume, and is responsible for the high plasma density. The ions from the second discharge flow through the anode aperture into the extraction region.

Duoplasmatron source can be configured to produce both, negative and positive ions. In the case which we're dealing with Helium ions, they are produced on their positive charge mode, . After being extracted from the source, He^+ ions are injected into a Lithium charge-exchange canal. Inside this canal, Lithium vapour exchange electrons with Helium beam, becoming this negative.

Now the He^- ions are coming into the accelerator tank. For the same terminal voltage the ions accelerated in the first type can achieve much more energy, since they are accelerated twice, once to the terminal voltage itself and another, after negative to positive charge exchange, till the end of the accelerator. The charge exchange is obtained by stripping of electrons when ions cross a well defined region at the terminal, which is filled with high purity nitrogen gas.

After the He ions have been accelerated, they are going through the quadrupole which focalize the He^+ ion beam before being irradiated on the sample.

Rutherford Backscattering Spectrometry, RBS.

Rutherford backscattering spectrometry (RBS) is a powerful Ion Beam Analysis (IBA) technique used in materials science for the determination of the composition (and structure when combined with ion channelling).

The fundamental of this technique is irradiating a sample with a high energy ion beam (H^+ or He^+ ions at 1-5Mev). The energy transfer during the elastic collision process between the incident ions and the solid is analyzed in terms of energy conservation, Eq. 1.7 :

$$\text{Eq. 1.7:}\quad E_1 = k \cdot E_0$$

Where *k* is the kinematical factor, Eq. 1.8:

$$\text{Eq. 1.8:}\quad k = \frac{m_1 \cos\theta \pm \sqrt{m_2^2 - m_1^2 (\sin\theta)^2}}{m_1 + m_2}$$

Those light ions that are backscattered by the nucleus of the atoms and collected by a detector placed at angles higher than 90° and lower than 180°. A schematic representation of a typical experimental setup is presented in Figure 1.13:

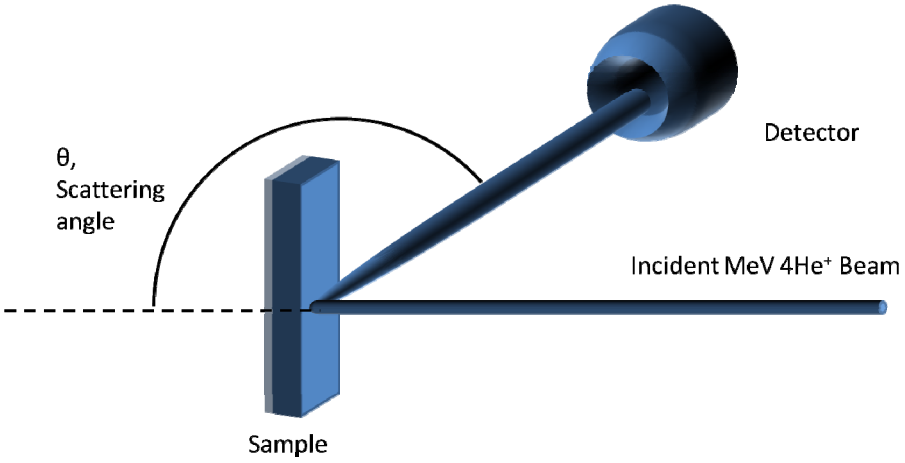

Figure 1.13: Schematic representation of the experimental setup for a RBS experiment.

The higher the mass of an atom that is hit by an ion beam, the higher the energy of the ion will be after backscattering. This results in mass discrimination and, by counting the scattered ions as a function of energy, the number of atoms of each element present can be determined.

Apart from mass information, the main skill of RBS is the depth resolution (in the nm scale). During the flight path through the sample, the ions lose energy, and this energy loss per unit distance is known for every material, allowing the conversion of the RBS spectrum into a depth profile. For example, an ion scattered at a certain depth will lose more energy (on the way in and out of the target) than an ion scattered by the same atom but at the sample surface.

1.4.4. Thermo-gravimetry.

The thermal analyses were carried out with a SDT Q600 TA Instruments. The samples can be heated from room temperature up to 1150°C.

By mean of this technique, the mass of a substance is measured as a function of temperature, while the substance is subjected to a controlled temperature program.

Thermogravimetry (TG) technique measures the quantity and rate of weight change of a given sample as function of temperature and/or time into a controlled atmosphere. In a general way, it allows measuring in order to determine the composition of the materials and predict its stability at temperatures up to 1150°C. Therefore, this technique can characterize materials which present losses or increase weight due to decomposition, oxidation or dehydratation.

These measurements were carried out in the Instituto de Ciencia de Materiales de Madrid (ICMM) in the support laboratory of thermal analysis.

1.4.5. Reflectance Spectrometry: Ultraviolet-Visible and Near-Infrared (UV-Vis-NIR) spectrum.

Reflectance spectroscopy is the study of light as a function of wavelength that has been reflected or scattered from a solid, liquid, or gas. The incident wavelength used in this technique can vary from UV to X-ray, depending on the sample characteristics or information we want to extract from the spectrum. In our case we have used a range wavelength within the UV-Vis-NIR spectra. This spectromety is very usefull to characterize the absorption, A, transmission, T, and reflectivity, R, of materials, where A+T+R=1. The principle of this technique is represented on Figure 1.14:

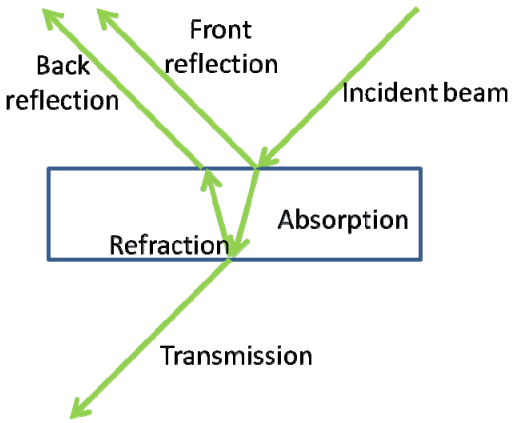

Figure 1.14: Diagram of the beam paths in UV-Vis-NIR spectrometry.

We have used a spectrophotometer from Perkin-Elmer model Lambda 950, placed at the facilities of Instituto de Cerámica y Vidrio (ICV). With this spectrophotometer is possible to scan from 200 nm up to 3300 nm wavelength.

A typical spectrophotometer consists of three main parts:

- Light Sources: One Tungsten lamp covering wavelengths down to 320 nm, and one Deuterium lamp ranging from 320 nm down to 200 nm.
- Monochromator: The incoming light pass through the grating filtering a monochromatic light beam.
- Detectors: Silicon photodiode in the range of UV-Vis, and PbS for the NIR range.

In particular, the spectrophotometer used in our experiments dispose of a double monochromator in order to increase the resolution, and a double beam system which allows measuring the baseline and the sample at once, so that, possible variation on the beam intensity does not affect to the measurements. A scheme of the spectrophotometer is presented in Figure 1.15:

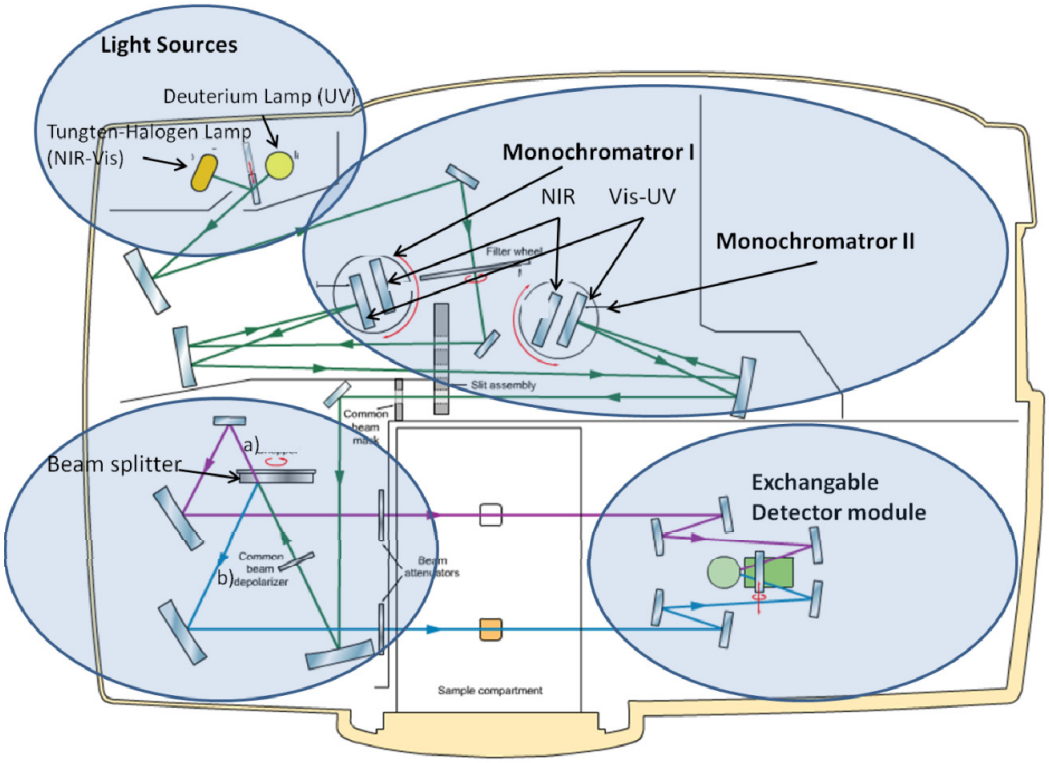

Figure 1.15: Schematic representation of the used spectrophotometer able to cover the UV-Vis-NIR range spectra. It is possible to differentiate the light sources, the double monochromator, the beam splitter which splits in two the light beam: a) reference beam and b) sample beam, and finally the exchangeable detector module.

Moreover, in the detector module we have use an accessory to measure variable angle specular reflectance, capable to perform direct reflectance measurements between 8 to 70° incident beam. A scheme of this device is presented on Figure 1.16:

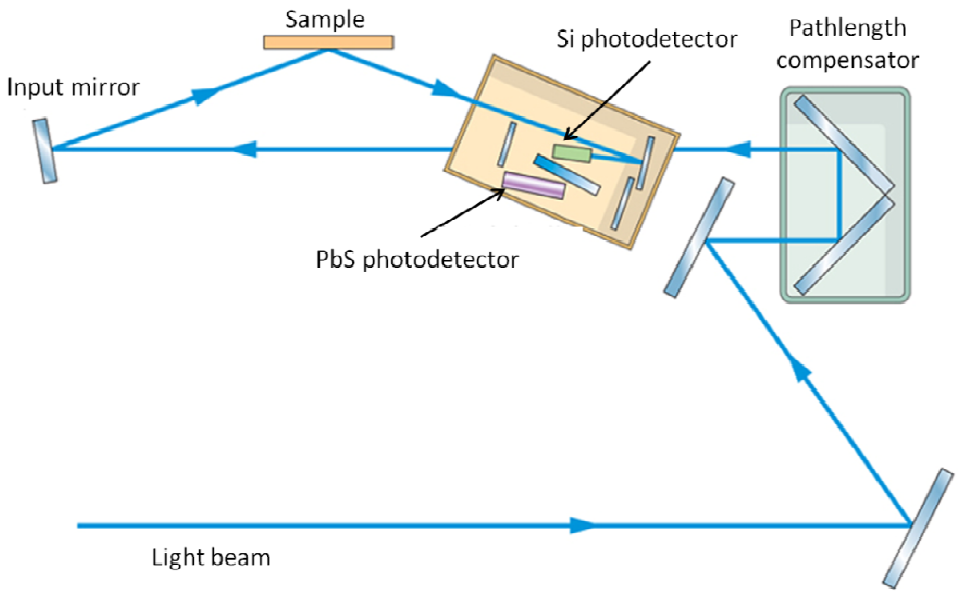

Figure 1.16: Scheme of the variable incident angle device for specular reflectance. The sample remains at the same position while the input mirror and the detectors assembly can change their angle and position, so that is possible measuring between 8 to 70° of incidence angle beam.

This technique is very useful for characterization of films and the study of the interferences created, colorimetry or photocatalitic properties of semiconductors.

1.4.6. Photoluminescence spectrometry.

The photoluminescence (PL) measurements were performed in Labram HR800 VIS-NIR model from Jobin Yvon [18]. The light source is a He-Cd laser (325 nm), using a diffraction grating of 1200 l/mm and lens of 40X. Spectra acquisition time: 0.5 s.

Photoluminescence spectroscopy is a contactless, non-destructive method of probing the electronic structure of materials. Light is directed onto a sample, where it is absorbed and imparts excess energy into the material in a process called photo-excitation.

In the case of photo-excitation, this luminescence is called photoluminescence. The intensity and spectral content of this photoluminescence is a direct measure of various important material properties.

Photo-excitation causes electrons within the material to move into permissible excited states. When these electrons return to their equilibrium states, the excess energy is released and may include the emission of light (a radiative process) or may not (a nonradiative process). The energy of the emitted light (photoluminescence) relates to the difference in energy levels

between the two electron states involved in the transition between the excited state and the equilibrium state. The quantity of the emitted light is related to the relative contribution of the radiative process.

The most common radiative transition in semiconductors is between states in the conduction and valence bands, with the energy difference being known as the band gap. Band gap determination is particularly useful when working with new compound semiconductors.

Radiative transitions in semiconductors also involve localized defect levels. The photoluminescence energy associated with these levels can be used to identify specific defects, and the amount of photoluminescence can be used to determine their concentration.

1.4.7. Infra-red spectrometry.

Molecular spectrometry is the study of the interaction of the electromagnetic radiation with matter. Depending on the spectra region which is scanned, i.e. the energy of the used radiation, characterized by the wavelength (λ) or wave number (cm^{-1}), this interaction will be of different nature. The molecules change their vibrational and rotational energy state when absorbs infrared (IR) radiation. The study of IR spectra in the case of solid and liquid samples, only must be taken into account the changes in vibrational energy states, which makes possible the characterization of the main functional groups of the molecular structure of a given compound.

Although the IR spectra extends from 10 up to 14000 cm^{-1}, approximately, from the functional and applications point of view, it is divided in three regions: Far IR, medium IR and near IR.

The equipment used in our experiments is a FT-IR Bruker IFS66v, with a spectral range of measure from 20 up to 7000 cm^{-1}. These measurements were carried out at the Interdepartmental Research Service (SIdI) from Autonomous University of Madrid (UAM).

1.4.8. Photoelectrochemical characterization.

Electrochemical Workstation CHI760C (three electrode system) is being used for the water splitting test. Photoelectrochemical cell (PEC) or photoanode, is connected to the working electrode (WE) while the Pt electrode (counter-electrode, CE) is connected to the auxiliary electrode (AE), plus an Ag/AgCl electrode as the reference electrode (RE). Electrodes are then being immersed into 0,5M of sodium chloride (NaCl, as the electrolyte for bare ZnO) or into the 0,25M Na_2S + 0,35M $NaSO_3$ mixture (as the electrolyte for CdS-coated ZnO). The

experimental set-up is showed in Figure 1.17a and b). Note that for the photoanode side, only the ZnO or ZnO/CdS surface can be immersed into the electrolyte. Other part such as the FTO surface and the crocodile clip must not touch the electrolyte to avoid short circuit. Exposed area of FTO at the side or bottom edges of the PEC must be covered by nail polish and dried in order to prevent direct contact between electrolyte and the FTO.

Xenon lamp (ScienceTech Inc.) is used as the light source to provide 110 mW/cm^2 of solar light (AM 1.5 condition). At one side of the electrolyte container, there is a transparent quartz window (area = 1.3 cm × 1.3 cm) in order to allow solar light passes through the container and illuminates on the sample. Both Linear Sweep Voltammetry (LSV) and Amperometric i-t curve are being measured and recorded by this workstation.

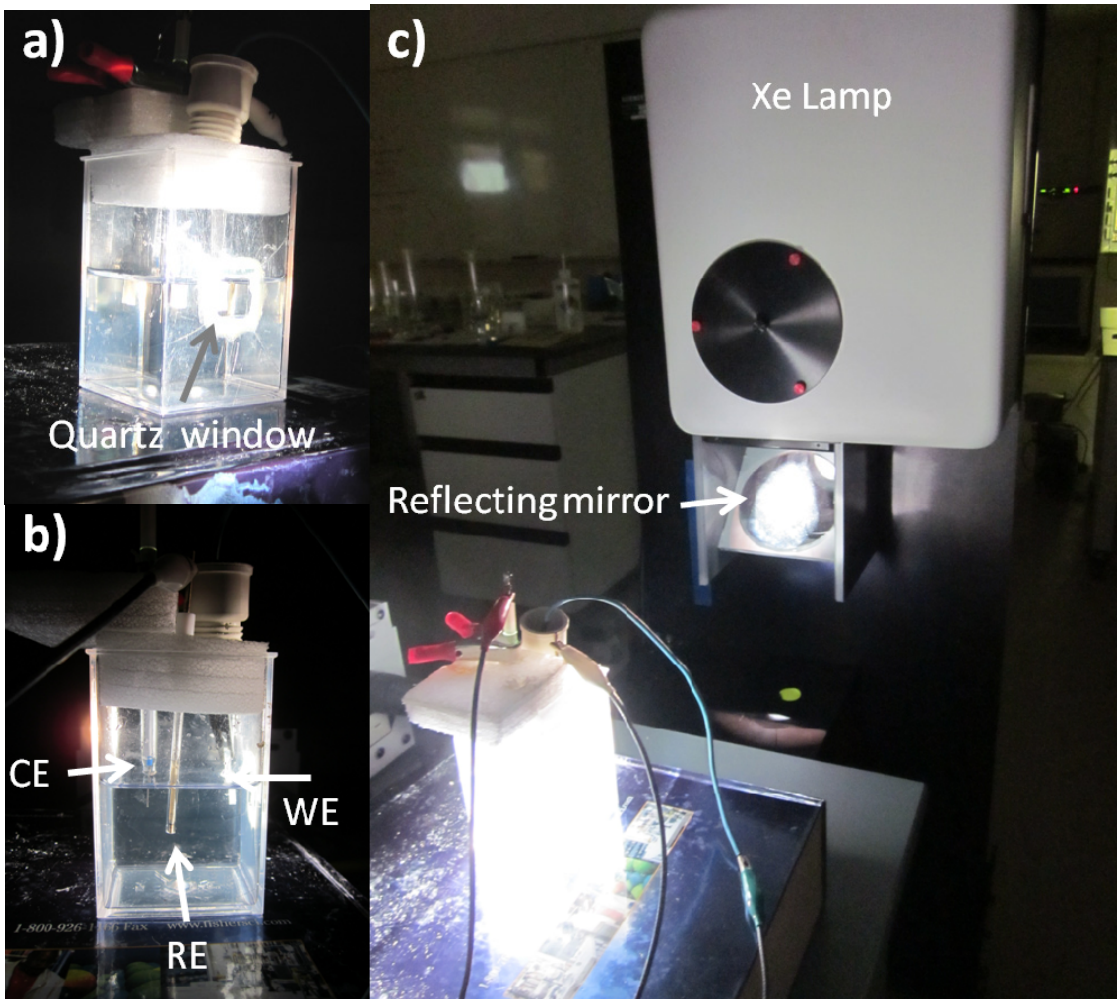

Figure 1.17: Electrolyte container a) with quartz window view; b) three electrodes (WE, CE, RE) view, and c) solar light simulator source with the three electrodes set-up.

Other test like Incident Photon to Charge Carrier Efficiency (IPCE) and reflectivity were scanned at Zolix Solar Cell Scan100 instrument (see Figure 1.18)[19]. IPCE indicates the ratio of the number of photons incident on a solar cell to the number of generated charge carriers. Specifically, QE is a measure of the external efficiency, while IPCE is a measure of the internal efficiency; that is, the photons reflected back from the surface of the cell are not considered.

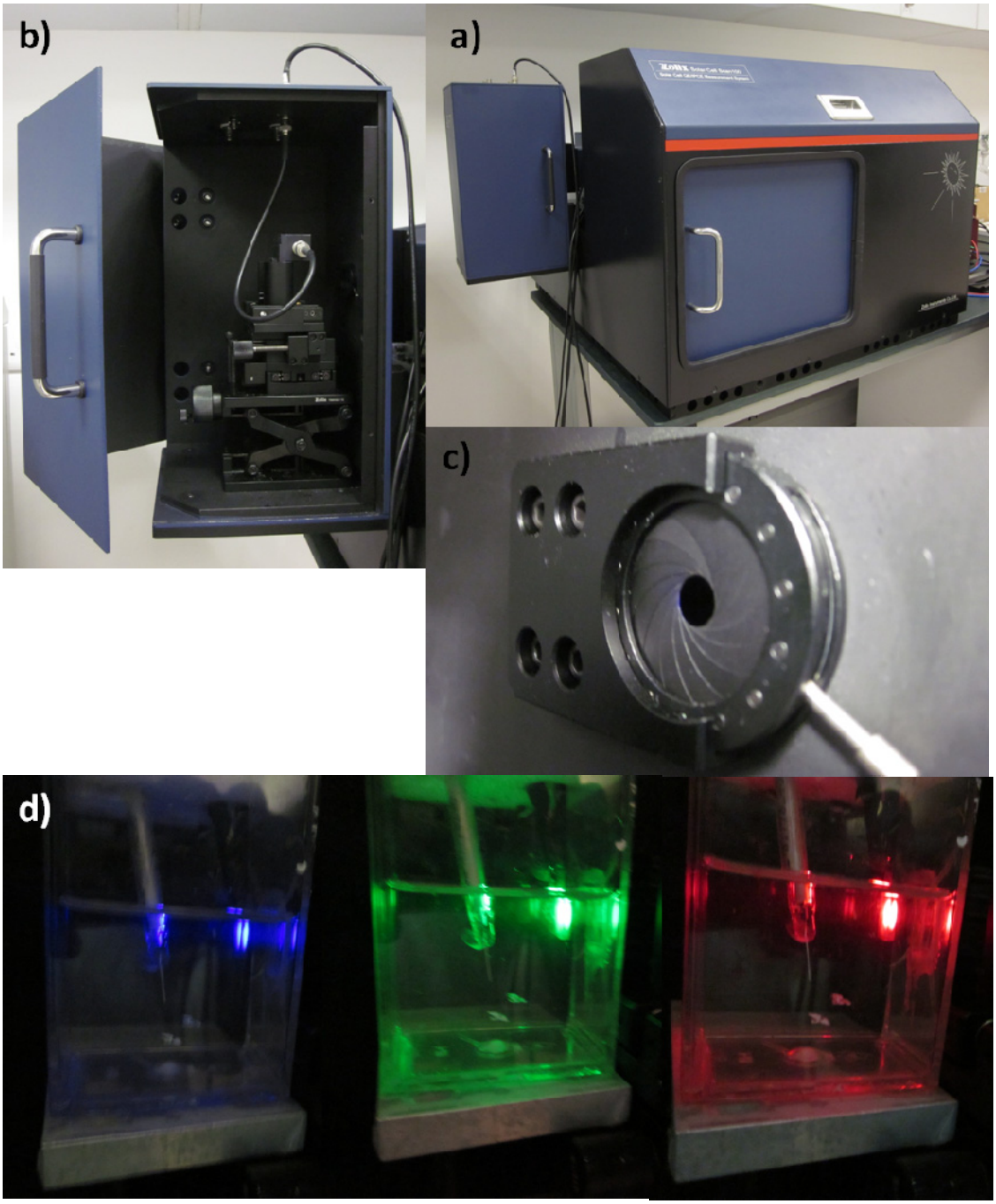

Figure 1.18: a) Zolix Solar Cell Scan100 instrument; b) chamber where the measurements are carried out; c) entrance hole of monochromatic light; d) sequence of images of a PEC exposed to monochromatic light while it is measured.

1.4.9. Vibrating Sample Magnetometer

This technique was developed by Foner, who built the first Vibrating Sample Magnetometer, (VSM) in 1959 [20].

Its operation is based on the induction Faraday's Law. First we have to calibrate the system; we have to relate the magnetization value of the pattern with its induced voltage. To measure the magnetization of one material using this system, the sample is placed between two detector coils and begins to vibrate with simple harmonic motion.

The hysteresis loops were obtained with an EV7 VSM from LOT-Oriel Company [29] in ICMM-CSIC. This equipment uses an electromagnet which, depending on the distance between its poles, it is possible applying a maximum external field of 1.8 T. The accuracy which the system is able to stabilize the applied field is less than 0.1 Oe and the maximum distance between the pole pieces is 82 mm. The most important parts of the VSM are: the vibrator which causes oscillatory movement of the sample; the fastening system of the rod where is placed the sample; the detection coils and the electromagnet. The alternate voltage induced in the coils is detected by a lock-in amplifier that avoids drift and filters out all other signals with different frequency of that of the oscillation of the sample.

References

1. Montero-Moreno, J.M., M. Sarret, and C. Mueller, *Self-ordered porous alumina by two-step anodizing at constant current: Behaviour and evolution of the structure.* Microporous and Mesoporous Materials, 2010. **136**(1-3): p. 68-74.
2. http://www.goodfellow.com/.
3. http://www.chemical-ecology.net/java/solvents.htm.
4. Li, A.P., et al., *Polycrystalline nanopore arrays with hexagonal ordering on aluminum.* Journal of Vacuum Science & Technology a-Vacuum Surfaces and Films, 1999. **17**(4): p. 1428-1431.
5. Masuda, H., et al., *Highly ordered nanochannel-array architecture in anodic alumina.* Applied Physics Letters, 1997. **71**(19): p. 2770-2772.

6. Otero, D.N., *Fabricación y Caracterización de Arreglos de Nanohilos Magnéticos en Películas Nanoporosas de Alúmina Anódica*, in *Applied Physics Department*2006, Universidad Autónoma de Madrid.
7. Instruments., K., *Series 2400 SourceMeter. User's Manual.* 2011.
8. Masuda, H. and M. Satoh, *Fabrication of gold nanodot array using anodic porous alumina as an evaporation mask.* Japanese Journal of Applied Physics Part 2-Letters, 1996. **35**(1B): p. L126-L129.
9. Masuda, H. and K. Fukuda, *ORDERED METAL NANOHOLE ARRAYS MADE BY A 2-STEP REPLICATION OF HONEYCOMB STRUCTURES OF ANODIC ALUMINA.* Science, 1995. **268**(5216): p. 1466-1468.
10. Masuda, H., F. Hasegwa, and S. Ono, *Self-ordering of cell arrangement of anodic porous alumina formed in sulfuric acid solution.* Journal of the Electrochemical Society, 1997. **144**(5): p. L127-L130.
11. Jessensky, O., F. Muller, and U. Gosele, *Self-organized formation of hexagonal pore arrays in anodic alumina.* Applied Physics Letters, 1998. **72**(10): p. 1173-1175.
12. Li, A.P., et al., *Hexagonal pore arrays with a 50-420 nm interpore distance formed by self-organization in anodic alumina.* Journal of Applied Physics, 1998. **84**(11): p. 6023-6026.
13. Furneaux, R.C., W.R. Rigby, and A.P. Davidson, *THE FORMATION OF CONTROLLED-POROSITY MEMBRANES FROM ANODICALLY OXIDIZED ALUMINUM.* Nature, 1989. **337**(6203): p. 147-149.
14. Nielsch, K., et al., *Self-ordering regimes of porous alumina: The 10% porosity rule.* Nano Letters, 2002. **2**(7): p. 677-680.
15. Li, J.J., et al., *Large-scale synthesis of nearly monodisperse CdSe/CdS core/shell nanocrystals using air-stable reagents via successive ion layer adsorption and reaction.* Journal of the American Chemical Society, 2003. **125**(41): p. 12567-12575.
16. Cullity, B.D., *"Elements of X-Ray Diffraction".* Editorial Addison Wesley London, 1978.
17. http://www.cmam.uam.es/.
18. http://www.inspirenano.com/Equipment/Equipment-Items/FOCAS/Horiba-Jobin-Yvon-Inverted-LabRAM-HR800-VIS-NIR.aspx.
19. http://www.zolix.com.cn/templates/channelen/index_37_20.html.
20. Foner, S., Review of scientific instruments, 1959. **30**: p. 548-557.

Chapter 2. Study in Low Voltage Anodization of Aluminium based on Sulphuric acid electrolytes.

2.1. Introduction.

In the last decades, the synthesis of low dimension structures on previously designed templates become to prevail over other traditional synthesis strategies. In this regard, it is noticeable the use of Nanoporous Anodic Alumina Films (NAAF) as templates, particularly, those obtained from sulphuric acid solutions by double anodization process at different temperatures, voltages and acid concentrations [1-7] or by using highly ordered two-dimensional nanoparticles arrays as a pre-pattern for subsequent anodization [8]. Recently the growth of NAAF in hard anodization conditions with the possibility of modulate the pore walls [9-17] is really opening a new era in the synthesis of more sophisticated functional nanostructures.

Nowadays, one of the most difficult tasks in the study of structures at nanometric level is the determination of their characteristic geometric parameters with higher accuracy. Great scientific and technological efforts to determine parameters such as: porosity, pore diameter distributions or interpore spacing have been made. Among them we can mention: i) ellipsometry studies [18-21] in which the final results are highly dependent on the previous analytical information for developing optimized structural models; ii) gas adsorption experiments where not always is clear the solid – fluid interactions that could be determinant in the adsorption hysteresis and capillary condensation [22] and also the collective desorption phenomena could have great influence on the results specially in the smaller pore diameter and spacing ranges [23]; iii) pore filling technique [24-26] which could give place to irreversible phenomena in the starting matrices and also an overestimation of the pore sizes. Surface parameters can also be evaluated by Transmission Electron Microscopy (TEM) [27], Atomic Force Microscopy (AFM) [28] and the most extended Scanning Electron Microscopy (SEM). Regarding the latest, the used technique could lose reliability due to low image quality, researcher subjectivity or poor statistic analysis, particularly, in the case of profile studies through several pores [29, 30]. Fast Fourier Transform (FFT) is one of the most used powerful

tools for SEM micrographs processing [5, 31-35]. However, recently, novel methods based on pair distribution function, angular distribution functions and grain analysis [36, 37] as well as on derivatives and autocorrelation functions of cumulative frequency distributions of the objects brightness [38] have been reported to reach further quantitative analysis of the morphological and geometrical features of self-ordering hexagonal lattices.

From the physical-chemical point of view, it is widely accepted that the highly ordered NAAF growth takes place by mean of quasi-static self-ordering process enhanced by the effect of external electric field in potentiostatic conditions [39]. In addition, it has been demonstrated that the optimum self-ordering conditions occur only under specific values of internal and external thermodynamic parameters such as, temperature, electrolyte concentration, etc. [27]. In this way, the pore growth constitutes collective phenomena in which the pores locate in those places where preferable thermodynamic conditions exist. So, just under self-ordering regime the pore growth tendency should be that equivalent to a minimum energy configuration, i.e., forming ideal equilateral triangles among them. Deviations from the ideal self-ordering conditions will provoke local or total loss of order and symmetry in the nanoporous structure.

Taking into account the significant statistical nature of the phenomena described above in this work, we use self-correlation function (SCF) given by Eq. 2.1 for HRSEM image processing to evaluate the ordering degree of porous surfaces, geometric parameters and porosity of NAAF:

Eq. 2.1: $$G(n\delta, m\varepsilon) = \sum_{n,m} f(x,y) f(x+n\delta, y+m\varepsilon)$$

where: f(x, y) and f(x+nδ, y+mε) denotes the intensity measured on the image area in the (x, y) coordinates and (x+nδ, y+mε) respectively; δ and ε stand for the pixel lengths along x and y axis respectively; and, n and m are integer numbers.

The application of SCF to HRSEM micrographies gives a mathematical image in the real-space, here identified as self-correlation image (SCI), i.e., G(nδ, mε) in Eq. 2.1. So, SCI's represent an alternative to FFT and pair distribution functions to evaluate the ordering degree of a given surface, and, in addition, they allow a easier and faster data treatment for determining NAAF geometric characteristics, such as, interpore distances and particularly pore diameters which is

not possible to determine by previously mentioned methods. This statistical tool also leaves out the subjective factors and interpretations involved in other techniques.

In order to determinate surface parameters in highly ordered arrays of low dimensional pores it has been applied SCF to three different series of NAAF grown in sulphuric acid solutions as electrolyte in a systematic study. In this way we have calculated ordering degree, pore diameter, interpore distance, and porosity mean values of such nanostructures in a broad size range.

The study of the composition of the anodic alumina is also a very important task in order to understand the growth mechanism of the nanopores. In particular, the study of the anion incorporation into the alumina matrix is a fundamental issue and the focus of important works since long time ago [24, 40]. Several techniques have been used for compositional and formation mechanism studies in different publications. It is common the use of Rutherford Backscattering Spectrometry (RBS), in which García-Vergara et al. are specialist [41-43], or Thermo-Gravimetry (TG) [44-46], or Infra-red spectrometry (IR) [45, 47, 48] in compositional studies of anodic alumina. The broad range of fabrication parameters which we have employed during the development of the samples concerning this chapter, allow us to perform a systematic and deep study for the composition of the NAAF's by combining three different and complementary techniques as RBS, TG and IR.

Others important topics as the oxide formation efficiency during the aluminium anodization process and the volume expansion factor have been broached in this chapter. These two issues are also directly related to the formation and growth mechanism of anodic aluminium oxide, giving rise to recent and outstanding publications with theoretical and mathematical models [49, 50]. The study of the volume expansion factor has very interesting applications in the study of confined anodic alumina growth [51]. Other works suggest a change in the alumina growth, pore generation and self-ordering mechanism basing their studies in the volume expansion factor [39, 52-55].

The next task broached in this work has been the optical characterization and the study of the optical properties by mean of an optical model based on a effective medium. It is of crucial importance the approximation of the effective medium in order to calculate the refraction index. An effective medium is considered when a random unit cell embedded in the effective medium is not detectable in an experiment using electromagnetic radiation confined to a

specific wavelength range [56]. Regarding this topic there are several interpretations to discuss, since there are several alternatives, as D.E. Aspnes described [57]. D.E. Aspnes developed an effective medium theory from basic principles. He generalizes the Clausius-Mossotti equation to obtain the Lorentz-Lorentz, Maxwell-Garnett and Bruggeman expressions. If we have a heterogeneous medium with two composites, *a* and *b*, which are mixed in an atomic scale, with two dielectric functions, ε_a and ε_b, and their volumetric fractions are f_a and f_b, and we assume they are in vacuum, i.e. ε=1, then we have the Lorentz-Lorentz effective medium expression Eq. 2.2:

$$\textbf{Eq. 2.2:}\quad \frac{\varepsilon-1}{\varepsilon+2} = f_a \frac{\varepsilon_a-1}{\varepsilon_a+2} + f_b \frac{\varepsilon_b-1}{\varepsilon_b+2}$$

But, if the two composites consist on large regions and, they are not in vacuum but in a host medium, ε_h, then we have Eq. 2.3:

$$\textbf{Eq. 2.3:}\quad \frac{\varepsilon-\varepsilon_h}{\varepsilon+2\varepsilon_h} = f_a \frac{\varepsilon_a-\varepsilon_h}{\varepsilon_a+2\varepsilon_h} + f_b \frac{\varepsilon_b-\varepsilon_h}{\varepsilon_b+2\varepsilon_h}$$

In addition, if *b* is a small fraction and *a* is the rest, then the composite *b* is the host, i.e. $\varepsilon_b = \varepsilon_h$. Then, Eq. 2.3 can be expressed as the Maxwell-Garnett effective medium equation, Eq. 2.4:

$$\textbf{Eq. 2.4:}\quad \frac{\varepsilon-\varepsilon_a}{\varepsilon+2\varepsilon_a} = f_b \frac{\varepsilon_b-\varepsilon_a}{\varepsilon_b+2\varepsilon_a}$$

In the case where f_a and f_b are comparable, then, both medium can be considered as host medium. In order to simplify, it is possible to choose $\varepsilon = \varepsilon_h$ in Eq. 2.3, so that, we would obtain the Bruggeman expression, also known as Effective Medium Approximation (EMA), Eq. 2.5:

$$\textbf{Eq. 2.5:}\quad 0 = f_a \frac{\varepsilon_a-\varepsilon}{\varepsilon_a+2\varepsilon} + f_b \frac{\varepsilon_b-\varepsilon}{\varepsilon_b+2\varepsilon}$$

Here, we considered two possibilities which we could apply to our porous films:

- Maxwell-Garnett effective medium (M-G, from now on).
- Bruggemann expression or EMA.

The optical properties related to the porous anodic alumina have been widely studied [19, 58-60]. Here we focus this work on the study of the refraction index and other characteristics of the NAAF as porosity and thickness, which can be calculated from the former. Several works are related to do this, and many of them use the Bruggemann approximation in their calculus from spectroscopy ellipsometry[18-21, 58, 61]. J. Vereecken et

al. [18, 21, 58] assume an optical model of three layers, Al(substrate)/Al + Al_2O_3/Al_2O_3+voids, the fittings are not very good but it could be due to roughness or the use of hexagonal pattern even if the porous are not ordered. Others justify the use of Bruggemann approximation because it is used for porosities higher than 20-30% and distinguish between the cylindrical porosities and nano-porosities intrinsic to the anodic alumina which would be around 33% [19, 20]. They relate these nanoporosities to the volume expansion due to gas bubbles originated during the anodization process [62], and take into account the optic anisotropy of the porous anodic alumina.

Some others relate de refraction index with the thickness of the film [63]which is quite doubtful since the refraction index is an intrinsic parameter of the material. To our opinion, the variation is due to other parameters since the samples were grown under different conditions, which could affect to their composition. NAAFs are also characterized by optical transmission spectra [64, 65] demonstrating that the refraction index is not dependent on the thickness, but it is dependent on the composition of the samples.

On the other hand, it is possible to study the refraction index and also the thickness by reflectance spectroscopy and basing the calculus in the Maxwell-Garnett effective medium model [66]. In this work they assume a lot of approximations. The calculus start from assume that the refraction index of the pure alumina is a constant, i.e. not dependent on the wavelength, and only take into account the cylindrical porosities, but even with this they obtain quite accurate thickness values and refraction index which are inside of what would be expected.

Finally, the use of NAAF's as template for magnetic materials is very extended due to the high versatility and wide range of opportunities which offer mostly since the appearing of self-ordered NAAF. The hexagonally ordered structure of the pores, together with the nanoscale diameters and variation of aspect ratio allows the modification of magnetic properties of magnetic materials[67-75]. In this work we take advantage of the reduced pore diameters of the NAAFs fabricated and perform Co electroplating into the nanopores to study their magnetic properties.

2.2. Fabrication of low anodization voltage NAAF's on Sulphuric acid based electrolytes.

The general experimental procedure is described in section **1.1.1**. Aluminium foils (99.999% from Goodfellow) were cleaned and electro-polished. H_2SO_4 aqueous solutions with 3, 10 and 20 wt % were used as electrolytes to grow the NAAF series. The Aluminium foils were anodized by two-step potentiostatic anodization process applying 28, 25, 23, 20, 17, 14, 11, 8 and 5V. The sample labels and general anodization conditions used in this work are shown in *Table 2-1.*

Table 2-1: Sample labels, electrolyte acid concentration and applied voltages.

		Applied Voltages (V)								
Sample Series	**[H_2SO_4] (wt %)**	**28**	**25**	**23**	**20**	**17**	**14**	**11**	**8**	**5**
A	**3**	A28	A25	A23	A20	A17	A14	A11	A8	A5
B	**10**		B25	B23	B20	B17	B14	B11	B8	B5
C	**20**		C25	C23	C20	C17	C14	C11	C8	C5

The anodization processes were performed using a homemade electrochemical cell made with Teflon, with an inner chamber surrounding its walls (Figure 1.2). A cooling liquid is continuously flowing within the chamber. This cooling system provides a high thermal stability to the process. In both anodization steps, the electrolytes temperature was kept constant at 0.0 ºC and the same stirring rate was applied. In all cases, the first anodization time was 16 hours, the second anodization time for the A Series was 150 minutes and for B and C Series was 20 minutes in order to maintain the thickness of the most NAAF within a range not larger than 10µm. NAAF surface images were received from High Resolution Scanning Electron Microscope (HRSEM), Philips XL-30.

The main characteristics of both the technique and the facility used for the compositional analysis of the samples are described in section 1.4.3 Rutherford Backscattering Spectrometry (RBS) was performed in order to determine the sulphur concentration of the samples due to the incorporation of anionic species from the electrolyte into the alumina. These experiments were carried out by irradiating He^+ ions at 3035 eV which is the oxygen resonance energy . IR spectra were collected with a FT-IR Bruker IFS60v spectrometer in Diffuse Reflectance regime . The thermal analyses were carried out with a SDT Q600 TA Instruments doing Thermo-

Gravimetric Analysis (TGA) simultaneously. The samples were heated from room temperature to 1100°C with a heating rate of 10°C/min under Nitrogen atmosphere at flow of 100ml/min.

The main features of the reflectance technique are described in section 1.4.5. Reflectance spectra were performed in a Perkin Elmer spectrophotometer Lambda 950 with 45° incidence angle of wavelengths between 200-2650nm. In our special case, we have used a configuration which differs a little from the typical. We measured the samples at an incident angle of 45° by using the Universal Reflectance Accesory (URA). The reason for this is increasing the optical pathway of the thinner NAAF's to win data out of the spectra interferences. The data processing was carried out by using Mathematica software, with which were developed a simple iterative method to do calculations of refraction index and thickness values of the NAAF's.

2.3. Study of current densities and kinematic of NAAF growth.

2.3.1. Study of current densities.

The evolutions of current densities in function of the time for the different samples are represented in *Figure 2-1*. We could set sample A25 as the reference sample since is grown under typical conditions for self-ordering [76, 77]. Two different behaviours of the current density can be observed in the graphs represented in *Figure 2-1*. First, the typical anodization curves when the current density reaches a steady-state related with a homogeneous growth, and second, high and non-uniform current densities obtained by using parameters higher than the typical conditions for this kind of anodization. In this case, we have the sample A28 with 28V which is higher than the usual 25V or samples B25 and C25 which were grown with 10 and 20wt% sulphuric acid concentration, much higher than the typical 3wt%.

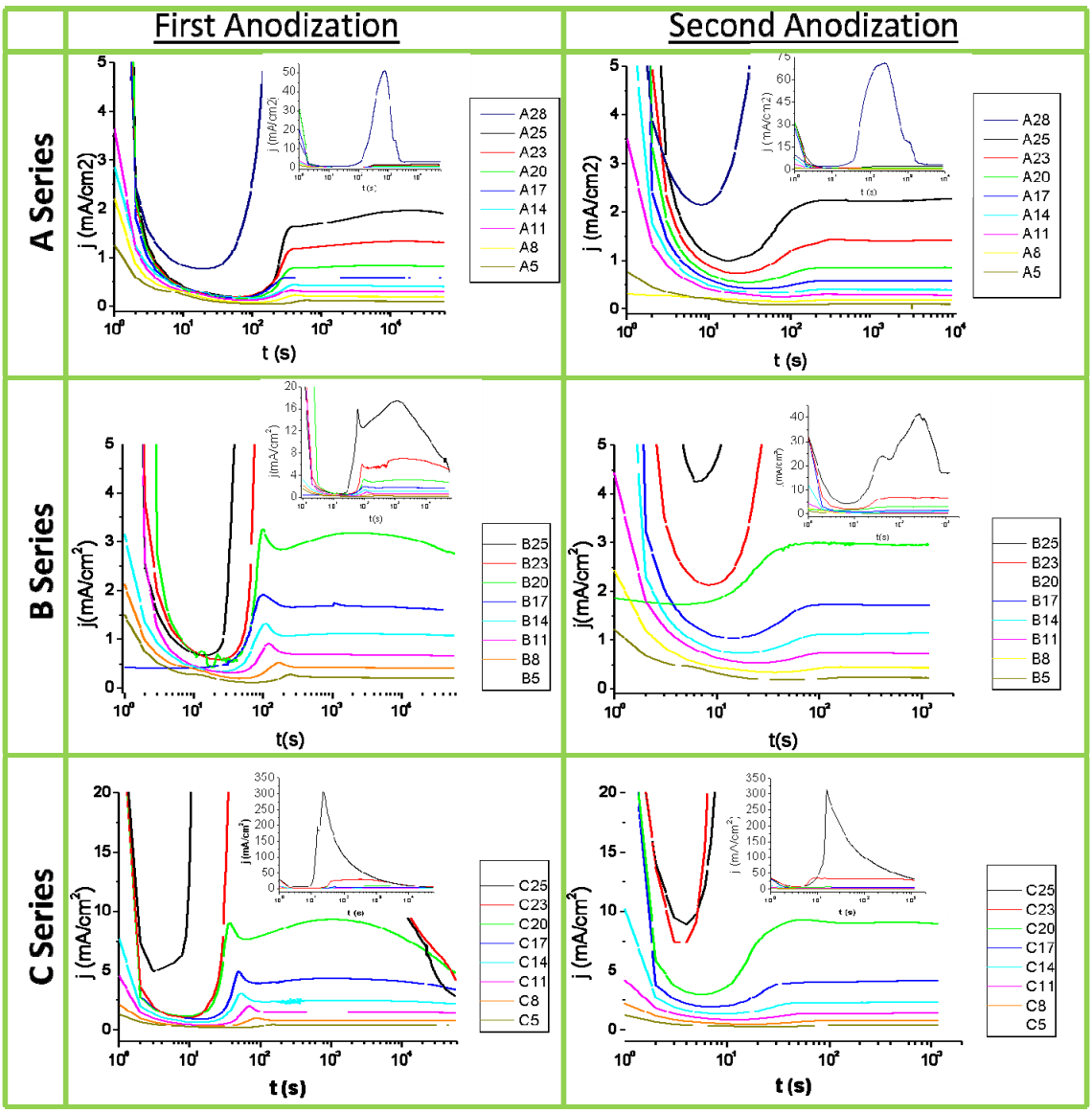

Figure 2-1: Current densities evolution in function of the time for A, B and C Series for first anodization (16h) and second anodization (150 minutes for A Series and 20 minutes for B and C Series respectively). In the insets are represented the higher current densities which are out of scale.

These high current densities provokes what has been called “white burning”[78] which induces mechanical instabilities on the surface of the samples [79, 80] as we can observe in some examples showed in *Figure 2-2*, having A25 sample as reference.

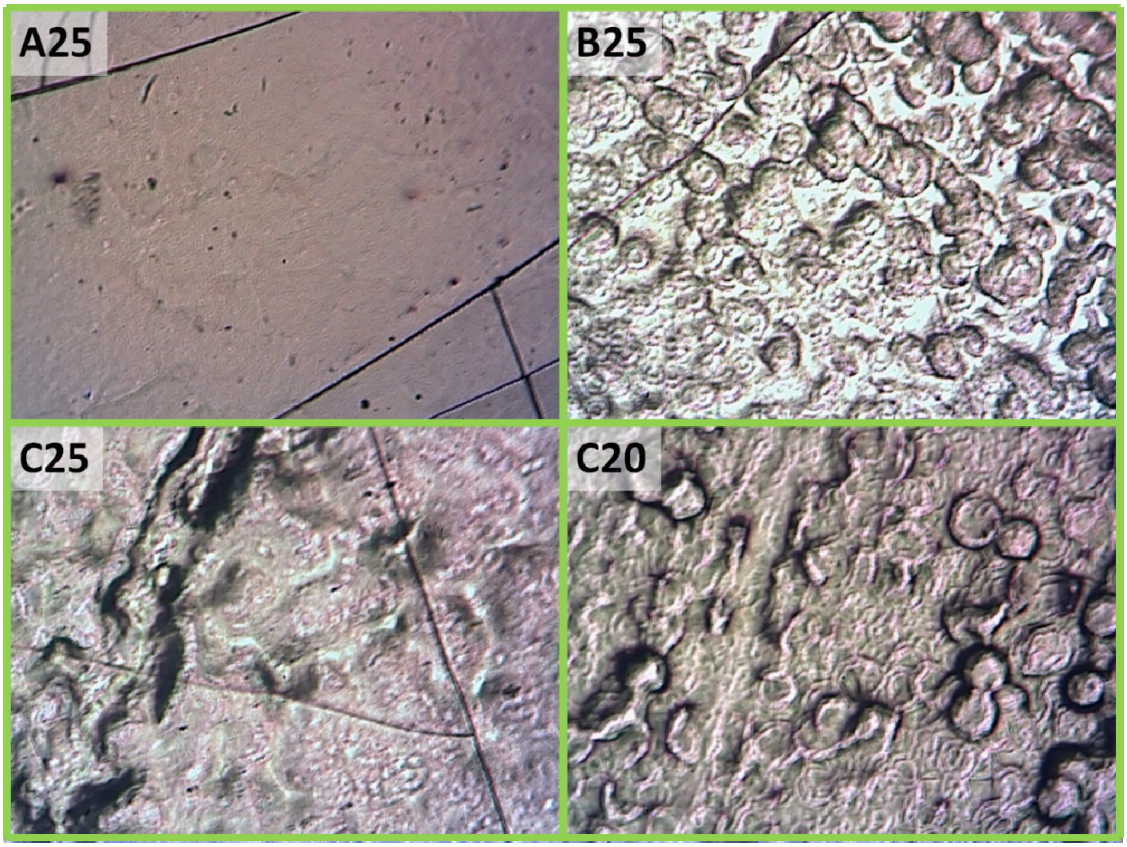

Figure 2-2: Optical microscope images of the surface from samples A25, B25, C25 and C20. The images were taken with x50 magnification lens.

From these graphs represented in Figure 2-1 we can intuit a dependence of the average current density for each sample on the applied potential. So, in we have represented this average current density in function of the applied voltage *Figure 2-3*. Samples with non-uniform current density have been excluded for this study. From these graphs an exponential dependence on the applied voltage is observed in all the series. As can be observed there is no difference between the current densities of the first and second anodization for the same sample, except for those with the higher voltages and sulphuric acid concentrations as A25, B23, C23 and C20. The simple explanation for this fact is that, after certain anodization time the current density begins to decrease slightly as can be observed in the first anodization graphs of *Figure 2-1*, so, since for the second anodization we use a shorter times, the current density sill have not began to decrease.

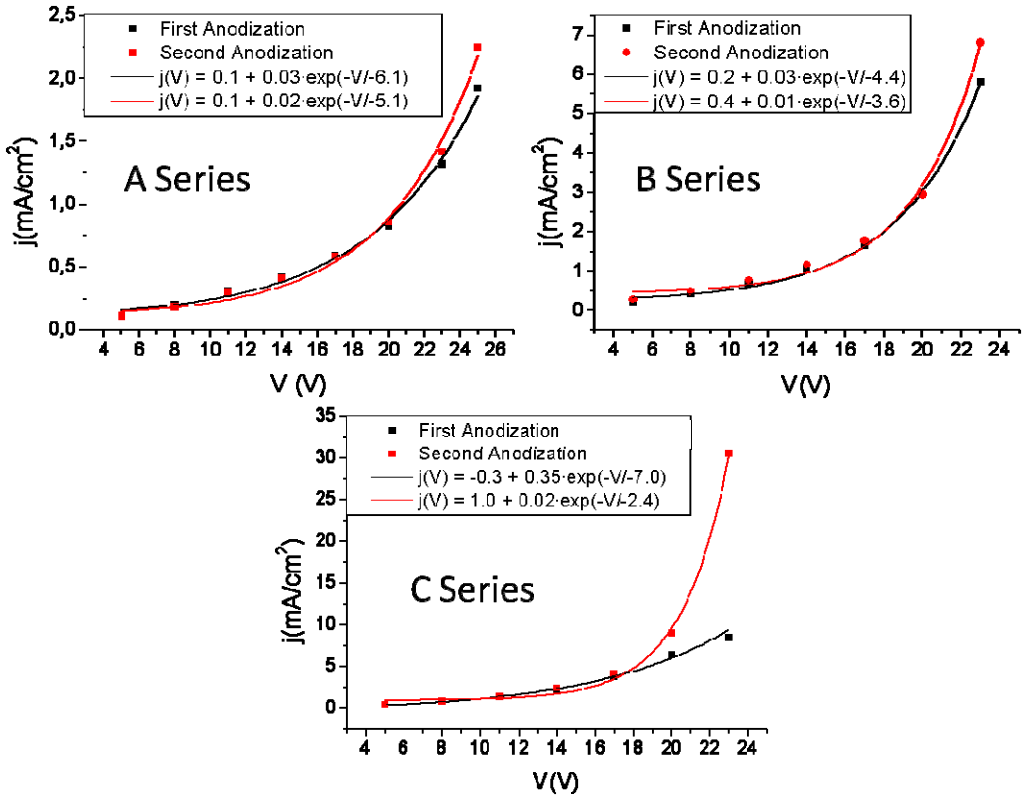

Figure 2-3: Average current densities for A, B and C Series on first and second anodization and its dependence on the applied voltage.

It also can be observed the influence of the sulphuric acid concentration in the electrolyte for each anodization voltage. We can see this more clearly in the graphs of *Figure 2-4*. In these graphs, the current density has been represented in function of the applied voltage and sulphuric acid concentration in the electrolyte for each series and voltages. It can be observed that, the higher sulphuric acid concentration and voltage, the higher the current density.

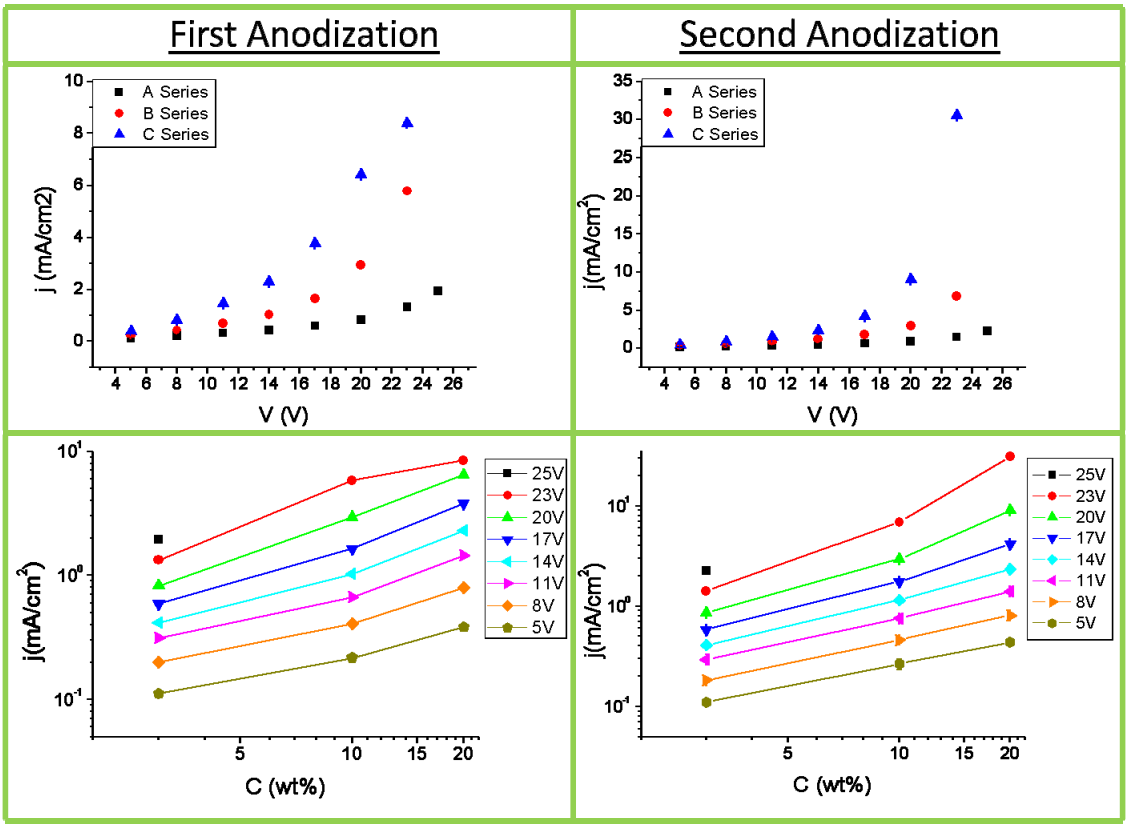

Figure 2-4: Dependence of the average current density on the applied voltage and sulphuric acid concentration in electrolyte for first and second anodization.

It is not easy to determine the moment when the barrier layer begins to become porous layer at the first stages of the growth. But in order to have an idea of the time it takes to start the pore formation we have noticed the minimum current density point for the first and second anodization of each series. It is clear that at that point the anodic alumina has already initiated the porous layer formation, as we can observe in *Figure 2-5* where is showed the second anodization interrupted when the current density reaches the minimum value.

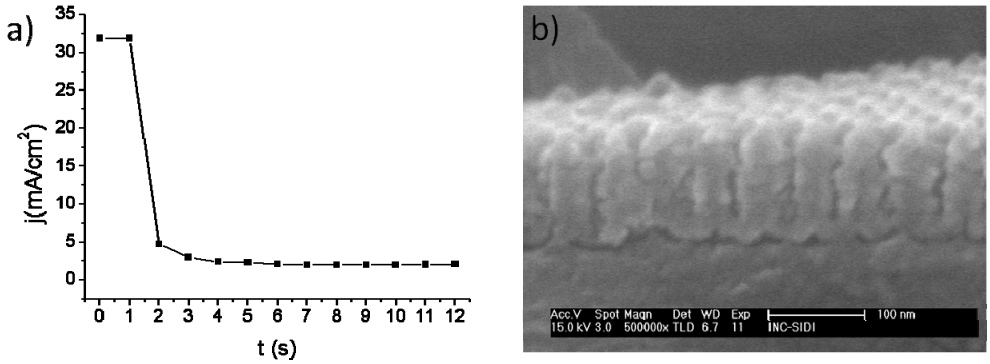

Figure 2-5: a) Evolution of current density for a sample grown applying 23V using a 10wt% sulphuric acid based electrolyte during 12 seconds of second anodization; b) Cross-section micrograph of that sample.

These points have been represented on the graphs of *Figure 2-6*. We can observe an exponential dependence on the applied voltage with the time which reaches the minimum value of current density. Moreover, this time is longer for the first anodization process than for the second. This is because, for the first anodization process, the Aluminium substrate is flat and there is no preferential ways for the electric field to go through the anodic alumina, at the contrary than during the second anodization, when the pattern is formed on the substrate, so the electric field lines focuses directly on the pits.

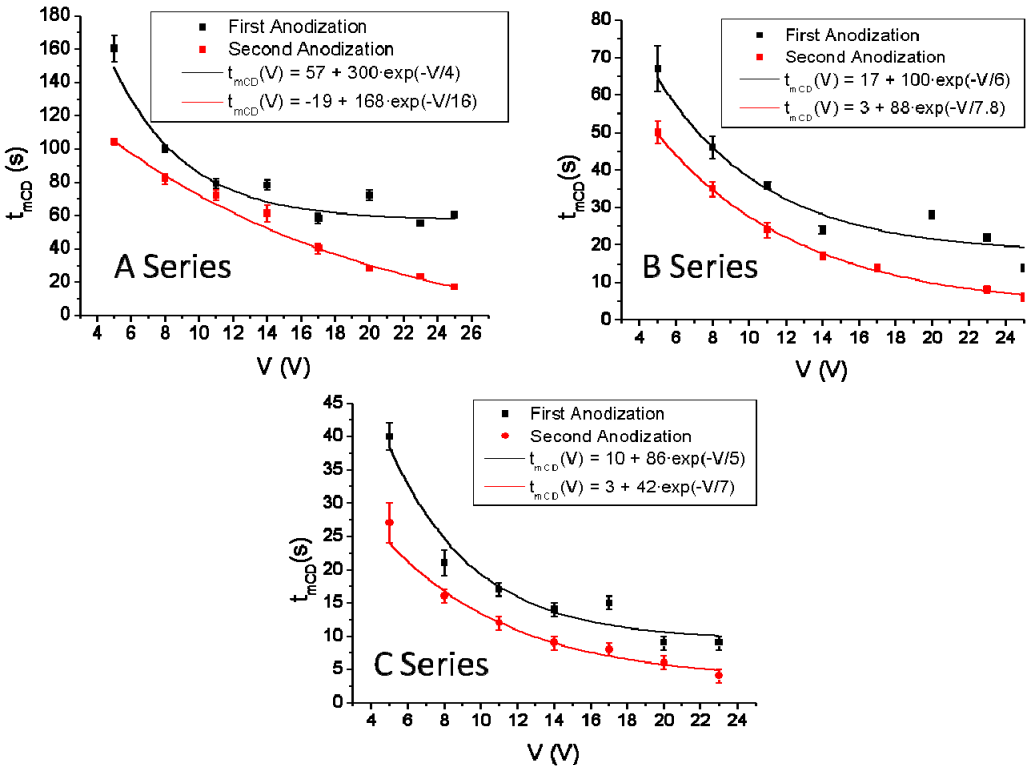

Figure 2-6: Time to reach the minimum value of current density in function of the applied voltage for A, B and C Series.

We can appreciate that the sulphuric acid concentration in the electrolyte also has influence on the time which takes to start the pore formation. This is represented on the graphs of the *Figure 2-7*.

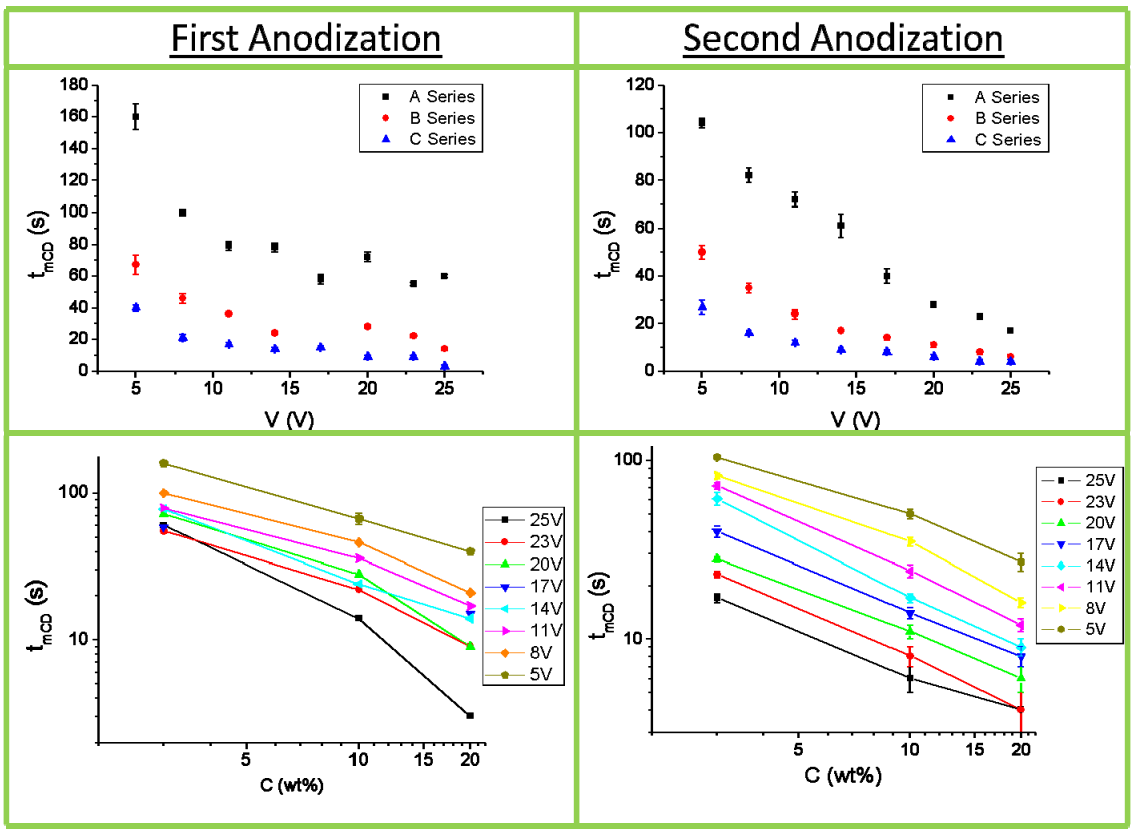

Figure 2-7: Time to reach the minimum value of current density in function of the applied voltage and sulphuric acid concentration in the electrolyte for each series during first and second anodization.

2.3.2. The kinematic of NAAF growth.

Thickness characterization by HR-SEM micrographs gives us the opportunity of having a precise measurement, but the main problem is that this is a destructive method. Sometimes, getting a good cross-sectional view is not so easy. Depending on the thickness of the sample is better doing in one or another way. When the film is thick enough we can detach it from the Aluminium substrate and deposit it on other surface, as in our case, Silicon substrate, placing the edge of the NAAF on the edge of the Si substrate (*Figure 2-8***¡Error! No se encuentra el origen de la referencia.**a). If the film thickness is only hundred of microns or even less, the easiest way we have used is cutting the sample with a paper guillotine. The cut will generate cracks on the NAAF which will allow us taking good micrographs of the cross-section (*Figure 2-8*b).

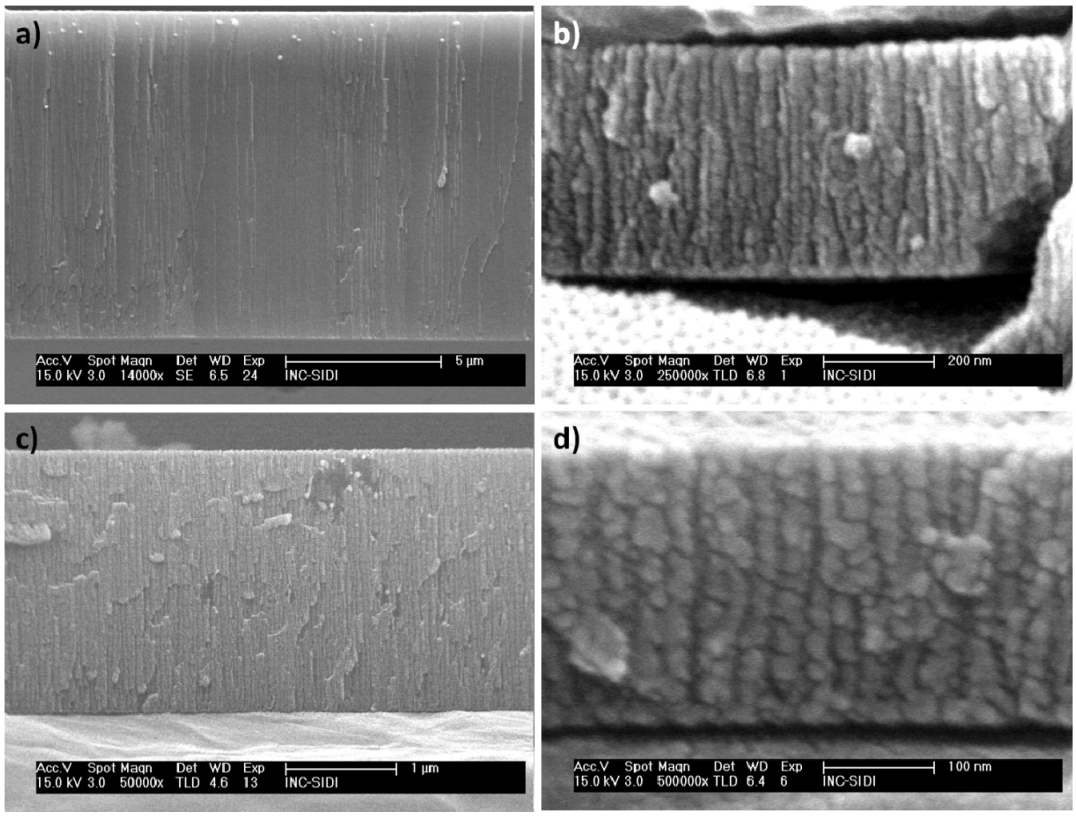

Figure 2-8: Cross-sectional view of NAAF`s; a) detached from the Aluminium substrate, sample A25; and, b)B11 c) A17 d B8) on Aluminium substrate.

As we already mentioned in section 2.2, after 16 hours of first anodization for all the samples, the second anodization was carried out during 150 minutes for A Series and 20 minutes for B and C Series. In *Table 2-2* are presented the thicknesses of the grown NAAF and their growth rate where it make sense.

Table 2-2: Thickness and growth rate of A, B and C Series obtained by HR-SEM characterization.

	A Series		B Series		C Series	
V(V)	Thickness (µm)	Growth Rate (µm/h)	Thickness (µm)	Growth Rate (µm/h)	Thickness (µm)	Growth Rate (µm/h)
25	10.5±0.05	4.21±0.02	10.0±0.04		42.9±0.5	
23	6.33±0.01	2.53±0.01	4.65±0.01	14.00±0.05	20.8±0.2	62.3±0.5
20	3.77±0.01	1.51±0.01	1.96±0.01	5.90±0.03	6.00±0.01	18.00±0.04
17	2.38±0.01	0.95±0.01	1.08±0.01	3.25±0.01	2.72±0.01	8.15±0.02
14	1.62±0.01	0.65±0.01	0.69±0.01	2.06±0.02	1.47±0.01	4.40±0.02
11	1.15±0.01	0.46±0.01	0.41±0.01	1.22±0.01	0.86±0.01	2.60±0.01
8	0.70±0.01	0.28±0.01	0.25±0.01	0.76±0.01	0.50±0.01	1.50±0.01
5	0.38±0.01	0.15±0.01	0.14±0.03	0.42±0.01	0.24±0.01	0.71±0.01

For samples A28, B25, C25 and C23 we have not estimated the growth rate. This is because the current density is not uniform, as can be observed in *Figure 2-1*, which implies that the growth rate is not constant along the anodization process..

The measurements presented in **¡Error! No se encuentra el origen de la referencia.** are represented in **¡Error! No se encuentra el origen de la referencia.** so that can be observed the dependence of the growth rate on the applied experimental parameters. *Figure 2-9***¡Error! No se encuentra el origen de la referencia.**a shows that the growth rate increase exponentially with the applied voltage, but there is also other dependence with the sulphuric acid concentration used in the electrolyte which can be observed in *Figure 2-9***¡Error! No se encuentra el origen de la referencia.**b. This graph shows a quasi-linear dependence, although is presented is scale log-log for a better and easier eye recognition.

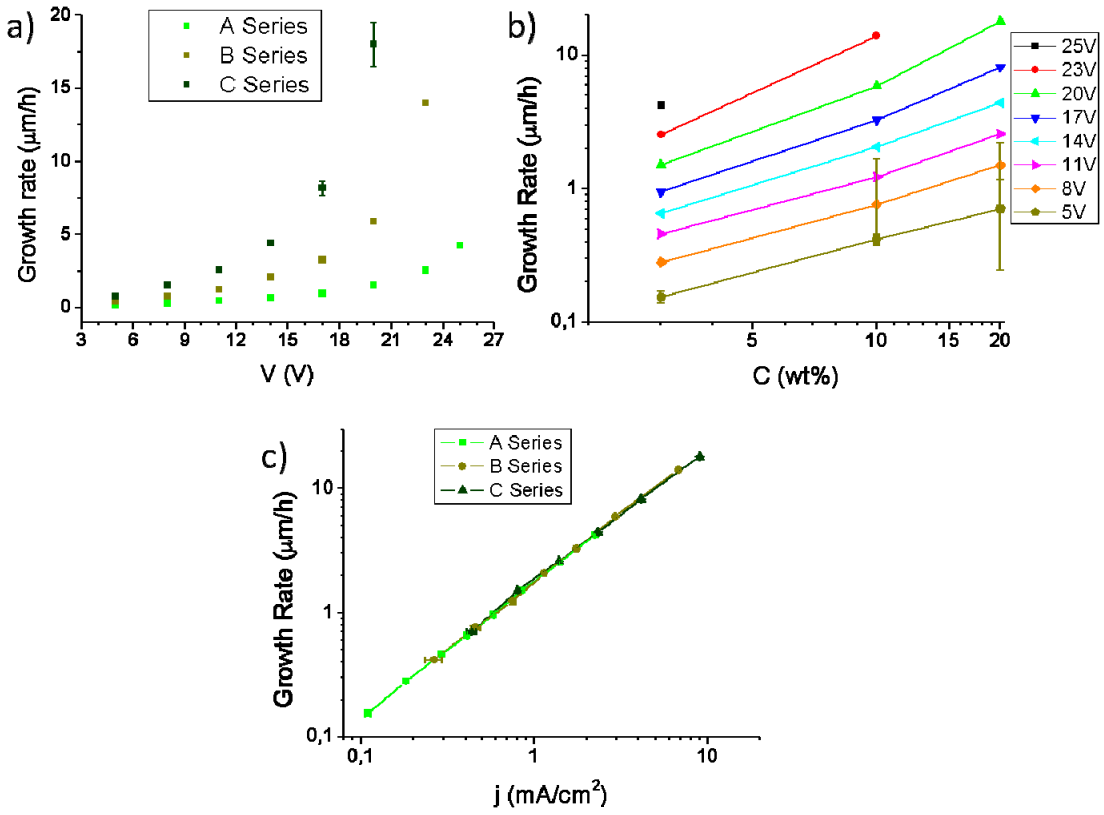

Figure 2-9: NAAF growth rate dependence on the applied experimental conditions, i.e. a) applied voltage and b) Sulphuric acid concentration. C) Relation between the NAAF growth rate and the current density.

In *Figure 2-9*c, we can observe the relation between the NAAF growth rates and the current densities which results from the applied experimental conditions. This graph is also presented

in log-log scale in order to make easy the visualization of the cuasi-linear dependence of the growth rate with the current densities into this range.

If we make a linear fitting of the data represented in the *Figure 2-9*c, we obtain a slope which is given in units of volume per charge, i.e, the volume of grown alumina in function of the charge going through the electrode. The results are presented in *Table 2-3*.

Table 2-3: Results of the linear fitting which slopes indicate the volume of grown alumina per unit of charge.

	Intercept (mA/cm^2)	Slope ($\mu m \cdot cm^2 \cdot h^{-1} \cdot mA^{-1}$)	Coefficient of Determination, R^2	Grown alumina volume per Coulomb ($\mu m^3 \cdot C^{-1}$)x1e7
A Series	-0,09438±0,001	1,838±0,003	0,99713	5,105±0,008
B Series	-0,10361±0,00133	1,958±0,003	0,99782	5,438±0,008
C Series	-0,15266±0,00686	2,003±0,004	0,99977	5,56±0,01

From here we can conclude that as the sulphuric acid concentration in the electrolyte increases, the volume of the NAAF also increase for the same quantity of charge going through the electrode. Preliminary we could say that, this fact indicates that, the efficiency of the anodization is higher for higher concentration of sulphuric acid in the electrolyte. In section 2.7 we will get an insight into this topic.

2.4. Micrographs analysis by application of Self-Correlation function and comparison with other techniques.

2.4.1. Micrographs analysis methodology.

The Self-correlation processes of the surface images were carried out by using the open software WSxM4.0 [81]. As it is inferred from Eq. 2.1, G(nδ, mε) will be non null whenever correlation exists among the pores of overlapped HRSEM images. This high spatial correlation will exist among pores growing under self-ordering condition. Therefore, when an image of a hexagonally ordered pore array in one domain is self-correlated, a perfect hexagonal spots array will be obtained (see *Figure 2-10*a). If two structural domains are involved, a like Moiré pattern will be formed as it is shown in *Figure 2-10*b. From the qualitative point of view, SCI's are in good agreement with the FFT maps obtained from the same HRSEM micrographs (see

the insets in *Figure 2-10*). Finally, if several small domains or non ordered pore arrays are involved, then the self-correlation leads to a ring shape surrounding the central spot or only a central spot. In our images, these patterns are formed due to the superposition of domain of nanopores at different angles.

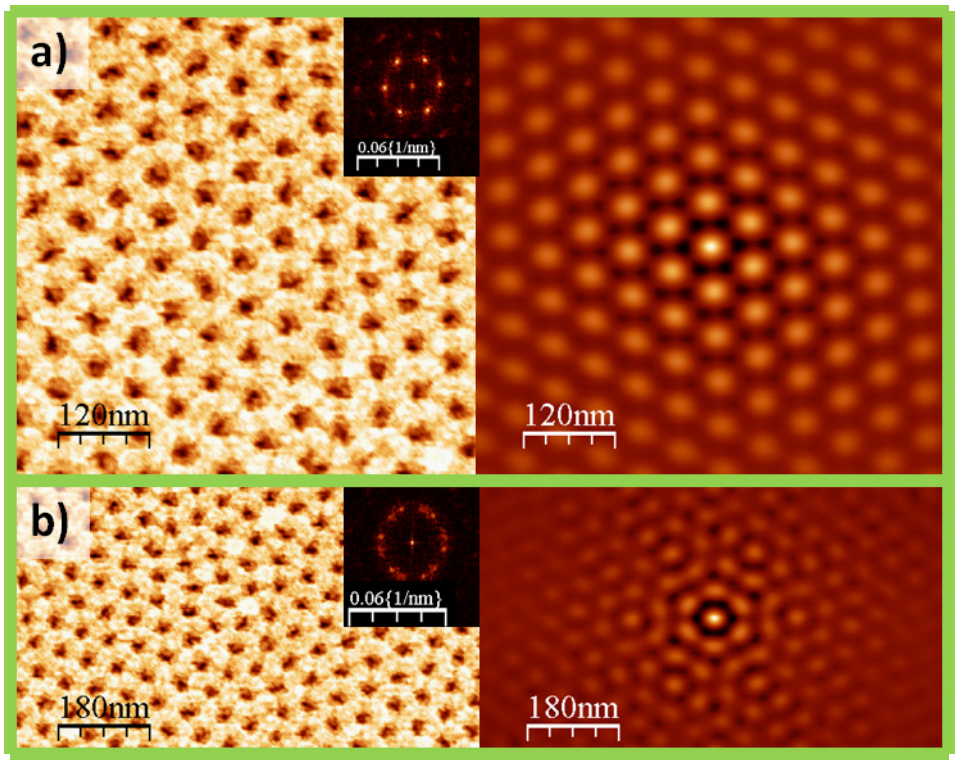

Figure 2-10: HRSEM micrographs (left) and their respective self-correlation images (right) taken from a NAAF sample grown under typical conditions for sulphuric acid electrolyte. Self-correlation of an image with a) single domain generates a hexagonal pattern, b) two domains generates a Moiré-like pattern. In the insets are represented the FFT of the HRSEM micrographs.

Among others, SCI's contain information about intensities over all HRSEM surface images as observed in the 3D self-correlation image shown in *Figure 2-11*a. So, not only qualitative but also quantitative analysis of ordering degree can be achieved. In order to perform a qualitative study the ordering degree, it is necessary to have approximately the same number of pores on each image independently of the selected area; so, in our case we selected around 255 pores per image. To carry out the quantitative analysis, the intensity (I) and full width at half maximum (FWHM) of both central spot (CS) and nearest neighbour (NN) of three crossing centre profiles are taken on each image. These profiles preferably made angles of 60º degrees between them and link the opposite vertex of a hexagon formed by the relative maxima, as seen in *Figure 2-11*b. As an example, one of these three profiles is displayed in *Figure 2-11*c. Surface parameters can be also easily determined with high accuracy starting from SCI by taking radial average profiles from each image. The obtained profile, shown in *Figure 2-11*d,

provides information about the intensity, spot widths and distance between them. In order to get a good statistics to determine interpore distances micrograph areas of up to 3.4 μm^2 were processed.

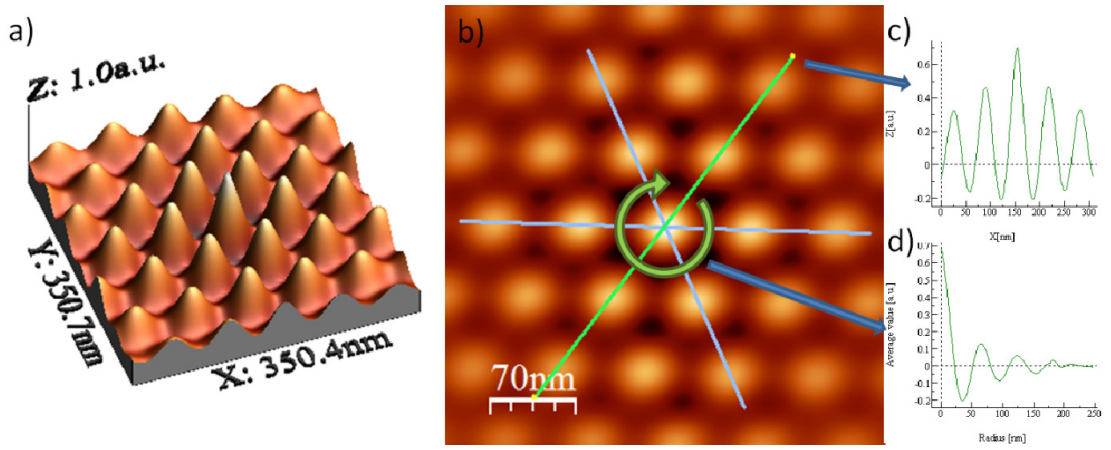

Figure 2-11: a) 3D Self-Correlation image where the XY plane represents the area and Z axis represents its intensity. b) 2D Self-Correlation image with three cross centre lines forming 60º between them. c) Profile from one of the cross centre line d) Profile from radial average.

Interpore distances were determined in SCI by measuring the peak to peak distances between CS and the NN. Determining pore diameters is not so trivial since defects in the hexagonal pattern distort the real sizes. Here we assume a quasi hexagonal centred pore arrays as an elemental cell. Actually, these cells could show moderate deformations. In this work, five elemental cells extracted from each HRSEM image sample have been self-correlated. A radial average profile is taken from the central spot of the SCI over the whole pixels located at the same distance from the central spot. Then, it is possible to calculate FWHM of the central spot and hence pore diameter as it'll be described later on.

2.4.2. Application of Self-Correlation Function on Ultra-High-Resolution SEM micrographs.

Table 2-4 shows top-views HRSEM micrographs and their respective SCI for the A, B and C series samples. In HRSEM micrographs it can be easily perceived the surface parameters and self-ordering evolution when the applied voltage decreases from 28 V down to 8V. From the HRSEM images processing, preliminary information about the periodicity of the nanopore arrays was obtained. An almost perfect hexagonal structure is showed in the SCI of sample A25 – the typical conditions for Aluminium anodization in sulphuric acid solution –, and that structure is gradually lost for larger and lower applied voltages. From SCI of samples A28, A25,

A23, B23, B20, C20 and C17 showed in *Table 2-4* respectively, it can be still deduced good quality of ordered NAAF, being remarkable samples A28, A25, B23 and C20. SCI of samples A17, B17 and C14 shows short range order up to second neighbour. No order can be make out for the rest of the samples on SCI's showed in *Table 2-4*.

This is explained considering that under these experimental conditions, the self-ordering conditions for the NAAF growth begin to be missed above certain critical applied voltage as can be observed in samples B25, C25 and C23 in agreement with a previous report by Ono et al. [78]. On the other hand, the self-ordering conditions loss also occurs for applied voltages lower than an optimum value for each sulphuric acid concentration[6, 12].

The evolution of the pore ordering in A, B and C series, shown in *Table 2-4*, can be explained by a model based on mechanical stress due to the volume expansion [39, 54]. Mechanical stress as consequence of the changes in the volume cause repulsive forces which, depending on its strength, lead to self-order or disorder, as well as macroscopic fractures across the alumina films. When the relation between applied voltage and acid concentration induces moderate volume expansion, tensile stress is also moderate and equilibrium exists among repulsive forces inducing self-ordering [27]. In our case, this condition is achieved for samples A28, A25, A23, B25, B23, B20 and C20. On the other hand, in case of strong or weak volume expansion, they lead to large tensile or compressive stress and therefore to disordering as can be apprehended in the rest of the samples in this study.

Table 2-4: HR-SEM top-view micrographs and their respective SCI's for A, B and C sample series after second anodization at 0ºC and applied voltages between 28 and 8V. The scale bar is the same for both micrographs and SCI's.

	A Series	B Series	C Series	
28V	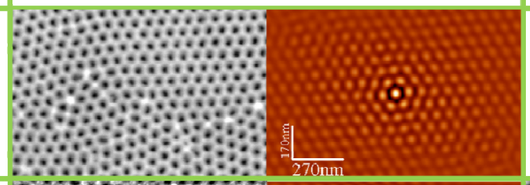			28V
25V	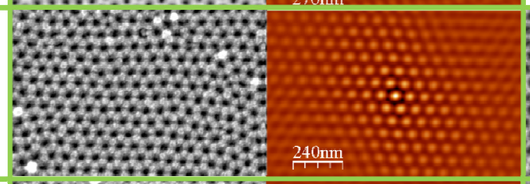	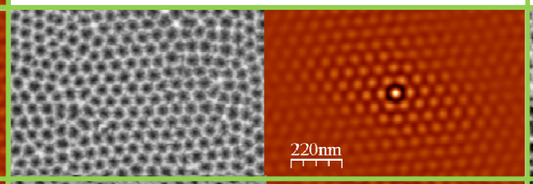	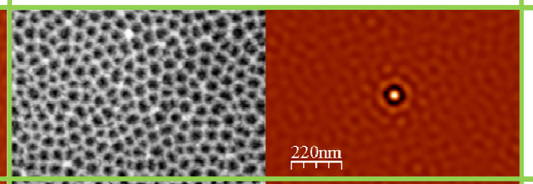	25V
23V	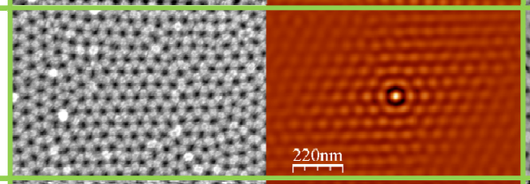	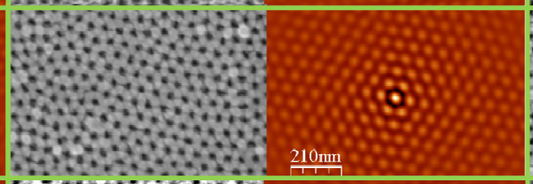	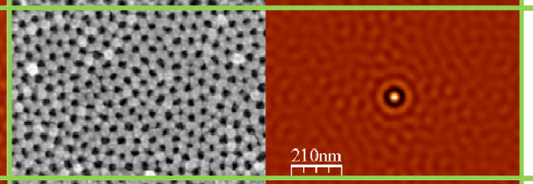	23V
20V	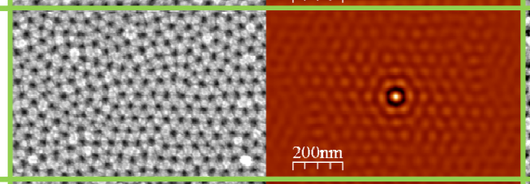	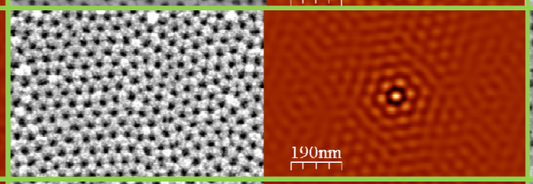	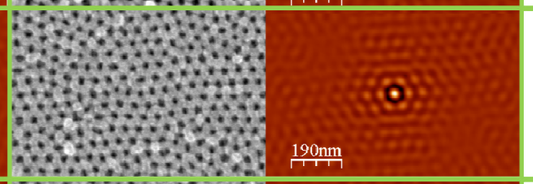	20V
17V	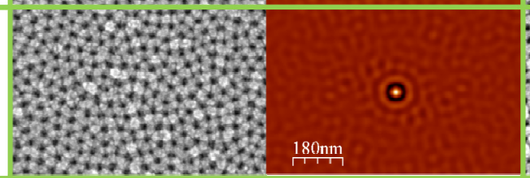	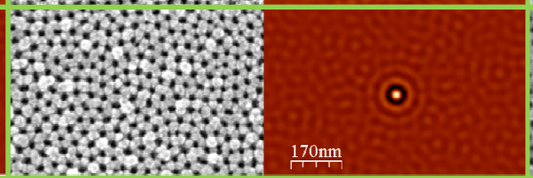	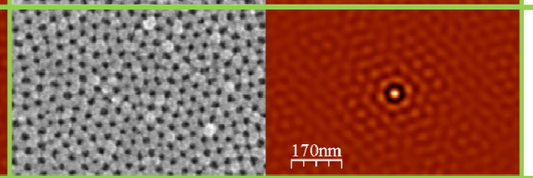	17V
14V	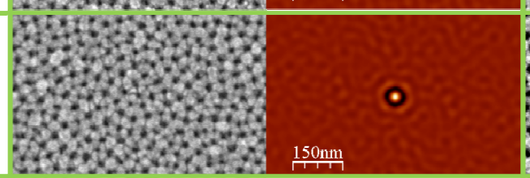	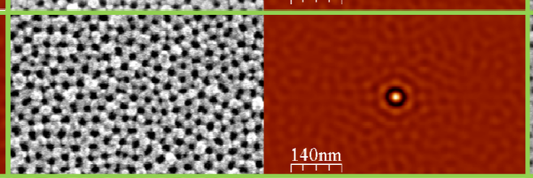	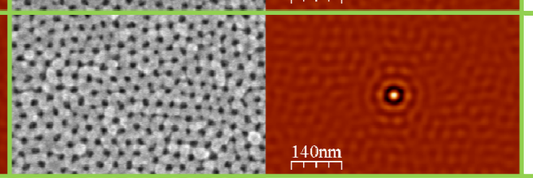	14V
11V	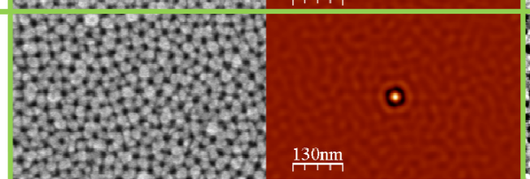	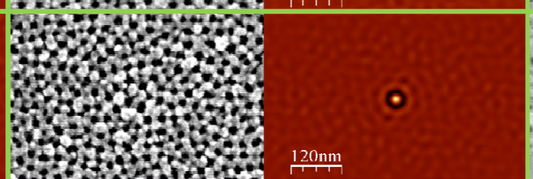	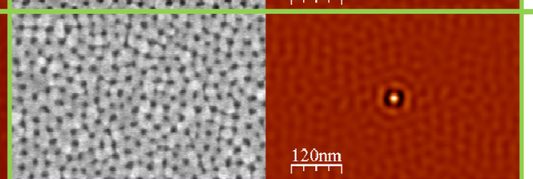	11V
8V	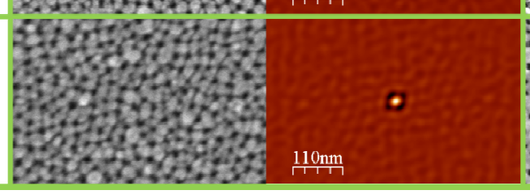	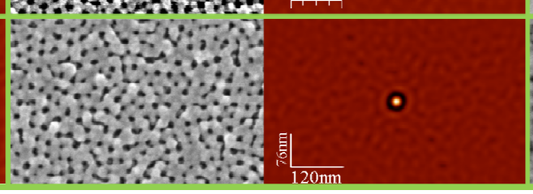	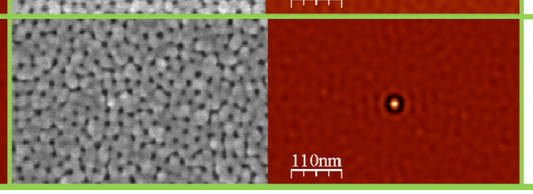	8V

These studies presented in section 2.5 were made over all sample series, except for those obtained at anodization voltages lower than 5V. This exclusion is justified since for those anodization conditions the pores loss their circumferential shapes (*Table 2-5*).

Table 2-5: UHR-SEM top-view micrographs and their respective Self-Correlation Images for: A5, B5 and C5 samples after second anodization at 0ºC. The scale bar is the same for both micrographs and SCI's.

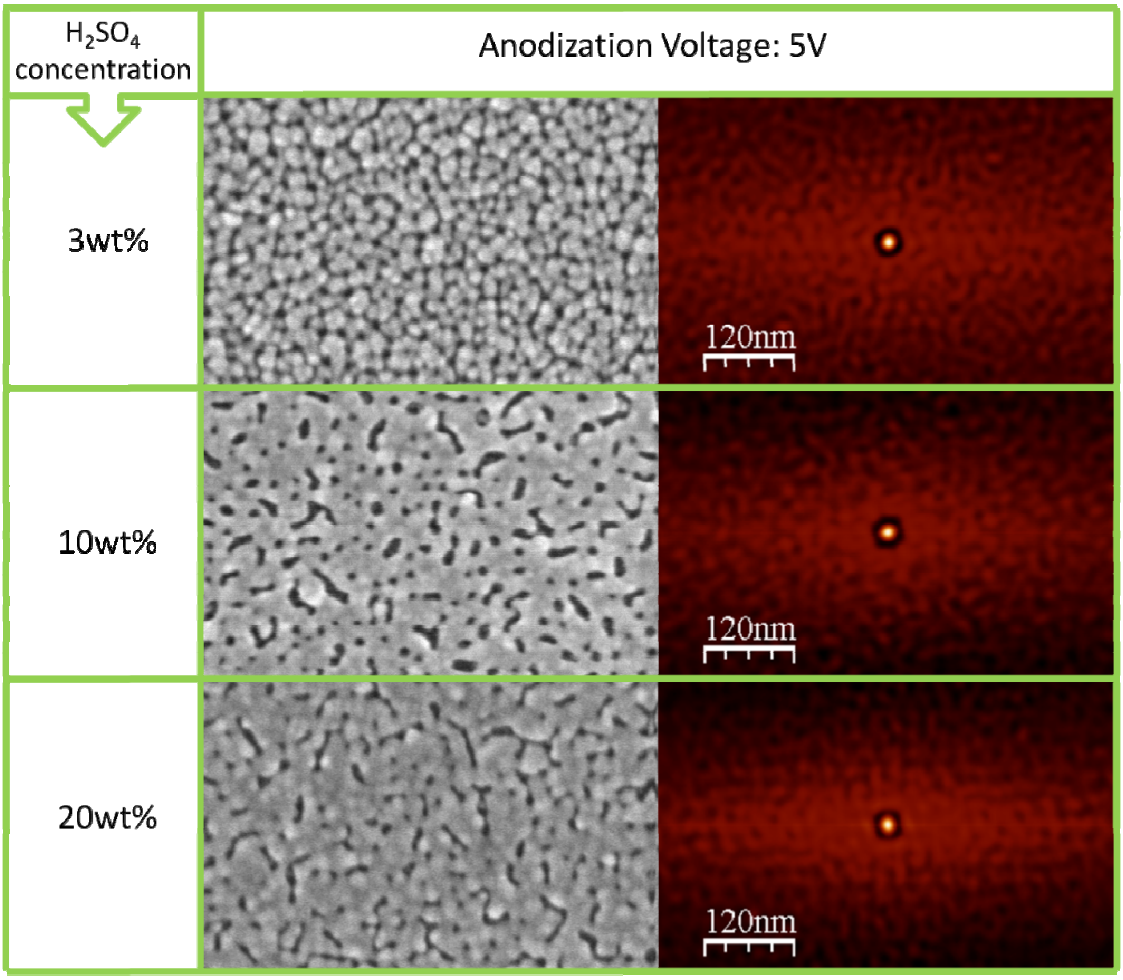

2.5. Study of the dependence of surface geometrical parameters with the applied voltage and acid concentration.

2.5.1. Preliminary analysis of SEM micrographs and its respective SCI´s.

The influence of the processed image areas on the surface parameters determination was also verified. The results show that the size of the processed areas has not influence in the determination of interpore distances when the area varies between 0.22 and 3.42 μm^2 since

the variation on the distances between maxima is around 1%. As an example, experimental data from A series is presented in *Table 2-6*.

Table 2-6: Measured Interpore distances for A Series in function of the area of the micrograph analyzed, mean value and standard deviation.

Area of micrograph analyzed (μm^2)	Pixel size (nm)	Interpore Distances (nm)							
		A28	A25	A23	A20	A17	A14	A11	A8
0.22	-	70	65,6	61,6	54,8	49,3	42,3	37,7	33,4
0.86	-	70	66	62,5	55,4	49,2	43,9	37,4	33,8
3.42	-	69,8	67,2	61	55,8	50,5	43,9	37,3	33,8
Mean value		69,93	66,26	61,7	55,33	49,66	43,36	37,46	33,66
Standard Deviation		0,11	0,83	0,75	0,50	0,72	0,92	0,20	0,23

Regarding pore diameters determination, it was found an increase in FWHM for profiles corresponding to large processed areas as it is shown for A samples series in *Figure 2-12*.

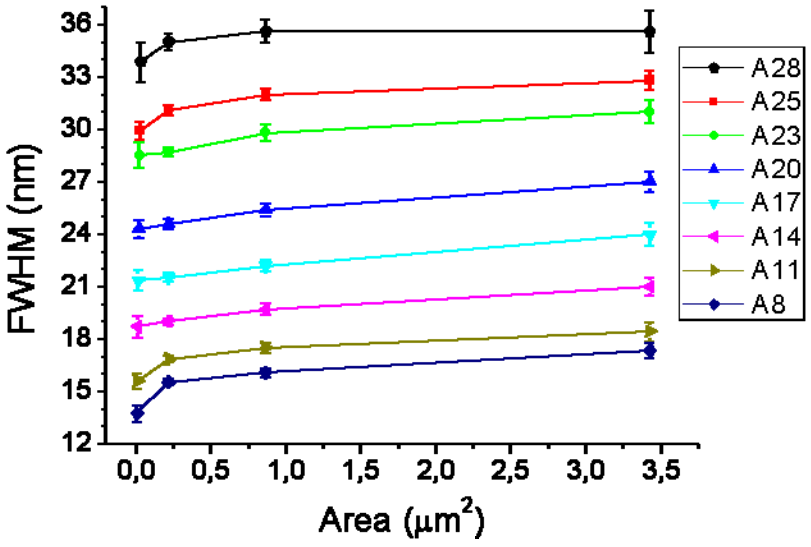

Figure 2-12: Influence of the self-correlated area determining FWHM for A series. Processed areas are: 3.42, 0.86, 0.22µm² and elemental cells.

This FWHM dependency is due to the presence of defects and inhomogeneities on the surface of the NAAF. Therefore, we consider that the more accurate method to determine pore diameters is measuring FWHM on SCI from the elemental cell as it was described before. FWHM values taken from the radial average profile of the SCI from the elemental cell do not necessarily correspond to geometrical values of the diameter mainly due to the influence of contrast and brightness; however, they follow the same trend for each sample. To obtain quantitative information about the diameter values we introduce a calibration method. The cross sectional view of the sample A25 -grown under typical anodization conditions- give us a mean pore diameter value of 24 nm, which agree with other results previously reported [27]. Since the mean value of FWHM obtained for the same sample is 30.0 nm (measuring the central spots profiles of the five elemental cells in the SCI) it is possible to apply a correction factor determined by the ratio between the actual diameter and the average value of FWHM for the sample A25, in this case 0.8. This correction factor is applicable to the average FWHM taken from the five elemental cells of each sample, and then, it is possible to determine their pore diameters. Note that it would not be possible to apply a correction factor as a constant on larger areas due to the variation of percentage of defects since the anodization parameters change. This fact can be observed in *Figure 2-13* where has been represented the dependence of the FWHM of the central spot on the anodization voltage for areas of 3.42 μm^2.

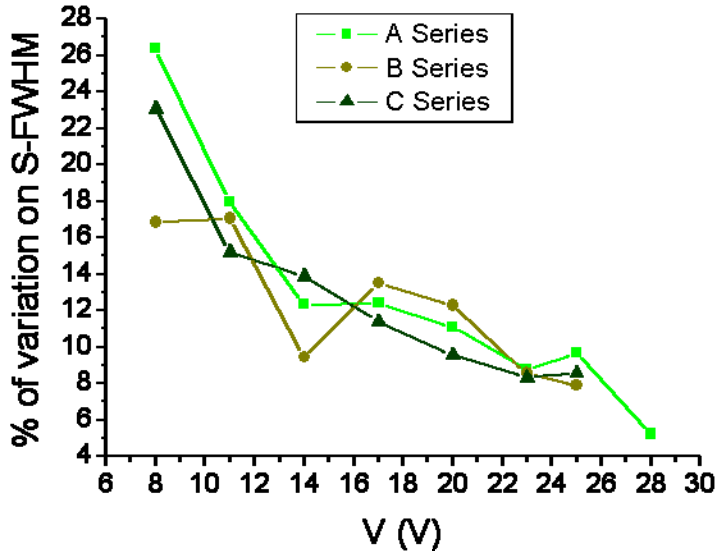

Figure 2-13: Percentage of variation on S-FWHM regarding to elemental cells for 3.4µm² areas in function of the applied voltage. The percentage increase related to the higher level of defects as decrease the anodization voltage.

2.5.2. Results of geometrical parameters determination.

A quantitative analysis on the ordering degree of the obtained samples were also done; such type of analysis have been widely made based on FFT in which, the spot intensities and their FWHM ratios (I/FWHM) can be evaluated. This ratio is accepted as the spatial order parameter consistent with the human recognition ability [34]. In our study, we have used images with the same number of pores but, since they represent magnifications from other images, we have less number of pixels per image as well. If the quantity of pixels decreases in each image from the same sample series, then the intensity of the SCI also decreases independently of the pore ordering degree. In order to avoid this non desirable effect and to make possible the comparison between them, we have normalized the I and FWHM ratio of the NN regarding to the I and FWHM ratio of the CS from the three crossing centre profiles previously described (see *Figure 2-11*b and *Figure 2-11*c). So, the normalized spatial order parameter (NSOP) can be calculated from the following equation (*Eq. 2.6*):

$$\textit{Eq. 2.6:}\quad NSOP = \frac{\sum_{NN=1\ldots,6}\left|\frac{I_{NN}}{FWHM_{NN}}\right|}{\left|\frac{I_{CS}}{FWHM_{CS}}\right|}$$

In this way, the normalized spatial order parameter of an ideal hexagonally ordered pore array would be equal to 1. The obtained results are represented as a function of the applied voltage in *Figure 2-14*.

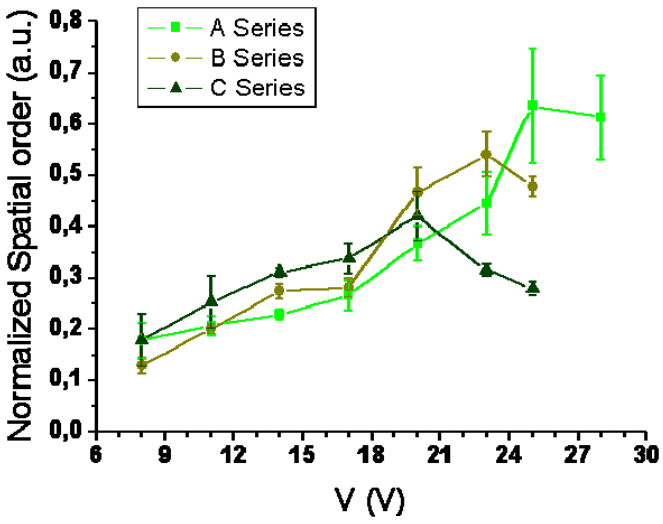

Figure 2-14: Normalized spatial order parameter of the NAAF SCI's in function of applied voltage.

These graphs confirm what it could be previously qualitatively deduced from SCI in *Table 2-4* i.e., the hexagonal largest range order for 3, 10 and 20 wt% was obtained for 25, 23 and 20 V, respectively, in agreement with those previously reported [34, 39, 54]. It could be a little surprising the fact that the voltages to get ordered nanopores are very close among them for concentrations so different (3, 10 and 20wt%). Nevertheless, the current densities obtained for these voltages are just below the critical current density to prevent the well know "white burning", condition to get self-ordering. In this work, we have found the existence of an anodization voltage window to achieve NAAF in self-ordering regime for each temperature and acid concentration. It is worth it to mention that for each acid concentration exists a decreasing maximum shifted to lower voltages when the electrolyte concentration increases. Besides, it is relevant the high ordering parameter value obtained for sample B20 which fall out of the regular range mentioned before. These latest trends need additional confirmation since searching experimental parameters to get an optimum ordering degree for B and C sample series are the subject of another work.

Figure 2-15 shows the values of the interpore distance calculated from the SCIs for different samples. The well known linear dependence of the interpore distances with the applied voltage can be observed. In addition, we found that the interpore distances become shorter for higher sulphuric acid concentrations at the same anodization voltage values.

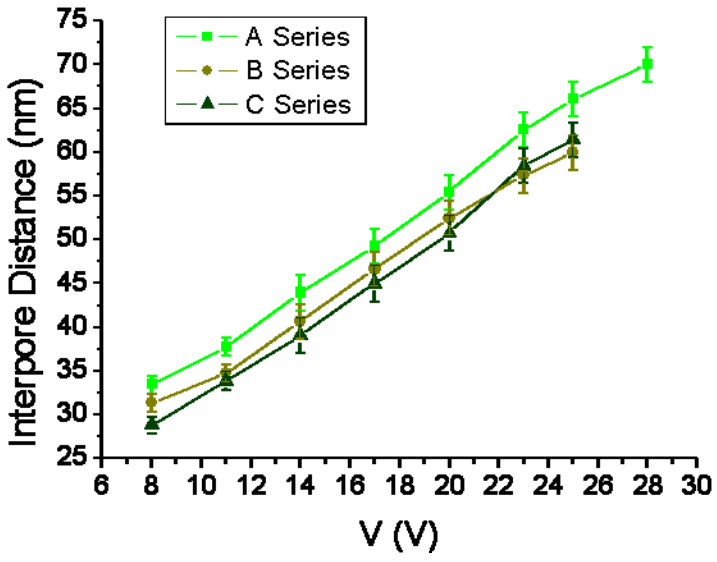

Figure 2-15: Dependence of inter-pore distances for A, B and C Series on applied voltages.

In *Figure 2-16* the values of the pore diameter for the different samples are represented. As it was expected, pore diameters show also a linear dependence on the applied voltage. In

addition, *Figure 2-16* reveals that A sample series have diameters larger than those of B and C sample series for equal applied voltages, however, there are no significant differences between the pore diameters of the B and C series samples.

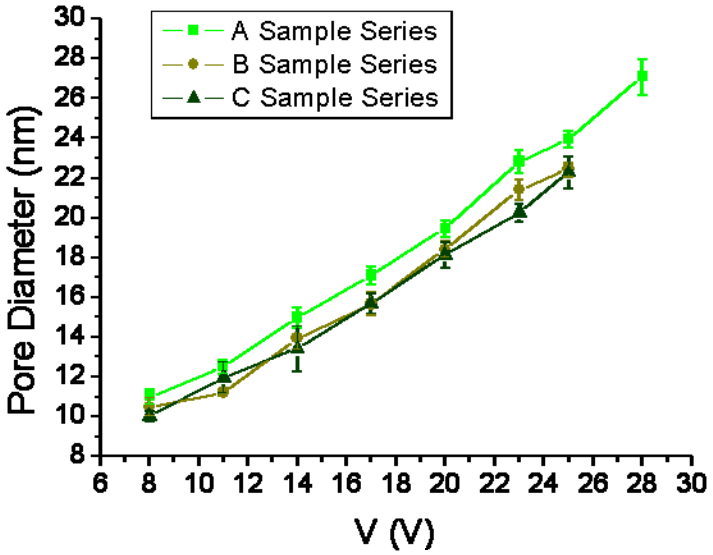

Figure 2-16: Dependence of Pore Diameter for A, B and C Series on applied voltages.

In *Table 2-7* the surface parameters and coefficients of the samples with the highest ordered nanoporous array of each electrolyte (A28, A25, B23, B20 and C20) are given. As can be seen, inter-pore distances can be reduced 15 nm from the sample A25 down to sample C20 keeping large spatial order and Interpore Distance/Voltage ratio (ID/V) between 2.65 and 2.50nm/V.

Table 2-7: Surface geometric parameters and surface geometric parameters/Voltage ratio for the highest spatial order samples of each sulphuric acid concentration and applied voltage.

	A28	A25	B23	B20	C20
Interpore Distance (nm)	70±2	66±2	57±2	52±2	51±2
Pore Diameter (nm)	27.1±0.9	24.0±0.4	21.4±0.5	18.4±0.4	18.1±0.6
Interpore Distance/Voltage (nm/V)	2.50±0.07	2.64±0.08	2.49±0.09	2.6±0.1	2.5±0.1
Pore Diameter/Voltage (nm/V)	0.97±0.03	0.96±0.02	0.93±0.02	0.92±0.02	0.91±0.03

The values for interpore distances obtained by the SCF's method have been compared to those obtained by a method based on pair distribution function. This method represents the distribution of distances between a certain particle and the rest particles contained into a given volume or area. In our case, we have applied this method on 19 nanopores from each micrograph of samples A28, A25, B23, B20, C20 and C17, within a radius of 420nm. The results are showed in *Figure 2-17*.

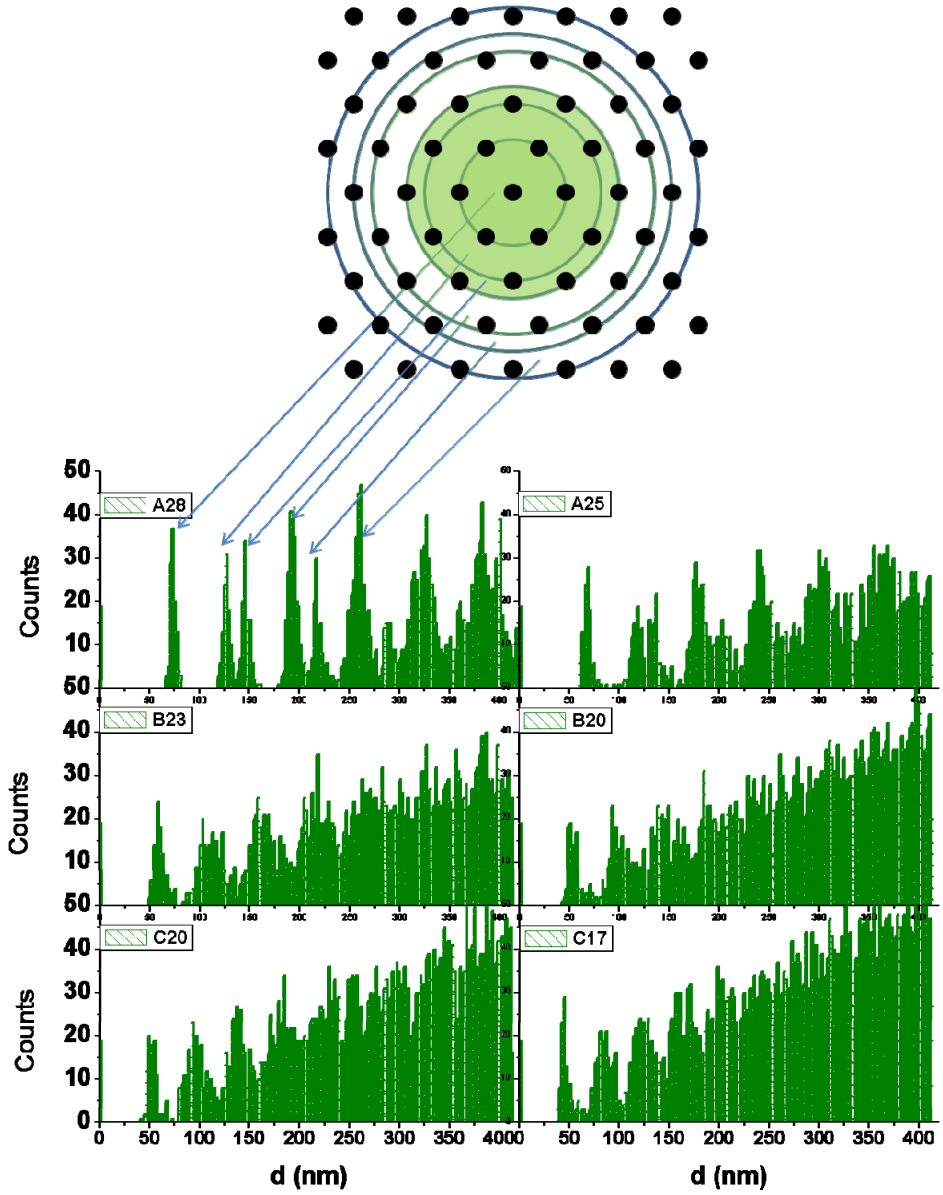

Figure 2-17: Interpore Distances distribution within a radius of 420nm for samples A28, A25, B23, B20, C20 and C17.

The first peak indicates the distance distribution among the pores of the NN and so on. The peak attributed to the NN was analyzed by Gaussian fitting obtaining information about the distance and the width distribution. As can been observed in *Table 2-8*, those values agree with those on *Table 2-7*.

Table 2-8: Interpore Distances of the nearest neighbours regarding to reference pores, measured from a pair distribution function based method, for the samples A28, A25, B23, B20, C20 and C17. In order to know the interpore distance and their distribution of the nearest neighbour, a Gauss fit was performed to the curve corresponding to the nearest neighbour pores.

	A28	A25	B23	B20	C20
Interpore Distance (nm)	73	68	58	53	52
FWHM (nm)	5.6	7.6	9.5	10.6	5.4

It also can be observed from *Table 2-7* that, pore diameter can be reduced 6 nm keeping hexagonal order and the Pore Diameter/Voltage ratio (PD/V) between 1.0 and 0.9. Nevertheless, sample C17 also shows order up to fifth neighbour, with interpore distances and pore diameters of 45±2 and 15.5±0.5 nm respectively. On the other hand, from *Figure 2-15* and *Figure 2-16*, it can be deduced that, for each sample series, ID/V and PD/V ratios do not keep constant but they increase exponentially up to 4.2nm/V for interpore distances and 1.37nm/V for pore diameters (see *Figure 2-18*). The ratios for low voltage anodizations are above the typical condition values for mild anodization i.e. 2.5nm/V and 1.0nm/V for interpore distances and pore diameters respectively, which are in good agreement with the ratios calculated starting from SCI's of the samples prepared under self-ordering regime.

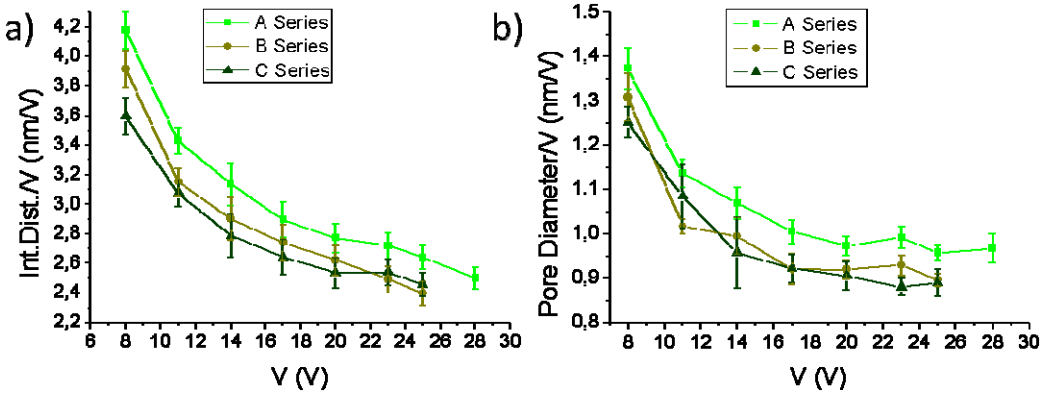

Figure 2-18: Dependence on applied voltage of ratios: a) interpore distance/V and b) Pore diameter.

Finally, the porosity has been calculated starting from the surface parameters obtained by SCI's processing. From $P=\pi/2\sqrt{3}(PD/ID)^2$, porosity keeps nearly constant for all the sample

series and seems to be independent on the range of applied voltages and sulphuric acid concentrations used (see *Figure 2-19*).

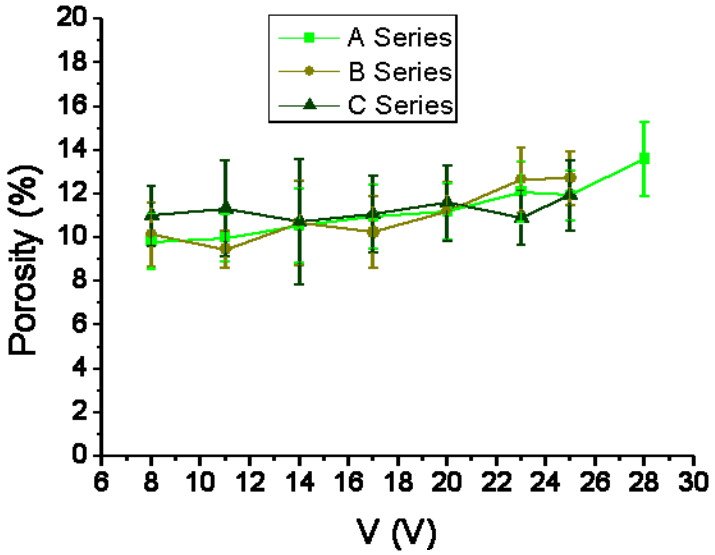

Figure 2-19: Dependence on applied voltage of porosity for A, B and C Series.

However, we have distinguished between samples within self-ordering regimes (A28, A25, A23, B25, B23, B20 and C20) and outside self-ordering regimes. The average values for the samples within and outside this regime are 12.2±0.8% and 10.5±0.5% respectively. So, it is clear that samples grown under self-ordering regime obey the 10% porosity rule for sulphuric acid electrolytes [16], but the porosity of those samples outside of those special conditions also maintain those values approximately.

2.6. Compositional and structural analysis.

In this section we have carried out a conscientious study of the composition of the anodic alumina grown in our experiments under different conditions by using three different and complementary techniques. From this study we are able not only to confirm and quantify the components of the anodic alumina, but also how these elements are incorporated inside the alumina matrix.

2.6.1. RBS

RBS measurements were performed on samples from A, B and C series those grown under 25, 20, 17 and 14V, previously described. As we see in Figure 2-20, Figure 2-21 and Figure 2-22 are registered the signals of all the elements that we expected to find in the sample, i.e., Aluminium, Oxygen and Sulphur.

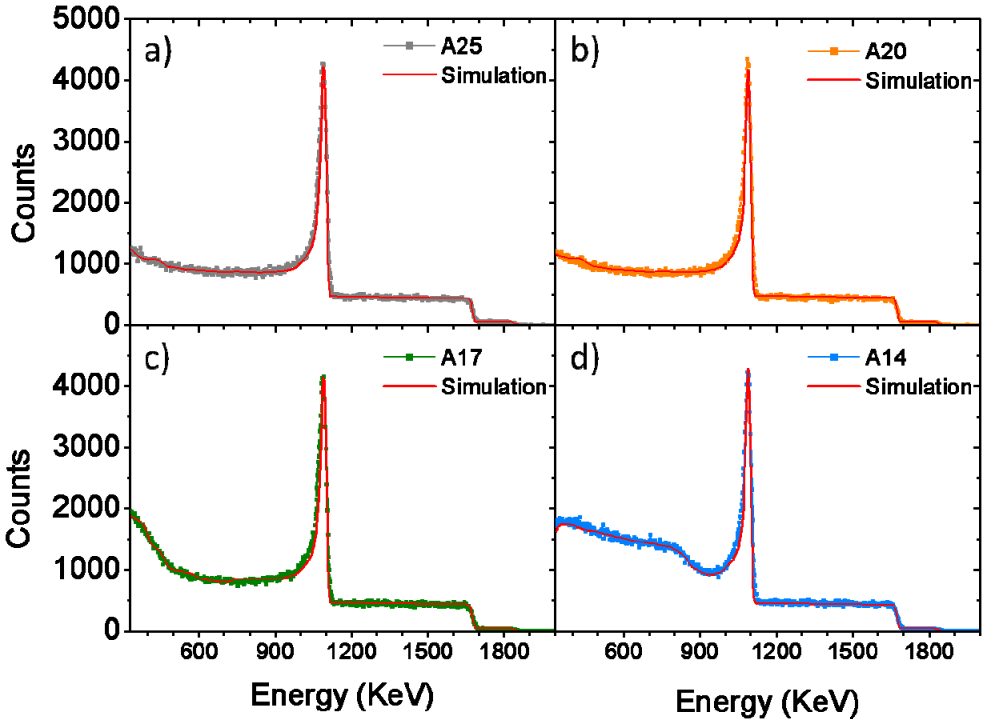

Figure 2-20: RBS spectrum at 3035 Mev He^{+} of the A series, experimental spectrum and fitting simulation for a) A25, b) A20, c) A17 and d) A14

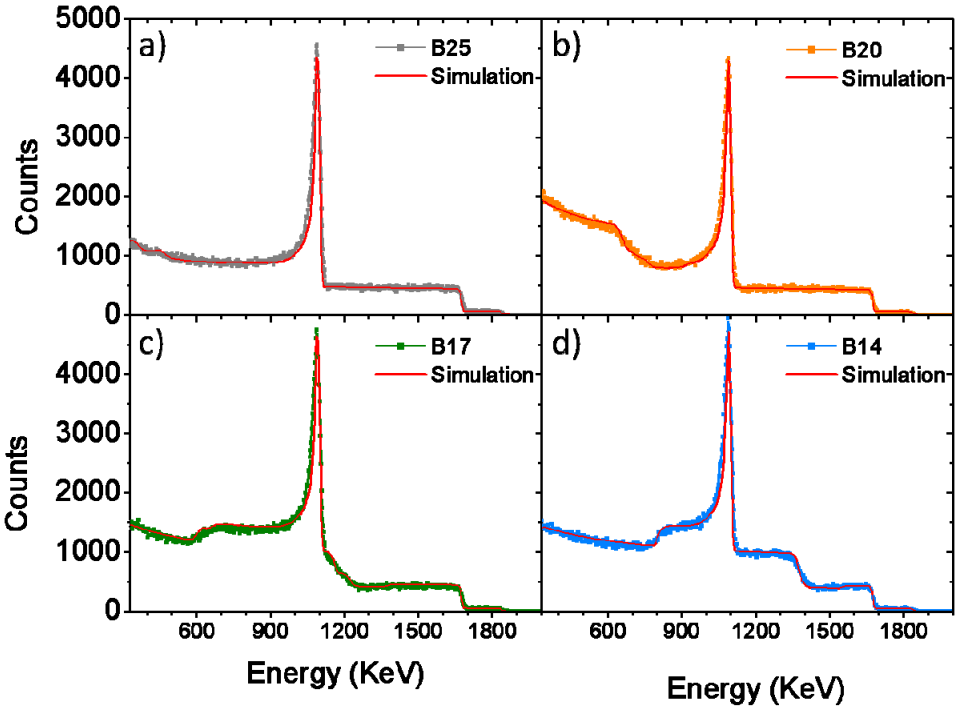

Figure 2-21: RBS spectrum at 3035 Mev He^+ of the B series, experimental spectrum and fitting simulation for a) B25, b) B20, c) B17 and d) B14.

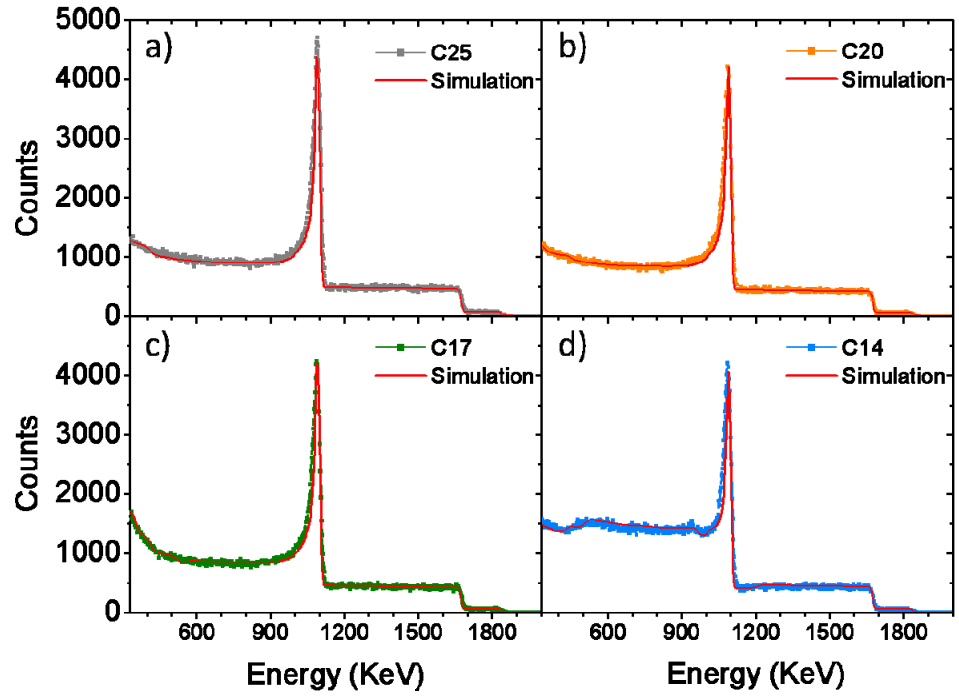

Figure 2-22: RBS spectrum at 3035 Mev He^+ of the C series, experimental spectrum and fitting simulation for a) C25, b) C20, c) C17 and d) C14.

In the experimental spectrum in Figure 2-20, Figure 2-202 and Figure 2-22 we have observed that backscattered atoms have reached the aluminium substrate in samples A14, A17, B14, B17, B20, C14 and C17, because these samples have thicknesses lower than 2,7µm which is the penetration deep of the He^+ ions into our NAAFs.

Figure 2-23 shows the enlarged signal corresponding to the sulphur nuclei incorporated into the alumina matrix in function of the applied voltages and the sulphuric acid concentration into the electrolyte. In these figures it is possible to observe a decrease of the signal of these sulphur nuclei as decrease the applied voltage from 25 to 14V. A similar behaviour has been found when we observe the signal in function of the concentration of sulphuric acid into the electrolyte, since the concentration of sulphur atoms increase as increase the concentration of acid in the electrolyte from 3 to 20wt%.

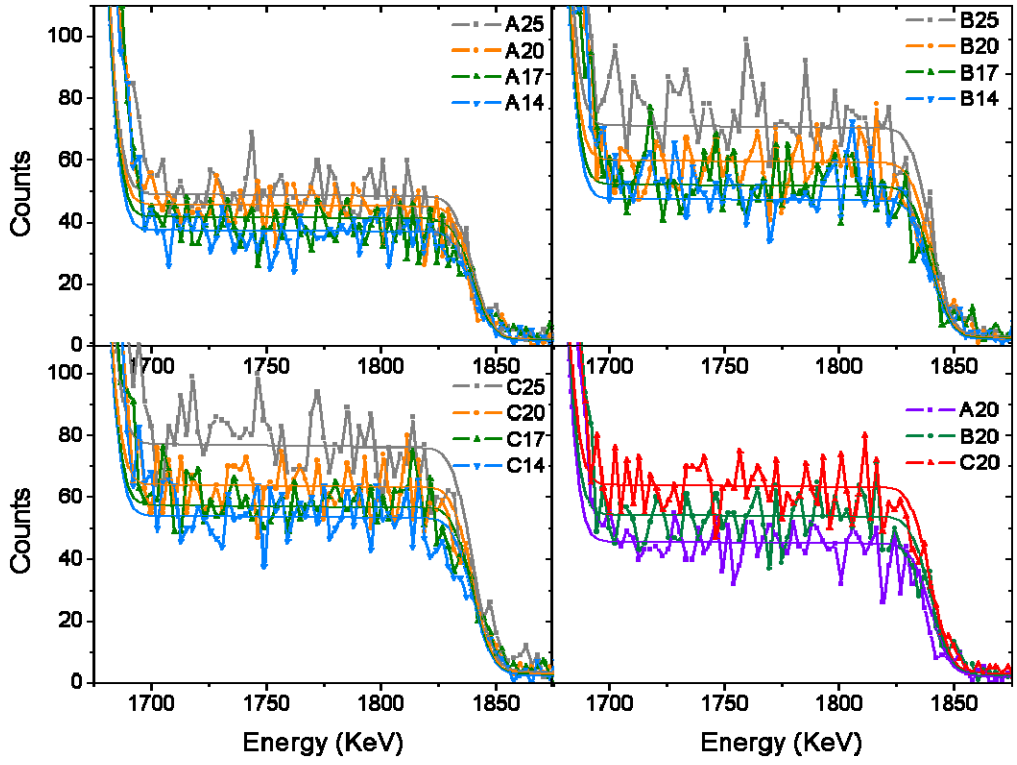

Figure 2-23:Detailed representation of the RBS spectra showing the signal coming from the Sulphur atoms incorporated into the anodic alumina for samples grown under 25, 20, 17 and 14V applied voltage for a) A, b) B and c) C Series.

We could identify the amount of sulphur nuclei contained in each sample based on their synthesis conditions from the simulations performed with SIMNRA program. After analyze the RBS simulations of all the samples we have quantified and verified that the higher the anodizing voltage and higher concentration of sulphuric acid into the electrolyte, the higher

amount of sulphur atoms incorporated into the alumina matrix of the samples. We also have observed that the sulphur nuclei concentration remains constant throughout the thickness of porous alumina films which have been analyzed in this study.

, this agrees with other studies, since the incorporation of anions SO_4^{-2} occurs mainly in linked form [5], this incorporation has its origins in the conversion of the porous layer barrier layer, and so it is logical that the concentration is uniform throughout the sample.

From the data extracted from the simulations, we have determined the composition of the analyzed alumina samples which results are presented in Table 2-9.

Table 2-9: Aluminium, Oxygen and Sulphur nuclei normalized concentration.

Series	Sample	[Al][1]	[O][1]	[S][1]
A	A25	0,355	0,616	0,029
	A20	0,365	0,608	0,027
	A17	0,360	0,615	0,025
	A14	0,350	0,628	0,022
B	B25	0,339	0,624	0,038
	B20	0,340	0,628	0,032
	B17	0,365	0,607	0,029
	B14	0,355	0,619	0,026
C	C25	0,339	0,617	0,044
	C20	0,334	0,628	0,039
	C17	0,340	0,626	0,035
	C14	0,355	0,613	0,033

[1] SIMNRA normalized concentration of the all elements in the samples.

As shown in Table 2-9, there is an increase of sulphur nuclei concentration as we go down in each series, so the C series has more sulphur because these samples were synthesized at the highest concentration of sulphuric acid.

2.6.2. Infrared

In order o identify the way in which occurs the addition of sulfur nuclei within the alumina, we performed infrared spectra in diffuse reflectance regime, because the samples had the

aluminum substrate. In Figure 2-24 we see the typical spectrum of an alumina porous anodic layer.

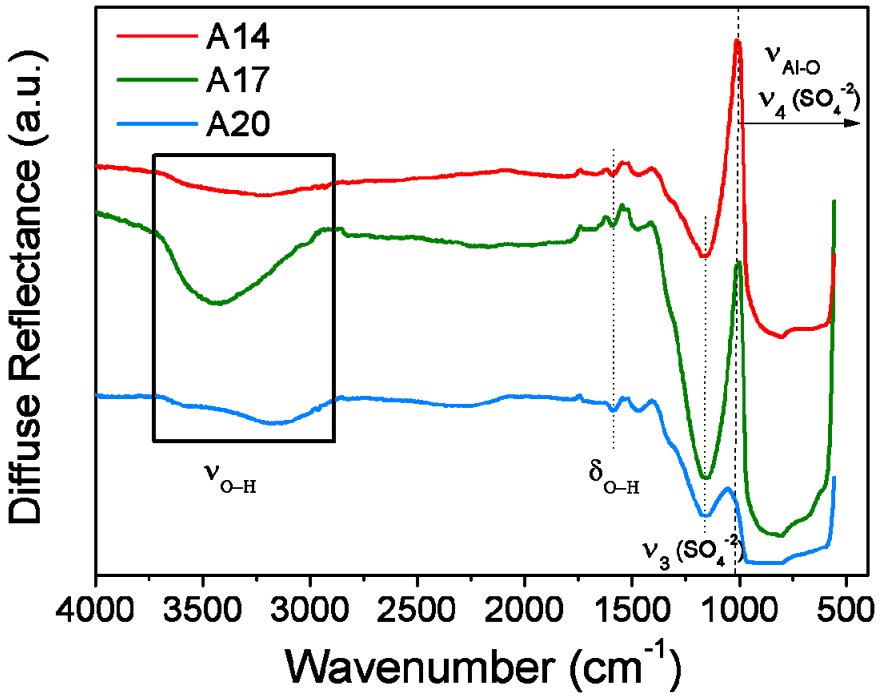

Figure 2-24: DRFTIR of sample A14 in red, A17 in green and A20 in blue.

The broad band centered at 3440 cm^{-1} corresponding to the stretching vibration of H_2O (ν_{O-H}) and the band at 1620 cm^{-1} corresponds to the vibration of deformation (δ_{O-H}), these bands correspond to H_20, so indicates that we have hydrated alumina. Analyzing the infrared spectra of all samples of this work (not showed) is observed qualitatively that all the samples show the vibrations corresponding to water, thereby confirming that all samples are hydrated. Regarding the presence of SO_4^{-2}, we only can identify the band ν_3 to 1160 cm^{-1} (normally appears at 1130 cm^{-1}), the band ν_4 also characteristic of this ion appear around 613 cm^{-1}, but we can't identify because it appears overlapped with other stretching bands of Al-O bonds (ν_{Al-O}), because below 1000 cm^{-1} the alumina presents a saturated wide band. Neither we can see ν_1 band, near to ν_3, with these bands we can conclude that the ion is free within the structure of alumina (symmetry group Td) [7] probably bounded by weak electrostatic forces to the alumina displacing Oxygen atoms. This could explain the shift to higher wavenumber of ν_3 band (SO_4^{-2}).

So, starting from this and from the elements nuclei concentration obtained from RBS analysis in Table 2-9, we have presented the following approach, $Al_2O_x(SO_4)_y$ for anodic alumina. The empirical formulae are presented in Table 2-10:

Table 2-10: Empirical formulae of anodic alumina obtained from RBS and IR analysis.

Series	Sample	Empirical formula
A	A25	$Al_2O_{2.82}(SO_4)^{-2}_{0.16}$
	A20	$Al_2O_{2.74}(SO_4)^{-2}_{0.15}$
	A17	$Al_2O_{2.86}(SO_4)^{-2}_{0.14}$
	A14	$Al_2O_{3.09}(SO_4)^{-2}_{0.13}$
B	B25	$Al_2O_{2.79}(SO_4)^{-2}_{0.22}$
	B20	$Al_2O_{2.94}(SO_4)^{-2}_{0.19}$
	B17	$Al_2O_{2.70}(SO_4)^{-2}_{0.16}$
	B14	$Al_2O_{2.90}(SO_4)^{-2}_{0.15}$
C	C25	$Al_2O_{2.60}(SO_4)^{-2}_{0.26}$
	C20	$Al_2O_{2.84}(SO_4)^{-2}_{0.23}$
	C17	$Al_2O_{2.87}(SO_4)^{-2}_{0.20}$
	C14	$Al_2O_{2.72}(SO_4)^{-2}_{0.18}$

Therefore we have confirmed our initial hypothesis that the incorporation of sulphate ions in the sample occurs in greater extent with the increment of voltage and acid concentration, this relation is shown in Figure 2-25.

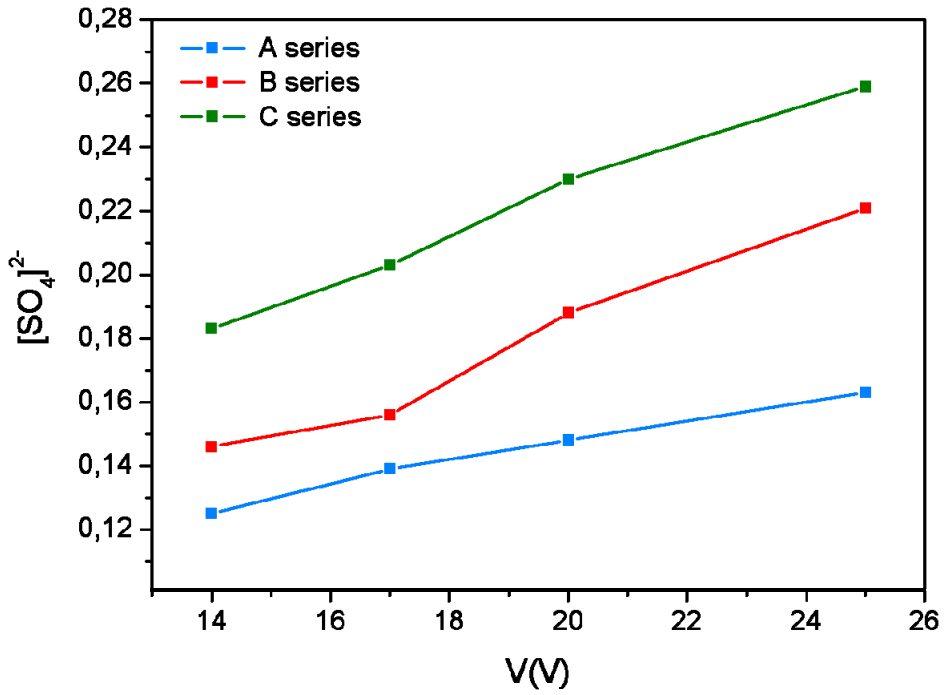

Figure 2-25: Variation of the sulphate ions concentration as a function of anodization voltage for each series, for the samples in which it is not possible to see the substrate, we only can quantify the amount of sulphates in the thickness where He^+ ions are backscattered.

It is known that during anodization, alumina is also incorporated water molecules [5], but we could not quantify the amount of H2O in each sample by this technique.

2.6.3. TG

In *Figure 2-26* we see the thermograms of A sample series, B20 and C20 in order to observe the behaviour of weight losses in function of the applied voltage and sulphuric acid concentration into the electrolyte. In the thermogram there are three areas of losses; in the first zone the weight loss corresponds to dehydration of the sample, in the second area the loss is due to deshydroxilation and the third zone in which weight loss is due to the ejection of impurities such as sulphates, this elimination occurs as SO_2 [8].

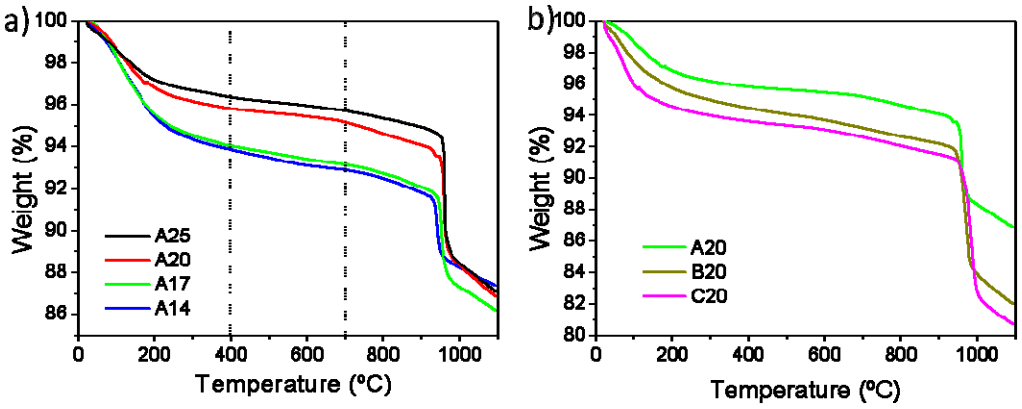

Figure 2-26: Thermo-Gravimetric curves of NAAFs from a) A series and b) those anodized at 20V for A, B and C series.

As can be seen in *Figure 2-26*a and b accordingly to the anodization conditions, samples show different losses of H_2O, OH^- and SO_4^{-2} differentiated in three different zones[9]. Analyzing the percentages of weight loss corresponding to water (up to 400^0C) from *Figure 2-26*a presented in Table 2-11 for A sample series, we can observe a greater ejection of water physically and chemically adsorbed, as decrease the applied voltage. These values vary from 3.65% up to 6.15%. Observing *Figure 2-26*b which quantitative analysis results are also presented in Table 2-11, we also can deduce an increase in water content as increase the concentration of sulfuric acid into the electrolyte.

Table 2-11: Weight loss percentage for A sample series, B20 and C20.

Samples	H_2O	OH	SO_4^{-2}	Total
A25	3,65	0,65	8,61	12,91
A20	4,20	0,64	8,31	13,14
A17	5,97	0,89	6,95	13,81
A14	6,15	0,98	5,51	12,64
B20	5,57	1,26	11,19	18,02
C20	6,40	1,00	11,91	19,31

Regarding to the behaviour of sulphates ions incorporations, we can quantify it by assuming that they begin to be ejected from 700°C. Their concentrations decrease with the applied voltage from 8.61 to 5.51% for the analyzed samples. We also can observe an inverse

dependence compared to the water content for the A sample series as decrease the applied voltage. On the other hand, the loss of sulphate ions increases from 8,31 up to 11.91% for samples grown under 20V as the sulphuric acid concentration into the electrolyte increase from 3 to 20%. This fact corroborates those results obtained from RBS showed in Figure 2-25.

We have different phase change temperatures mainly due to two factors: the content of sulphates and water. Samples which have higher levels of sulphates require a higher energy (higher temperature of phase change) in order to eliminate the sulphates and make the change of phase. Samples that containing more water, after removal have more room to remove sulphates and recrystallized, so require less energy intake for it and possess lower temperature phase change. We have been identified the phase change temperatures and are shown in Table 2-12.

Table 2-12: Phase change temperature for series A and 20V.

Sample	Tª (ºC)
A14	941,4
A17	952,1
A20	958,4
A25	960,6
B20	971,0
C20	988,7

The corresponding diffractograms of the samples analyzed are showed in *Figure 2-27*. The results of the analysis show that after the thermal annealing at 1100°C, the previous anodic alumina has become γ-alumina. These results agree with other studies performed in anodic alumina grown with sulphuric acid based electrolytes [45], oxalic acid based electrolytes [45, 48] or other growth methods but always annealed at temperatures not higher than 1100°C[82]. That is a cubic system with lattice face centered and space group: $Fd\bar{3}m$ (227).

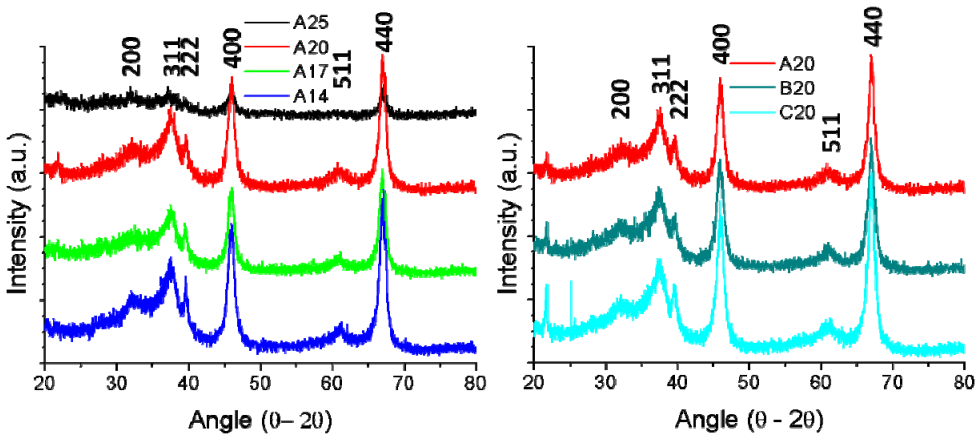

Figure 2-27: X-ray diffraction spectra for a) A25, A20, A17 and A14, and b) A20, B20 and C20, after annealing at 1100°C.

From the wide diffraction peaks we can infer that the crystallite size forming the anodic alumina after annealing are very small. We confirm this fact after analysis by the Scherrer formulae. The calculated crystal sizes are about 10nm, whit the main contribution of the peaks (440) and (400).

2.6.4. Study of mass density of NAAF.

In samples with thicknesses lower than 2,7µm, in which the He^+ ions have reached the aluminum substrate, we have been able to determine the density of the samples. In order to do this we take the values of the thickness of each NAAF, measured previously by HRSEM (*Table 2-2*,). This calculation has been possible to be performed for samples A14, A17, B14, B17, B20, C14 and C17. The formula used for calculating the density can be seen in Eq. 2.7:

Eq. 2.7:
$$\rho = \left(\frac{[M_S(at\%_S)+M_{Al}(at\%_{Al})+M_O(at\%_O)]N}{N_A\ \Delta x}\right)$$

Where ρ is the density (g/cm^3), N_A is the Avogadro number (mol^{-1}), M is the atomic weight of each atom (g/mol), at% is the concentration in SIMNRA normalized to 1 for each atom, N is the atomic concentration (at/cm^2) and Δx is the layer alumina thickness measured on SEM (cm).

Once the calculation of the density was made, this data must be corrected with the porosity of the sample, due to the contribution of the pores, thus obtaining two densities: one corresponding to the porous anodic matrix and the other to the anodic alumina after deduct the cylindrical porosity. The porosity of the sample was calculated in section 2.5.2 The data obtained can be seen in Table 2-13:

Table 2-13: Evolution of density and porosity in the synthesized samples.

Samples	Density (g/cm^3) Porous Anodic matrix	Porosity (%)	Density (g/cm^3) Anodic alumina
A14	2,28	10,5±1,7	**2,53±0,04**
A17	2,33	10,9±1,5	**2,57±0,04**
B14	2,27	10,7±1,9	**2,53±0,05**
B17	2,33	10,2±1,6	**2,57±0,04**
B20	2,38	11,2±1,3	**2,64±0,03**
C14	2,31	10,7±2,9	**2,56±0,07**
C17	2,42	11,0±1,7	**2,67±0,05**

As we can be seen in Table 2-13, density values range between from 2.28 to 2.42 g/cm3, unlike other authors that placed this value around 3.2 g/cm3 [6]. Within each series there is an increase in the density of the alumina, due to increased concentration of sulphur, as sulphur has greater atomic weight and therefore would cause an increase thereof.

In Table 2-13, the variation in density is more remarkable with the increasing of anodization voltage that with the concentration of the acid. We have greater density variation within the same series if we increase the voltage, than if we compare samples anodized at the same voltage but with different acid concentration. We can conclude that density is more affected by the anodization voltage that the concentration of acid used during synthesis. For this reason there is a gradual variation in density within the same series but not happens the same when we compared samples of different series.

2.7. The volume expansion factor and efficiencies of anodization processes.

Another important topic, as the volume expansion factor has been broached in this chapter. By this fact, it is possible to know the volume of Aluminium which is consumed during the anodization process and the volume of alumina which is generated from the Aluminium consumed atoms. From the previous data obtained from the slope we can infer that the volume expansion factor will be higher for the higher concentrations.

In order to calculate the volume expansion factor, first we have to know the volume of Aluminium which has been consumed during the anodization. This is relatively easy to know when the Aluminium is sputtered on the surface of a substrate because the thickness (or volume) is previously knew, but in our case we have to do some assumptions. We have to assume that during the process on the Aluminium electrode only Aluminium ions (Al^{3+}) are generated. For the calculus of consumed Aluminium we use the Faraday's Law for electrolysis and the charge passed in the electrodes of the cell. In order to simplify and do it more intuitive we have calculated in terms of thickness, so:

Eq. 2.8:

$$m = \frac{Q}{F} \cdot \frac{At_w}{z} = \rho \cdot V \quad \rightarrow \quad \frac{\sigma}{F} \cdot \frac{At_{W_{Al}}}{z} = \rho_{Al} \cdot h$$

Where σ is the charge density (current per unit area), F is the Faraday's constant, $At_{W_{Al}}$ is the atomic weight of Aluminium, z is the valence number, ρ_{Al} is the density of the Aluminium (as indicated in the specification of the company) and h is the thickness of consumed Aluminium.

So, finding h and dividing the thickness of the NAAFs generated (see *Table 2-3*) by h, i.e. the consumed Aluminium during the anodization process, we obtain the volume expansion factor, which is represented in *Figure 2-28*, showing the dependence on the applied voltage and its relation with the current densities.

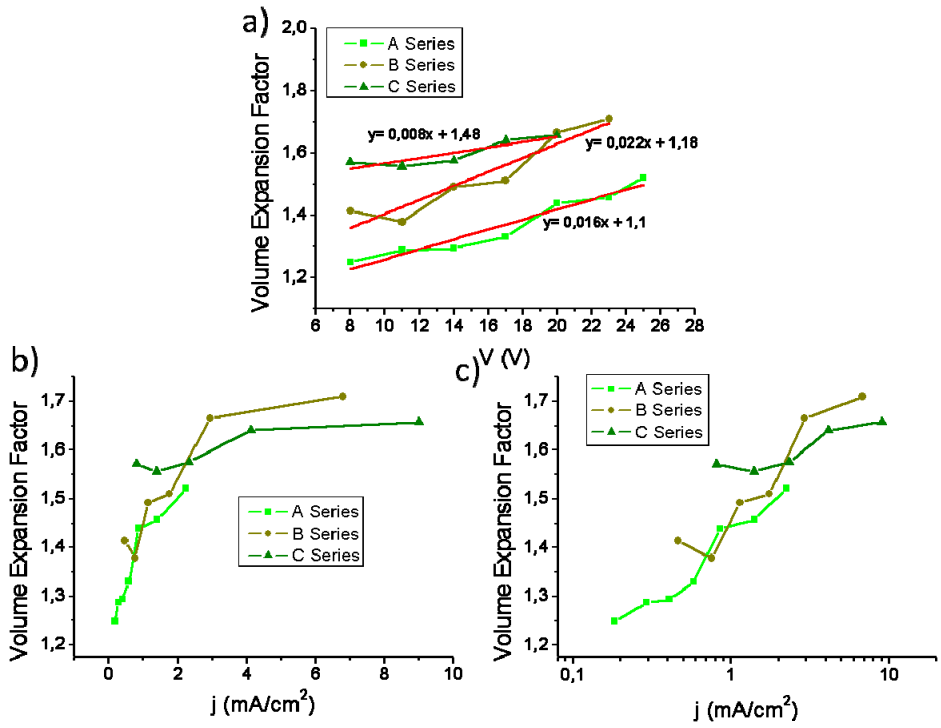

Figure 2-28: Volume expansion factor in function of: a) the applied voltage and b) the current density with linear scale and c) logarithmic scale for the A, B and C series.

It is clear that the volume expansion factor increase with the applied voltage and also with the sulphuric acid concentration in the electrolyte, increasing from ~1.25 up to 1.70. If we compare our results obtained in potentiostatic conditions to other in galvanostatic conditions, we find that the relation between the volume expansion factor and the applied voltage is the same [52]. Particularly, if we focus in B Series the dependence of the volume expansion factor is $y = 0{,}022x + 1{,}18$ at 0°C, which fits very well with those obtained for the same sulphuric acid concentration into the electrolyte, i.e. 10wt% but under galvanostatic conditions, $y = 0{,}0217x + 1{,}1$ and temperature fixed at 18 and 22°C. This fact indicates that the volume expansion factor is not only independent on the temperature of the electrolyte [52], but also in the source mode, i.e. potentiostatic and galvanostatic conditions. This volume expansion generates mechanical stress at the metal/oxide interface and is related with the self-ordering mechanism [27]. In our case, the samples with the best self-ordering have volume expansion factors ranging between 1.5 and 1.7 which differs a little with those data which estimated that for self-ordering conditions the volume expansion factor should the between 1.3 and 1.4 [39, 54]. This difference could be explained by taking into account that the later estimation it was assumed that the density of the alumina was 3.2gr/cm^3, and as we saw in section 2.6.474, at least, for our samples the mass density also differs from that value. It is worth to remark that the fact of the value of the volume expansion factor is in between these values do not implies that there is pore self-ordering, in the same way that the fact that the porosity values are around 10%. In the other hand our values match quite well with the results presented in other works for samples grown in electrolytes based on sulphuric acid under galvanostatic conditions [53], and from *Figure 2-28*b and c could be perceived a logarithmic dependence of the volume expansion factor on the current densities, which would implies that it would be related to the electric field since the logarithm of the current is proportional to electric field [83].

We can also evaluate the efficiency of the anodization processes for the samples which have been possible to determine the density of the Aluminium atoms through the whole thickness of the NAAF till the substrate. This calculation has been carried out dividing the Aluminium atoms density inside the alumina matrix by the anodized Aluminium atoms. The aluminium atoms density is taken from the RBS simulation and the anodized Aluminium atoms from the Faraday's law Eq. 2.8. The efficiency data is presented in Table 2-14 and in Figure 2-29 in function of the resultant current density.

Table 2-14: Efficiency of the anodization processes under different anodization conditions.

Efficiency	A Series	B Series	C Series
20 V	-	0,67	-
17 V	0,55	0,62	0,66
14 V	0,51	0,59	0,63

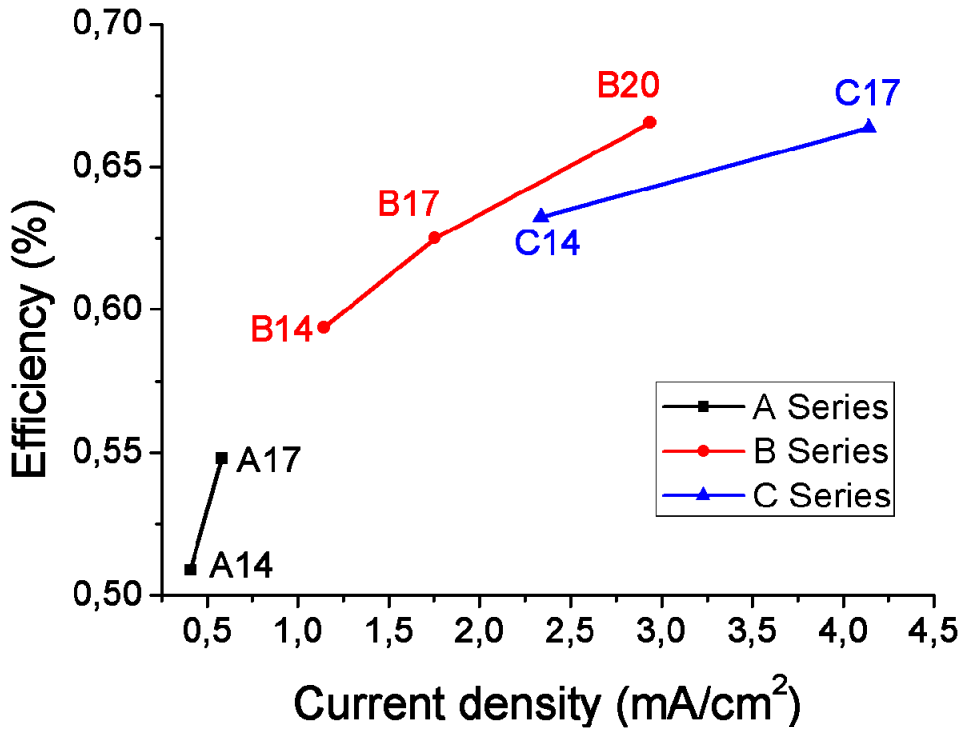

Figure 2-29: Efficiency related to the current densities associated to different potentiostatic anodization processes.

From Table 2-14 we can observe that the efficiency increases with the anodizing voltage and with the sulphuric acid concentration into the electrolyte, and in Figure 2-29 we observe a similar behaviour to the volume expansion factor represented in *Figure 2-28*. We also can observe that there is a tendency of the efficiency to be limited around 70% under moderated anodizing conditions. This efficiency increasing comes with an increase of the sulphur atoms incorporation into the alumina matrix as we can see in Table 2-9. However, the water content of the anodic alumina is not concerned by the efficiency increasing regarding the current density yielded by the potentiostatic anodizing conditions.

2.8. Optical properties of NAAF and its applications.

In this section, we have used reflectance spectrometry to calculate the refraction index of the NAAFs and their thicknesses by a non-destructive method. From the obtained results it is also possible to infer volume fraction impurities which were not possible observing by SEM. Theses calculus has been developed based in two different models, one based on an iterative method and the second one on the Maxwell-Garnett model.

2.8.1. Refraction index calculation by iterative method.

The reflectance spectra are presented in Figure 2-30 for the A, B and C series. In the spectra appear interferences, know as Fresnel interferences. These interferences are created by the constructive and destructive superposition of the electromagnetic waves reflected on the NAAFs.

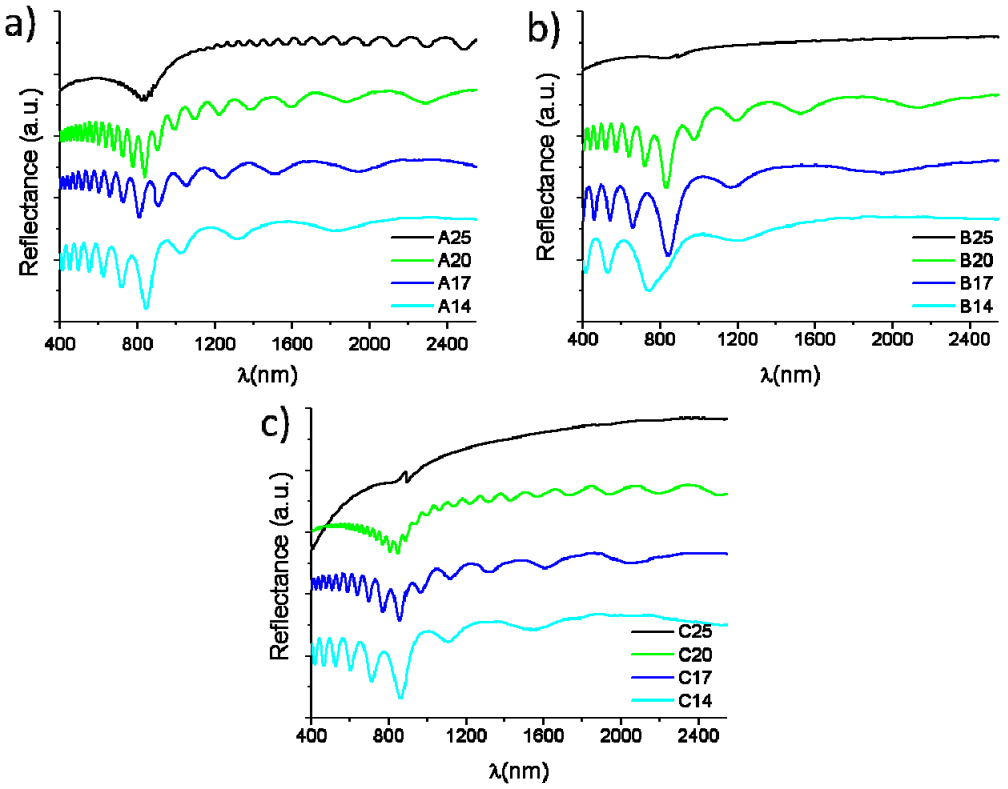

Figure 2-30: Reflectance spectra of NAAF's grown under 25, 20, 17 and 14V for a) A, b) B and c) C sample series.

The wavelength of the maxima must be taken in a region where the spectrum has no absorption band, otherwise we would not have trustable values. So, we have selected the region with wavelengths between 400 and 2550nm. We can make a qualitative and

preliminary observation from the Fresnel interferences. The thicker the NAAF, the less Fresnel interferences and the more shifted to the UV range where lower wavelengths. As increase the thickness of the NAAF, the number of interference fringes increase and shift to the Vis and NIR. And for the thicker samples (thickness higher than 10µm), the Fresnel interferences are shifted to the NIR up to the sample is thick enough to present no more interferences. Around 840nm there is an absorption peak typical from the Aluminium, and at 890nm there is a spike due to the change of monochromator from NIR to Vis-UV.

Starting from these interferences, we can calculate the refraction index of each NAAF. We only use the Snell's Law, Eq. 2.9 , and the Bragg's equation, Eq. 2.10, and take the wavelength of the maxima of the generated interferences in the spectra.

Eq. 2.9: $$n_1 \cdot \sin\theta_1 = n_2(\lambda_i) \cdot \sin\theta_2(\lambda_i)$$

Eq. 2.10: $$\begin{cases} 2 \cdot n_2(\lambda_i) \cdot h_{SEM} = m_i \cdot \lambda_i \\ 2 \cdot n_2(\lambda_i) \cdot h_{SEM} = (m_i + 1) \cdot \lambda_{i+1} \end{cases} \Rightarrow \quad n_2(\lambda_i) = \frac{\lambda_{i+1}}{2 \cdot h_{SEM} \cdot \cos\theta_2(\lambda_i) \cdot \left(\frac{\lambda_i - \lambda_{i+1}}{\lambda_i}\right)}$$

Where n_1 is the refraction index of air which value is 1.003≈1, $n_2(\lambda_i) = n_{NAAF}(\lambda_i)$ is the refraction index of the NAAF as function of the wavelength, θ_1 is the angle of the incident beam which is fixed at 45°, $\theta_2(\lambda_i) = \theta_{NAAF}(\lambda_i)$ is the angle of the refracted beam through the alumina film which depends on the wavelength, λ_i is the wavelength of the beam, and h_{SEM} is the thickness of the NAAF previously measured on SEM micrographs.

The mathematical algorithm created is based in an iterative method in which we force to converge both $\theta_2(\lambda_i)$ and $n_1(\lambda_i)$ to their actual value. So, we start with whatever initial value of n_{NAAF} that we use to calculate a value for $\theta_{NAAF}(\lambda_i)$ with Eq. 2.9, represented in Figure 2-31. Samples B25 and C25 could not be analyzed because of lack of interferences in their reflectance spectra.

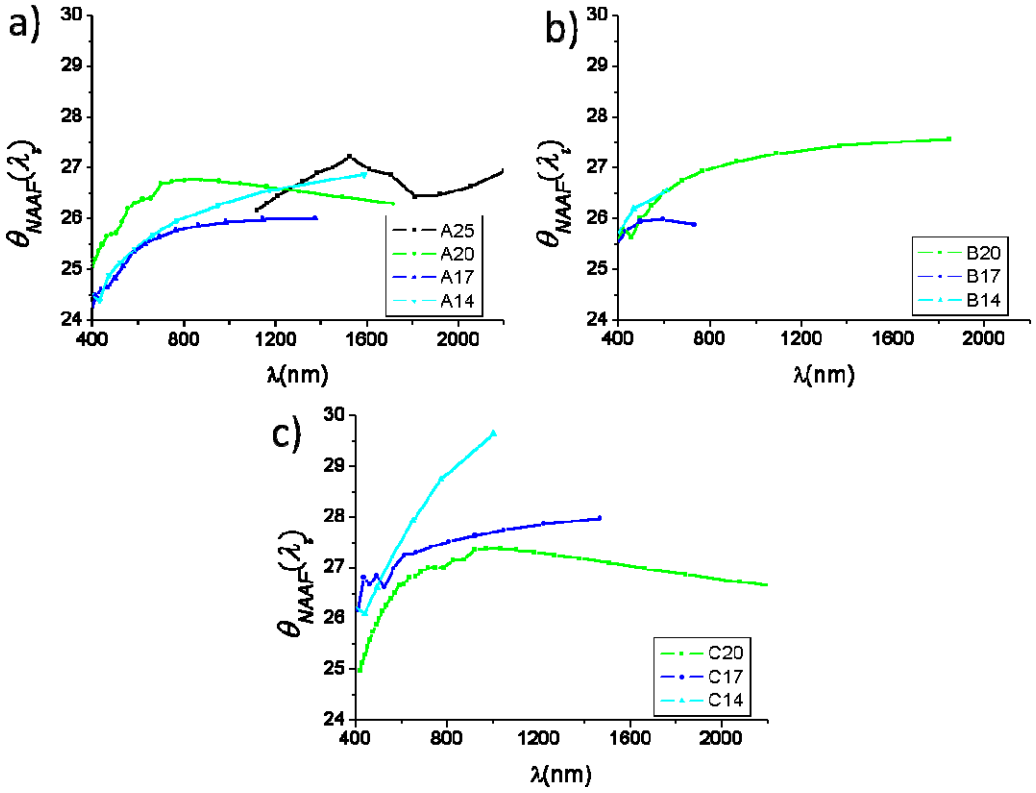

Figure 2-31: Angle of the refracted angle into the NAAF matrix. The incident beam angle is 45° for samples grown at a) 25, 20, 17 and 14v for A Series, and 20, 17 and 14V for b) B series and c) C series.

These angles are introduced in Eq.2.10 so that we obtain a value of $n_{NAAF}(\lambda_i)$. Then we calculate the absolute value by resting the initial value of n_{NAAF} to $n_{NAAF}(\lambda_i)$, and we impose that it has to be less than 0.0001. If the difference is higher than the limit we impose, i.e. 0.0001, the program will take the new calculated value to keep on running till the result the rest be less than 0.0001. We have represented the result of this calculus obtained from this program in Figure 2-32.

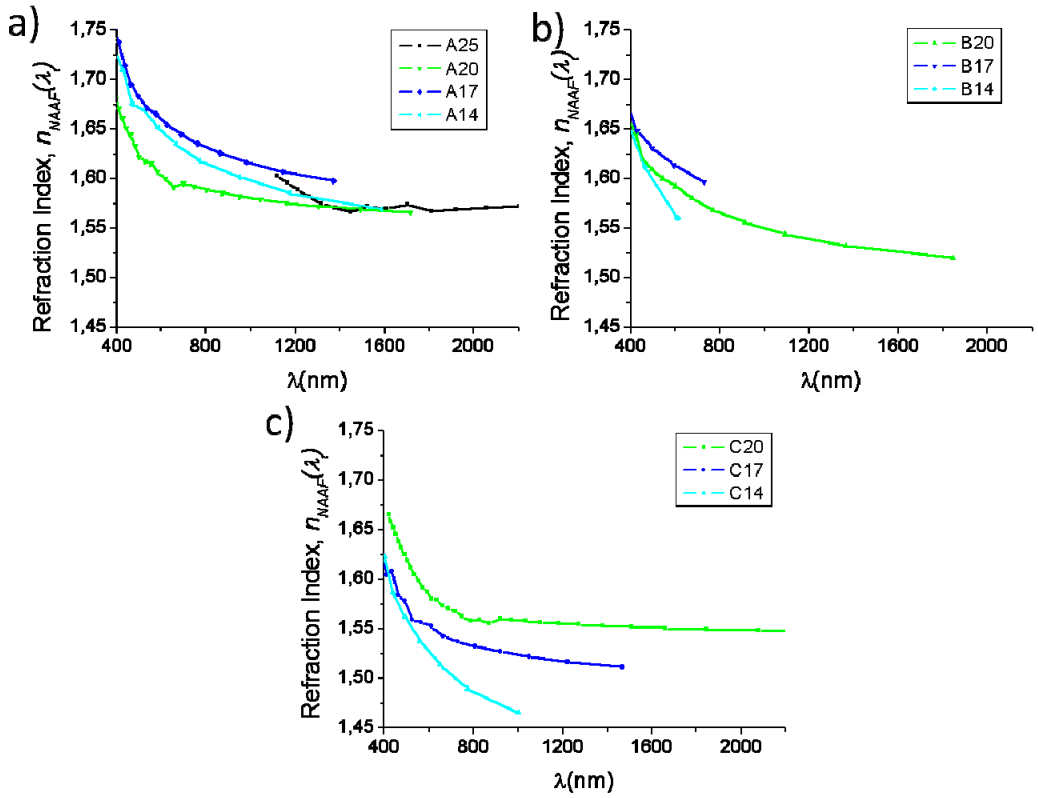

Figure 2-32: Refraction index in function of the incident wavelength for samples grown at a) 25, 20, 17 and 14v for A Series, and 20, 17 and 14V for b) B series and c) C series.

We can observe from Figure 2-32 that the behaviour of the refraction index is approximately constant in the NIR range, but not in the Vis range when it increases significantly. On the other hand, it is not possible to establish a direct relation between the applied anodization voltage for each series and the refraction index, but if we pay attention to the dependence on the sulphuric acid concentration into the electrolyte in the Vis range spectra, we can find as follow in Figure 2-33:

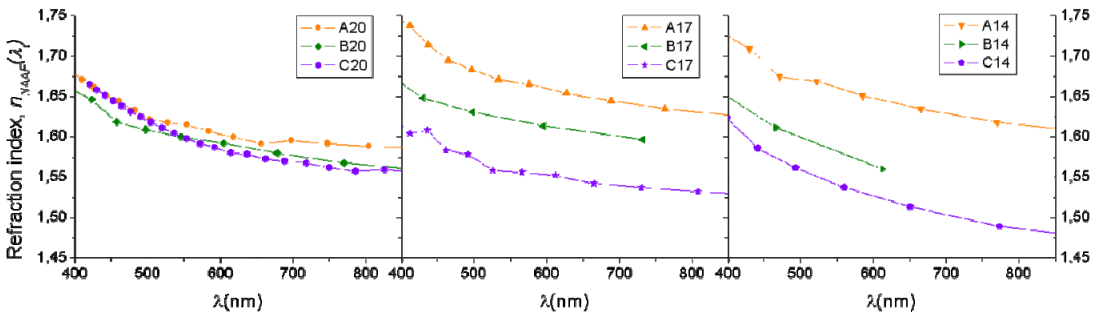

Figure 2-33: Refraction index as a function of the incident wavelength for samples anodized with 3, 10 and 20wt% sulphuric acid concentration under applied voltage of a) 20V, b) 17V and c) 14V.

In Figure 2-33 it is clear the relation between the concentration of sulphuric acid into the electrolyte and hence the sulphate ionic concentration with the refraction index obtained for these samples. The lower the sulphate ions concentration, the higher the refraction index.

2.8.2. Non-destructive method based on Maxwell-Garnett's effective medium model for NAAF thickness determination.

This method based on Maxwell Garnett's model allow us to evaluate the thickness of the NAAF's quite precisely starting only from the reflectance spectra and without the necessity of prepare the sample for a cross-section view in an electronic microscope, which after would not be easy to recover for later experiments.

We have adopted the Maxwell-Garnett effective medium model since, is closest to the morphology of the anodic film, with well separated pores, embedded in a continuous alumina film. The Bruggemann model is better suited for aggregate structures in which the two components appear in almost equal distributions to form a space-filling random mixture.

So, the Maxwell-Garnet effective medium equation presented in Eq. 2.4 can be presented as Eq. 2.11, in order to simplify:

Eq. 2.11:
$$\varepsilon_{eff} = \frac{\varepsilon_a \cdot (\varepsilon_b + 2\varepsilon_a + 2f_b(\varepsilon_b - \varepsilon_a))}{\varepsilon_b + 2\varepsilon_a - 2f(\varepsilon_b - \varepsilon_a)}$$

We have assumed that our anodic alumina is transparent in the wavelength range we have used, that is, the absorption coefficient, *k* in $n_c = n + ik$ is equal to 0, so $\varepsilon^{1/2} = n$. We also have based our calculus on the Palik's alumina refraction index as function of wavelength. From now on, the components *a* and *b* will be *alumina* and *air*, respectively, and $\varepsilon_{eff} = \varepsilon_{MG\text{-}NAAF}$. So, we can rewrite Eq. 2.11 as Eq. 2.12:

Eq. 2.12:
$$n_{MG-NAAF}(\lambda_i) = \left(\frac{n_{PAL}(\lambda_i)^2 \cdot \left(n_{Air}{}^2 + 2n_{PAL}(\lambda_i)^2 + 2f_{Air}(n_{Air}{}^2 - n_{PAL}(\lambda_i)^2) \right)}{n_{Air}{}^2 + 2n_{PAL}(\lambda_i)^2 - 2f(n_{Air}{}^2 - n_{PAL}(\lambda_i)^2)} \right)^{1/2}$$

The obtained values of the refraction index are introduced in Eq. 2.9 to obtain the angle of the refracted beam into the NAAF in function of the wavelength. Note that the values of $n_{MG\text{-}NAAF}(\lambda_i)$ depend on the f_{Air} which, at this point, are the values of the cylindrical porosity represented in *Figure 2-19*.

Once we have the reflected angle into the NAAF's, we can also calculate the thickness based of the Maxwell-Garnett effective medium model by finding h in Bragg's equation, Eq. 2.13:

$$\textbf{Eq. 2.13:}\quad h_{MG}(\lambda_i) = \frac{\lambda_{i+1}}{2 \cdot n_{MG-NAAF}(\lambda_i) \cdot \cos\theta_{NAAF}(\lambda_i) \cdot \left(\frac{\lambda_i - \lambda_{i+1}}{\lambda_i}\right)}$$

Since we get a thickness value for each maximum wavelength, we do an average with these values which are presented in Table 2-15 and compared with those showed in *Table 2-2*. The error presented in column h_{MG} *(µm)* is the standard deviation of the obtained values.

Table 2-15: Thickness of studied samples measured by SEM and Reflectance and the relative variation.

	h_{SEM} *(µm)*	h_{MG} *(µm)*	$(h_{SEM} - h_{M-G})/ h_{SEM}$ *(%)*
A25	10.5±0.05	9.9±0.3	6,3
A20	3.77±0.01	3.6±0.2	3,9
A17	2.38±0.01	2.4±0.1	-0,8
A14	1.62±0.01	1.6±0.1	1.2
B20	1.96±0.01	1.9±0.1	4,9
B17	1.08±0.01	1.05±0.05	2,8
B14	0.69±0.01	0.67±0.03	3,1
C20	6.00±0.01	5.6±0.2	6,8
C17	2.72±0.01	2.5±0.2	7,5
C14	1.47±0.01	1.36±0.09	7,3

As we can observe in Table 2-15, the percentage of deviation regarding the thickness measured in the SEM micrographs are always lesser than 8%, and the estimated error in thickness calculations based on the Maxwell-Garnett model are as well less than 7%. So these calculated thickness values by this non-destructive method are in good agreement with the actual values. Nonetheless, we have noticed that the present deviations are always in the same way, that is, the thicknesses we estimate are always lower or almost equal than those measured on SEM micrograph. This takes us to the next section.

2.8.3. Nanoporosity and anion incorporation influence on refraction index.

Since our calculi are dependent on the volumetric fraction, in this case, cylindrical porosity, it could be point to that there is something more which is no present in our calculi that impede us geting more precise thickness values.

Let's take a look at the refraction indexes calculated by the Maxwell-Garnett effective medium method (Figure 2-34):

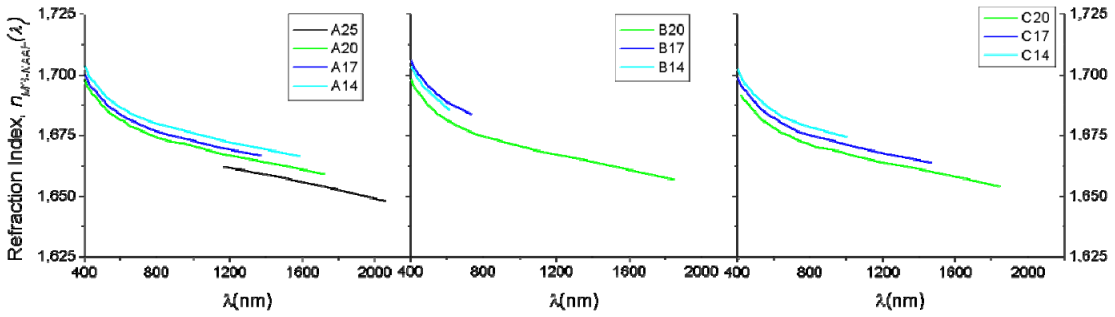

Figure 2-34: Refraction index obtained by applying the Maxwell-Garnett method taking into account only the cylindrical porosity.

If we compare Figure 2-32 and Figure 2-34, we can observe a significant difference in the refraction index values. It was expected since the values obtained with the Maxwell-Garnett effective medium we have not take into account the effect of the water and anion incorporation probed in Section 2.6. Moreover, these calculi start from the refraction index of the Palik's alumina, which is pure and has crystalline structure, while the anodic alumina is anion contaminated and has amorphous structure.

So, from this difference in the refraction index values, we can confirm that the sulphates ions and physical adsorbed water incorporation has significant influence on the optical properties of the anodic alumina matrix, which presence range between 12 and 20% of the mass weight, as we saw in the previous section, and it is necessary take it into account for calculations. This fact makes clear that these impurities have different dielectric constants and must be treated like that.

For more precise results it would be required an effective medium model extremely complicated, by including, at least, two more elements to the heterogeneous model with their different and dielectric constants [57]. Moreover, it could be possible to consider optical anisotropy due to the distribution of the secondary porosities[19].

2.9. Narrowing Co nanowires: Study of the effect on magnetic properties.

2.9.1. Fabrication of Co Nanowires by potentiostatic electro-chemical deposition.

For the development of this study, we have selected the samples A25, B23 and C17 (see chapter 3) since the pore diameters are getting reduce while remain self-ordering domains. In first place, these samples were etched as explained in section 1.1.5 in order to become the NAAF into a NAAM. The thickness of the starting NAAFs was fixed to be around 50µm in order to avoid mechanical breaking of the alumina during the etching. After the removal of the barrier layer, a 150nm Gold layer thickness is deposited by sputtering before electrochemical deposition under potentiostatic conditions (see section 1.2.2.). The electrolyte containing the Co source consists of an aqueous solution composed by 0.9M $CoSO_4$ and 0.5M H_3BO_3. The potentiostatic electrochemical deposition (PECD) was carried out by applying -1.0V. The temperature of the electrolyte is maintained at 30°C with a slow stirring of 150rpm in order to maintain homogeneous pH and temperature of the electrolyte during the electrochemical deposition process.

The PECD were carried out in two sample series. The PECD times are 90s and 25s in order to obtain similar geometrically structured with different Co nanowires lengths. The registered data obtained from PECD is presented in Figure 2.35.

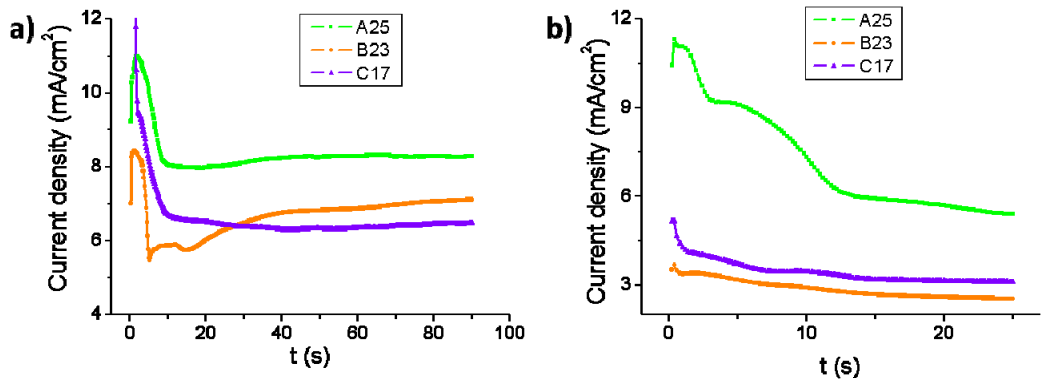

Figure 2.35: Current density of Co PECD carried out during a) 90s and b) 25s.

The nucleation of the Co nanowires at the sputtered Gold electrode takes place within the first 10 to 20 seconds of the PECD. After that, the electrodeposition current density becomes more stable and the nanowires begin growing.

2.9.2. **Electronic micrograph and structural characterization of Co nanowires.**

The samples were observed by SEM in order to make accurate measurements of the electrodeposited nanowires lengths. In Table 2-16 are presented cross sectional micrographs of the samples electrodeposited during 90 and 25s.

Table 2-16: Micrographs of the electrodeposited samples under same condition during 90 and 25s.

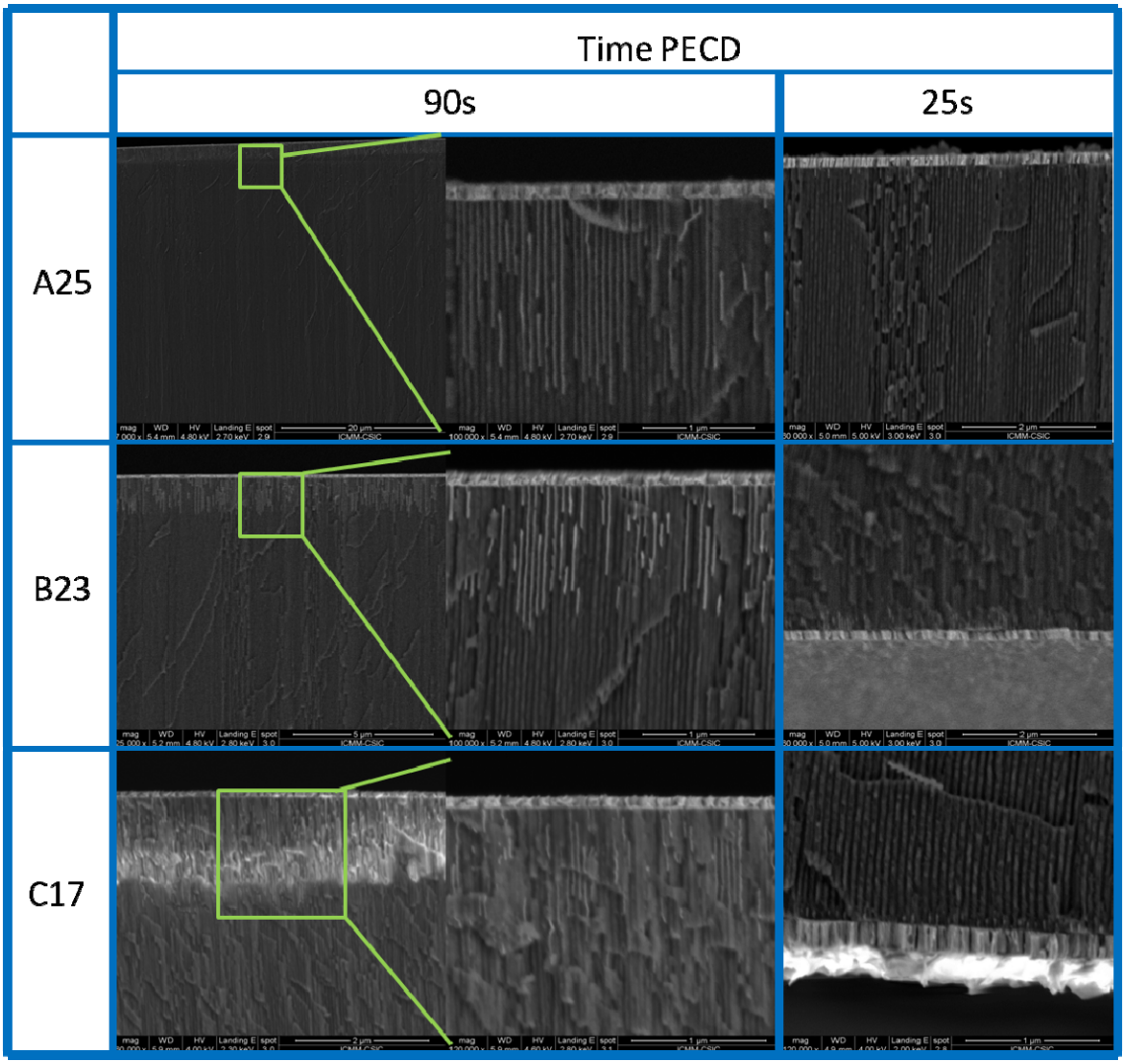

In these micrographs (Table 2-16) we can see the sputtered Gold layer instead of the barrier layer. This metallic layer which acts as electrode has a thickness of 150nm approximately. As shown in the lower magnification micrographs, the Co electrodeposition process is quite homogeneous. On the other hand, at higher magnifications we can observe some broken Co nanowires, but this is due to the cleavage planes of the NAAF. In Table 2-17 are presented the geometrical characteristics of the electrodeposited Co nanowires measured from SEM micrographs.

Table 2-17: Distance among nanowires, diameter and length of the electrodeposited Co nanowires in function of the sample template and electrodeposition time.

	PECD time (s)	NW to NW distance (nm)	Nanowires Diameter (nm)	Length
A25	90	40±2	26±1	1.6±0.2 µm
	25	40±2	26±1	0.15±0.05 nm
B23	90	34±2	23±1	1.2±0.1 µm
	25	34±2	23±1	0.1±0.05 nm
C17	90	26±2	19±1	1.2±0.1 µm
	25	26±2	19±1	0.2±0.05 nm

The length deviation in the shorter series of nanowires is high percentile, but we have to take into account that the nucleation of the nanowires do not occur at once, i.e. some of them nucleate and begin growing before than others. That is the reason why the nanowires do not have the same length and the difference reach 50% regarding the shorter nanowires. The pore diameter has also been increased in all the samples due to the chemical etching necessary to open the barrier layer.

X-ray diffraction patterns are shown in Figure 2.36 of the samples series after 90s Co PECD. The peak which appears at 41.61° can be ascribed to the (110) which should appear at 41.55° and the peak which appears at 47.46° can be ascribed to the (101) which should appear at 47.41°. The spectrum pattern can be assigned to polycrystalline hcp structure, as was expected. The samples of Co nanowires electrodeposited during 25s did not show Co diffraction pattern since the material is not enough to give back a signal, although fcc signal was expected for these samples[70].

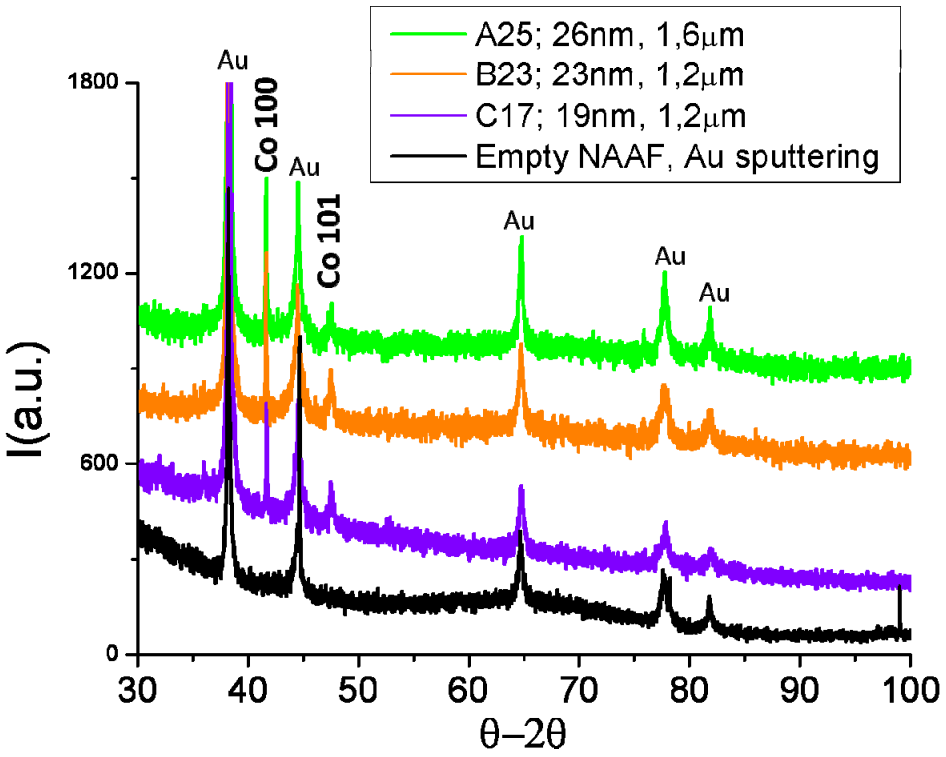

Figure 2.36: X-ray diffraction spectrum of electrodeposited Co nanowires arrays during 90s.

The results obtained from the grain size and orientation parameter analysis of the samples electrodeposited 90s are presented in Table 2-18.

Table 2-18: Orientation parameter and grain size for samples with lengths between 1.2 up to 1.6 µm.

Sample template	Plane orientation	Orientation parameter	Grain size (nm)
A25	Co (100)	0,961	60,5
	Co (101)	0,0390	0,4
B23	Co (100)	0,934	87,8
	Co (101)	0,0659	1,1
C17	Co (100)	0,924	68,1
	Co (101)	0,0757	1,5

The crystal structure of the Co polycrystalline nanowires is clearly textured in the direction (100) with orientation parameters higher than 0.92, and with grain sizes between 61 and 89nm.

2.9.3. **Magnetic characterization.**

The hysteresis loops measured in parallel and perpendicular to the nanowires axis are showed in Table 2-19 for three kind of sample template electrodeposited with nanowires of different lengths.

Table 2-19: Hysteresis loops for samples templates A25, B23 and C17, electrodeposited during 90 and 25s.

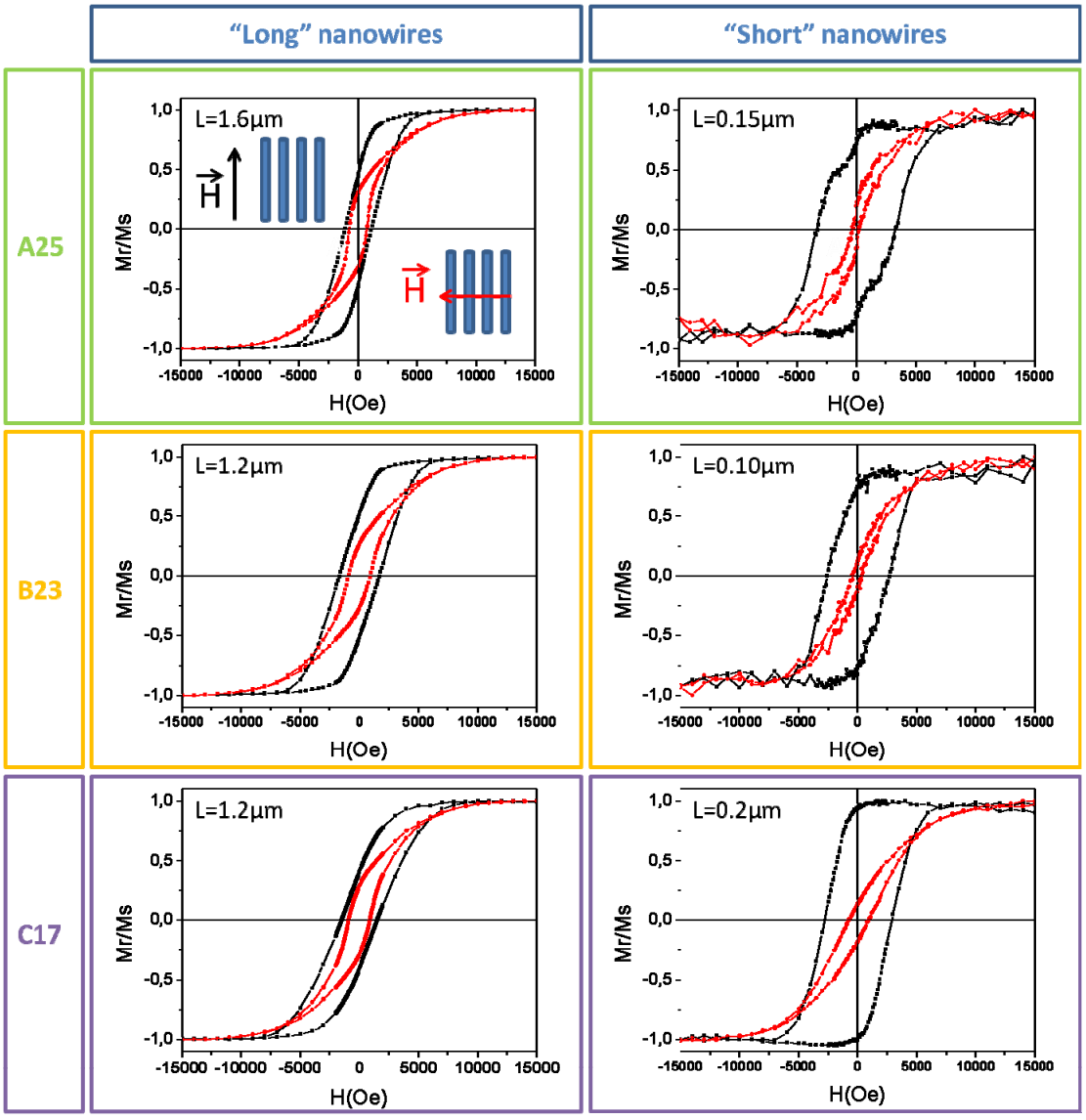

When the length of the nanowires is shorter than 200nm, the magnetic properties change regarding the long ones. The easy axes of the shorter nanowires is found parallel to the wire axis, as expected from Co with fcc structure [70]. In the case of the sample A25 with short Co nanowires, an interesting two phase behaviour can be observed on the coming out of

saturation when the sample is measured parallel to the wire axis. Here, the length of the sample is close to the limit at which the hcp structure is expected to appear. This feature indicate the possibility that both hcp and fcc structures coexist in these nanowires.

For both long and short Co nanowires, the perpendicular hysteresis loops have a higher magnetic susceptibility than the parallel loops, as is expected for hcp structure. The coercivity in the perpendicular applied field to the nanowires trends to increase as the nanowires are placed in close proximity to each other, but at the same time, as less is the distance among the nanowires, the less are their diameters, counteracting the increase of the coercivity field. This is represented in Figure 2.37, where the ratio of Interpore Distance and diameter of the nanowires is a factor which indicates the proximity among the nanowires and their diameters. From Figure 2.37 it could be possible to point out stronger dipolar coupling as the nanowires are closer to each other.

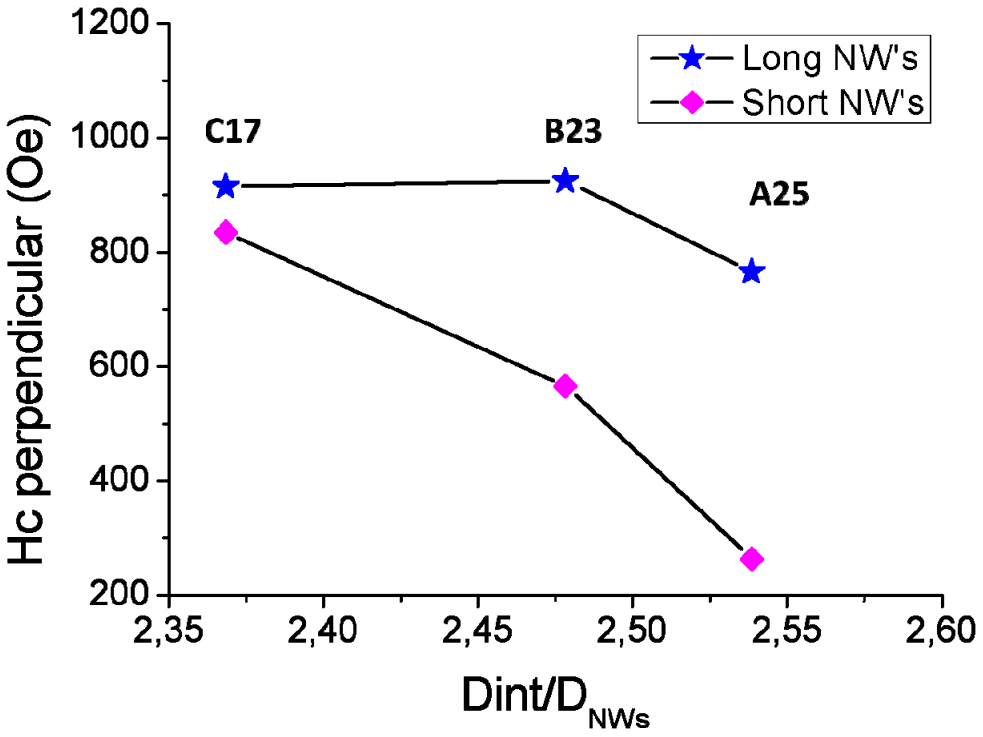

Figure 2.37: Coercive field dependence on the ratio of Interpore distance and nanowires diameter (D_{NWs}) when magnetic field is applied perpendicular to the nanowires.

Angle dependence studies of magnetic properties also were performed in these samples, as showed in Figure 2.38. Figure 2.38a exhibit an nearly isotropic behaviour regarding the coercive field, whereas Figure 2.38b shows a strong anisotropy.

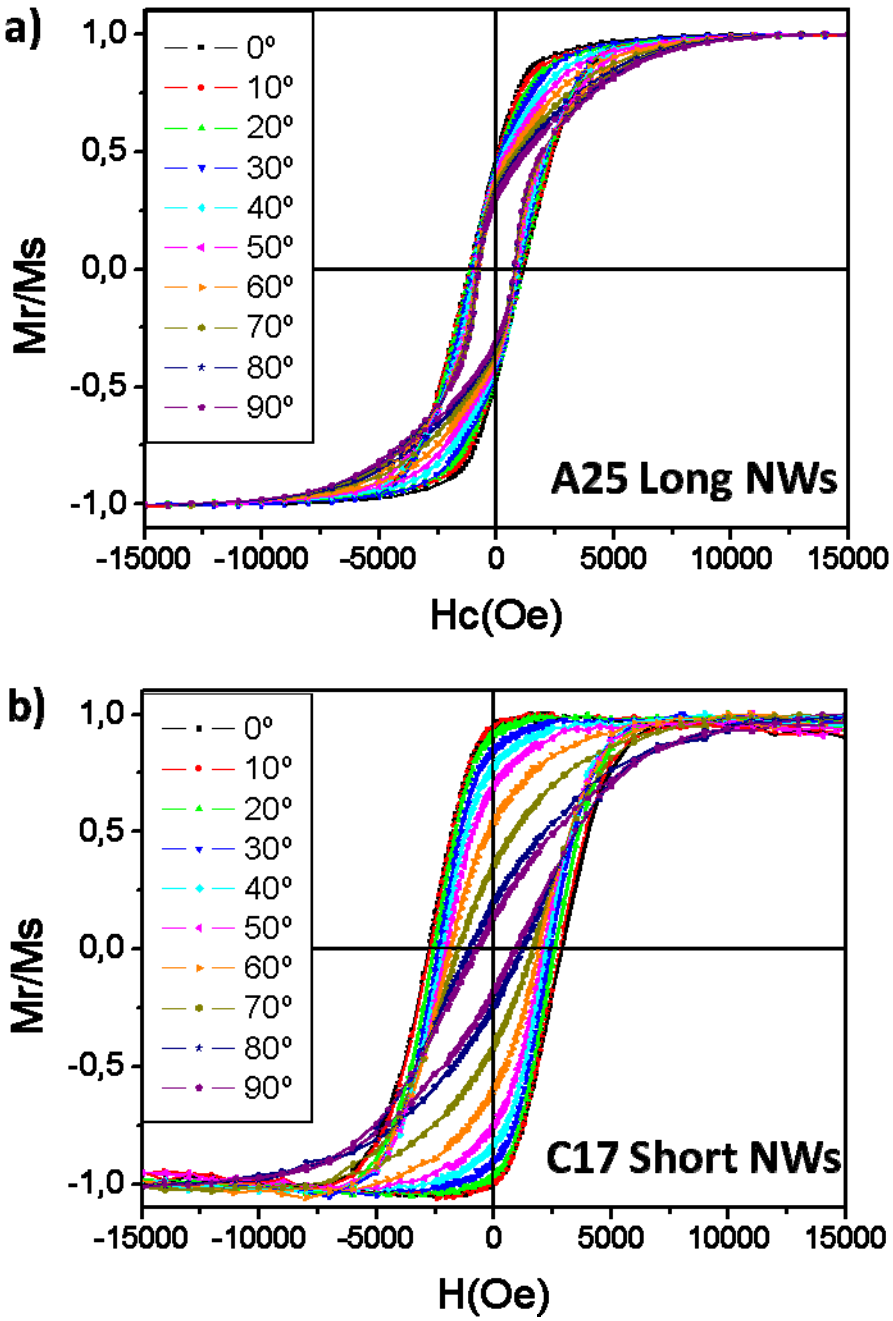

Figure 2.38: Hysteresis loops performed by increasing the angle between the axis of the nanowires regarding the applied magnetic field from 0 up to 90° with step of 10° for sample a) A25 long NWs and b) C17 short NWs.

The magnetic properties as function of the magnetic field angle regarding the nanowires are represented in Table 2-20. The long nanowires present an almost isotropic behaviour with the angle, although the strength of the uniaxial anisotropy seems to increase as decrease the ratio $Dint/D_{NWs}$. This is consequence of stronger magnetostatic coupling between the nanowires. On the other hand, the short Co nanowires present a very strong magnetic anisotropy in the

coercive field. The strength of the magnetic anisotropy also decreases with the ratio Dint/D_{NWs}. It is remarkable the case of the sample A25 for long and short nanowires, where the variation of the coercive field is almost 10 times higher for the shorter than for the longer ones, decreasing from 3300 down to 250 Oe.

Table 2-20: Coercive field and remanence of the normalized magnetic moment for the sample templates A25, B23 and C17 with long and short nanowires.

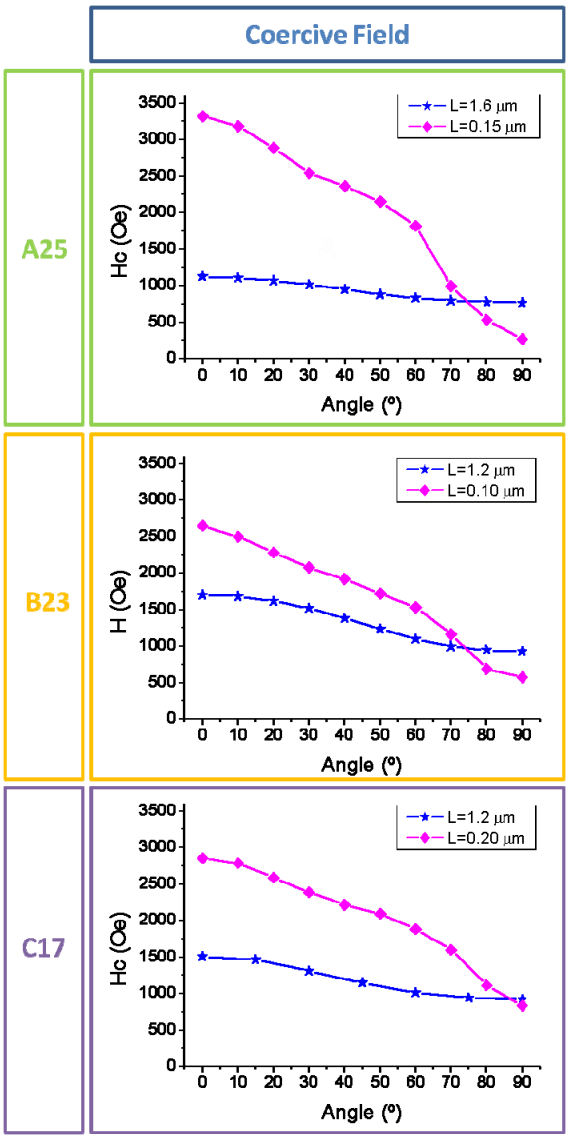

2.10. Summary.

Self-correlation functions (SCF) can be used for high resolution scanning electron microscopy (HRSEM) images processing, especially, from self-assembled systems like nanoporous anodic alumina films (NAAF) and membranes. Self-correlation Images constitute a powerful tool for surface HRSEM images characterization and take into consideration large surface areas; in this way this technique presents an alternative to Fast Fourier Transform and Pair Distribution Function analyses. Moreover, the SCI's represents real-space images and can also be used to make direct measurements of relevant surface parameters easily and faster, particularly, in ordered nanostructured surfaces.

This study, following extensive and systematic experimental work, has demonstrated, using a SCF and SCI based technique, with high accuracy, that is possible to reduce the interpore distance by 15 nm and the pore diameter by 6nm within self-ordering regimes, by increasing the concentration of sulphuric acid of the electrolyte from 3 up to 20wt% and by decreasing the applied voltage from 25 down to 20V, complying also with the 10% porosity rule. Moreover, the porosity values of the samples outside the self-ordering regimes remain constant and around 10%. The ratio interpore distance and applied voltage remains around 2.5nm/V for self-ordered nanoporous independently on the sulphuric acid concentration into the electrolyte.

From compositional studies we have observed that sulphur nuclei contents incorporated into the alumina matrix are between 2 and 4.5%, forming sulphate ions. The NAAF also contains adsorbed water into their walls which measured quantities are lesser than 7%.

We also have observed that there is an increase in the volume of grown alumina for the same quantity of charge flowing through the electrodes in the cell, starting from that we could infer an increase in the efficiency of the anodization as increase the concentration of sulphuric acid in the electrolyte. Moreover, from the results obtained in the calculus of the volume expansion factor it has been noticed that this values also increase with the applied voltage and the sulphuric acid concentration, obtaining values which range between 1.5 and 1.7 for the best self-ordered samples, indicating that the mechanical stress generated in the metal/oxide interface for these conditions is optimal for achieve self-ordering under these experimental parameters, but obtaining these values for one sample do not implies self-ordering conditions.

The refraction index calculated by a iterative method based on Bragg and Snell equations are between 1.5 and 1.6. The thicknesses of the NAAFs are also calculated with a mathematical algorithm based on the Maxwell-Garnett effective medium model.

Finally, as an example, some samples were used for electrochemical deposition of Co in order to obtain arrays of ordered Co nanowires with different diameters. The magnetic characterization shows a very high coercive field reaching values even above 3KOe.

References

1. Masuda, H., et al., *Long-range-ordered anodic porous alumina with less-than-30 nm hole interval.* Japanese Journal of Applied Physics Part 2-Letters & Express Letters, 2006. **45**(42-45): p. L1165-L1167.
2. Masuda, H., et al., *Long-range-ordered anodic porous alumina with reduced hole interval formed in highly concentrated sulfuric acid solution.* Japanese Journal of Applied Physics Part 2-Letters & Express Letters, 2006. **45**(12-16): p. L406-L408.
3. Sulka, G.D. and K.G. Parkola, *Temperature influence on well-ordered nanopore structures grown by anodization of aluminium in sulphuric acid.* Electrochimica Acta, 2007. **52**(5): p. 1880-1888.
4. Sulka, G.D. and K.G. Parkola, *Anodising potential influence on well-ordered nanostructures formed by anodisation of aluminium in sulphuric acid.* Thin Solid Films, 2006. **515**(1): p. 338-345.
5. Sulka, G.D., et al., *Synthesis of well-ordered nanopores by anodizing aluminum foils in sulfuric acid.* Journal of the Electrochemical Society, 2002. **149**(7): p. D97-D103.
6. Zhang, F., et al., *Nano-porous anodic aluminium oxide membranes with 6-19 nm pore diameters formed by a low-potential anodizing process.* Nanotechnology, 2007. **18**(34).
7. Aerts, T., et al., *Comparison between the influence of applied electrode and electrolyte temperatures on porous anodizing of aluminium.* Electrochimica Acta, 2010. **55**(12): p. 3957-3965.

8. Matsui, Y., K. Nishio, and H. Masuda, *Highly ordered anodic porous alumina with 13-nm hole intervals using a 2D array of monodisperse nanoparticles as a template.* Small, 2006. **2**(4): p. 522-525.
9. Lee, W. and J.C. Kim, *Highly ordered porous alumina with tailor-made pore structures fabricated by pulse anodization.* Nanotechnology, 2010. **21**(48).
10. Lee, W., J.C. Kim, and U. Gosele, *Spontaneous Current Oscillations during Hard Anodization of Aluminum under Potentiostatic Conditions.* Advanced Functional Materials, 2010. **20**(1): p. 21-27.
11. Lee, W., *The Anodization of Aluminum for Nanotechnology Applications.* Jom, 2010. **62**(6): p. 57-63.
12. Lee, W., et al., *Structural engineering of nanoporous anodic aluminium oxide by pulse anodization of aluminium.* Nature nanotechnology, 2008. **3**(4): p. 234-239.
13. Lee, W., R. Scholz, and U. Gosele, *A continuous process for structurally well-defined Al2O3 nanotubes based on pulse anodization of aluminum.* Nano Letters, 2008. **8**(8): p. 2155-2160.
14. Sulka, G.D., A. Brzózka, and L. Liu, *Fabrication of diameter-modulated and ultrathin porous nanowires in anodic aluminum oxide templates.* Electrochimica Acta, 2011. **56**(14): p. 4972-4979.
15. Losic, D., *Preparation of Porous Anodic Alumina with Periodically Perforated Pores.* Langmuir, 2009. **25**(10): p. 5426-5431.
16. Losic, D. and M. Lillo, *Porous Alumina with Shaped Pore Geometries and Complex Pore Architectures Fabricated by Cyclic Anodization.* Small, 2009. **5**(12): p. 1392-1397.
17. Lim, J.H., et al., *Synthesis of mild-hard AAO templates for studying magnetic interactions between metal nanowires.* Journal of Materials Chemistry, 2010. **20**(41): p. 9246-9252.
18. Delaet, J., et al., *CHARACTERIZATION OF VARIOUS ALUMINUM-OXIDE LAYERS BY MEANS OF SPECTROSCOPIC ELLIPSOMETRY.* Applied Physics a-Materials Science & Processing, 1992. **54**(1): p. 72-78.
19. Galca, A.C., et al., *Structural and optical characterization of porous anodic aluminum oxide.* Journal of Applied Physics, 2003. **94**(7): p. 4296-4305.
20. Kooij, E.S., et al., *Optical anisotropy and porosity of anodic aluminum oxide characterized by spectroscopic ellipsometry.* Electrochemical and Solid State Letters, 2003. **6**(11): p. B52-B54.
21. Schram, T., et al., *Spectroscopic ellipsometry: a non-destructive technique for surface analysis.* Advanced Engineering Materials, 1999. **1**(1): p. 63-66.

22. Bruschi, L., et al., *Adsorption hysteresis in self-ordered nanoporous alumina.* Langmuir, 2008. **24**(19): p. 10936-10941.
23. Casanova, F., et al., *Gas adsorption and capillary condensation in nanoporous alumina films.* Nanotechnology, 2008. **19**(31).
24. Dekker, A. and Middelho.A, *TRANSPORT NUMBERS AND STRUCTURE OF POROUS ANODIC FILMS ON ALUMINUM.* Journal of the Electrochemical Society, 1970. **117**(4): p. 440-&.
25. Ono, S. and N. Masuko, *Evaluation of pore diameter of anodic porous films formed on aluminum.* Surface and Coatings Technology, 2003. **169-170**: p. 139-142.
26. Takahashi, H. and M. Nagayama, *The determination of the porosity of anodic oxide films on aluminium by the pore-filling method.* Corrosion Science, 1978. **18**(10): p. 911-925.
27. Nielsch, K., et al., *Self-ordering regimes of porous alumina: The 10% porosity rule.* Nano Letters, 2002. **2**(7): p. 677-680.
28. Sui, Y., *Characterization of anodic porous alumina by AFM*

MATERIALS LETTERS. Materials letters, 2001. **48**(3-4): p. 127-136.
29. Sunseri, C., et al., *Porosity of anodic alumina membranes from electrochemical measurements.* Journal of Solid State Electrochemistry, 2006. **10**(6): p. 416-421.
30. Belwalkar, A., et al., *Effect of processing parameters on pore structure and thickness of anodic aluminum oxide (AAO) tubular membranes.* Journal of Membrane Science, 2008. **319**(1-2): p. 192-198.
31. Almasi Kashi, M., *The effect of pH and composition of sulfuric-oxalic acid mixture on the self-ordering configuration of high porosity alumina nanohole arrays.* Journal of physics. D, Applied physics, 2007. **40**(15): p. 4625.
32. Almasi Kashi, M., et al., *Optimum self-ordered nanopore arrays with 130-270nm interpore distances formed by hard anodization in sulfuric/oxalic acid mixtures.* Journal of Physics D-Applied Physics, 2007. **40**: p. 7032-7040.
33. Almasi Kashi, M., *The effect of temperature and concentration on the self-organized pore formation in anodic alumina.* Journal of physics. D, Applied physics, 2005. **38**(14): p. 2396.
34. Shingubara, S., et al., *Ordered two-dimensional nanowire array formation using self-organized nanoholes of anodically oxidized aluminum.* Japanese Journal of Applied Physics Part 1-Regular Papers Short Notes & Review Papers, 1997. **36**(12B): p. 7791-7795.

35. Stępniowski, W.J. and Z. Bojar, *Synthesis of anodic aluminum oxide (AAO) at relatively high temperatures. Study of the influence of anodization conditions on the alumina structural features.* Surface and Coatings Technology, 2011. **206**(2-3): p. 265-272.

36. Hillebrand, R., et al., *Quantitative analysis of the gram morphology in self-assembled hexagonal lattices.* ACS nano, 2008. **2**(5): p. 913-920.

37. Abdollahifard, M.J., et al., *A histogram-based segmentation method for characterization of self-assembled hexagonal lattices.* Applied Surface Science, 2011. **257**(24): p. 10443-10450.

38. Hillebrand, R., et al., *Characterization of microrod arrays by image analysis.* Applied Physics Letters, 2009. **94**(16).

39. Jessensky, O., F. Muller, and U. Gosele, *Self-organized formation of hexagonal pore arrays in anodic alumina.* Applied Physics Letters, 1998. **72**(10): p. 1173-1175.

40. Wood, G.C., et al., *A model for the incorporation of electrolyte species into anodic alumina.* Journal of the Electrochemical Society, 1996. **143**(1): p. 74-83.

41. Garcia-Vergara, S.J., et al., *Mechanical instability and pore generation in anodic alumina.* Proceedings of the Royal Society A: Mathematical, Physical and Engineering Science, 2006. **462**(2072): p. 2345-2358.

42. Garcia-Vergara, S.J., et al., *Tracer studies of anodic films formed on aluminium in malonic and oxalic acids.* Applied Surface Science, 2007. **254**(5): p. 1534-1542.

43. Garcia-Vergara, S.J., et al., *Stress generated porosity in anodic alumina formed in sulphuric acid electrolyte.* Corrosion Science, 2007. **49**(10): p. 3772-3782.

44. Gasenkova, I.V., N.I. Mazurenko, and E.V. Ostapenko, *Chemical composition and surface morphology of anodic alumina determined by electron microscopy and thermogravimetry.* Journal of Surface Investigation, 2011. **5**(5): p. 1005-1010.

45. Mata-Zamora, M.E. and J.M. Saniger, *Thermal evolution of porous anodic aluminas: a comparative study.* Revista Mexicana De Fisica, 2005. **51**(5): p. 502-509.

46. McQuaig, M.K., Jr., et al., *The effect of high temperature heat treatment on the structure and properties of anodic aluminum oxide.* Journal of Materials Science, 2011. **46**(1): p. 243-253.

47. Vrublevsky, I., et al., *Effect of heat treatment on the structure of incorporated oxalate species and photoluminescent properties of porous alumina films formed in oxalic acid.* Applied Surface Science, 2008. **254**(22): p. 7326-7330.

48. Xu, W.L., et al., *Effects of high-temperature annealing on structural and optical properties of highly ordered porous alumina membranes.* Applied Physics Letters, 2004. **85**(19): p. 4364-4366.

49. Hebert, K.R., et al., *Morphological instability leading to formation of porous anodic oxide films.* Nat Mater, 2012. **11**(2): p. 162-166.

50. Houser, J.E. and K.R. Hebert, *The role of viscous flow of oxide in the growth of self-ordered porous anodic alumina films.* Nature Materials, 2009. **8**(5): p. 415-420.

51. Oh, J. and C.V. Thompson, *Abnormal Anodic Aluminum Oxide Formation in Confined Structures for Lateral Pore Arrays.* Journal of the Electrochemical Society, 2011. **158**(3): p. C71-C75.

52. Vrublevsky, I., et al., *The study of the volume expansion of aluminum during porous oxide formation at galvanostatic regime.* Applied Surface Science, 2004. **222**(1-4): p. 215-225.

53. Zhou, F., et al., *Volume expansion factor and growth efficiency of anodic alumina formed in sulphuric acid.* Journal of the Electrochemical Society, 2011. **158**(6): p. C202-C214.

54. Li, A.P., et al., *Hexagonal pore arrays with a 50-420 nm interpore distance formed by self-organization in anodic alumina.* Journal of Applied Physics, 1998. **84**(11): p. 6023-6026.

55. Vrublevsky, I., et al., *Effect of the current density on the volume expansion of the deposited thin films of aluminum during porous oxide formation.* Applied Surface Science, 2003. **220**(1-4): p. 51-59.

56. Wackelgard, E., *The experimental dielectric function of porous anodic alumina in the infrared region; A comparison with the Maxwell-Garnett model.* Journal of Physics-Condensed Matter, 1996. **8**(23): p. 4289-4299.

57. Aspnes, D.E., *OPTICAL-PROPERTIES OF THIN-FILMS.* Thin Solid Films, 1982. **89**(3): p. 249-262.

58. Delaet, J., et al., *SPECTROSCOPIC ELLIPSOMETRY CHARACTERIZATION OF ANODIC FILMS ON ALUMINUM CORRELATED WITH TRANSMISSION ELECTRON-MICROSCOPY AND AUGER-ELECTRON SPECTROSCOPY.* Surface and Interface Analysis, 1992. **19**(1-12): p. 445-449.

59. Guo, P.T., et al., *Morphology and transmittance of porous alumina on glass substrate.* Applied Surface Science, 2011. **257**(8): p. 3307-3312.

60. Huang, K., et al., *Asymmetric light reflectance effect in AAO on glass.* Optics Express, 2011. **19**(2): p. 1301-1309.

61. Kotz, R., B. Schnyder, and C. Barbero, *ANODIC-OXIDATION OF ALUMINUM IN SULFURIC-ACID MONITORED BY EX-SITU AND IN-SITU SPECTROSCOPIC ELLIPSOMETRY.* Thin Solid Films, 1993. **233**(1-2): p. 63-68.

62. Palibroda, E., T. Farcas, and A. Lupsan, *A NEW IMAGE OF POROUS ALUMINUM-OXIDE.* Materials Science and Engineering B-Solid State Materials for Advanced Technology, 1995. **32**(1-2): p. 1-5.

63. Chiu, R.L. and P.H. Chang, *Thickness dependence of refractive index for anodic aluminium oxide films.* Journal of Materials Science Letters, 1997. **16**(2): p. 174-178.

64. Fan, D.H., et al., *Anion impurities in porous alumina membranes: Existence and functionality.* Microporous and Mesoporous Materials, 2007. **100**(1-3): p. 154-159.

65. Xu, W.L., et al., *Optical transmission spectra of ordered porous alumina membranes with different thicknesses and porosities.* Optical Materials, 2006. **28**(10): p. 1160-1165.

66. Zhang, D.X., H.J. Zhang, and Y.L. He, *In-situ thickness measurement of porous alumina by atomic force microscopy and the reflectance wavelength measurement from 400-1000 nm.* Microscopy Research and Technique, 2006. **69**(4): p. 267-270.

67. Jaafar, M., et al., *Magnetic domain structure of nanohole arrays in Ni films.* Journal of Applied Physics, 2007. **101**(9).

68. Navas, D., et al., *Ordered Ni nanohole arrays with engineered geometrical aspects and magnetic anisotropy.* Applied Physics Letters, 2007. **90**(19).

69. Pirota, K.R., et al., *Size effect and surface tension measurements in Ni and Co nanowires.* Physical Review B, 2007. **76**(23).

70. Pirota, K.R. and M. Vazquez, *Arrays of electroplated multilayered Co/Cu nanowires with controlled magnetic anisotropy.* Advanced Engineering Materials, 2005. **7**(12): p. 1111-1113.

71. Nielsch, K., et al., *Uniform nickel deposition into ordered alumina pores by pulsed electrodeposition.* Advanced Materials, 2000. **12**(8): p. 582-586.

72. Nielsch, K., et al., *High density hexagonal nickel nanowire array.* Journal of Magnetism and Magnetic Materials, 2002. **249**(1-2): p. 234-240.

73. Nielsch, K., et al., *Hexagonally ordered 100 nm period nickel nanowire arrays.* Applied Physics Letters, 2001. **79**(9): p. 1360-1362.

74. Sellmyer, D.J., M. Zheng, and R. Skomski, *Magnetism of Fe, Co and Ni nanowires in self-assembled arrays.* Journal of Physics-Condensed Matter, 2001. **13**(25): p. R433-R460.

75. Strijkers, G.J., et al., *Structure and magnetization of arrays of electrodeposited Co wires in anodic alumina.* Journal of Applied Physics, 1999. **86**(9): p. 5141-5145.

76. Masuda, H., F. Hasegwa, and S. Ono, *Self-ordering of cell arrangement of anodic porous alumina formed in sulfuric acid solution.* Journal of the Electrochemical Society, 1997. **144**(5): p. L127-L130.

77. Li, A.P., et al., *Polycrystalline nanopore arrays with hexagonal ordering on aluminum.* Journal of Vacuum Science & Technology a-Vacuum Surfaces and Films, 1999. **17**(4): p. 1428-1431.

78. Ono, S., et al., *Controlling factor of self-ordering of anodic porous alumina.* Journal of the Electrochemical Society, 2004. **151**(8): p. B473-B478.

79. Aerts, T., I. De Graeve, and H. Terryn, *Anodizing of aluminium under applied electrode temperature: Process evaluation and elimination of burning at high current densities.* Surface & Coatings Technology, 2010. **204**(16-17): p. 2754-2760.

80. Gaston-Garcia, B., et al., *Local Burning Phenomena in Sulfuric Acid Anodizing: Analysis of Porous Anodic Alumina Layers on AA1050.* Electrochemical and Solid State Letters, 2010. **13**(11): p. C33-C35.

81. Horcas, I., et al., *WSXM: A software for scanning probe microscopy and a tool for nanotechnology.* Review of scientific instruments, 2007. **78**(1).

82. Wang, J.A., et al., *Aluminum Local Environment and Defects in the Crystalline Structure of Sol−Gel Alumina Catalyst.* The Journal of Physical Chemistry B, 1998. **103**(2): p. 299-303.

83. Verwey, E.J.W., *Electrolytic conduction of a solid insulator at high fields - The formation of the anodic oxide film on aluminium.* Physica, 1935. **2**: p. 1059-1063.

Chapter 3. Alumina transition from Mild to Hard Anodization in sulphuric acid based electrolyte: What is in between?. Pulsed Anodization of Aluminium.

3.1. Introduction.

"Hard Anodization" (HA) concept was introduced by Csokan et al. [1, 2]in the early 60's, and it involves high current densities. But it has been more recently when HA has attracted the attention in academic research; firstly, in fabrication of alumina nanotubes and the study of their formation mechanism [3, 4] where they found voids within the pore walls formed during oxide grown process. Few years later, research studies achieve the formation of ordered nanostructures by HA process which we will see next.

To our knowledge, Chu SZ et al. [5] give rise to a series of articles related to HA techniques obtaining hexagonally ordered nanostructures. The HA process can be carried out by different methods or a combination of them. The later work uses sulphuric acid based electrolyte and a two-step anodization process. First, galvanostatic anodization: the voltage increases till reaches certain value, then, potentiostatic anodization at that voltage. Other processes are carried out only in galvanostatic mode with an aged (by addition of $Al_2(SO_4)_3$) sulphuric acid based solution [6], or only potentiostatic mode, although involves an increase of the applied voltage up to HA conditions [7].

The differences respect to Mild Anodization (MA) (i.e. the traditional anodization process) are quite significant. In first place we should mention that the structure of the resultant aluminium oxide is different. A proof of that is two different fracture modes shown in *Figure 3.1*. This fact reflect the nanotubular structure growth under HA conditions, since the junction among the alumina cells is much weaker than under MA conditions, possibly due to different growth mechanism, which will be discussed together with the presentation of the results obtained in our work.

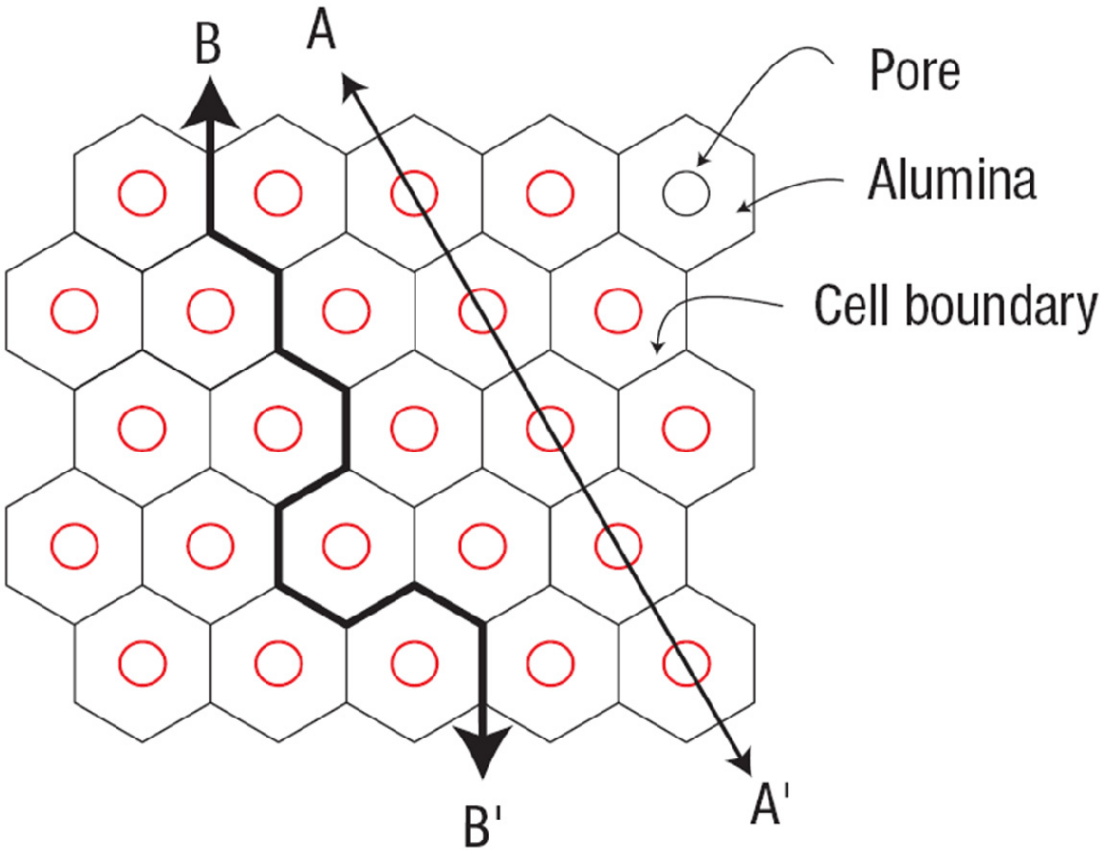

Figure 3.1: Illustration of fracture modes. The A-A' cleavage plane represents the fracture mode of NAAF grown under MA conditions, and the B-B' cleavage plane represents the fracture mode of anodic alumina grown under HA conditions [8].

Another significant difference is the geometrical growth parameters, which affect the morphology of the cells. The ratio interpore distance to applied voltage decreases for these type of films respect to the MA conditions, which is ~2.5nm/V [9, 10]. The value of this parameter in HA conditions is not constant. It can be modified as a function of applied voltage or current density between 2.0 down to 1.5nm/V [11, 12]. The pore diameter size is also affected respect to the MA since the diameter generated varies at a rate of ~1.0nm/V, while under HA conditions is ~0.4nm/V [7]. As a consequence, it has been found that porosity in hard anodized films is around 3 to 6% [5, 7] while for MA conditions it is around 10% [12, 13]. As it will be discussed above, these differences in the geometrical parameters can be explained by the growth mechanism and the electric voltage through the barrier layer which drives the oxide formation at the pore bottom [14].

The HA process can be performed by using a wide range of electrolytic baths based in sulphuric acid [5, 6], oxalic acid [7, 15, 16] or even phosphoric acid [17]. Even more, these

type of anodization can also be performed by mixtures of them, like sulphuric/oxalic acid based electrolytes [18, 19].

Usually, HA conditions come with a high heat generation at the pore bottom due to the high current densities going through the barrier layer, so reducing the anodization temperature below 0°C is necessary to achieve a stable high field anodization process [20]. That implies the use of a solvent such as ethanol, which avoids freezing the electrolytic bath.

The use of all of these kinds of electrolytes for HA processes has made possible to fill up the spaces in between the interpore distances between MA oxalic acid and MA phosphoric acid, (i.e., 100 – 480nm) and even surpass it reaching interpore distances of 1µm [15] (see *Figure 3.2*) within self-ordering conditions, which is a very important issue, opening new possibilities of self-ordered nanostructures in a wider range.

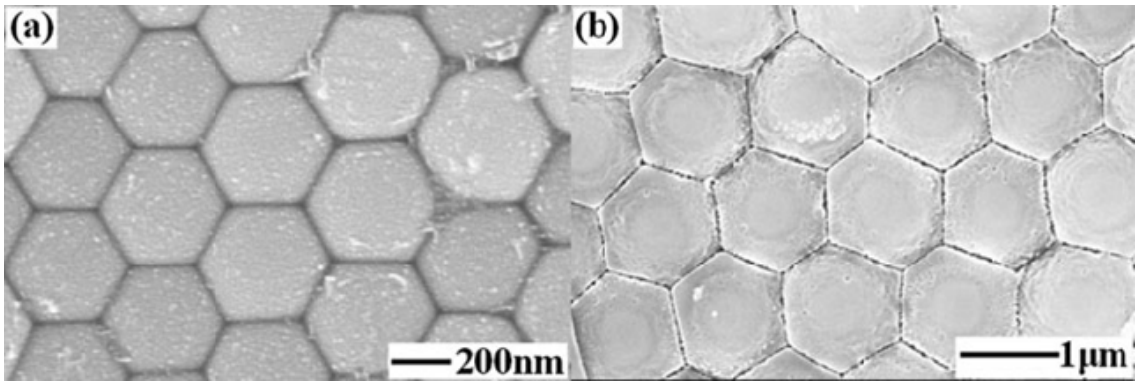

Figure 3.2: SEM micrographs showing barrier layer side surface of anodic alumina grown under HA conditions [15].

It has also been observed oscillations in the nano-channel diameter formed during the anodization process by mean of internal factors [11, 15, 16] (see *Figure 3.3*). These oscillations are attributed to different causes. One of them is the evolution of gas bubbles provoking plastic deformation of the nano-channels at the pore bottom [11]; others propose that the modulations are due to different speed motions of the metal/oxide and oxide/electrolyte interfaces [16]; and others to volume contractions of $Al(OH)_3$ formed near the ridges of the Aluminum and voids accumulation at the junctions of the alumina cells[15].

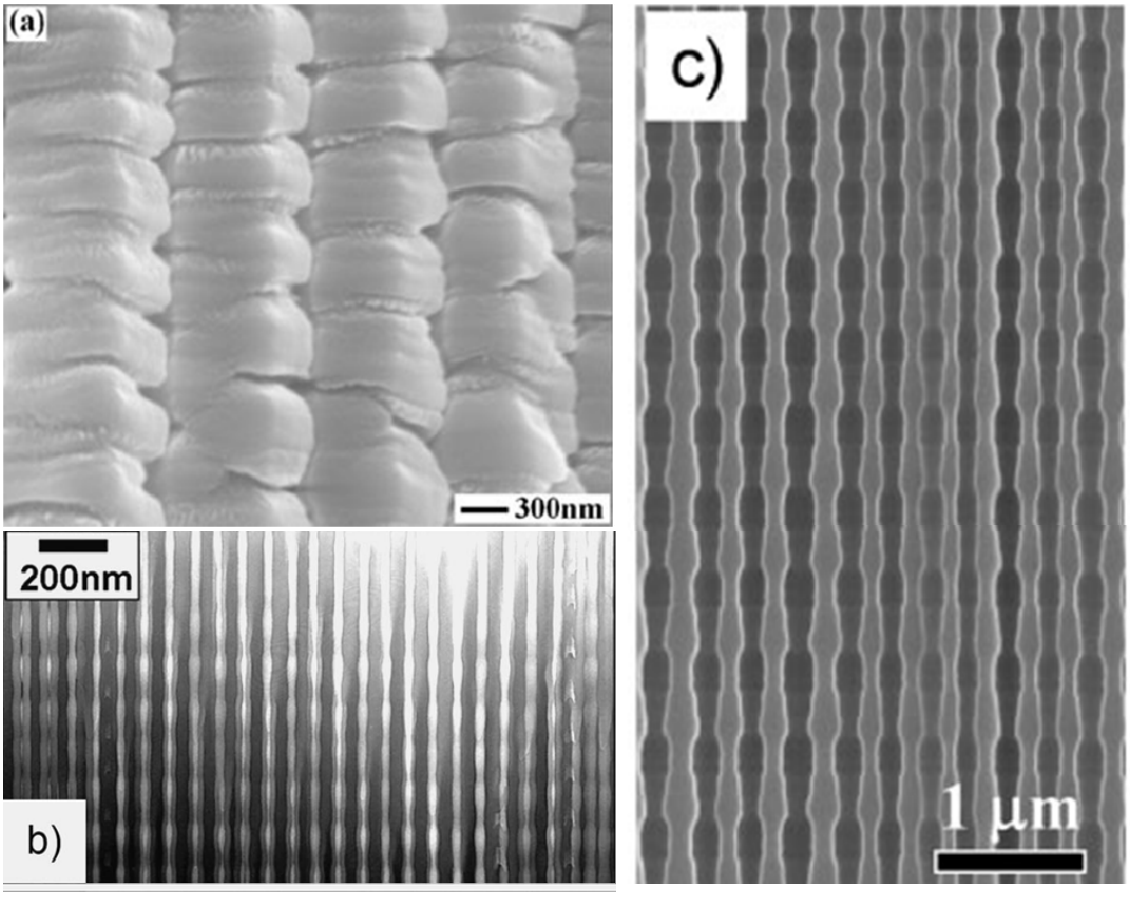

Figure 3.3: Modulation of anodic alumina nano-channels formed under HA conditions a)[15]; b) [11] and c) [16].

These modulations can also be controlled by external parameters. This fact allows controlling the shape, length and diameters of the modulated nano-channels. Woo Lee introduced this controlled modulation of diameters by complete exchange of anodization conditions, i.e. acid electrolyte, applied voltage and anodization temperature, for each modulated segment [7]. This method is quite complicated due to the big number of involved variables and taking into account that the interpore distance must remain the same. After that, some novel methodologies based in the combination of MA and HA made easier the way to obtain these modulated nanostructures. These novel methodologies gave rise to new anodization procedures as pulsed anodization (PA) by Woo Lee et al. [8, 21, 22] or cyclic anodization by Dusan Losic et al. [23, 24]. These processes can also be performed under potentiostatic or galvanostatic mode or with sulphuric or oxalic acid based electrolytes. The modulated nanostructures not only provide the possibility to use them as template for novel 1D modulated nanostructures [25, 26], but also 3D nanostructures [8, 24, 27] (see *Figure 3.4*).

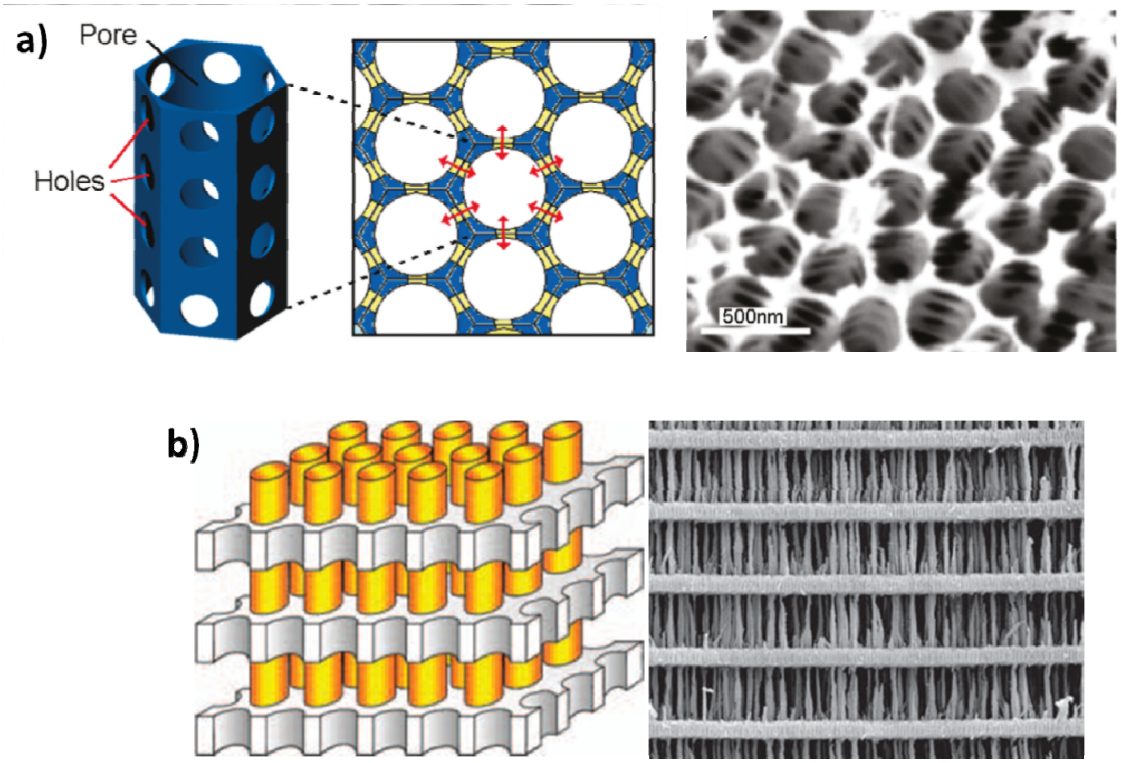

Figure 3.4: 3D nanostructures fabricated by the use of anodic alumina template grown by a) cyclic [24] or b) pulsed anodization [8].

In this chapter we present the results of HA processes obtained by potentiostatic and pulsed anodization performed in sulphuric acid based electrolyte. Different aspects of the anodic alumina have been analyzed and studied such as morphology, composition, and growth mechanism. Finally, NAAFs grown by PA have been used as template for the fabrication of modulated magnetic 1D nanostructures with high aspect ratio.

3.2. Fabrication of the samples under Hard Anodization conditions.

Aluminium foils were cleaned and electrochemically polished as described in Section 1.1.1. The use of a 3wt% concentration of sulphuric acid in the electrolyte at 0°C is common to all the experiments carried out in this chapter. The electrochemical processes which take place at the anode during Hard Anodization (HA) conditions provoke the rise of the temperature in the system. This fact increases the temperature of the electrolyte which is a non desirable consequence, so we have to pay special care in these experiments to maintain a stable temperature.

3.2.1. One step transition from Mild to Hard Anodization

In these experiments we apply two different anodization voltages. During the first stage of the anodization we apply the typical applied voltage for sulphuric acid anodization, i.e. 25V [28]. This voltage is applied during 4 hours. The length of this first stage is in order to prevent break-down or burning effect as much as possible, since during the second stage of the anodization process the applied voltage is increased by 0.7V/s up to 60V. This step is presented in Figure 3.5.

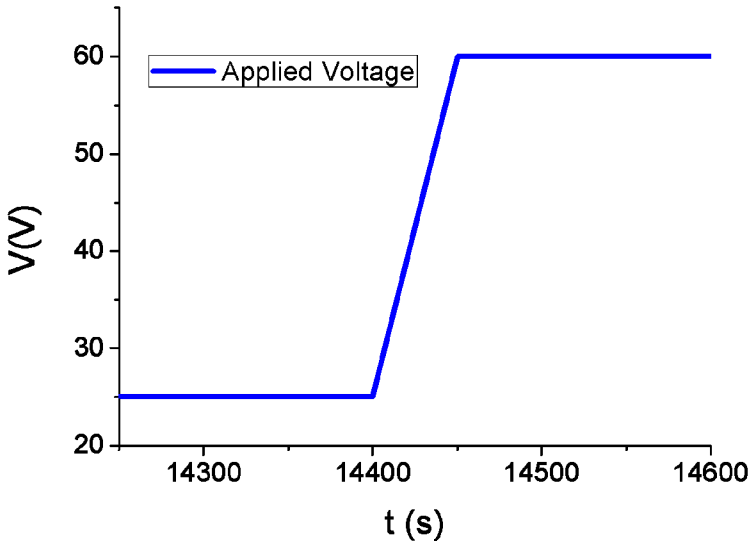

Figure 3.5: Voltage profile applied to the anodized aluminium foils.

After reaching this value, the voltage it is maintained for different length time from 6 up to 120 minutes as show Table 3-1. The current density generated at this point is too high and there are problems with the operating boundaries of the source-meter, so we have to reduce the exposed area to anodise. It means that the refrigerating area is also reduced, so the temperature of the electrolyte is higher. In this case the starting temperature is 2°C, instead of 0°C like in Chapter 2.

Table 3-1: Labels for samples, applied voltage during HA and length time of the process. All the samples were previously anodised at 25V during 4 hours.

Sample label	Voltage HA (V)	Time HA (min)
HA6	60	6
HA14		14
HA42		42
HA71		71
HA120		120

We have introduced some modifications to the experimental set-up showed in section 1.1.2 since we are working out of the boundaries of the Keithley 2400 Source-meter as we mentioned in section 1.1.2. In our case, we apply voltages above 21V, but the current generated during HA is going to be higher than 105mA. To solve this problem we need a new configuration. The new configuration requires that the Keithley voltage source is able to measure currents above 105mA, so it has to work with voltages below 21V. Then, we need an auxiliary power source to be placed in serial with the Keithley power source in order to sum their voltages. In this way, we program the Keithley power source to 20V and connect in serial with the auxiliary source at 5V and increased up to 40V.

3.2.2. Periodical alternation of voltage pulses with different lengths, periods and shapes.

The experiments of this section are based on the anodization of Aluminium foils by periodically alternated pulses of 25V, called Mild Anodization (MA) pulse, and 35, 37 or 39V for the Hard Anodization (HA) pulse. The starting substrate is an Aluminium foil nano-patterned after a first anodization during 16h. We have used the improved cell showed in Figure 1-2 in Section 1.1.2.

It is also necessary some modification in the experimental set-up since the high current densities which generate the HA pulses present the same problem than that in previous section. The Keithely power supply is also connected in serial with the auxiliary source in order to sum their voltages, but in this case, the Keithley voltage source is programmed in order to apply the pulses. In this way, the auxiliary power supply applies 24V during the whole anodization process and the Keithley voltage source applies the resting voltages, i.e. 1V for MA pulse and up to 11, 13 or 15V for the HA pulses, being within the source multi-meter range of 21V – 1.05A.

The software was developed with Labview programming. It allows registering the applied voltage, the current and the charge going through the electrode. In the interface it can be distinguished three independent stages for input anodization parameters. In the first and third stages is possible to fix the length, the period of measure and the voltage independently. The second stage is the main part of the software. In this stage is possible to select the shape of the HA pulse, among square, triangular or exponential pulse. Then we can select the amplitude of the HA pulse, the length, period, period of measure and number of pulses. In Table 3-2 are presented the main parameters used for our experiments during the anodization process.

Table 3-2: Main parameters used for MA and HA pulses during the anodization process.

Mild Anodization Pulses		Hard Anodization Pulses		
Pulse length (s)	Amplitude (V)	Pulse Shape	Pulse length (s)	Amplitude (V)
		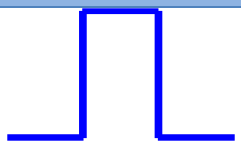	0.1 – 1.0	35
150 - 600	25		1.3-1.5	37
		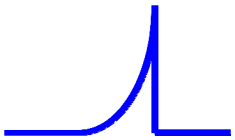	1.5	39

This range of parameters allows multiple combinations for pulsed anodization.

3.3. Morphological and compositional dependence on the current density during HA conditions.

3.3.1. Current density analysis.

The evolution of current densities as a function of the time for the different samples is represented in Figure 3.6. The temperature of the electrolyte rise up to 4°C during the first minutes of HA before returning to its nominal temperature.

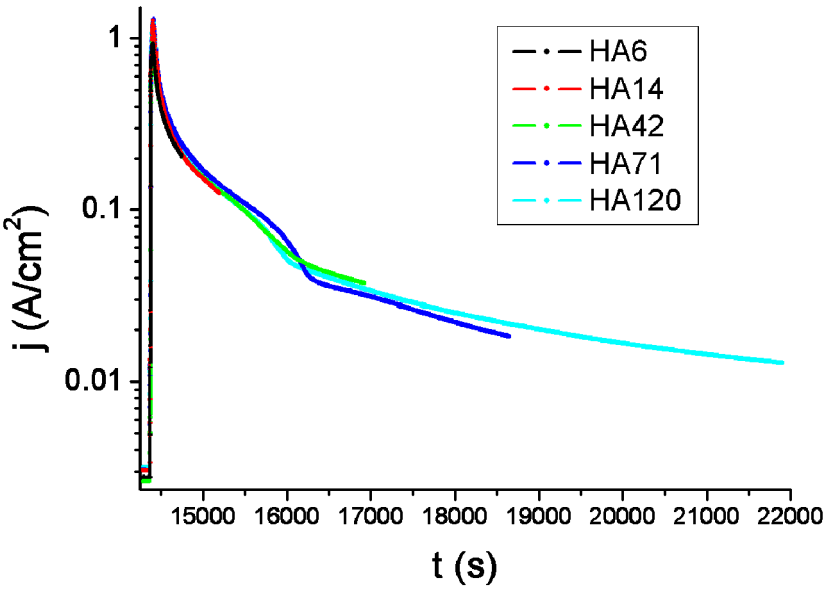

Figure 3.6: Current densities evolution after the transition in one step from MA (25V) to HA (60V).

In Figure 3.6 it can be clearly observed a shoulder in the range of current density between 60 and 40 mA/cm^2. A similar effect was also observed during anodization in galvanostatic conditions at 120mA/cm^2 in the range of voltages between 27 and 32V [11]. We will get an insight into this effect in next section.

The anodizations were stopped when reached current densities presented in Figure 3.7.

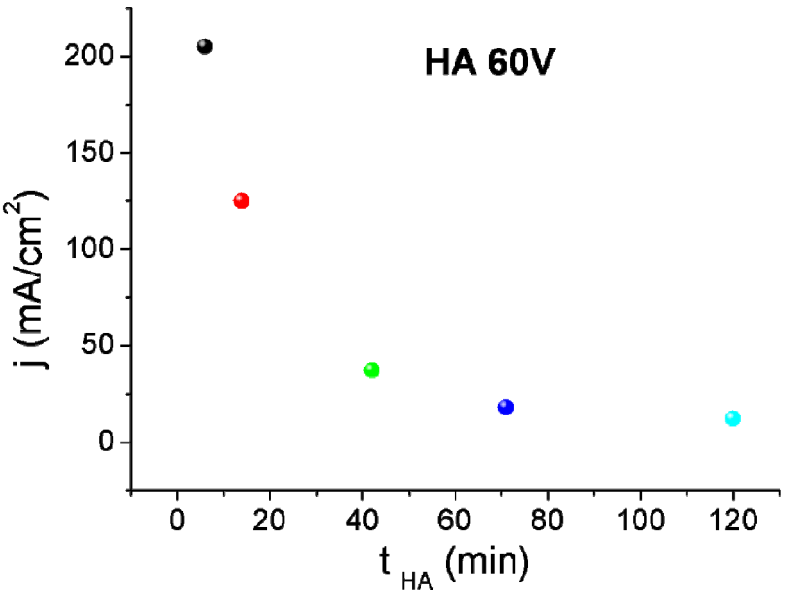

Figure 3.7: Current densities of the samples when the anodizations were stopped for each sample.

Here it is also observed the exponential decay of the current density as the anodization time increase. This behaviour has been attributed to the diffusion-limited electrochemical oxidation of aluminium at the pore base as a consequence of fast growth of anodic alumina during HA conditions [7]. So, this decrease of current density was expected since the diffusion path along the nano-channels increases with time.

3.3.2. Morphology analysis.

In order to observe the morphology of the anodic alumina and the anodised side of the Aluminium substrate, we proceeded in two steps. In the first step we immerse half of the sample into the chromic acid solution described in section 1.1.3, so that the alumina is dissolved and the Aluminium substrate is exposed. At this point, it is very easy to cut the aluminium substrate without cracking the anodic alumina remaining in the other piece. The piece with the anodic alumina is chemically etched in order to remove the Aluminium substrate leaving the free standing anodic alumina. In this way, it is possible to observe with the SEM both nano-patterned aluminium substrate and the anodic alumina barrier layer side at once. With the naked eye, we can observe that the surface is quite ridged for all the samples. The first morphological characteristics we observe in the micrographs are severe plastic deformation and mechanical instabilities in the micro-scale (Figure 3.8), attributed to the local burning phenomena [29].

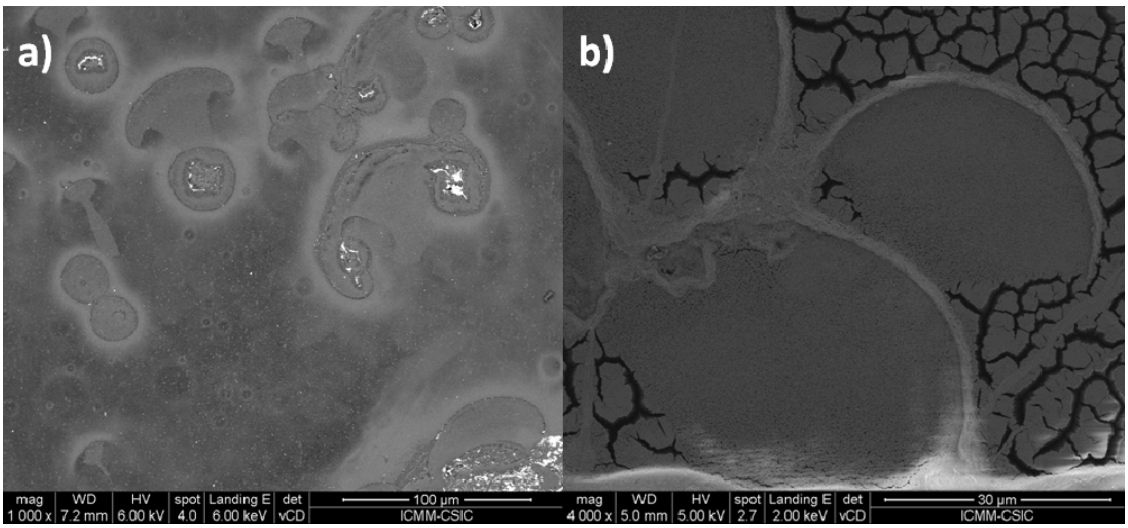

Figure 3.8: Anodic alumina bottom side of sample a) HA6 and b) HA14.

At higher magnifications it is also observable inhomogeneities not only on the surface (Figure 3.9a) but also inner inhomogeneities of different types prolonged deep through the anodic alumina film as showed in Figure 3.9b, c and d. This deformation observed on the surface has

been attributed to the generation of intense local heat during the HA process [11], but to the best of our knowledge, these kind of structures has not been shown up to now. At lower scale, it has been found defects caused by intermetallic compounds enclosed inside the bulk Aluminium with significant presence of other elements like Fe or Si, but the size of the deformations are of a few microns [30]. This could give us a clue of the inhomogeneities present in our samples. We could speculate that the conical structure of alumina, showed in Figure 3.9c, are formed due to small aluminium grains incorporated into the Aluminium bulk which are also anodized. The other kind on deformation has a planar structure as showed in Figure 3.9d. From the formed shape, we could attribute it to a grain boundary. The grains we referred here are not small grains, but the grain which form the Aluminium bulk.

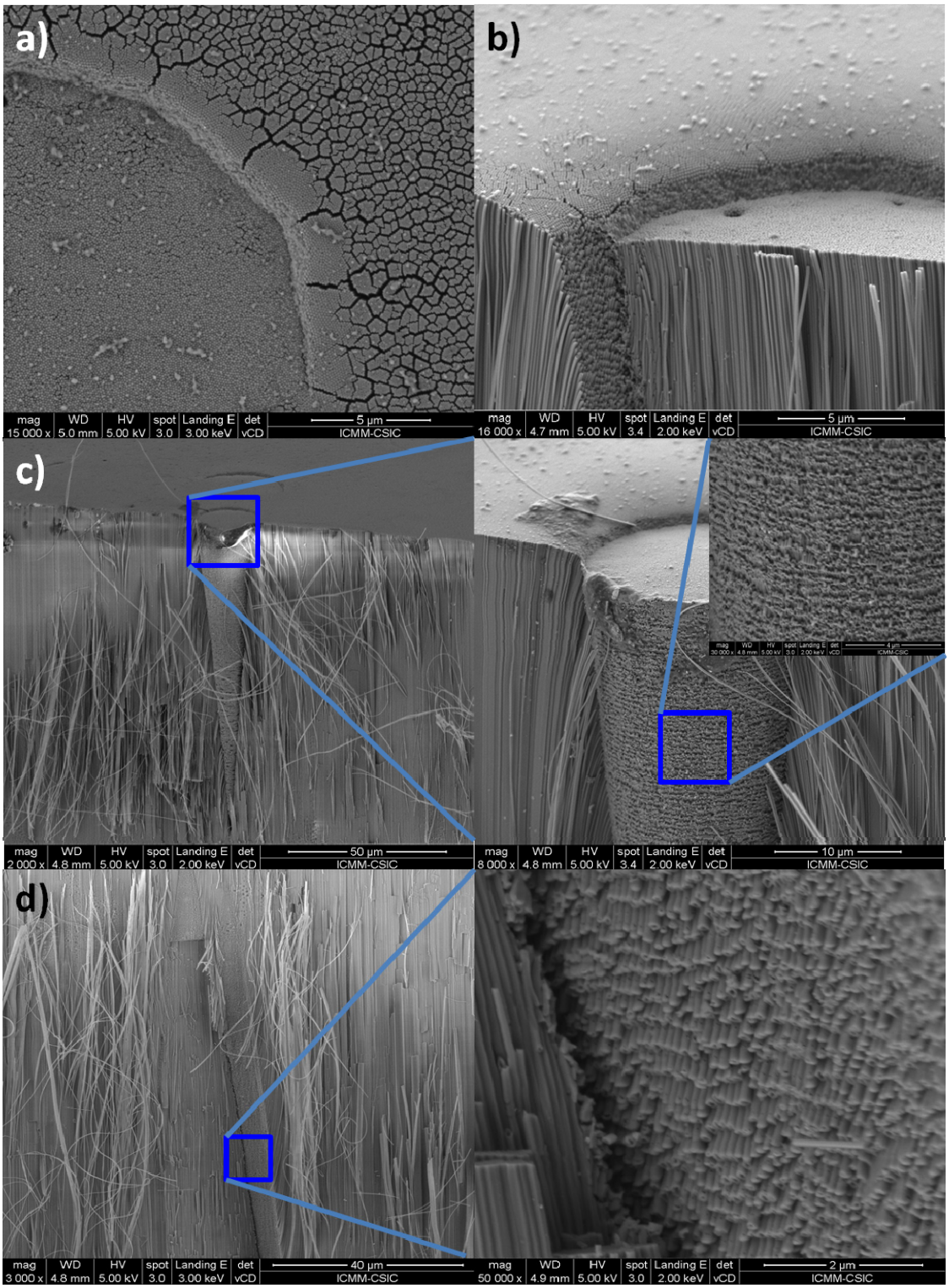

Figure 3.9: a) Inhomogeneity on the barrier layer side surface; b) Cross-sectional view of a similar inhomegeneity; c) Conical structure of anodic alumina at different magnifications; d) Plane cleavage on cross-section of NAAF.

We have also observed the whole cross-section of the anodic oxide film from which we obtain valuable information. The thickness of the MA section is roughly 20µm for all the samples. Note that the growth rate is approximately 5µm/h, a little higher than the obtained in the

Chapter 1. This is attributed to the temperature of the electrolyte during MA in these experiments, i.e. 2°C instead of 0°C. On the other hand, we have also measured the thickness of the HA sections for each sample. These values are summarized in Table 3-3. In this table it is also given the average growth rate for each sample since the growth rate is not constant. We have calculated the consumed Aluminium and the volume expansion factor during HA process, as described in section 2.7.

Table 3-3: These values are regarding the HA section, excluding the MA section.

Sample	Thickness (µm)	Average Growth Rate (µm/min)	Charge density (C/cm^2)	Consumed Aluminium (µm)	Volume Expansion Factor
HA6	121	20,16667	147,1	50,78467	2,38261
HA14	185	13,21429	235,7	81,37285	2,27349
HA42	263	6,2619	333,9	115,27532	2,28149
HA71	304	4,28169	421,7	145,58731	2,08809
HA120	344	2,86667	457,6	157,98139	2,17747

Table 3-3 shows the extremely high speed growth in HA conditions, especially during the first minutes when the average growth rate can be more than 160 times higher than for the MA. This fast growth rate is one of the main characteristics in this kind of anodizations [7, 17, 20].

From cross-sectional view we can observe the transition between the MA process at 25V and the HA process at 60V (Figure 3.10).

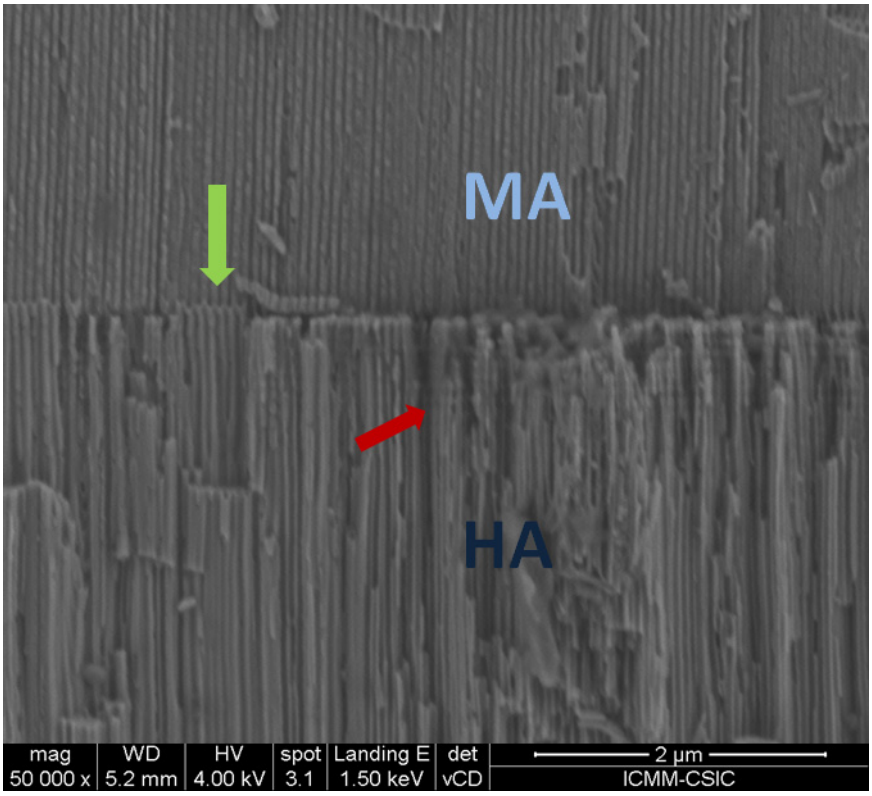

Figure 3.10: Cross section view of the transition from MA (25V) to HA (60V). The green arrow indicates the change of the morphology of the alumina nano-channels and the red arrow the small oscillations on the diameter.

It is possible to observe the transition from the typical structure of the nano-channels during MA to the tube like structure for HA. In the MA section the cleavage planes are crossing transversally the pore array, i.e. through the pore centres. After changing the conditions to HA the previous situation does not occur anymore. The junction strength of the alumina cells is weaker than the cell walls, so the cleavage takes place through the boundaries of the cells [5]. Immediately after this, a small modulation on the cell appears. These fluctuations in the tube diameter are generated when the voltage ramp is taking place and the current density is increasing extremely fast. At the same time the temperature of the system is increasing drastically due to the Joule heating effect (the temperature of the electrolyte increase from 2 to 6°C) and the gas evolution on the electrode is evident with the naked eyes. One possible explanation to these modulations could be a plastic deformation of the tubes due to the fluctuations of Oxygen bubbles formation at the pore bottom [11, 31]. Schwirn et al. observed similar modulation in their experiments under galvanostatic conditions in the range between 27 and 32V [11].

Surprisingly, this is not the only transition which occurs during the anodization. We could find a second one during the HA process for the samples HA14, HA42 and HA71 (Figure 3.11). This

transition is not externally induced. The fact that we could observe this phenomenon only in these samples does not imply that was not present in the other samples, maybe we could not found it or the transition was no so evident. This phenomenon is similar in all the samples where was observed, but does not always occur at the same point of the thickness. We speculated that this second transition could be ascribed to the shoulder showed in the current density (Figure 3.6) but it is also present in sample HA14.

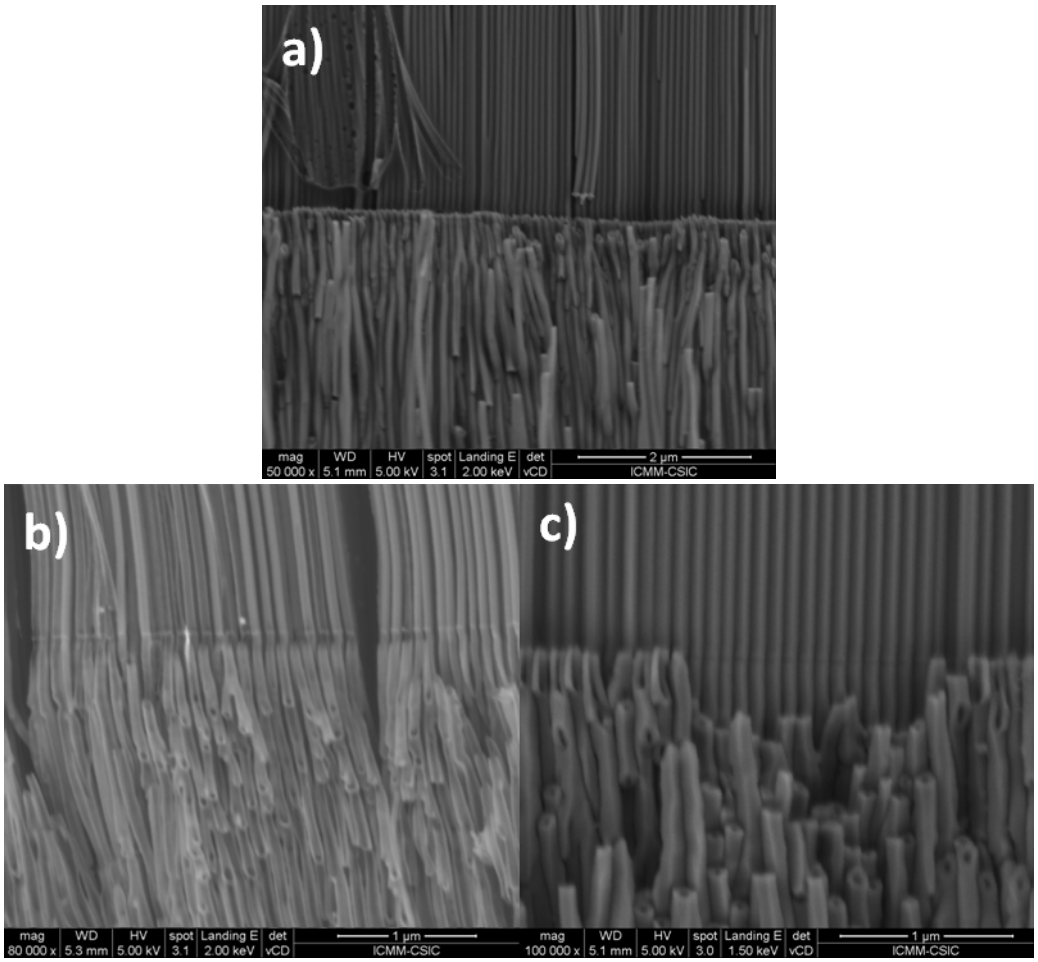

Figure 3.11: Second alumina transition occurred during the HA process. a) Sample HA14, b) Sample HA42, c) Sample HA71.

As can be observed in Figure 3.11, straight alumina nano-tubes from HA suddenly become distorted at this second transition point. They also increase their size, increasing therefore the repulsive stress among them, which leads to a higher weakness at the cell junctions. On the other hand, it is also possible to observe how some of the nano-tubes get branched which is usual in this kind of process [3]. The most similar phenomenon we could find in the literature is presented by Woo Lee et al. [16], where the anodization processes were carried out in oxalic acid based electrolytes.

In Figure 3.12 shows how the distorted alumina nano-tubes are rearranged and become straight again as the anodization process keeps on running.

Figure 3.12: Micrographs composition of cross section view of alumina transition during HA process.

In order to give an explanation to this phenomenon we have to take into account several aspects to analyze. The fact that this second transition does not take place at the same point could be explained because the thickness of the sample is not uniform. The centre of the alumina film is thicker than near the boundary of the anodized area. This is macroscopically

observable. So, the appearance location of this second transition could depend on the radial distance respect to the centre of the sample where we were scanning. As I previously mentioned, this phenomenon could not be observed in all samples since this is not induced by an external parameter, so it must be a consequence of internal stresses. The enormous alumina growth rate and volume expansion factor[9, 32] causes also intense mechanical stress at the aluminium/oxide interface which also presents microscopic inhomogeneities on their surface as shown in Figure 3.8. But the mechanism of this spontaneous phenomenon is not understood.

The micrographs of the barrier layer side of the NAAF and the nano-patterned aluminium substrate obtained from the analyzed samples are presented in Table 3-4.

Table 3-4: Alumina barrier layer side and nanopatterned Aluminium substrate SEM micrographs with their respective SCF images for samples HA6, HA14, HA42 and HA71.

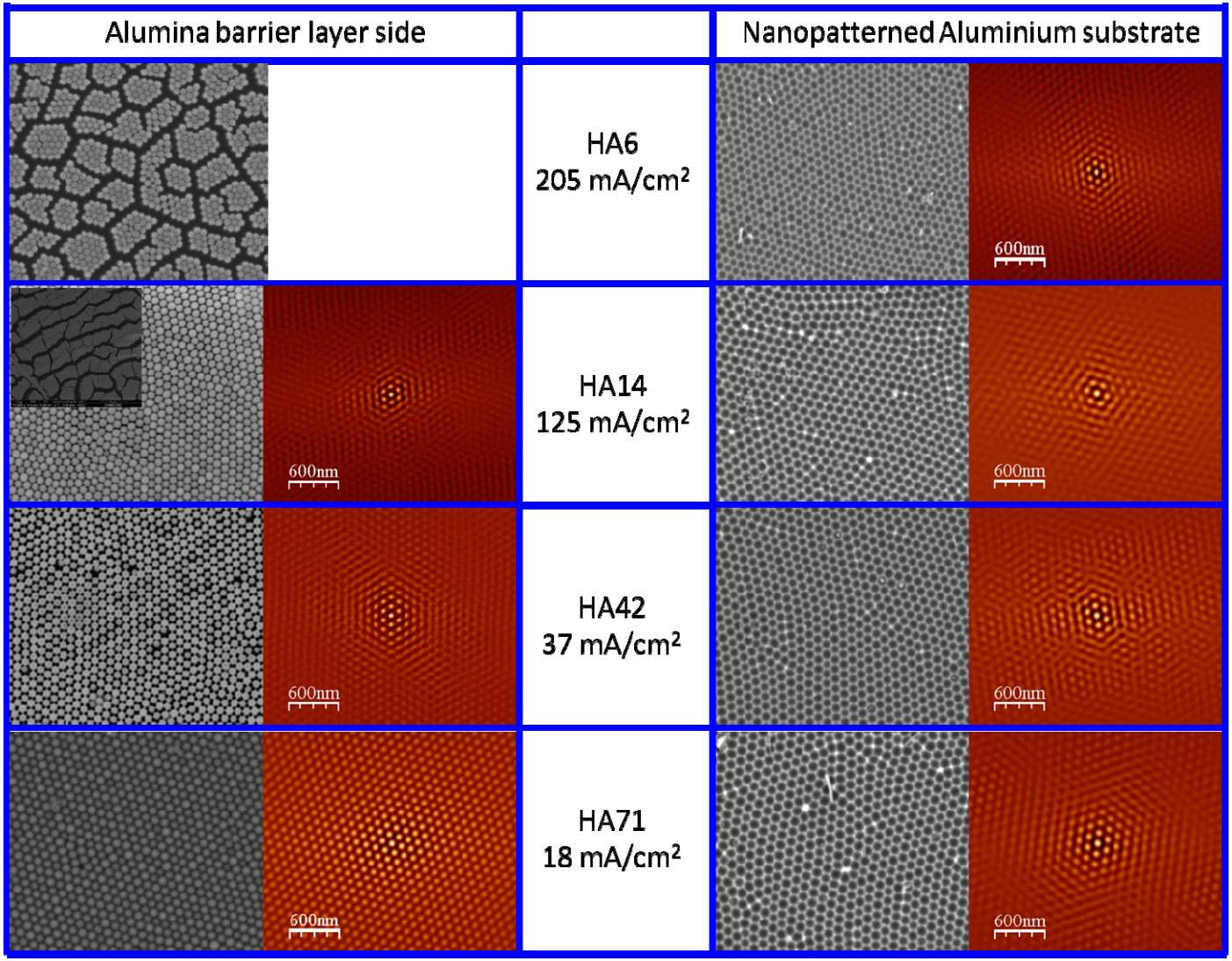

On the left side of the Table 3-4 are presented the barrier layer side of the NAAF together with their SCI's, except for the sample HA6 from which SCI would not be possible to obtain neither qualitative or quantitative information, although it is not necessary to identify hexagonal order among the cells. On the right side of Table 3-4 are presented the respective nano-patterned Aluminium substrate side for all the analyzed samples.

From the qualitative point of view, the differences in self-ordering are almost imperceptibles, making clear that large self-ordered domains can be obtained in very short periods of HA. This is a remarkable results obtained by this method. The experimental parameters during HA processes are quite far from those used under MA conditions. As we saw in section 2.4.2, self-ordering can be explained by a moderate volume expansion factor and mechanical stress promoting repulsive forces among the cells[9, 32]. Under HA conditions the volume expansion factor and mechanical stress generated at the Aluminium/oxide interface are extreme, and the growth process of the anodic alumina is different than for MA, since here the rapid oxide formation generates high mechanical stress at the Aluminium/oxide interface due to the huge volume expansion. This high mechanical stress trends to be minimized by reducing the cell size. As the mechanical stress at the interface gets higher for a given voltage, the cell size should decrease for a given voltage [7]. This interfacial stress gives rise to repulsive forces between the nano-tube cells and the barrier layer, and there repulsive forces are the main forces promoting hexagonal self-ordering. The high current density generated during the HA process maybe most important factor as a consequence of the starting experimental parameters and promoting forces which allows this large self-ordering domains in so short times.

Table 3-5 summarizes the experimental parameters together with the geometrical ones taken from processing the corresponding SCI's. We can observe that 6 minutes after switching to 60V the D_{Int}^{Al} has still not reached a constant value. This takes around 14 minutes after what it is stabilized to 120nm. This implies that under HA conditions the applied voltage is not the only factor which determines the distances centre-centre of the alumina cells. This evidences that the high current density plays a critical role in the geometrical parameters of anodic alumina [16], since the distance among the centre of the cells increase even at fixed applied voltage. Moreover, the cell size measured on the barrier layer side of the alumina (D_{CS}^{Alox}) differs from the inter-tube distance measured on the nano-patterned Aluminium side of the substrate (D_{Int}^{Al}).

Table 3-5: Experimental and geometrical parameters for the samples under HA conditions and its ratio with the 60V of applied voltage.

t_{HA} (min)	6	14	42	71
j_{tHA} (mA/cm^2)	205	125	37	18
D_{CS}^{Alox} (nm)	75±2	95±3	105±3	110±4
D_{Int}^{Al} (nm)	100±3	120±4	115±4	120±4
ς_{HA}^{Al} (nm/V)	1.65±0.03	2.00±0.07	1.92±0.07	2.00±0.07

This could lead to confusion or interpretation mistakes. If we want to know the actual value of the distance between cells centre-centre, we measure the distance on the Aluminium substrate which remains unalterable. We cannot interpretate the distances measured on the barrier layer surface side of the alumina as inter-tube distances mainly because of the growth mechanism of the cells, which differs from the MA process. During the alumina formation under HA conditions, the region between the inner and the outer walls, i.e. the triple cell union junction, consists of voids [33, 34]. It was also observed that there is a distribution of the voids during the formation of the anodic alumina [4]. The presence of the voids is revealed during the etching for detaching the anodic alumina from the Aluminium substrate, which gives rise to nano-channels [6], although the depth of these new nanopores was not studied. In the micrographs of the alumina barrier side presented in Table 3-4 we can observe small gaps between the nano-tubes which sizes decrease together with the current density. This makes clear why the D_{CS}^{Alox} measured on the SCI are smaller than D_{Int}^{Al} in Table 3-5. It is confirmed in Figure 3.13, where Figure 3.13a shows how the nano-tubes bend and bundle due to the gap left by the voids after chemical etching. This fact cannot be evaluated in Figure 3.13b where the nano-tubes are close-packed. So, we can deduce voids level decreases with the generated current density for a given applied voltage.

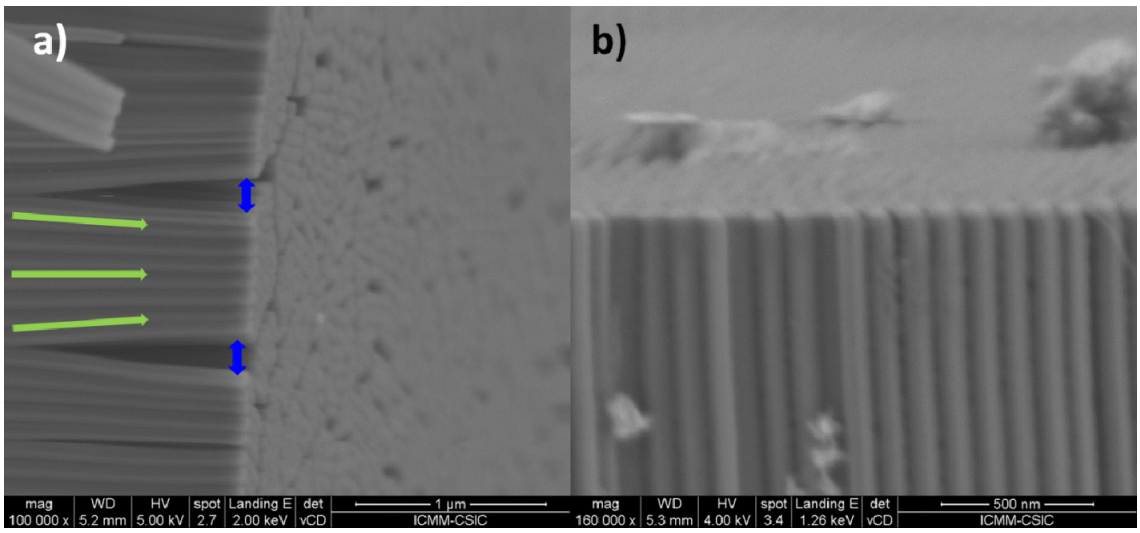

Figure 3.13: a) Barrier layer cross section view of sample HA6 and, b) HA71. The green arrows indicate the bending of the alumina nano-tubes and the blue arrows the gap left

From all this information we can establish that, the same that the high current density induces weak strength among the cell junctions, also, the presence of void in the tripe union junctions, which is higher as higher is the current density, is other factor which weaken the union of the nano-tubes.

As we can observe in Table 3-5, the ratio between the inter-tube distance measured on the nano-patterned Aluminium substrate and the applied voltage are approximately 2nm/V except for the sample HA6 in which is lower, 1.65nm/V, and current density higher than for the others. This so high current density implies that the growth rate is extremely fast and the volume expansion is also high provoking higher mechanical stress among the cells, and this mechanical stress trends to be reduced by reducing the cell size confirming that was previously mentioned. As consequence there is no linear relation between the inter-tube distance and the applied voltage.

3.4. Periodical Modulation along the nano-channels.

3.4.1. Previous considerations.

The anodization processes which HA are involved require special cares. Here, temperature is a key factor since small variations may cause unsatisfactory results. That is why be able to maintain the temperature unchanged along the whole process is of crucial importance.

In Figure 3.14 we can observe the influence of anodization temperatures in pulsed anodization processes.

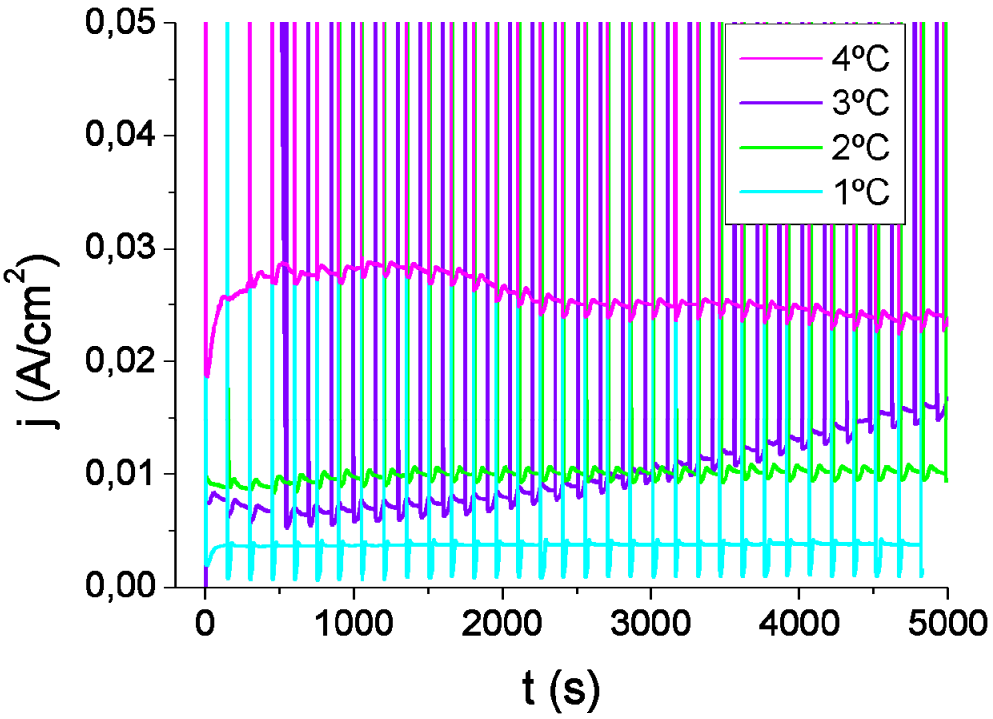

Figure 3.14: Current density evolution during pulsed anodization processes carried out at 4, 3, 2 and 1°C.

Figure 3.14 shows how change makes a difference of 3°C during pulsed anodization process, being the current density inhomogeneous for the higher temperatures, which effect is reflected directly in the alumina grown. If the temperature of the electrolyte is 4°C the current density is unusually high and unstable. When temperature rise up from 2 to 3°C, the current density increase up to double obtaining an inhomogeneously grown alumina. This occurs because the recovery time of the current density from HA pulse to HA pulse changes because of the temperature. The process is more stable at 2°C but the current density it still too high regarding what it would be expected. The best results are obtained when the temperature of the electrolyte range between 0 and 1°C, when the recovery time for the current density during the MA pulse is similar after each HA pulse. At these temperatures, the current density during each MA pulse has the same behaviour than the initial stage of a typical mild anodization, the growth is the most homogeneously possible and it is very important trying to remain it as stable as possible. So, this is the ideal temperature range for these kinds of experiments. But, as we could observe, even a small difference of temperature between 0 and 1ºC has significant effect on the behaviour of the current densities (Figure 3.15).

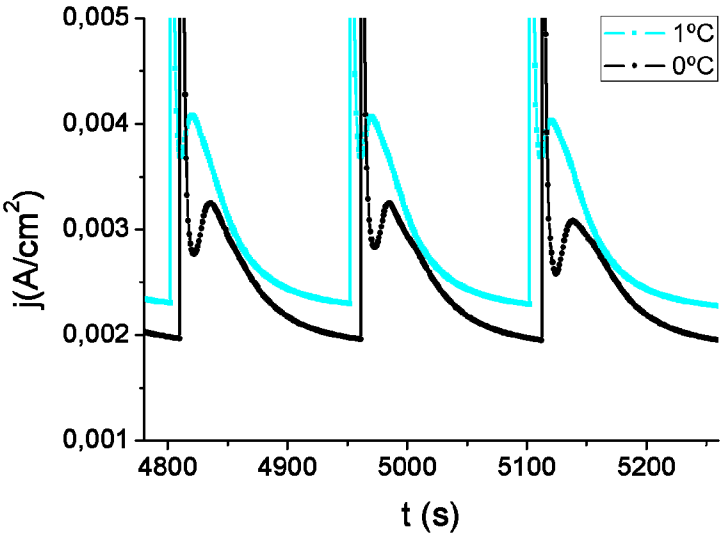

Figure 3.15: Detail of the current density behaviour during PA process at 1°C and 0°C.

From Figure 3.15, we can deduce that the growth process is slower at 0°C than at 1°C since the current density is lower and the time employed in reach the maximum of the curve belonging to the MA section takes approximately 7 seconds more than at 1°C.

From the current density curves we also can deduce that the minimum MA pulse time necessary for the current densities to reach a steady-state value usually is not less than 120 seconds [8]. That is why starting from there it is possible to apply MA pulses lengths as long as desirable (Figure 3.16).

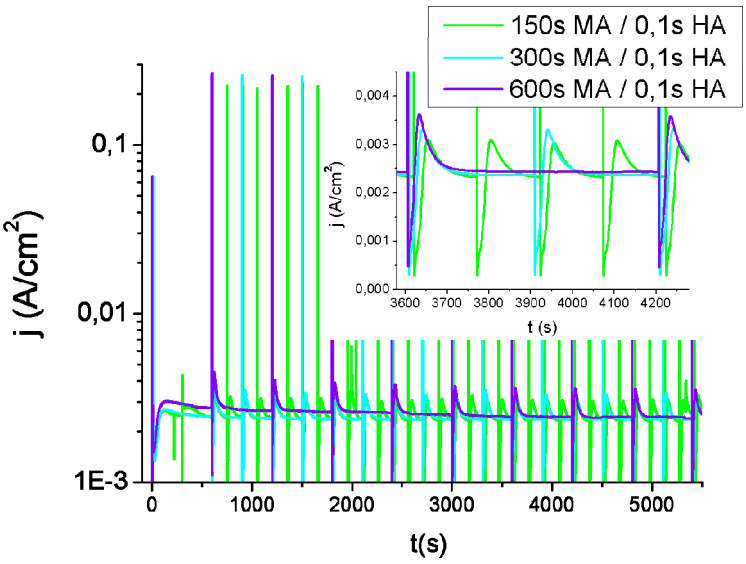

Figure 3.16: Current density evolution during pulsed anodization with square voltage HA pulses of 35V. The lengths of the pulses are 150, 300 and 600s for MA sections and 100ms for HA sections. In the inset is showed a detail of the MA current density curves for the different pulse lengths.

In the inset of Figure 3.16 we can see more detailed the behaviour of the current density after a HA pulse. The current density decrease down to almost cero immediately as the MA pulse is applied and then increase again up to reach a steady-state value typically associated to the traditional conditions of anodization with sulphuric acid. This behaviour can be explained as follow. The current density under potentiostatic conditions is directly associated with the ions which go through the barrier layer, so the current density depends on its thickness and also on its chemical composition [35]. The effective electric field across the barrier layer is equivalent to the applied voltage divided by the thickness of the oxide at the pore bottom, i.e. $E=\Delta U/d_{BL}$, being U, the applied voltage and d_{BL}, the thickness of the barrier layer. Knowing this, the current density is proportional to the effective electric field, i.e., the gradient of the applied voltage across the barrier layer, as indicated in Eq. 3.1.

Eq. 3.1: $$j = j_0 \cdot \exp(\beta \cdot E) = j_0 \cdot \exp\left(\frac{\beta \cdot \Delta U}{d_{BL}}\right)$$

Where j represents the current density and j_0 and β are constants which depend on the material. So, immediately after a HA voltage pulse, the thickness of the barrier layer is thicker than during MA conditions, that implies that the effective electric field is lower, leading to an abrupt decrease of the current density. In our case, the current density is recovered within the first 120s of the MA process, and this recovering is directly related to the thinning of the barrier layer, which also implies an increase on the effective electric field through the oxide at the pore bottom.

Still there is controversy in the scientific community explaining this point. There are two models which could explain the mechanism of variation of the thickness of the barrier layer. The more extended is the Field Assisted Dissolution (FAD) which defends an equilibrium of electric field enhanced oxide dissolution at the alumina oxide/electrolyte interface and electrochemical growth at the metal/alumina oxide interface [35-38]. Those who support this theory maintain that the dissolution mechanism at the oxide/electrolyte interface remain the same in HA conditions and the main difference consist of the different conditions in the balance of oxidation and dissolution rate since the electric field changes from MA to HA [23]. On the other hand, a new explanation has appeared more recently. Field-induced plasticity (FIP) also called field-assisted flow (FAF) which takes places within the barrier layer during the film growth. The material flows from the centre of the pore bottom toward the cell boundaries. This displacement is facilitated by the stress due to electrostriction and the expansion of the aluminium during its conversion of metal to oxide. This has been observed experimentally by García-Vergara et al. [39-43] and also confirmed by theoretical modelling of

FAF by Houser and Heber [14, 44]. In our opinion, these two growth models coexist in PA. While the FAD is the main dominant mechanism during MA process, the FIP is the growth mechanism during the HA pulse promoting the tubular formation. This could explain the two different structures of alumina segments and the fracture cleavage planes presented in PA.

The recovery time is influenced by the anion incorporation from the electrolyte to the anodic alumina being faster as higher is anion concentration. Since the anodic alumina grown in sulphuric acid based electrolyte contains the highest levels of incorporated impurities the recovering time is shorter than any other Aluminium anodizing electrolyte.

As previously mentioned, the current density is related to the ions going through the barrier layer. So, for HA conditions where the current density could be 100 times higher than for MA it is also expected an increase on the anion incorporation to the anodic alumina at the barrier layer. Moreover, Woo Lee et al. found nano-cavities into the walls of the alumina matrix which implies that the mass density of the alumina grown under HA conditions is lower than that of the alumina grown under MA conditions [8]. These two factors become the HA-alumina mechanically low stable and easy etching with acidic solutions.

Other problem we found during the preliminary studies is the mechanical instability of the alumina structure grown under pulsed anodization conditions, mainly when the HA pulse lengths are longer then 250ms, probably due to the high mechanical stress generated during the HA pulses are being applied. An example of these mechanical instabilities we could find is presented in Figure 3.17.

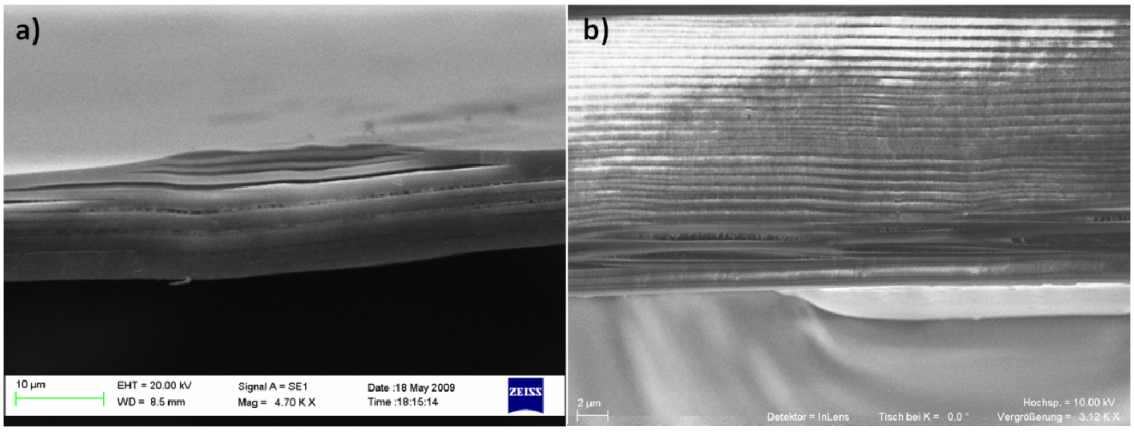

Figure 3.17: Mechanical instability presented in sample with HA pulse length of a) 1s and b) 500ms.

Since anodic alumina grown by pulsed anodization has an extremely fragile structure, we look for solution to solve this inconvenient, which is a non desirable effect and could make unviable their use as template or other functionalities.

The idea is giving some extra stability to the NAAF. In order to do this we grow a previous film under MA conditions before the pulsed anodization (PA) section and another one after, i.e. with a “sandwich” like architecture (Figure 3.18).

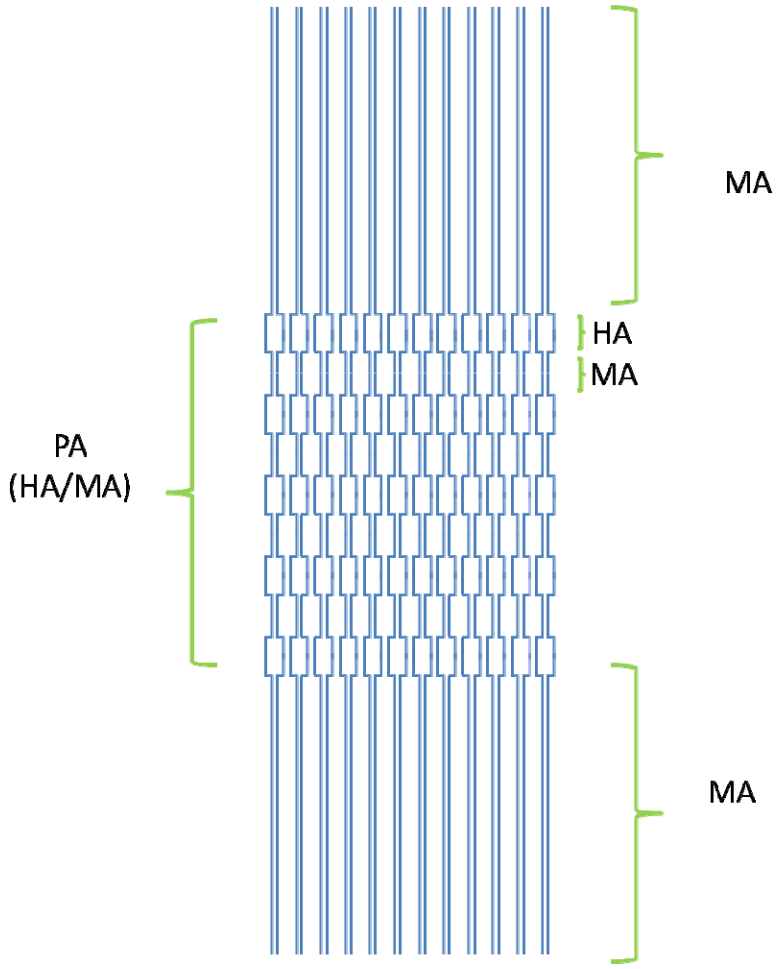

Figure 3.18: Schematic diagram of the proposed system, “sandwich” like architecture, composed of two MA sections holding the PA section.

The experimental results are showed in Figure 3.19. In Figure 3.19a is represented the current density during the first MA section, the PA section and the final MA section. It is also represented a several detailed periods of the PA where we can appreciate the homogeneity of the anodization process.

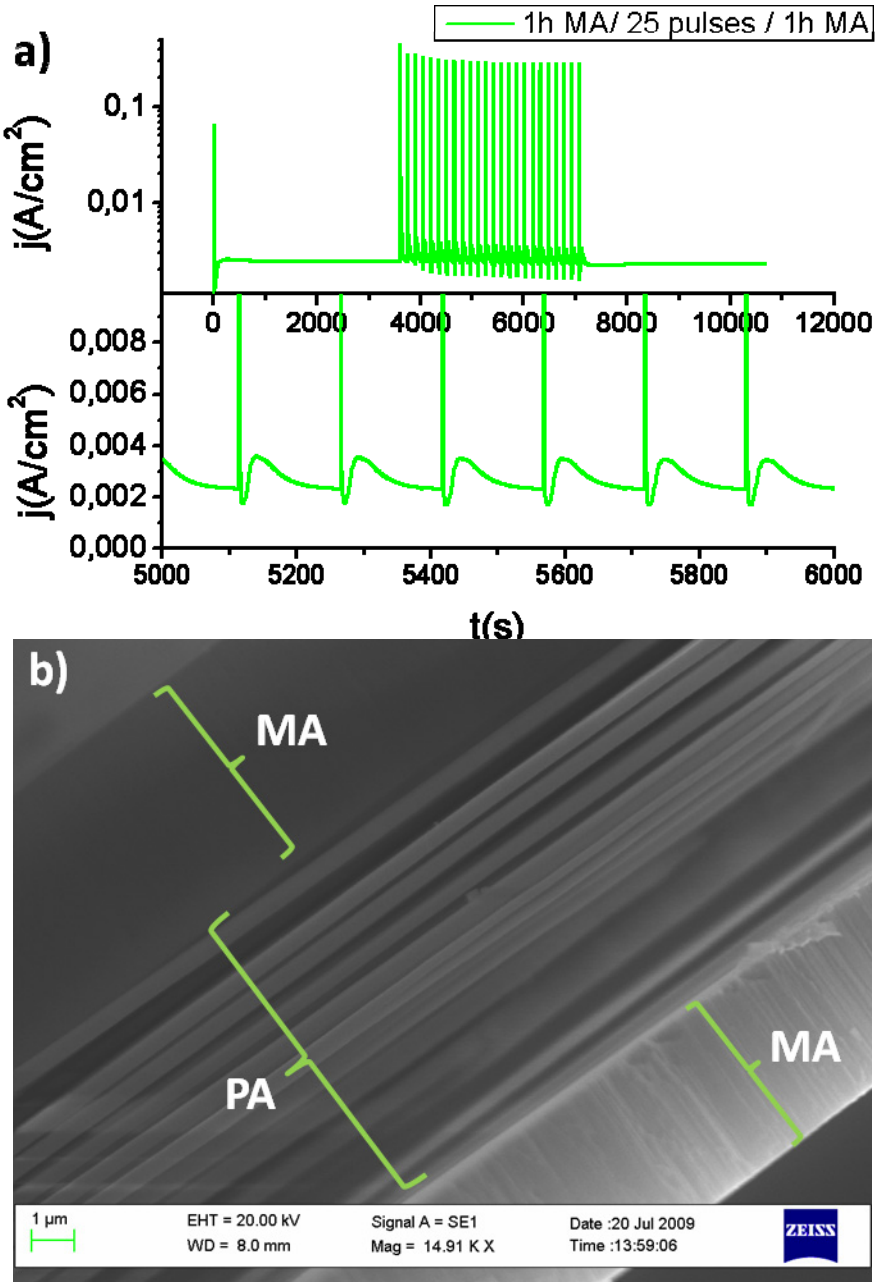

Figure 3.19: a) Current density evolution during the MA/PA(150sMA;500ms)/MA process with a detail of the PA curves; b) SEM micrograph of the resulting combination of applied voltages.

In Figure 3.19b the micrograph shows clearly the result of the three sections (MA/PA/MA) in which is divided the anodization.

Other effect which comes instabilities can be found commonly in these kinds of anodizations (Figure 3.20). The red lines indicate that the surfaces of the planes are non parallel which implies inhomogeneity during the grown.

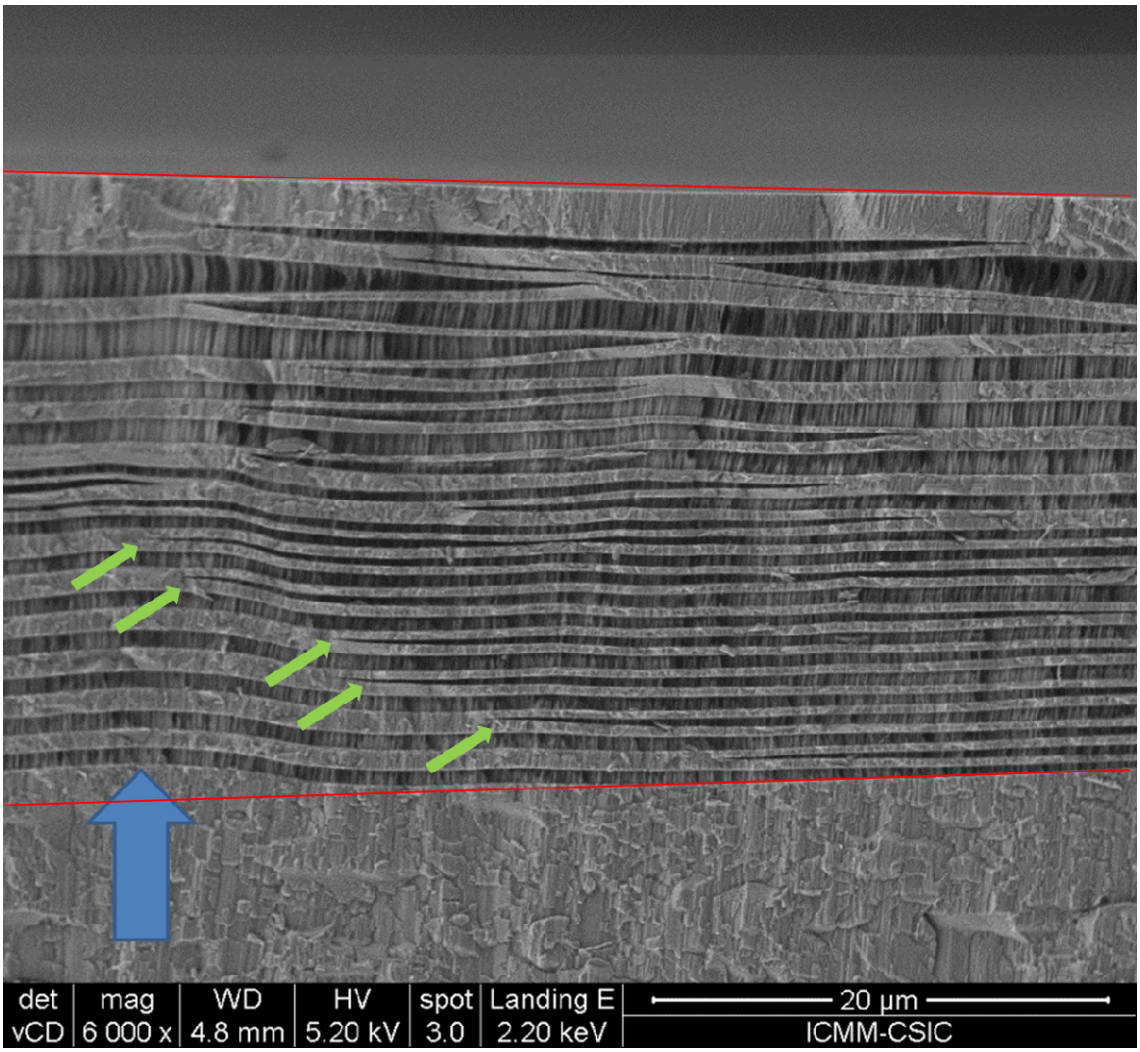

Figure 3.20: Mechanical instabilities generated during the PA grown due to plastic deformation of the Aluminium substrate.

This could be explained since the metal/oxide interface become ridged due to plastic deformation of the Aluminium substrate coming from local burning under the pulsed HA conditions [29] as shows the blue arrow. At the same time, two MA anodic alumina layers, apparently, become one at the points showed by the green arrows, just under the microscopic deformation pointed out by the blue arrow.

3.4.2. Applying three different signals shapes during HA pulses.

As we mentioned in Table 3-2, the shape of the HA pulses can be varied. In our case we could apply square, triangular and exponential profiles. In Figure 3.21 are represented these three cases.

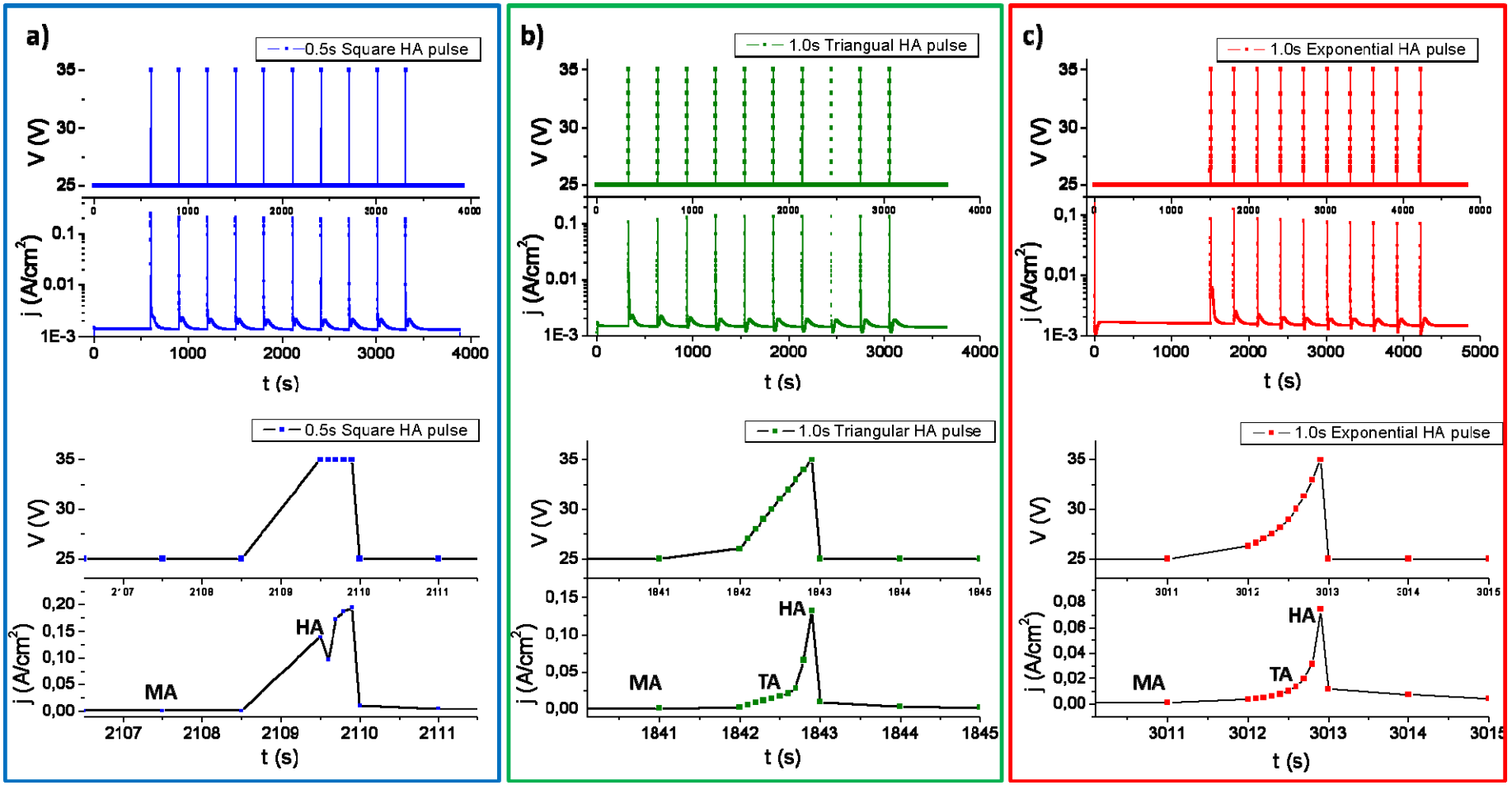

Figure 3.21: Applied voltage sequence and their correspondent current density evolutions for three different PA processes a) Square HA pulses, b) Triangular HA pulses and c) Exponential HA pulses, with their respective detailed HA voltage pulse and consequent evolution of the current density in that period. The three cases consist of 10 pulses MA(300s, 25V)/HA(35V).

Note that in Figure 3.21a there is not a ramp in the applied voltage from MA to HA pulse, but just a skip form one to the other pulse. The behaviour of the current densities for the square pulse pulses differs quite a lot from the triangular (Figure 3.21b) and exponential (Figure 3.21c), reaching the highest values. From the current density of the square pulse we can guess the first moments of a typical potentiostatic anodization process, when the curve reaches a minimum and then start increasing. The behaviour of the current density curve shapes for the triangular and exponential HA pulses is quite similar between them, maintaining a moderate current density as applied voltage increase, i.e. transitional anodization (TA) but for 34 and 35V when the current density increase drastically (HA) regarding the previous values. This transitional stage has also been reported by Losic et al. [23, 24] under galvanostatic processes. However, the maximum values reached during the exponential pulses are almost half of those reached by the triangular. The effect of the current density going through the electrodes is represented in Figure 3.22a where we can observe their evolution profile which is quite homogeneous for the three presented cases.

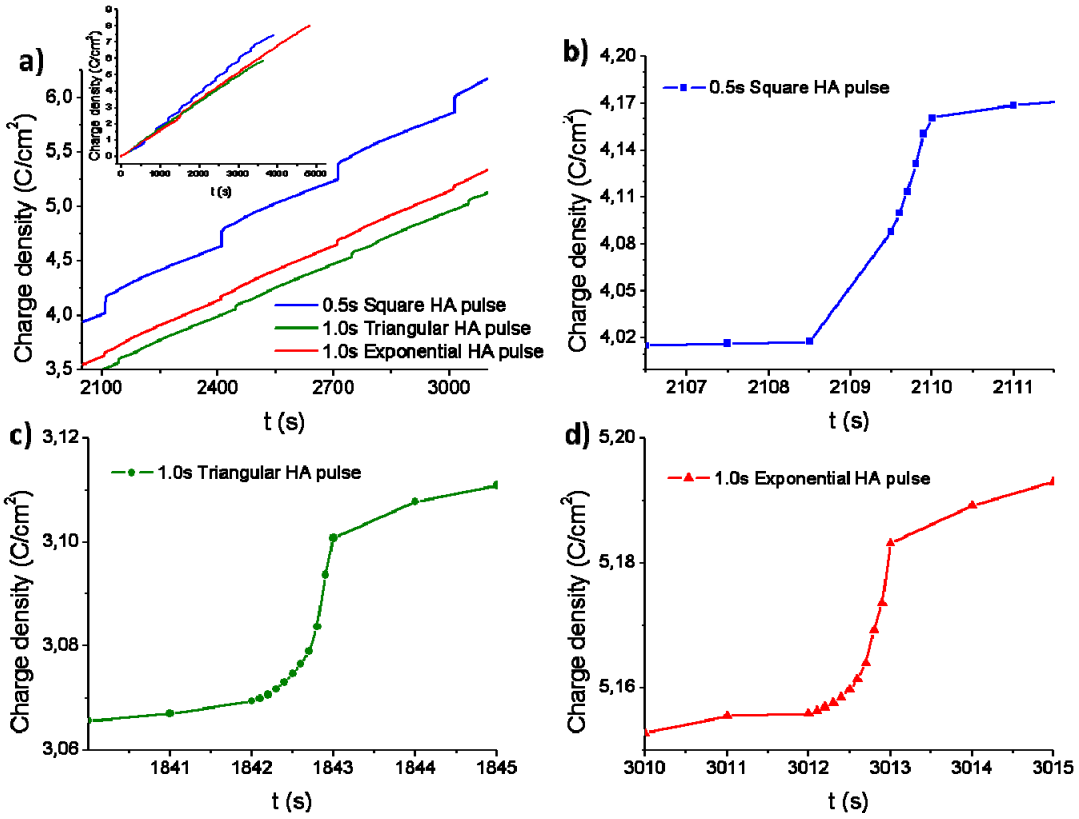

Figure 3.22: a) Charge density evolution of some pulses during the anodization processes for the three kinds of voltage pulse shapes. In the inset is presented the complete charge density evolution; b) Amplified region showing the charge density evolution during one: 0.5s square HA pulse, c) 1.0s triangle HA pulse and d) 1.0s exponential HA pulse.

In Figure 3.22b, c and d we can see in detail the evolution profile of the charge density for only one of each kind of pulses. Again, the big difference raises between the square HA pulse and the triangular and exponential ones which their respective charge densities gone through the electrodes differs from more than double. The registered charge density and current density is directly reflected on the HA segments of the anodic alumina as we can see in Figure 3.23.

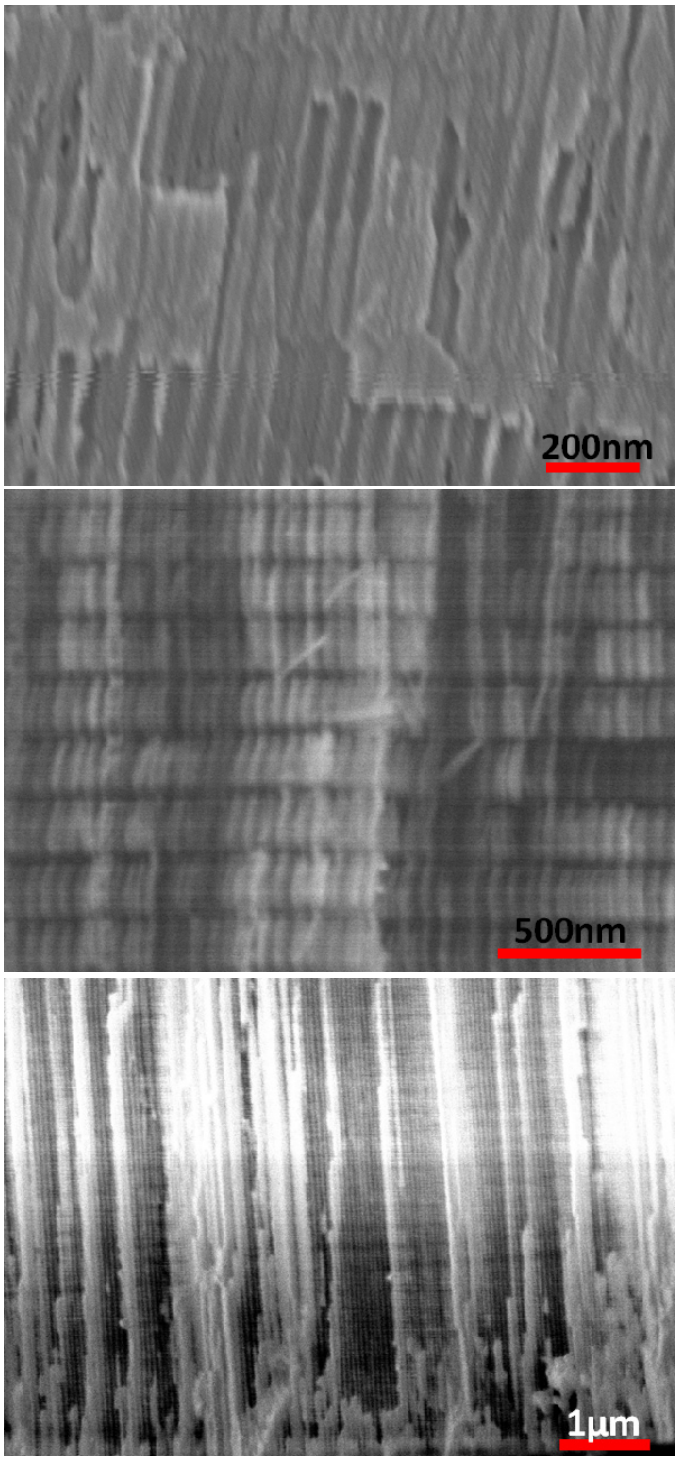

Figure 3.23: Cross section views of PA with MA (150s-25V) pulses common to a) 0.5s square HA pulse b) 1.0s triangle HA pulse and c) 1.0s exponential HA pulse.

In Figure 3.23a we can see clearly the modulation of the nano-channels. The narrower nano-channel diameters corresponds to the MA process, when the current density has the minimum values, and the wider to the HA process when the current density reaches the highest values.

In Table 3-6 are summarized the maximum current density reached during the HA pulse together with their respective charge densities and typical thickness of the segments belonging to the alumina anodized in the HA periods.

Table 3-6: Lengths, current and charge densities and thickness of the alumina segments grown for three HA pulse shapes at 35V.

HA pulse shape	HA pulse length (s)	$\rho_{HA\ pulse}$ (A/cm^2)	$\chi_{HA\ pulse}$ (C/cm^2)	Thickness of the HA alumina segment (nm)
	0.5	0.20	0.072	150
	1.0	0.14	0.032	50
	1.0	0.08	0.027	50

The thickness of the segments is not proportional to the charge density since there are other factors which are involved. As we could see in our previous experiments presented in chapter 2 and other publications [14, 45-47], the volume expansion of the alumina and the efficiency during alumina formation increase with the applied voltage. During the square HA pulse the voltage is the maximum applied along the length pulse, but in the triangular and exponential it is increasing up to reach the maximum value just at the end. So, it means that the total volume expansion and the efficiency are higher during the square pulse than during the other two kinds of pulses. These factors lead to larger segments for square HA pulses than for the triangular and exponential ones, even if the lengths of the later ones are longer that the squared pulse.

In order to see more clearly the effect of the triangular and exponential voltage pulses, we increased both amplitude and length of the pulses. The final voltage for the triangular shape pulse was established at 37V and for the exponential was 39V, both pulses were applied during 1.5s. The registered data from the electrochemical processes are represented in Figure 3.24.

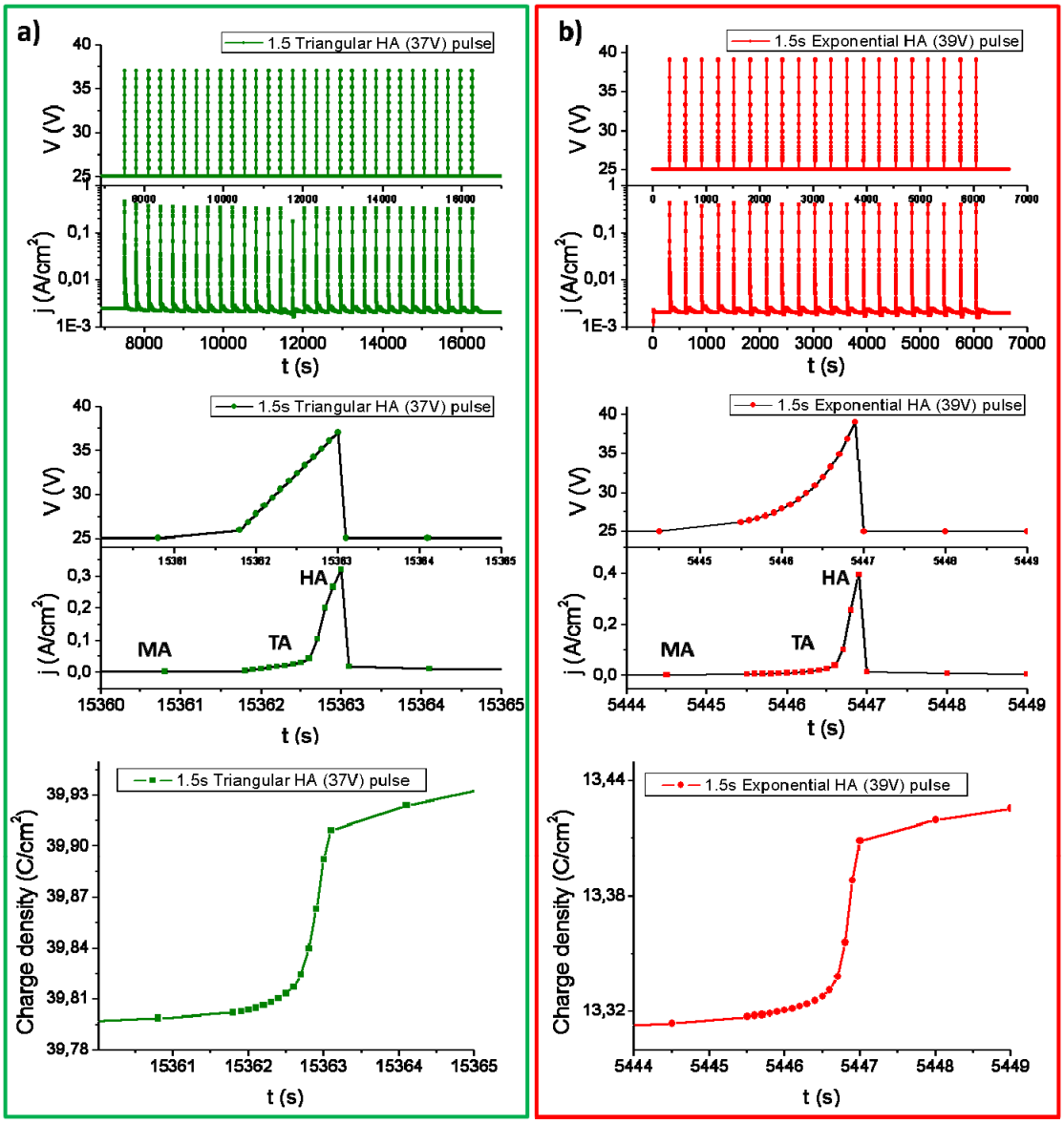

Figure 3.24: Current density evolution for the applied voltage sequence and individual pulse current density and charge density for: a) Triangular and b) Exponential HA pulses of amplitude 37 and 39V applied during 1.5s.

In the cases presented in Figure 3.24 the HA condition is much more evident than on the previous examples, reaching higher current densities as we can see in Table 3-7, passing through the electrodes more charge density and growing thicker segments of HA-alumina as those presented in Figure 3.25.

Table 3-7: Applied voltage, current and charge densities and thickness of the alumina segments grown for two HA pulse shapes for 1.5s.

HA pulse shape	HA pulse voltage (V)	$\rho_{HA\ pulse}$ (A/cm^2)	$\chi_{HA\ pulse}$ (C/cm^2)	Thickness of the HA alumina segment (nm)
	37	0.33	0.108	580
	39	0.40	0.091	420

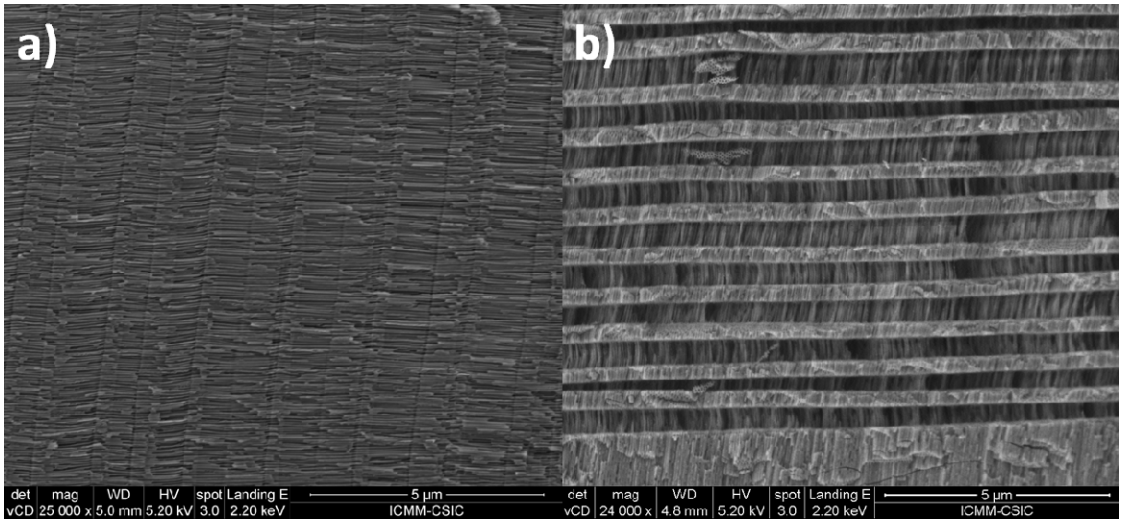

Figure 3.25: Cross section view of anodic alumina segments grown by PA a) Triangular HA pulse shape (1.5s, 37V) (vertically alligned) and b) Exponential HA pulse shape (1.5s, 39V), this sample shows over etching of 5wt% H_3PO_4.

With the traditional potentiostatic anodization process, the pore diameter can be controlled with the applied voltage since it is linearly dependent [13], but under HA conditions the applied voltage is not the only factor which affects it since the current density is also a critical parameter controlling the pore diameter, as we can observe in Figure 3.26.

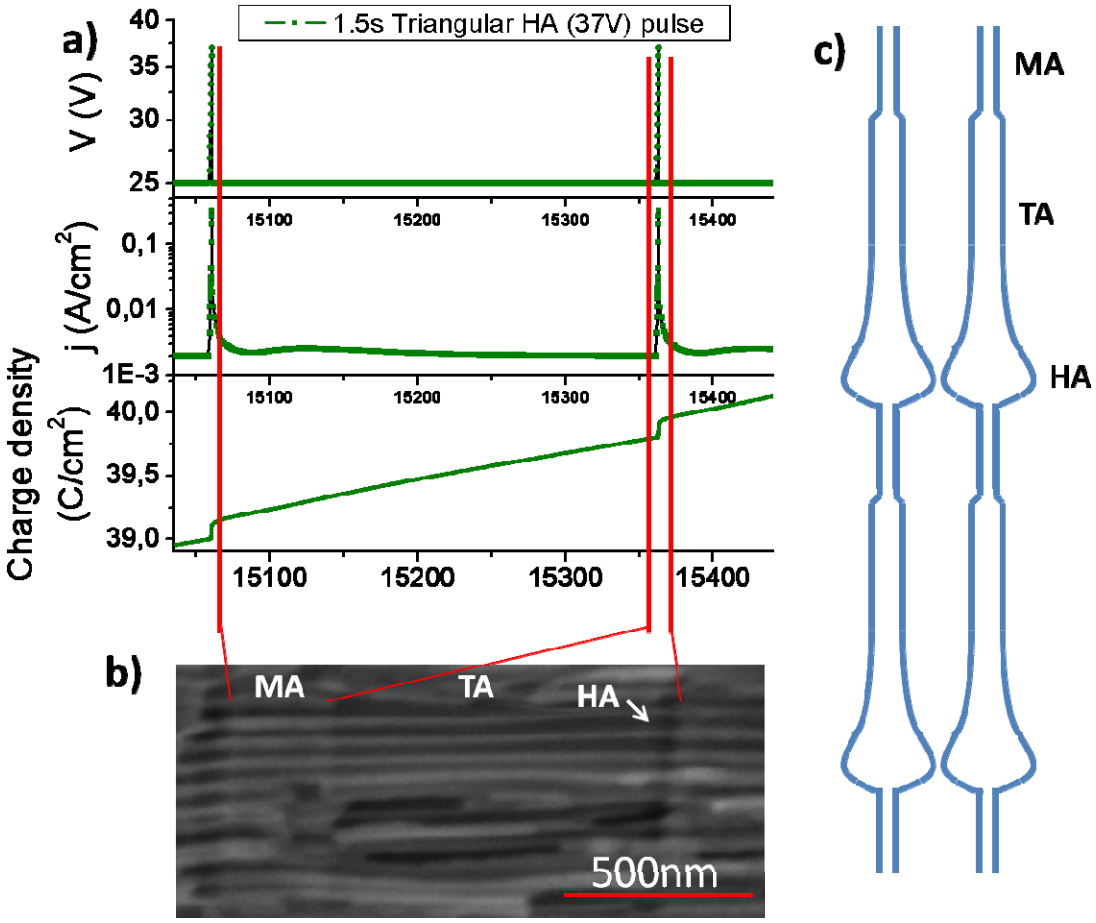

Figure 3.26: a) Sequence of two applied voltage pulses and evolution of the current and charge density, and b) the corresponding SEM micrograph of the alumina nano-channel formation; c) Schematic representation of the ideal structure of the alumina nano-channels.

The nano-channel diameter is strongly modified at the end of the HA pulse as we can see in the micrograph of Figure 3.26b and schematic representation in Figure 3.26c for a better understanding. The dissolution of the alumina is quite significant since the Joule heating is enhanced by the high current density reached at this point. Other possible explanation to this diameter modulation could come with the FAF model, since the high effective electric field may cause electrostriction at the pore bottom leading to the viscous flow of the anodic oxide toward the cell boundaries.

3.4.3. Controlled MA and HA pulse lengths.

In this case, the amplitude of the HA pulse was maintained fixed at 35V since was the voltage which better behaviour reported. It is possible to vary the thickness of the segments belonging to the MA and HA process by controlling the length of their respective pulses.

In Table 3-8 and Figure 3.27 are presented the PA series carried out for these experiments.

Table 3-8: Applied parameters for PA. MA process was carried out at 25V and HA at 35V. Before and after PA the samples were anodized at 25V during 1 hour.

25 pulses		12 pulses		6 pulses	
MA length (s)	HA length (ms)	MA length (s)	HA length (ms)	MA length (s)	HA length (ms)
	250		250		250
150	500	300	500	600	500
	750		750		750

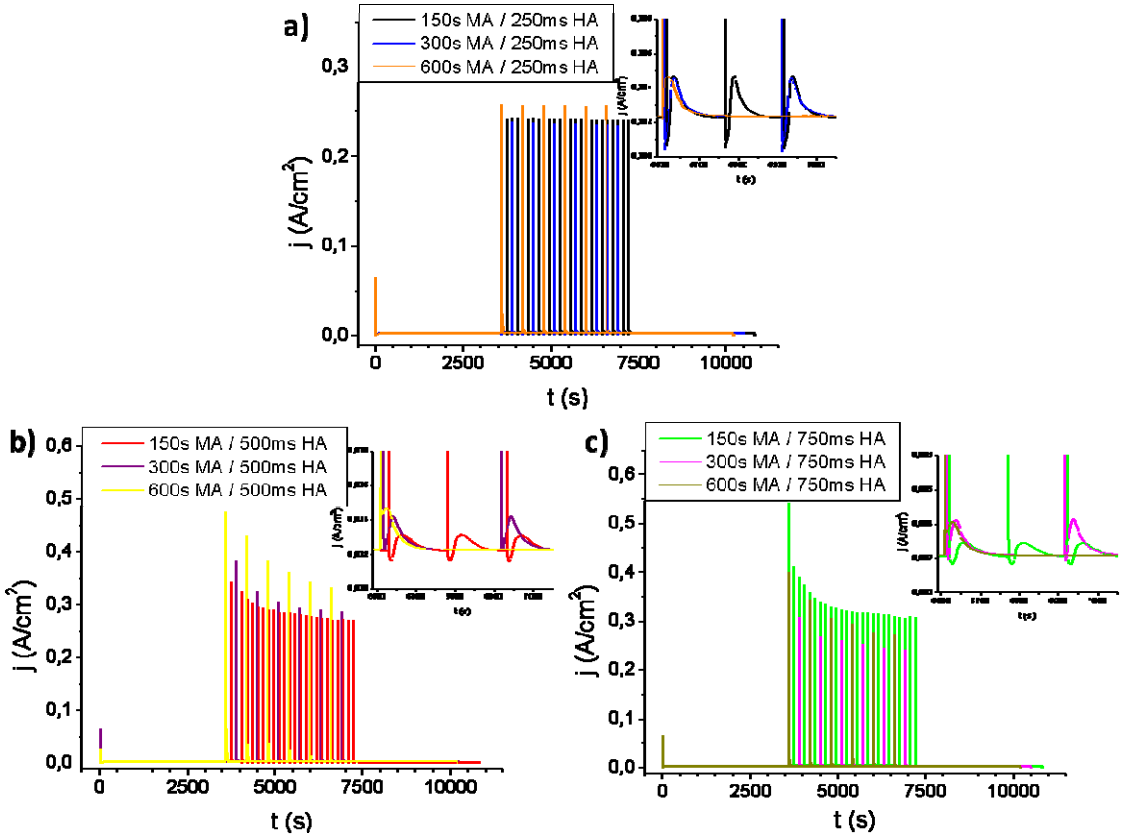

Figure 3.27: Current densities evolution during MA/PA(25V-35V)/MA processes at 150, 300 and 600s MA pulse lengths and a) 250ms, b) 500ms and c) 750ms HA pulse lengths with their respective inset for detailed current density during the MA pulse.

From Figure 3.27 we can observe that the current density during the HA pulses increase as longer is the length of the pulse and reaches a stable value after the 6th or 7th pulse. The current density of the MA pulses besides of being affected by small variation in temperature, it is also affected by the previous HA pulse, so that, by controlling only the pulse lengths, the

segments will not have always the same thickness. Moreover, after the anodization process, for the samples which has been applied HA pulses longer than 500ms some spots appear on the surface, similar to the case we saw in section 3.3 but less evident. This spots has its origin on the Aluminium substrate, and this fact also contributes to some inhomogeneities along the segments MA/HA. We can see some examples on Figure 3.28

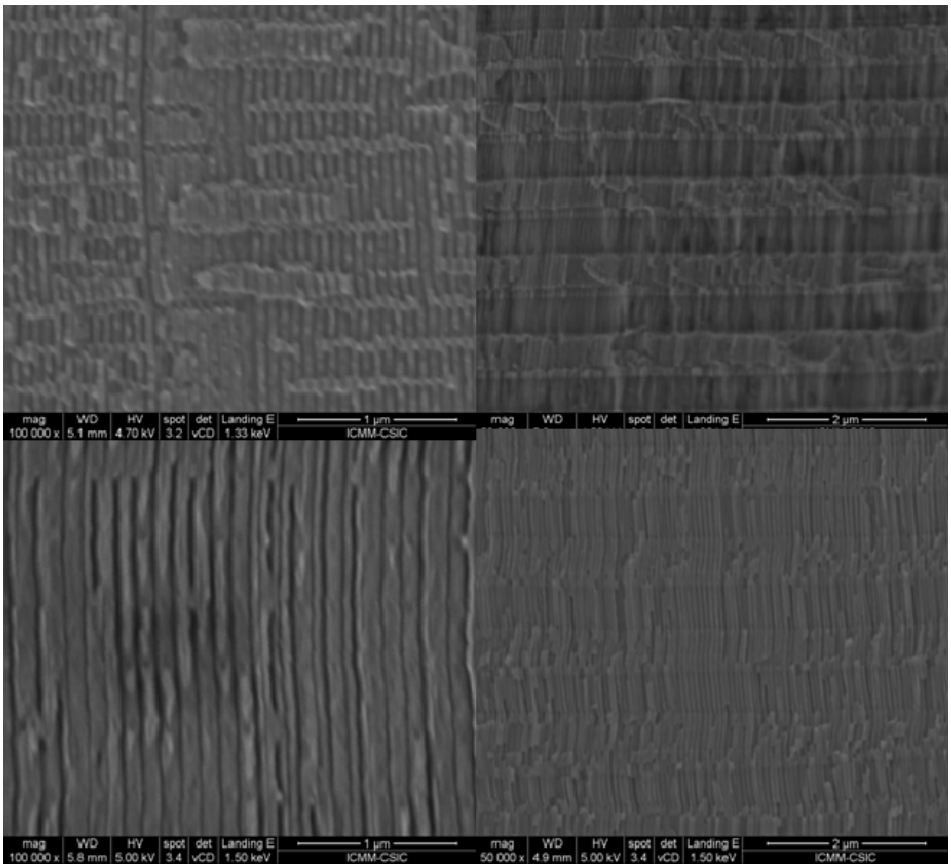

Figure 3.28: SEM micrographs for different samples with HA pulses form 0.25s up to 0.75s.

In Figure 3.28a we can observe small periodical modulation along the nano-channels, but no nano-tubes were formed since the extremely short HA pulse (150ms). On the other hand, the segments of nano-tubes and their diameter modulations can be seen clearly in Figure 3.28b. In Figure 3.28c it is possible to observe the change between the MA structure to the HA nano-tubes, which are very easy to distinguish due to their fracture modes, one through the centre of the alumina cells and the nano-tubes through the cell boundaries.

3.5. A template for synthesis of periodically modulated Co nanowires.

3.5.1. Fabrication of modulated Co nanowires by PECD.

For the development of this study we have used three different templates; one template corresponding to the sample A25 with straight nano-channels, and the second and third to pulsed anodizations, one with exponential (EXP) and other with square (SQR) profile pulses. Their main features are summarized in Table 3-9.

Table 3-9: Controlled experimental parameters applied in the fabrication of the NAAF used as templates.

Sample label	V_{MA} (V)	Signal profile	V_{HA} (V)	nº of pulses	First MA length (h)	MA pulse length (s)	HA pulse length (s)	Last MA length (h)
A25	25		-	-	18	-	-	-
SQR	25		35	30	5	300	0.5	5
EXP	25		39	30	5	300	1.5	5

The NAAF templates with modulated nano-channels has been grown with the "sandwich" structure in order to improve their mechanical stability, as mentioned in Figure 3.18 and Figure 3.19a. The PA section of the square pulses is the same than that showed in Figure 3.21a and the PA section of exponential pulses is the same than that showed in Figure 3.24b.

After the removal of the Aluminium substrate and the removal of the barrier layer transforming the NAAF into NAAM as described in section 1.1.5, the next step for PECD is described in section 1.2.2. The nano-channels are then filled by electroplating, so that, hexagonal arrays of Co nanowires are prepared characterized by periodic changes in diameter. The experimental conditions are exactly the same than that described in ... . The registered current density presented in Figure 3.29 agrees with other behaviours previously described

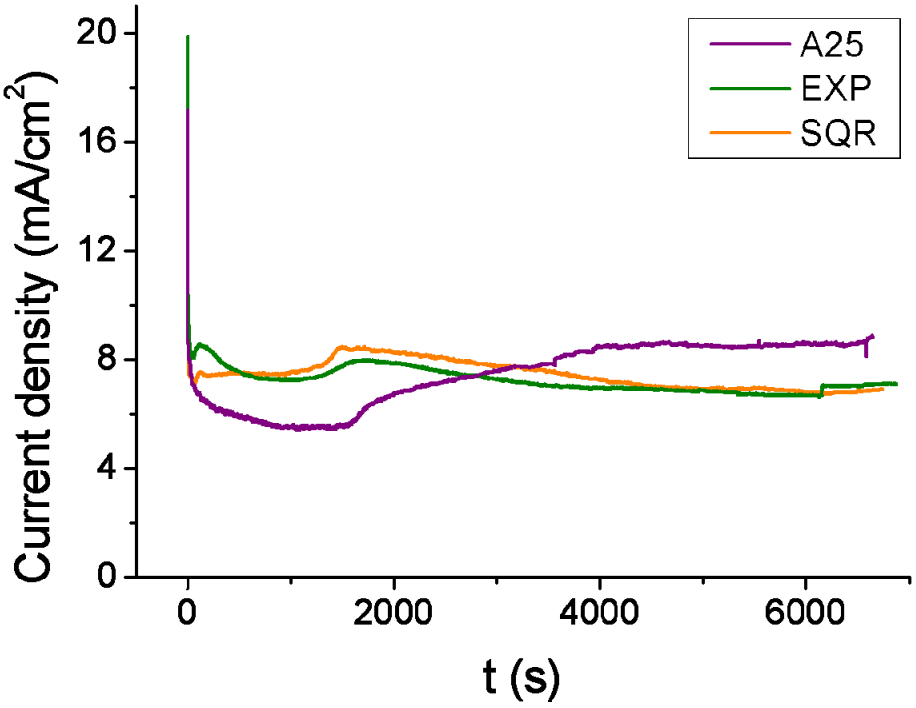

Figure 3.29: Current density of Co PECD into straight (A25) and modulated (EXP and SQR) nano-channels templates as function of electroplating time.

The current densities of the electrodeposition processes have a similar behaviour during the first 1500 to 2000s approximately. During the first seconds, when the current density decreases rapidly, takes place the nucleation of the nanowires. Then, the current density stabilizes and the nanowires grown into the nano-channels. After that the current density starts to increase, which is ascribed to the electroplating of material on the surface since the area of the electrode is being increased. In our case, it is clear for the template A25, but for the samples with modulated nano-channels the current density start to decrease slightly in both cases. The decreasing current densities could be attributed to a resistance imposed by the modulation of the nano-channels, which keep on being filled. It could be expected an oscillatory behaviour of the electrodeposition current density in the modulated diameter sector of the templates since the wider sections belonging to the HA segments has a large volume. This do not happen since during the growth, even being uniform, there is always slightly variations which could reach few hundreds of nanometres after several microns thickness, so that, ones overlap with others. After the electroplating process, metallic deposits were found on the surface on the bound of the electrolytic cell. These superficial deposits were detached with adhesive tape before structural and magnetic characterization.

3.5.2. Electronic micrograph and structural characterization of modulated Co nanowires.

The samples were characterized by SEM micrographs in order to observe the electrodeposited Co nanowires and its modulations in diameter along the nano-channels. We can observe in Figure 3.30 a micrograph of straight Co nanowires electrodeposited into the template type A25.

Figure 3.30: Cross section view of the electrodeposited Co nanowires into the NAAF of a sample type A25.

The micrographs of Figure 3.31 show the uniform electrodeposition on Co into the modulated section of the template with squared PA. The brighter strips in Figure 3.31a are the modulated segments during the HA pulses. They are brighter since there is more Co than in the MA segments due to the larger diameters of the nano-channels. In Figure 3.31b we also can observe that the segments have not equal lengths. We could attribute this fact to that which was explained in section 3.4.1. In Figure 3.31c we have a micrograph where the modulations are showed in more detail. In the MA segments the nanowires are narrow and after reach the HA segments expansion on their diameter can be clearly appreciated. We also can observe in Figure 3.31c small modulations in the HA section which can be attributed to the strong increasing of the current density. This effect was previously observed [7].

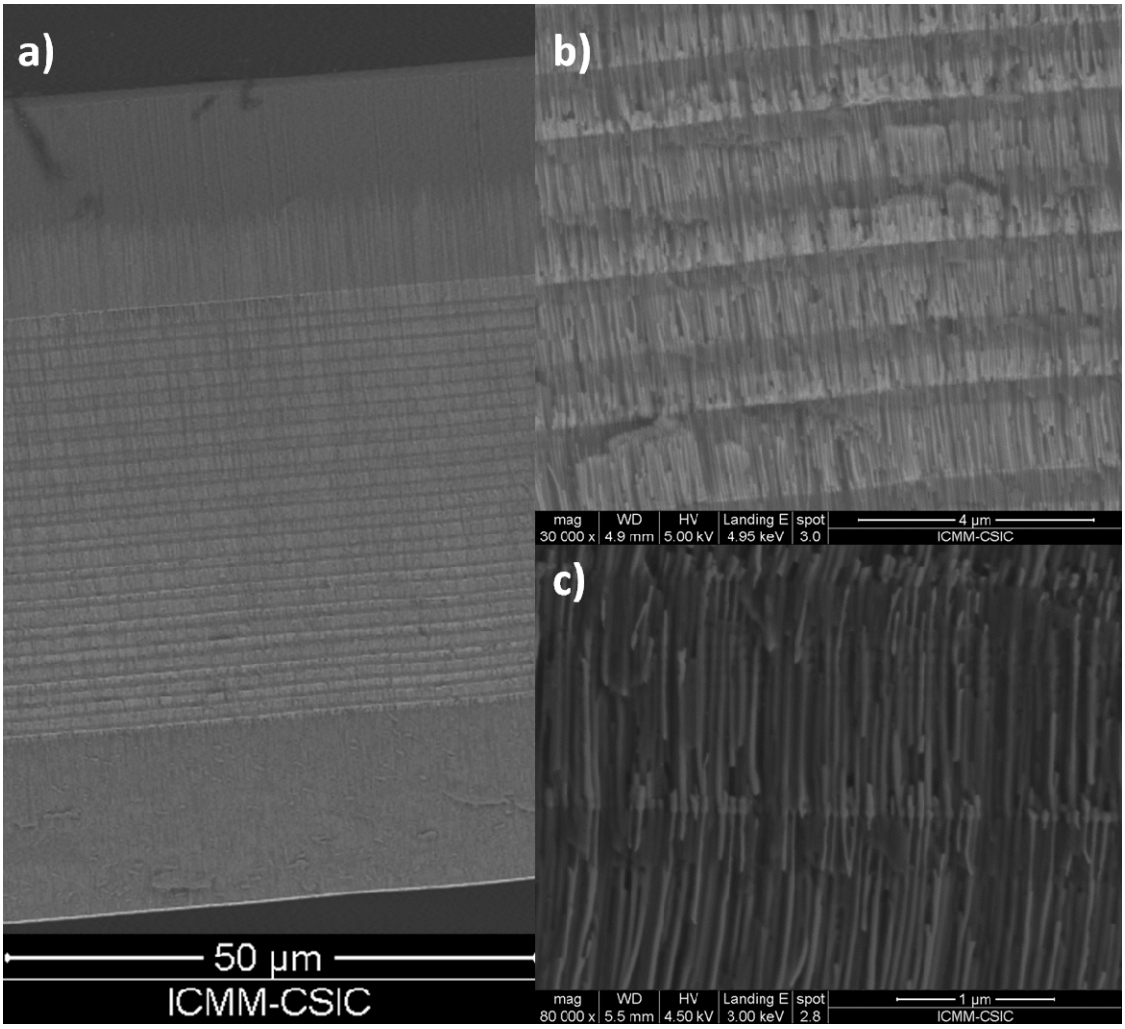

Figure 3.31: Cross section views of electrodeposited Co nanowires into a NAAM with squared PA. a) Total thickness of the sample, b) Strips formed by the Co electrodeposited HA segments, c) Detailed micrograph with the modulations of the Co nanowires.

In Figure 3.32 are presented micrographs of the Co electroplated sample anodized with exponential HA pulses. The homogeneity of the Co electroplating is showed in Figure 3.32a where it is also possible to observe the bright stripes formed by the Co filling the HA sections. The micrograph presented in Figure 3.32b shows the PA section where we can see that the electroplated Co nanowires in the HA segments reproduce a similar shape than that showed in Figure 3.26b and c.

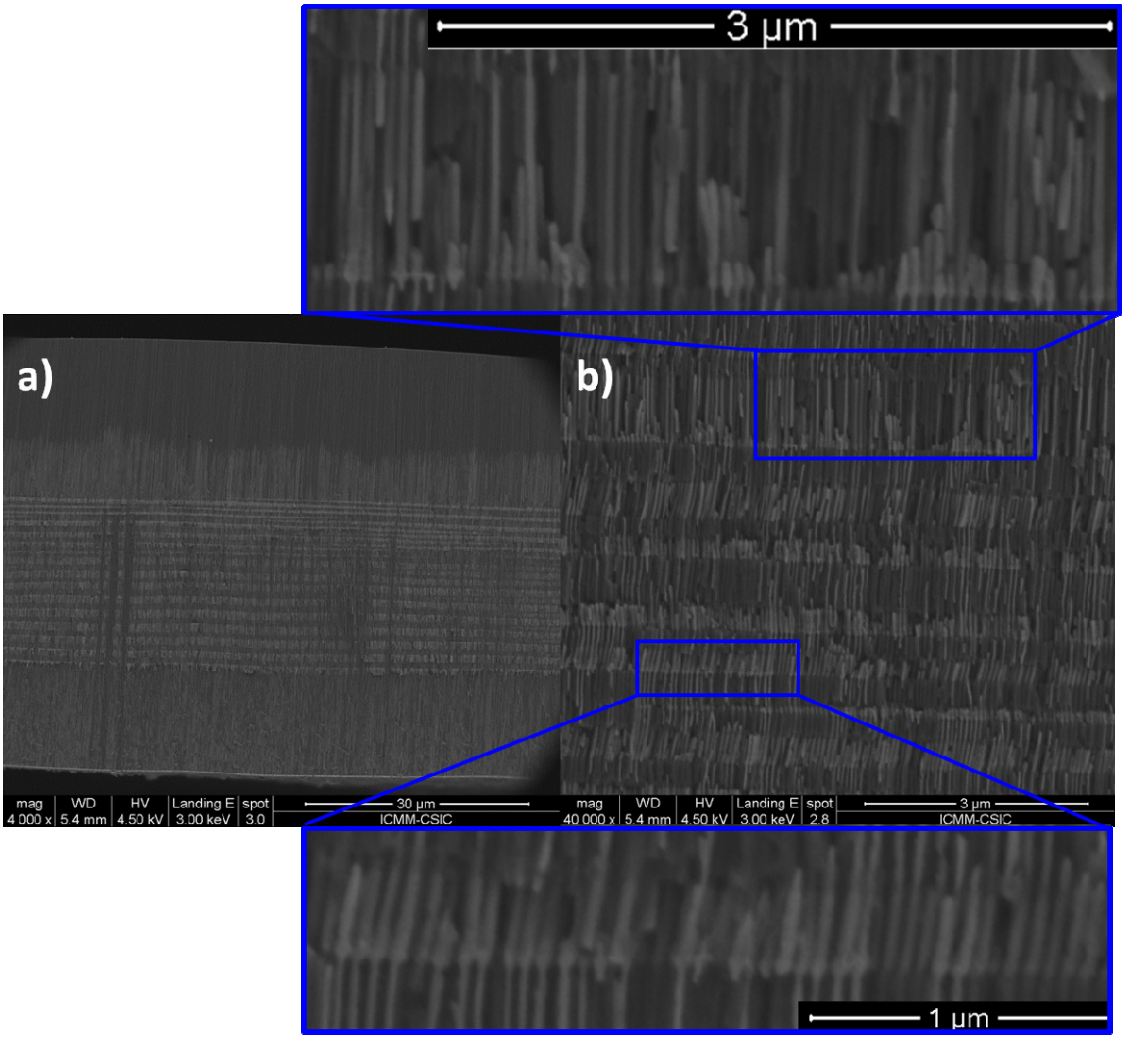

Figure 3.32: Cross section views of electrodeposited Co nanowires into a NAAM with exponential PA. a)Total thickness of the sample; b) PA section with magnifications of two zones where the modulations coming from the exponential HA pulses are showed.

The overall length of the electroplated nanowires range between 50 and 60µm and the centre to the centre distance among them is kept constant at 66nm. The diameter of the nanowires within the MA sections is 26 approximately. In the exponential HA segments the modulation of the diameter of the nanowires could vary from 30 in the narrower part up to 55nm in the wider part, approximately. In the case of the squared HA segments, the nanowire diameters are 40 to 45nm. A schematic representation of the ideal features of the electroplated nanowires is presented in Figure 3.33.

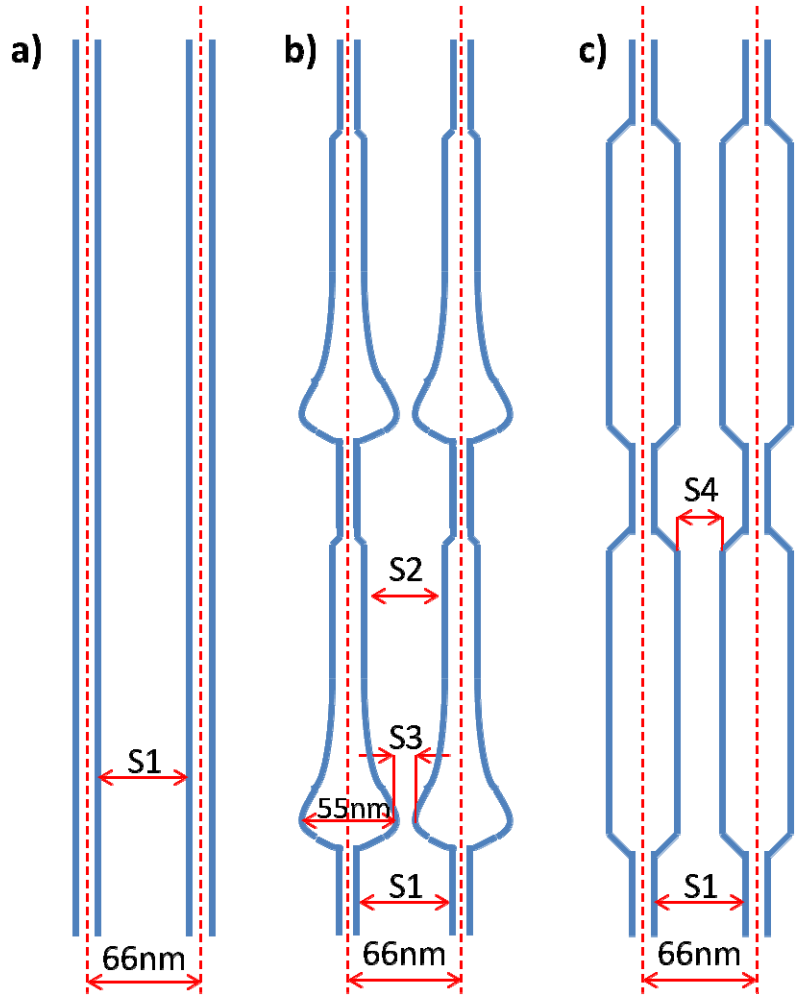

Figure 3.33: Schematic representation with ideal geometrical features of the electroplated nanowires in the cases of a) uniform diameter template; modulated diameter within b) exponential and c) squared HA pulses template. S1 = 40nm; S2= 35-30nm; S3 = 10-5nm; S4= 25-20nm.

The average length of the HA segments for the exponential and squared pulses are 0.65±0.2µm and 0.95±0.3 µm, respectively. On the other hand the average lengths of the MA segments within the PA section are 0.38µm for both samples, which fit quite well with the expected for the MA process on conventional sulphuric acid electrolyte anodizations.

The X-ray diffractograms of the electroplated Co nanowires are presented in Figure 3.34. The x-ray spectrum reveals three peaks belonging to policrystalline Co. The peak which appears at 41.61° can be ascribed to the (110) which should appear at 41.55°. The peak which appears at 47.46° can be ascribed to the (101) which should appear at 47.41°. The spectrum pattern can be assigned to polycrystalline hcp structure. The second order peak of (100), i.e. (200) is also present at 90.40°.

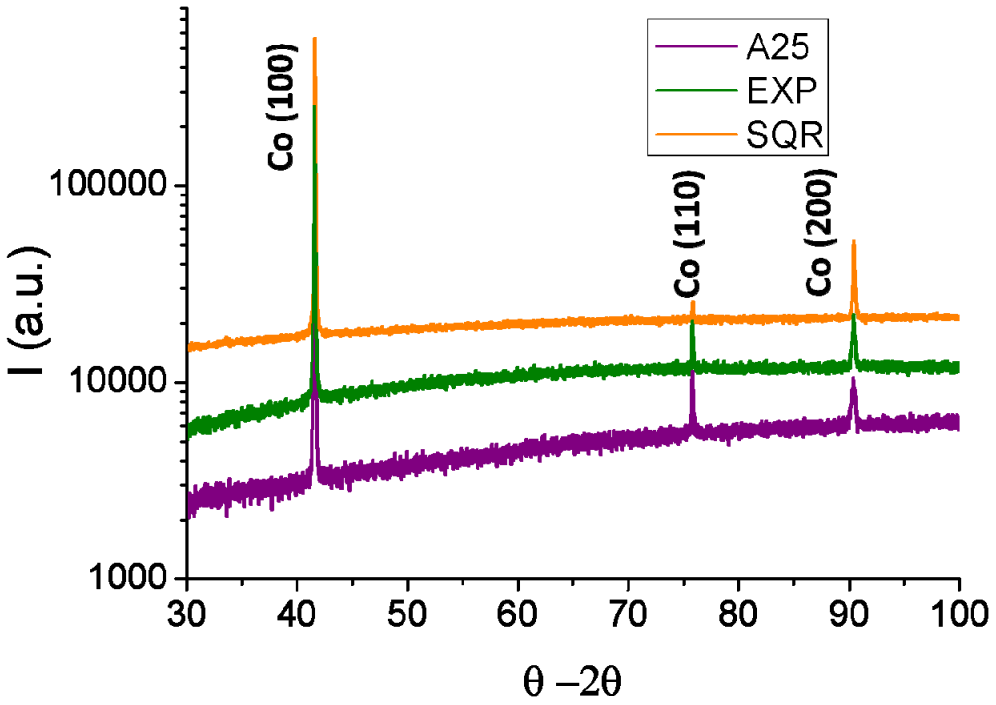

Figure 3.34: X-ray diffraction spectrum of electroplated Co nanowires into straight and modulated nano-channels.

From the analysis of the diffractograms by the Scherrer formulae we have obtained the grain size and their orientation parameter and presented in Table 3-10.

Table 3-10: Orientation parameter and grain size for samples with straight and modulated Co nanowires.

Sample template	Plane orientation	Orientation parameter	Grain size (nm)
A25	Co (100)	0,798	37,7
	Co (110)	0,2022	14,2
SQR	Co (100)	0,977	83,5
	Co (110)	0,0231	2,2
EXP	Co (100)	0,913	61,9
	Co (110)	0,0872	6,3

The forming crystals of Co nanowires are clearly oriented in the (100) direction. The straight nanowires have an orientation parameter of 0.80 for the (100) direction, while for the modulated nanowires are higher than 0.90 for the samples with exponential HA pulses,

reaching almost 0.98 for the sample with squared HA pulses, i.e. almost mono-crystalline nanowires, which also presents the largest nano-crystals, larger than 85nm.

3.6. Magnetic characterization of periodically modulated Co nanowires.

The magnetic hysteresis loops for the previously electroplated Co nanowires showed in the previous section are presented in Figure 3.35.

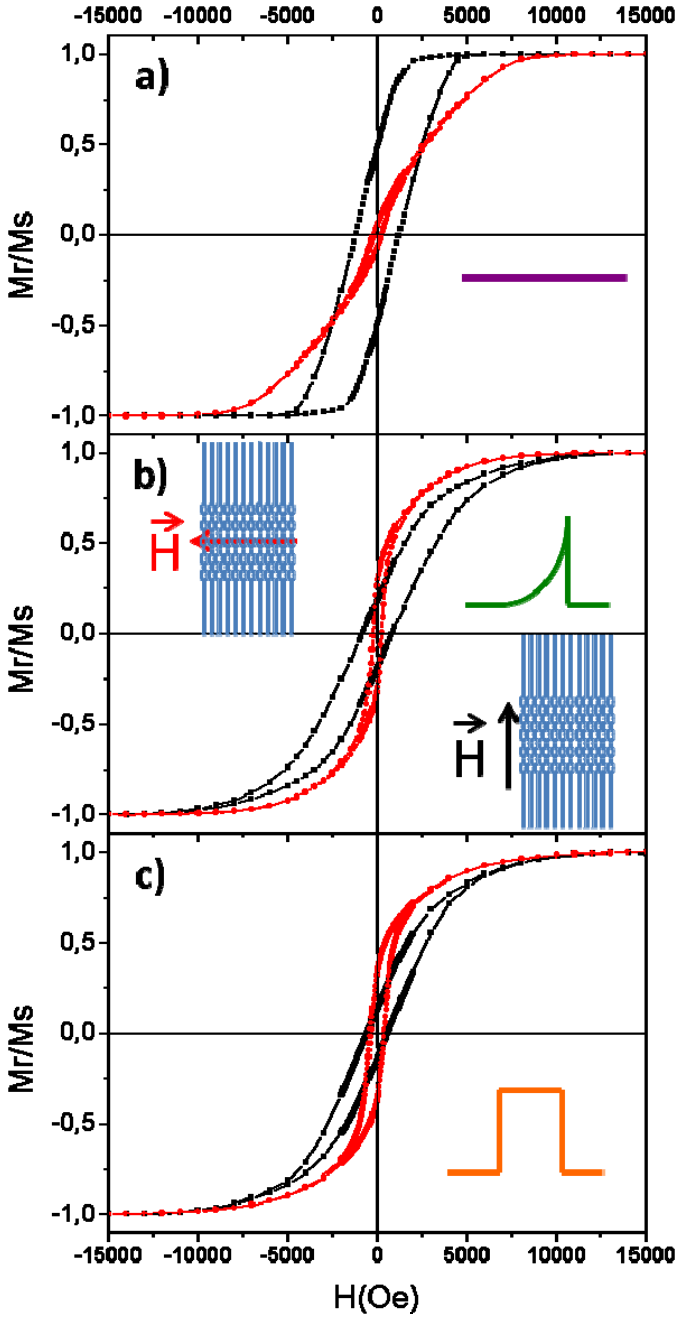

Figure 3.35: Parallel and perpendicular magnetic hysteresis loops for Co nanowires grown in NAAM templates grown with a) uniform pore diameter; PA section with b) exponential and c) squared HA pulses modulated nanowires.

The definition of parallel and perpendicular measurements is taken with respect to the wire long axis. As mentioned above, in the case of the template A25, the nanowires are characterized by uniform pore diameter of 25nm along the whole pore length. In agreement with previous work the array of nanowires is found to have easy axis of magnetization sitting preferentially along the wire long axis as shows Figure 3.35a. It should be remembered that the VSM hysteresis loop represent the overall magnetic response of the array, averaging over multiple magnetization reversal processes and accounting for neighbouring wire interactions. For this reason it should not be taken as representative for the magnetic behaviour of individual nanowires.

The direction of the magnetic easy axis is not as clearly establishes in the case of modulated nanowires as for continuous nanowires. This can be explained by accounting for the presence of different anisotropies within modulated nanowires. For instance, in the case of nanowires grown into exponential HA pulses NAAM template, Figure 3.35b, the difference between the parallel and perpendicular configuration is much less noticeable, both configuration showing similar values of remanent magnetization and the difference in the coercive field has been diminished, as shows Figure 3.36. The magnetic hysteresis loop, showed in Figure 3.35b, suggest the presence of two competing magnetic phases having axial and perpendicular magnetic anisotropy identified with the MA and HA segments of the nanowire, respectively. A first interpretation might, misleadingly, suggest that the change in anisotropy observed in the HA segments could be due to change in shape and/or magneto-crystalline anisotropy. However, it is well know that uniform nanowires having larger diameter, with aspect ratio comparable to the HA segments of the modulated nanowires, retain the easy along the wire axis. Similarly, the magneto-crystalline anisotropy remain constant between the different segment as the nanowires are grown from a single electroplating process and the length for each segment is well above the minimum length necessary to observe any change in the crystalline phase of electroplated Co nanowires.

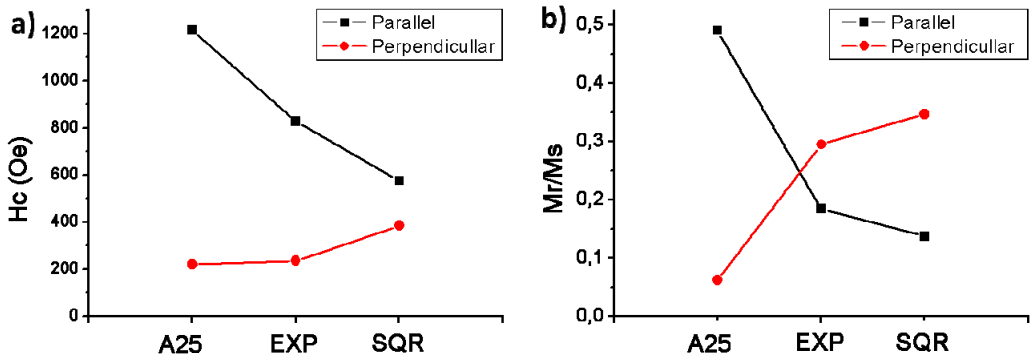

Figure 3.36: a) Coercive field and b) remanent magnetization for parallel and perpendicular applied magnetic field.

The change of anisotropy observed in modulated nanowires is, in fact, the resultant of lateral magnetostatic coupling between the HA segments of the nanowires. Due to their larger diameter, (see Figure 3.33b), the interaction among these segments is strong enough to force the magnetization to lay perpendicular to the nanowire axis.

This scenario is confirmed by sample prepared with squared HA pulses template. As we can observe in the hysteresis loop, Figure 3.35c, the easy axis of the system is found to lay perpendicular to the nanowire axis, with an enhancement of the perpendicular magnetic remanence and a drastic fall in the coercive field in the parallel direction to the nanowire axis (Figure 3.36). In this sample, the separation between the wider segments is represented in Figure 3.33c, where the separation is proportionally reduced regarding the sample represented by Figure 3.33b. Moreover, the proportion of segment having perpendicular anisotropy takes up to 45% of the total nanowire length, which is approximately 30% higher than for the exponential HA pulses sample template. From a magnetic point of view, this system can be thought as an array of vertical pillars intercalated by virtually continuous horizontal planes. The magnetostatic interaction between the segments with wider diameters is therefore stronger than the other contribution.

The angular dependence on the magnetic hysteresis loops has been also studied in order to deepen the understanding of the magnetic anisotropies of the Co nanowires (*Figure 3.37*).

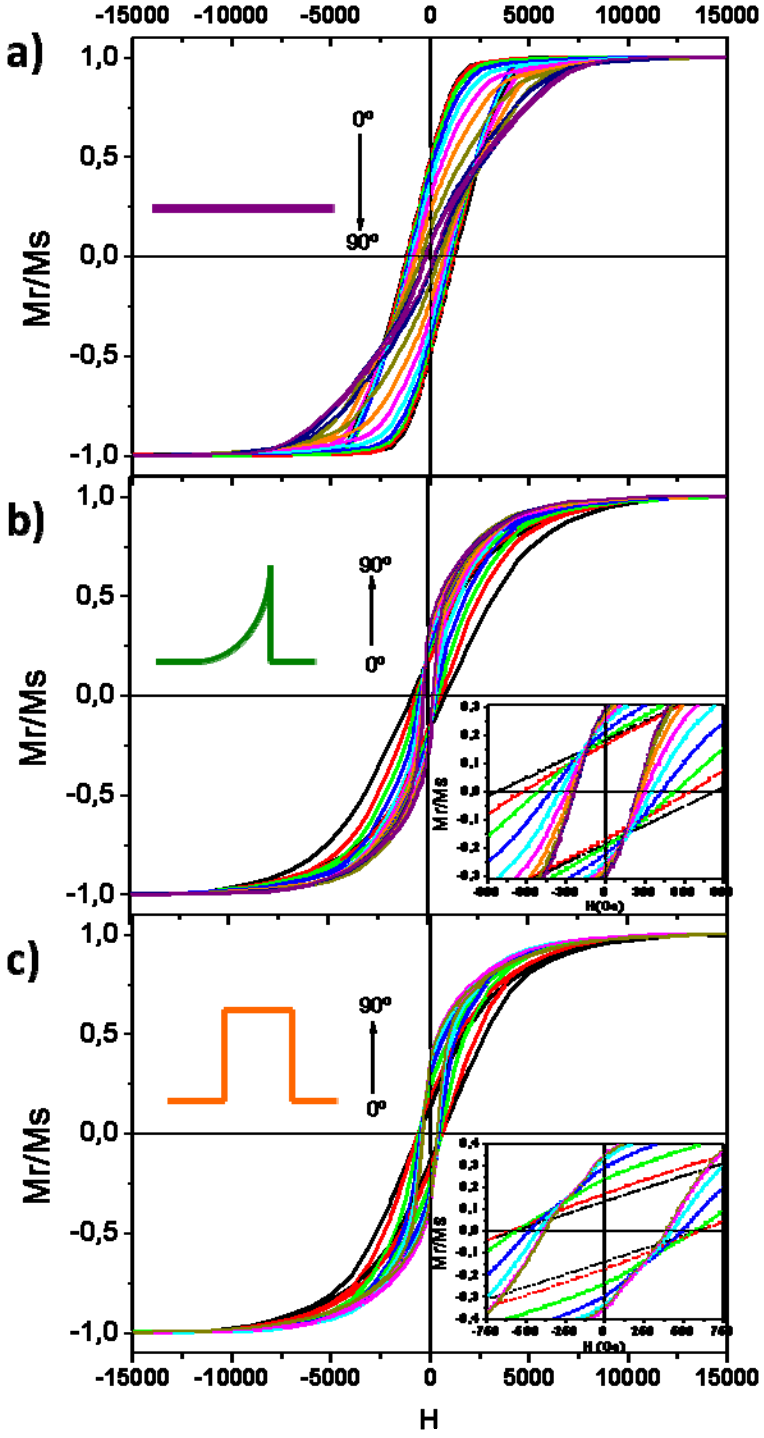

Figure 3.37: Angular dependence of the hysteresis loops for Co nanowires grown in NAAM templates grown with a) uniform pore diameter; PA section with b) exponential and c) squared HA pulses modulated nanowires.

These results are summarized in Figure 3.38, where the value of the coercive field and remanent magnetization moment normalized to the saturation magnetic moment as function of the measuring angle are compared. The results indicate the presence of uniaxial anisotropy

within the nanowires, the strength of which decreases as the volume and size of the modulated segments is increased.

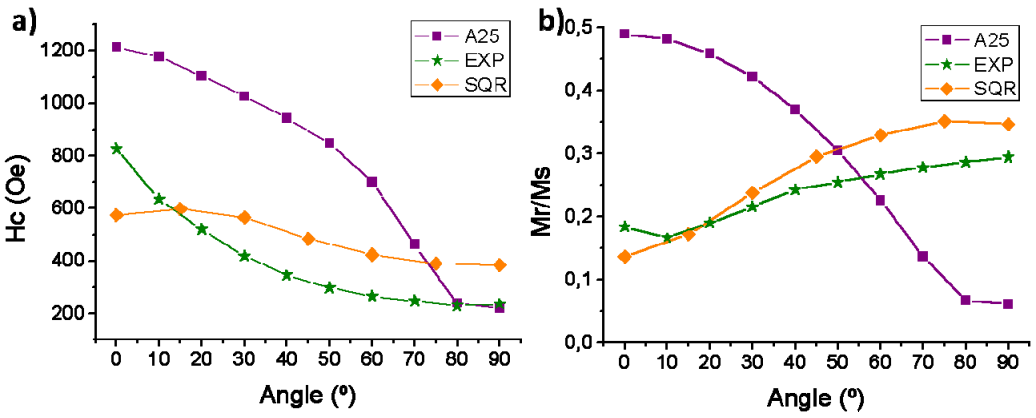

Figure 3.38: a) Coercive field and b) Normalized remanent magnetic moment for Co nanowires grown in NAAM templates grown with a) uniform pore diameter; PA section with b) exponential and c) squared HA pulses modulated nanowires.

3.7. Summary.

In this chapter, we have broached the topic of Hard Anodization in two different ways.

In first place, we have performed a series of anodizations in sulphuric acid based electrolytes by applying 25V during 4 hours, and afterwards we have increased the applied voltage up to 60V at a rate of 0.7V/min. Both, anodic alumina barrier layer side and nanopatterned Aluminium substrate has been broadly morphological characterized. Starting from SCI we could measure distances from center to centre and we observed a high orderd.

We could observe the tubular morphology of the anodic alumina grown under Hard anodization conditions. Moreover, we could observe sudden distortion of straight and ordered nanotubes. This could be due to internal mechanical stress, but further insights are needed for understand this phenomena.

Sencondly, a deep study in the so called Pulsed anodization which consist of periodically and controlled alternation of MA and HA pulses. The length and applied voltage of the pulses can be tuned, as well as shape, offering a broad range of possiblilities.

By varing these parameters we have obtained different diameters, lengths of the segments and compositions of anodic alumina belonging to each kind of pulses.Finally we have used this modulated walls to fabricate and characterize Co nanowires replicating the modulations.

References

1. Csokán, P., *Hard anodizing: Studies of the relation between anodizing conditions and the*

growth and properties of hard anodic oxide coatings. Electroplat. Metal Finish. , 1962. **15**: p. 75–82.
2. Csokán, P., *Some observations on the growth mechanism of hard anodic oxide coatings on*

aluminium. Trans. Inst. Metal Finishing 1964. **41**: p. 51–56.
3. Pu, L., et al., *Individual alumina nanotubes.* Angewandte Chemie-International Edition, 2001. **40**(8): p. 1490-+.
4. Mei, Y.F., et al., *Formation mechanism of alumina nanotube array.* Physics Letters A, 2003. **309**(1-2): p. 109-113.
5. Chu, S.Z., et al., *Fabrication of ideally ordered nanoporous alumina films and integrated alumina nanotubule arrays by high-field anodization.* Advanced Materials, 2005. **17**(17): p. 2115-+.
6. Zhao, S.Y., et al., *Novel structure of AAO film fabricated by constant current anodization.* Advanced Materials, 2007. **19**(19): p. 3004-+.
7. Lee, W., et al., *Fast fabrication of long-range ordered porous alumina membranes by hard anodization.* Nature Materials, 2006. **5**(9): p. 741-747.
8. Lee, W., et al., *Structural engineering of nanoporous anodic aluminium oxide by pulse anodization of aluminium.* Nature nanotechnology, 2008. **3**(4): p. 234-239.
9. Li, A.P., et al., *Hexagonal pore arrays with a 50-420 nm interpore distance formed by self-organization in anodic alumina.* Journal of Applied Physics, 1998. **84**(11): p. 6023-6026.
10. Li, A.P., et al., *Polycrystalline nanopore arrays with hexagonal ordering on aluminum.* Journal of Vacuum Science & Technology a-Vacuum Surfaces and Films, 1999. **17**(4): p. 1428-1431.
11. Schwirn, K., et al., *Self-ordered anodic aluminum oxide formed by H2SO4 hard anodization.* ACS nano, 2008. **2**(2): p. 302-310.
12. Mínguez-Bacho, I., et al., *Self-correlation function for determination of geometrical parameters in Nanoporous Anodic Alumina Films.* Applied Physics A: Materials Science & Processing, 2012. **106**(1): p. 105-112.
13. Nielsch, K., et al., *Self-ordering regimes of porous alumina: The 10% porosity rule.* Nano Letters, 2002. **2**(7): p. 677-680.
14. Houser, J.E. and K.R. Hebert, *The role of viscous flow of oxide in the growth of self-ordered porous anodic alumina films.* Nature Materials, 2009. **8**(5): p. 415-420.
15. Li, Y., et al., *Novel AAO films and hollow nanostructures fabricated by ultra-high voltage hard anodization.* Chemical Communications, 2010. **46**(2): p. 309-311.
16. Lee, W., J.C. Kim, and U. Gosele, *Spontaneous Current Oscillations during Hard Anodization of Aluminum under Potentiostatic Conditions.* Advanced Functional Materials, 2010. **20**(1): p. 21-27.
17. Li, Y.B., et al., *Fabrication of highly ordered nanoporous alumina films by stable high-field anodization.* Nanotechnology, 2006. **17**(20): p. 5101-5105.
18. Almasi Kashi, M., et al., *Optimum self-ordered nanopore arrays with 130-270nm interpore distances formed by hard anodization in sulfuric/oxalic acid mixtures.* Journal of Physics D-Applied Physics, 2007. **40**: p. 7032-7040.
19. Kashi, M.A., et al., *Fabrication of Self-Ordered Nanoporous Alumina with 69-115 nm Interpore Distances in Sulfuric/Oxalic Acid Mixtures by Hard Anodization.* Japanese Journal of Applied Physics, 2010. **49**(1).

20. Li, Y.B., M.J. Zheng, and L. Ma, *High-speed growth and photoluminescence of porous anodic alumina films with controllable interpore distances over a large range.* Applied Physics Letters, 2007. **91**(7).
21. Lee, W., R. Scholz, and U. Gosele, *A continuous process for structurally well-defined Al2O3 nanotubes based on pulse anodization of aluminum.* Nano Letters, 2008. **8**(8): p. 2155-2160.
22. Lee, W. and J.C. Kim, *Highly ordered porous alumina with tailor-made pore structures fabricated by pulse anodization.* Nanotechnology, 2010. **21**(48).
23. Losic, D. and M. Lillo, *Porous Alumina with Shaped Pore Geometries and Complex Pore Architectures Fabricated by Cyclic Anodization.* Small, 2009. **5**(12): p. 1392-1397.
24. Losic, D., *Preparation of Porous Anodic Alumina with Periodically Perforated Pores.* Langmuir, 2009. **25**(10): p. 5426-5431.
25. Pitzschel, K., et al., *Controlled Introduction of Diameter Modulations in Arrayed Magnetic Iron Oxide Nanotubes.* ACS nano, 2009. **3**(11): p. 3463-3468.
26. Pitzschel, K., et al., *Magnetic reversal of cylindrical nickel nanowires with modulated diameters.* Journal of Applied Physics, 2011. **109**(3).
27. Sulka, G.D. and K. Hnida, *Distributed Bragg reflector based on porous anodic alumina fabricated by pulse anodization.* Nanotechnology, 2012. **23**(7).
28. Masuda, H., F. Hasegwa, and S. Ono, *Self-ordering of cell arrangement of anodic porous alumina formed in sulfuric acid solution.* Journal of the Electrochemical Society, 1997. **144**(5): p. L127-L130.
29. Gaston-Garcia, B., et al., *Local Burning Phenomena in Sulfuric Acid Anodizing: Analysis of Porous Anodic Alumina Layers on AA1050.* Electrochemical and Solid State Letters, 2010. **13**(11): p. C33-C35.
30. Montero-Moreno, J.M., M. Sarret, and C. Mueller, *Self-ordered porous alumina by two-step anodizing at constant current: Behaviour and evolution of the structure.* Microporous and Mesoporous Materials, 2010. **136**(1-3): p. 68-74.
31. Garcia-Vergara, S.J., et al., *A flow model of porous anodic film growth on aluminium.* Electrochimica Acta, 2006. **52**(2): p. 681-687.
32. Jessensky, O., F. Muller, and U. Gosele, *Self-organized formation of hexagonal pore arrays in anodic alumina.* Applied Physics Letters, 1998. **72**(10): p. 1173-1175.
33. Ono, S., H. Ichinose, and N. Masuko, *DEFECTS IN POROUS ANODIC FILMS FORMED ON HIGH-PURITY ALUMINUM.* Journal of the Electrochemical Society, 1991. **138**(12): p. 3705-3710.
34. Macdonald, D.D., *ON THE FORMATION OF VOIDS IN ANODIC OXIDE-FILMS ON ALUMINUM.* Journal of the Electrochemical Society, 1993. **140**(3): p. L27-L30.
35. Thompson, G.E. and G.C. Wood, *Porous anodic film formation on aluminium.* Nature, 1981. **290**(5803): p. 230-232.
36. Hoar, T.P. and N.F. Mott, *A MECHANISM FOR THE FORMATION OF POROUS ANODIC OXIDE FILMS ON ALUMINIUM.* Journal of Physics and Chemistry of Solids, 1959. **9**(2): p. 97-99.
37. Thompson, G.E., et al., *Nucleation and growth of porous anodic films on aluminium.* Nature, 1978. **272**(5652): p. 433-435.
38. Thompson, G.E., et al., *ANODIC-OXIDATION OF ALUMINUM.* Philosophical Magazine B-Physics of Condensed Matter Statistical Mechanics Electronic Optical and Magnetic Properties, 1987. **55**(6): p. 651-667.
39. Garcia-Vergara, S.J., et al., *Tracer studies relating to alloying element behaviour in porous anodic alumina formed in phosphoric acid.* Electrochimica Acta, 2010. **55**(9): p. 3175-3184.
40. Garcia-Vergara, S.J., et al., *Mechanical instability and pore generation in anodic alumina.* Proceedings of the Royal Society A: Mathematical, Physical and Engineering Science, 2006. **462**(2072): p. 2345-2358.

41. Garcia-Vergara, S.J., et al., *Tracer studies of anodic films formed on aluminium in malonic and oxalic acids.* Applied Surface Science, 2007. **254**(5): p. 1534-1542.
42. Garcia-Vergara, S.J., et al., *Stress generated porosity in anodic alumina formed in sulphuric acid electrolyte.* Corrosion Science, 2007. **49**(10): p. 3772-3782.
43. Skeldon, P., et al., *A tracer study of porous anodic alumina.* Electrochemical and Solid State Letters, 2006. **9**(11): p. B47-B51.
44. Hebert, K.R., et al., *Morphological instability leading to formation of porous anodic oxide films.* Nat Mater, 2012. **11**(2): p. 162-166.
45. Vrublevsky, I., et al., *Effect of the current density on the volume expansion of the deposited thin films of aluminum during porous oxide formation.* Applied Surface Science, 2003. **220**(1-4): p. 51-59.
46. Vrublevsky, I., et al., *The study of the volume expansion of aluminum during porous oxide formation at galvanostatic regime.* Applied Surface Science, 2004. **222**(1-4): p. 215-225.
47. Zhou, F., et al., *Volume expansion factor and growth efficiency of anodic alumina formed in sulphuric acid.* Journal of the Electrochemical Society, 2011. **158**(6): p. C202-C214.

Chapter 4. Growth of ZnO nanostructures on NAAF and FTO templates. Solar energy application for Hydrogen generation.

4.1. Introduction.

ZnO is a wide band gap semiconductor (3.3 eV) with very attractive properties which make it a suitable for many applications [1]. Some of the most extended fabrication techniques are vapour-liquid-solid, which in the case of ZnO growth are necessary elevated temperatures between 800 and 950 °C [2, 3]; electrochemical deposition on templates like NAAF [4, 5], or solution growth [6-8]. ZnO growth can be controlled by mean of several fabrication techniques and its parameters, being possible obtaining many kinds of nanostructure with different names in function of their shape, such as nanorods, nanowires, nanobelts, nanospirals, nanohelixes, nanorings or hierarchical nanostructures.

In this work we have centred our attention in the solution growth technique, particularly in the hydrothermal growth [9]. This low-cost and simple method is candidate for mass production of oxide materials [10, 11].

Among all the potential applications which ZnO have, for our work it is of special interest the Photolectrochemical cell (PEC) application [12]. This interest comes from the increasing necessity of low cost and non-pollutant energy sources, since the conflictive situations which the countries with petroleum are involved, moreover, in order to avoid the global warming and greenhouse effect. Hydrogen presents an alternative to fossil fuels. It can be obtained from water which is a plentiful energy resource by splitting the molecule. However, this is not a thermodynamically spontaneous process.

$$2H_2O \xrightarrow{light} O_2 + 2H_2; \quad \Delta G \approx 237.2\ KJ/mol$$

For the splitting of the water molecule it is necessary to apply 1.23 V. This is possible without apply external voltage by illuminating a PEC with solar light, another plentiful source. A schematic diagram of the photoelectrochemical water splitting process is shown in *Figure 4.1*. The harvested photons with energy equal or above the energy gap, (i.e. in the case of ZnO, 3.3 eV) are absorbed by the semiconductor exciting electron from the valence band to the conduction band. Then, the electron goes through the circuit till the counter electrode, which

is a metallic electrode, where the reduction of water takes place and the hydrogen is produced in gas form as shows the reaction.

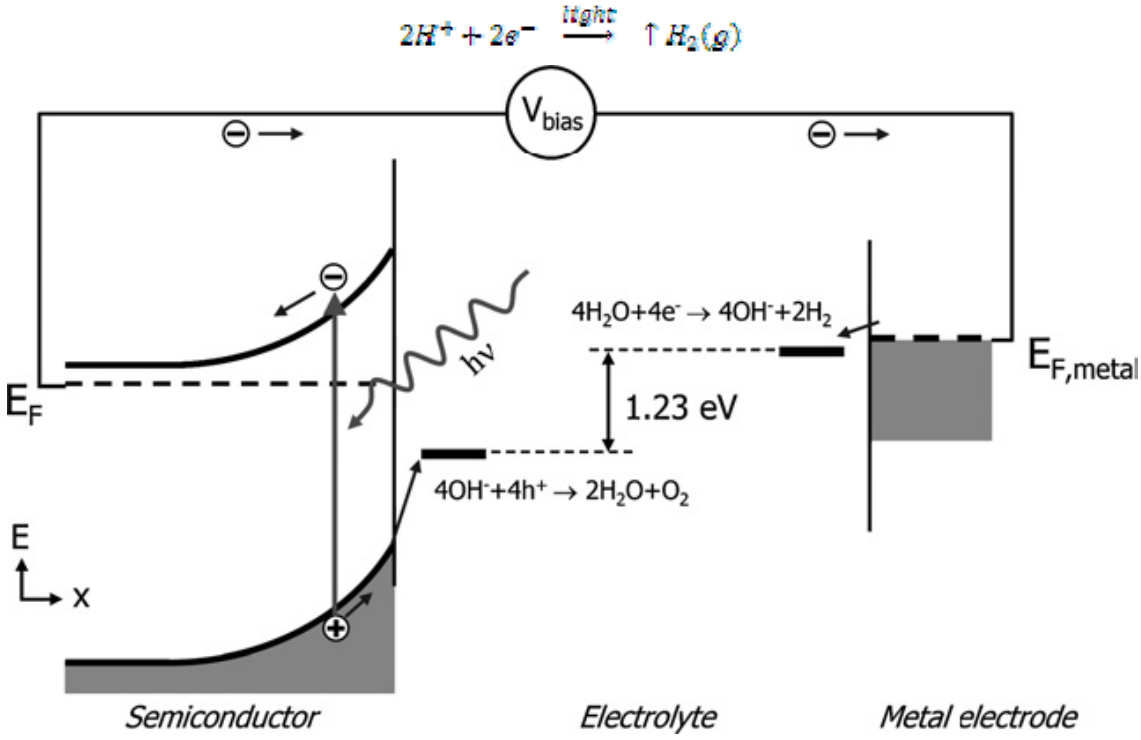

Figure 4.1: Energy diagram of a PEC cell for water splitting with a n-type semiconductor playing the role of photoanode [13].

On the other hand, the electron-hole created in the valence band goes to the surface of the semiconductor where oxidizes the water, as explained in the next reaction.

$$2H_2O \xrightarrow{light} O_2 + 4H^+ + 4e^-$$

Being the overall reaction as follows:

$$2H_2O \xrightarrow{light} O_2 + 2H_2 \qquad \Delta E = -1.23\,eV$$

So, the employed semiconducting materials must be capable to reproduce this equation. For that, Antonio Currao set these three requirements for any system harvesting and converting solar energy into chemical energy: a) the photoresponse of the system must optimally match the solar spectrum; b) photoexcited charges must be separated efficiently to prevent recombination; c) the charges must have sufficient energy to carry out the desired chemical reactions such as water splitting.

We cannot forget that the band gap of the material determines the range of spectral region which the semiconductor absorbs light. In our case, the ZnO absorbs light below 385 nm, so if we take a look at the intensity of the sun light for AM1.5 conditions [14], the absorbed light by ZnO is only about 5% of the spectra (i.e. Ultra-Violet range) (see *Figure 4.2*).

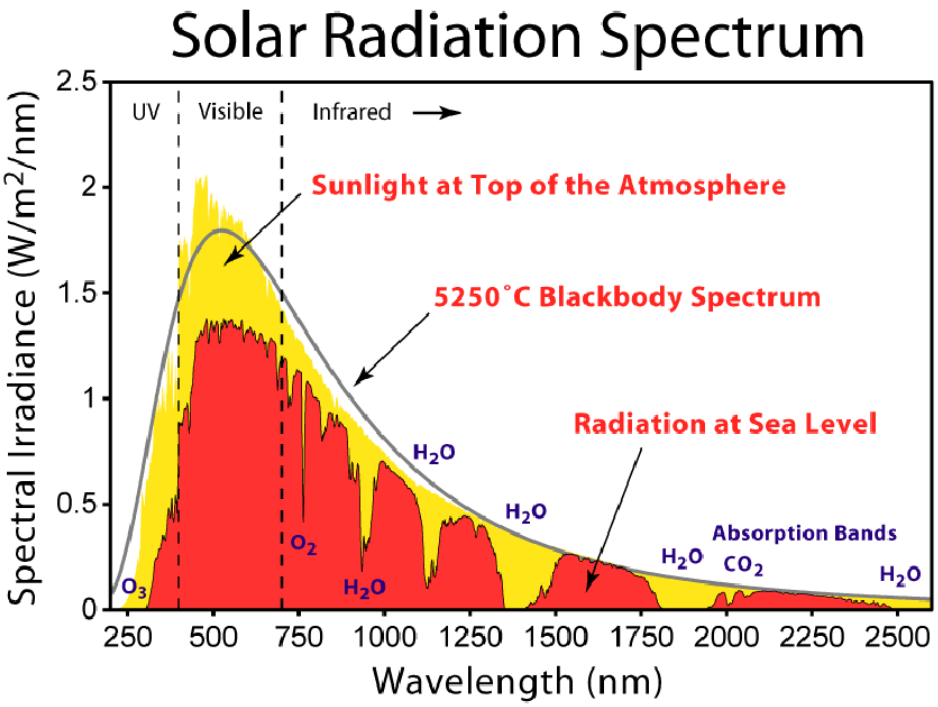

Figure 4.2: Solar radiation spectrum. The red spectrum is the radiation under AM1.5 conditions.

So, in order to increase the light range absorbable by the photoanode to the visible light, it is necessary that semiconductors such as ZnO and TiO_2 are coupled with other semiconductors such as CdS, CdSe ZnSe or ZnS [15-17]. In this way, the carriers density increase considerably. A schematic diagram of the band structures for CdS on ZnO is presented in Figure 4.3.

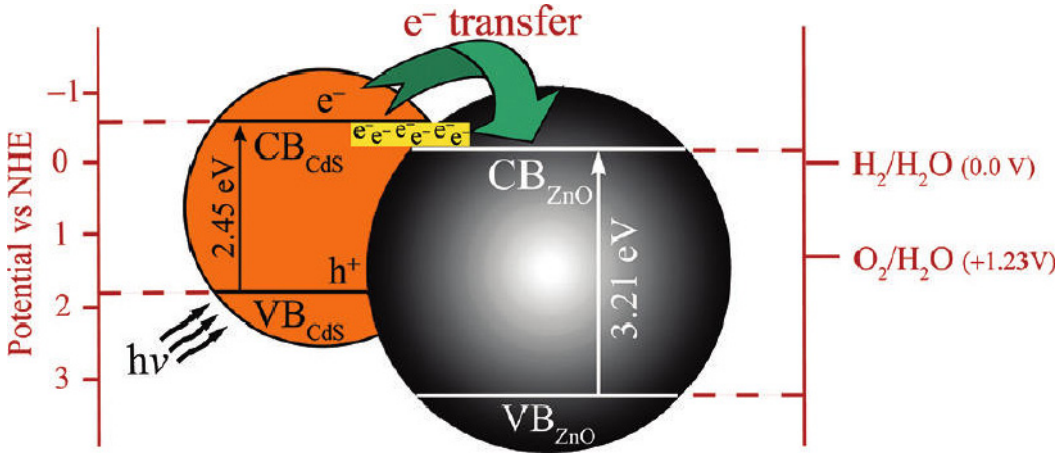

Figure 4.3: Schematic diagram of the structure band for coupling CdS/ZnO [18].

On the other hand, another key factor the order and vertical arrangement of the nanostructures, since it provides a higher interfacial area for light harvesting and increases the efficiency of the carriers transportation [19].

In the present work, we show different methods for ZnO nanowires fabrication although not fully successfully. Hence, we have tried an alternative way for synthesizing ZnO nanostructures.

4.2. Electrochemical routes to fabrication of 1D ZnO nanostructures on NAAF templates.

Several attempts to fabricate ZnO nanostructures have been carried out by using a wide range of techniques offering also different possibilities of structures, as nanowires, clusters, replicating nanostructures of NAAF hexagonal patterns or nanorods.

4.2.1. Electrodepostion of metallic Zn nanowires into NAAF template and subsequent thermal annealing.

One of the methods we have used to obtain 1D nanostructured ZnO is based in pulsed electrodeposition of metallic Zn in NAAF and subsequent annealing in order to oxide it [4]. In addition transition metals, as Mn in this case, were also used for the fabrication of nanowires. NAAF were grown under traditional oxalic acid conditions [20-23] by using the two step anodization method previously described in chapter 1 and the barrier layer were prepared for electroplating . The electrolytes were composed by aqueous solutions with 0.3 M $Zn(SO_4)\cdot 7H_2O$ and 0.4 M H_3BO_4 for pure metallic Zn electrodeposition and 0.4 M $ZnCl_2.4H_2O$, 0.4 M H_3BO_4 and 1.1 M $MnCl_2\cdot 4H_2O$ for metallic Zn:Mn electrodeposition. In the first case, the applied galvanostatic pulses were of 40 mA/cm^2, and for Mn addition, 40 and 130 mA/cm^2, while the potentiostatic pulse was set to 0V. Thermal annealing was carried out in a oven with air atmosphere by applying the following three stages with heating rate of 5 °C/min.: 1º: from room temperature to 100 °C during 30 minutes at heating rate; 2º: from 100 °C to 240 °C during 60 minutes; from 240 °C to 400 °C during 46 hours.

X-ray fluorescence (XRF) spectra and Micro X-ray fluorescence (μ-XRF) mapping were performed at the stations ID18 [24] and ID22 [25] in European Synchrotron Radiation Facility

(ESRF). The experiments were carried out by applying an excitation energy beam of 14.4 KeV and 12.0 KeV in ID18 and ID22, respectively.

In *Figure 4.4* is showed the XRF spectrum of an empty NAAF together with that of electrodeposited NAAF with only Zn as precursor in the electrolytic solution. The spectrum shows the K_α and K_β fluorescence lines of Zn. The escape peak coming from the Si(Li) solid state detector of Zn is indicated. These escape peaks appears at 1.72KeV (Si K_α energy) from the detected elements. The XRF spectra also reveal the presence of several elements in the sample such as Ni, Cu, Fe or Cr. The source of these elements can be attributed to different sources, like impurities in the precursors, remains from chemical etching of alumina, and impurities coming from the electrochemical cell where the sample is fabricated.

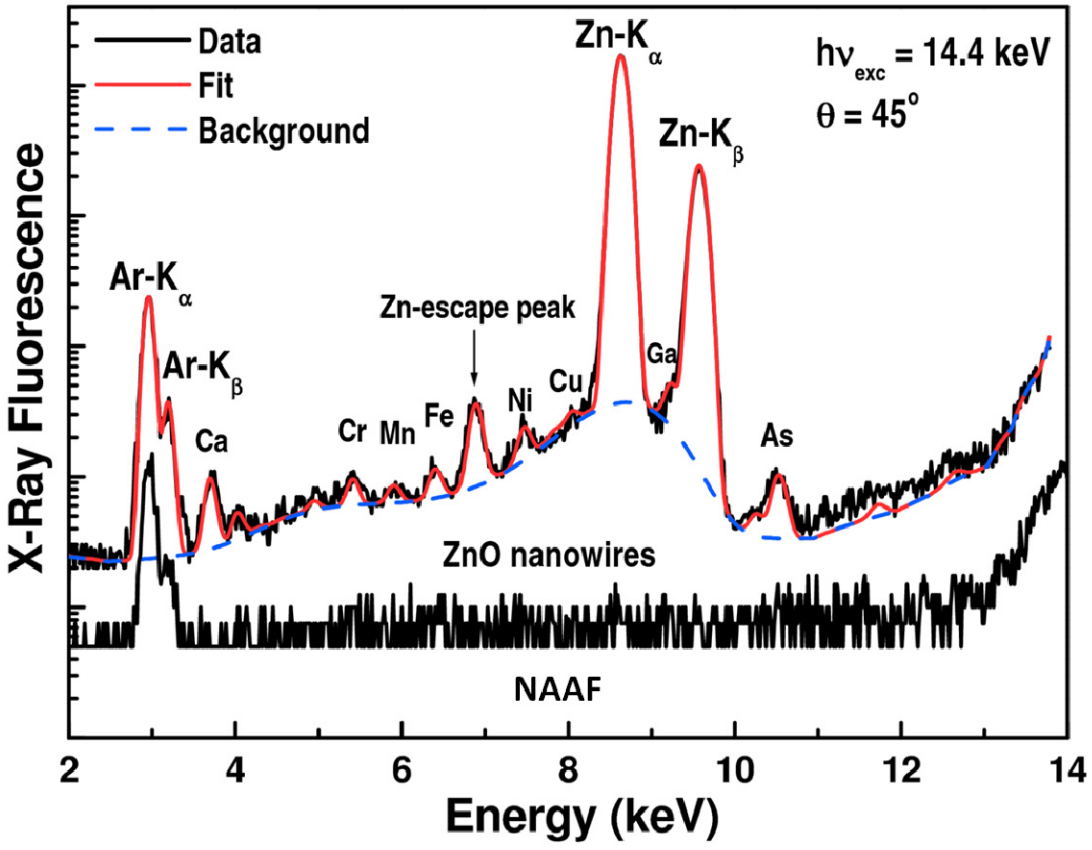

Figure 4.4: X-ray fluorescence spectra of Zn nanowires grown in NAAF template.

In order to confirm that the major elements were incorporated into the crystalline structure, Raman scattering measurements were performed. Figure 4 shows the typical Raman spectrum of ZnO nanowires, where two major bands are centred at 577 and 1152 cm^{-1}, with bandwidths at 30 and 46 cm^{-1}, respectively. These bands are attributed to the Raman A1(LO) phonon scattering and its corresponding overtones since the excitation wavelengths are close to the band gap and an enhancement of the polar A1(LO) mode is expected. Without background

subtraction and under near resonant conditions, the enhancement of the multi-LO phonon scattering of the ZnO nanowires is clearly observed when comparing 363.8 nm and 351.1 nm excitations. Up to now, multiphonon scattering processes have been previously reported for several low-dimensional ZnO systems [26, 27].

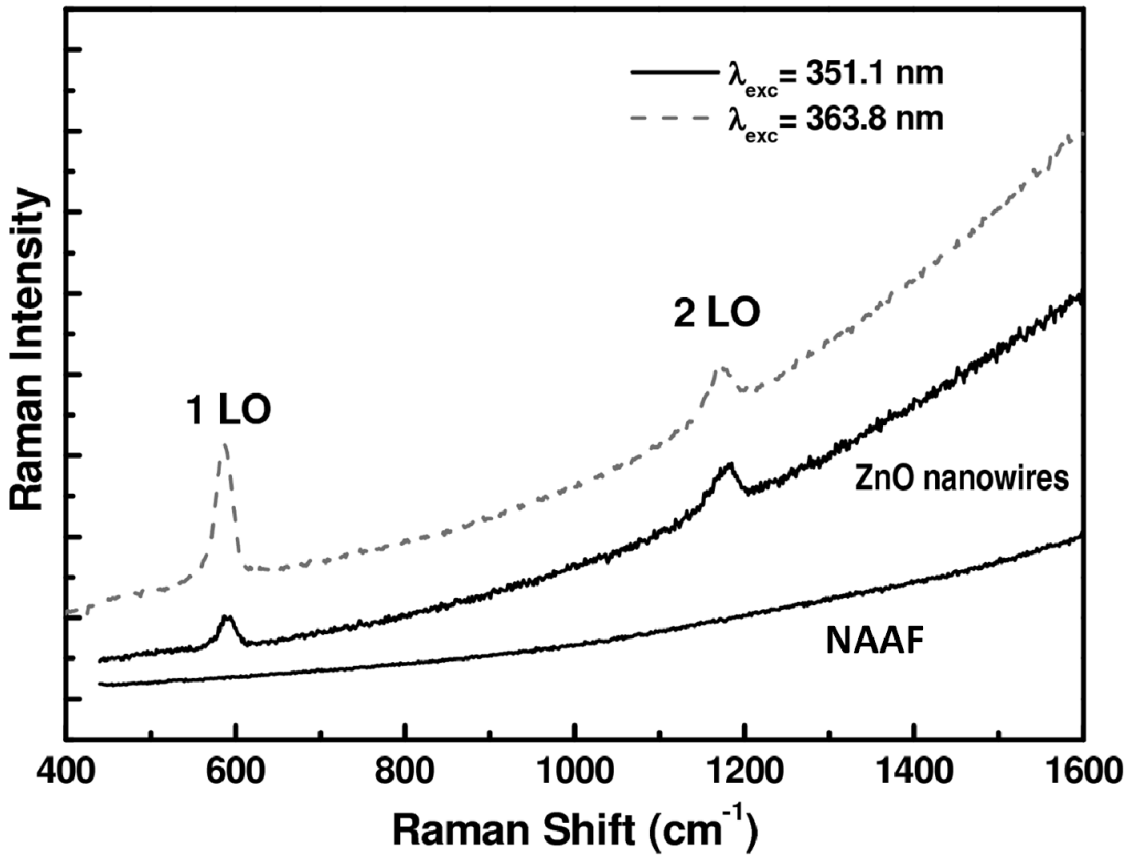

Figure 4.5: Room temperature Raman spectra of empty NAAF template and electrodeposited with ZnO nanowires. The incident wavelengths used are 351.1 and 363.8 nm.

Figure **4.6** shows XRF spectra of empty NAAF and electrodeposited samples with galvanostatic pulses of 130 mA/cm^2 and 40 mA/cm^2. The spectra show the K_α and K_β fluorescence lines of Zn and Mn. The escape peaks coming from the Si(Li) solid state detector of Zn and Mn are also indicated. The XRF spectra also reveal the presence the contaminating elements previously observed in the last case.

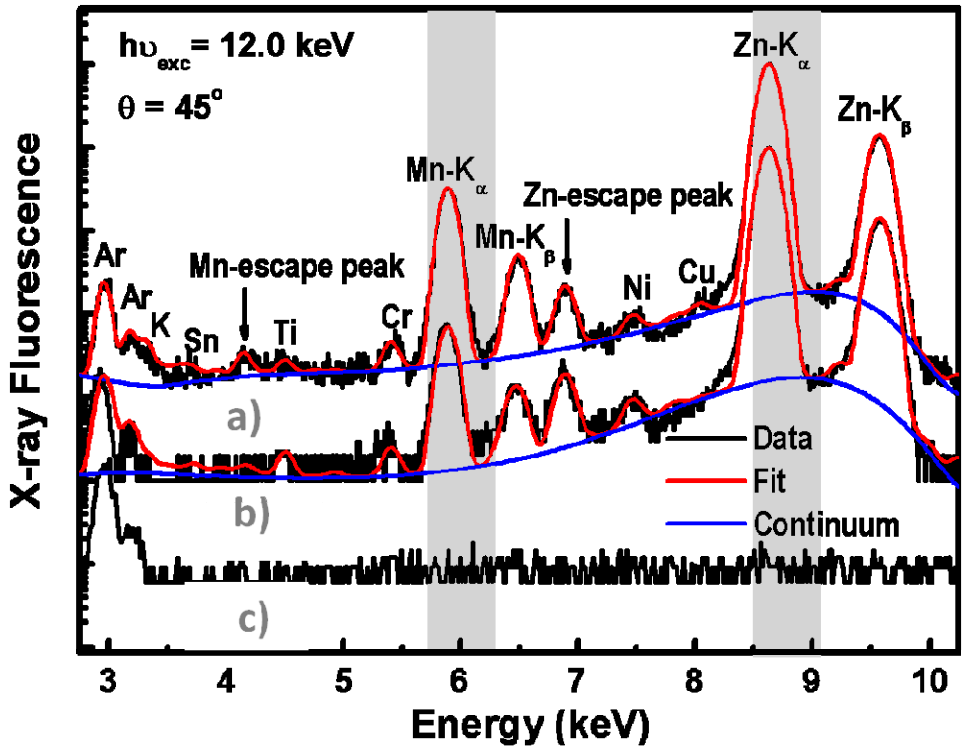

Figure 4.6: X-ray fluorescence spectra of nanowires grown in NAAF template by pulsed electrodeposition with galvanostatic pulses of a) 130 mA/cm^2 and b) 40 mA/cm^2. C) Empty NAAF is shown as reference.

Next, 3D μ-XRF maps are shown in *Figure 4.7*. The pixel size of the map is 0.33X0.33 μm^2 and the dimension maps are 13x5 μm^2. Since the diameter of the pores in these samples is ~40 nm we are not able to observe them individually, but we have a map of the local distribution of the elements. Each pixel represents one measure of fluorescence from which has been selected a region of interest (ROI), in this case, Mn.

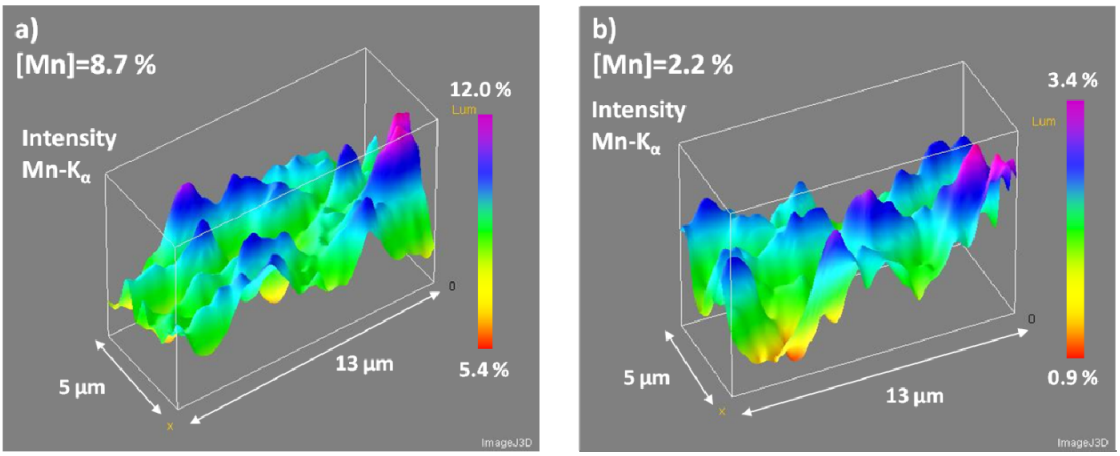

Figure 4.7: Micro X-ray fluorescence maps of Mn content in electrodeposited NAAFs with galvanostatic pulses of a) 130 mA/cm^2 and b) 40 mA/cm^2.

We can observe the local distribution of Mn contents. In the sample electrodeposited with galvanostatic pulses of 130 mA/cm^2 it was found to have an average Mn content of 8.7%, and in the μ-XRF map we observed a variation in the concentration between 5.4% and 12.0%. On the other hand, for the sample grown with pulses of 40 mA/cm^2, the detected Mn content is 2.2%, varying the local concentration between 0.9 and 3.4%.

4.2.2. Electrochemical route for direct synthesis of ZnO nanowires in NAAF template.

Other route we took for fabrication of ZnO nanowire is based on zinc nitrate baths. This precursor of ZnO has higher purity and avoids intermediate steps like thermal annealing to oxide metallic zinc. This method allows the direct synthesis of ZnO in one step.

The electrolyte is an aqueous solution based on $Zn(NO_3)_2{\cdot}6H_2O$, ranging concentrations from 0.01 M up to 0.1 M. The electrochemical processes were carried out at 80 °C, so that, the following reaction could take place:

$$Zn(NO_3)_2 \rightarrow Zn^{2+} + 2NO_3{}^-$$
$$NO_3{}^- + H_2O + 2e^- \rightarrow NO_2{}^- + 2OH^-$$
$$2OH^- + Zn^{2+} \rightarrow \downarrow Zn(OH)_2$$
$$Zn(OH)_2 \xrightarrow{\Delta} ZnO(s) + H_2O$$

The overall reaction would be:

$$Zn^{2+} + 2(NO_3)^- + 2e^- \rightarrow 2NO_2{}^- + ZnO(s) + H_2O$$

As we can deduce from the reaction, the function of the electric part of the process is increasing the concentration of hydroxide ions in the solution, so that, they can react with the zinc ions and forming zinc hydroxide which is meta-stable at this temperature and decompose to ZnO.

The pH of the aqueous solution is very stable along the process. The pH value at 23 °C is 3.90. After heat it up to 80 °C the pH decrease down to 3.70 and after the electrochemical process is 3.55.

We have used NAAFs grown by traditional oxalic acid based electrolyte with pore widening, and sulphuric based electrolytes as we saw in Chapeter 2, A25, B23, C20 and C17. For electrodeposition we also have used both pulsed and potentiostatic electrodeposition (see

sections 1.2.1 and 1.2.2.). Alternatively, we also try to synthesize whitout applying any electrical signal, just by applying temperature up to 80 °C.

In *Figure 4.8* are presented the current and voltage evolution with the number of applied pulses during pulsed electrodepositon. After certain pulses, the electric signals begin to increases drastically and the process is stopped.

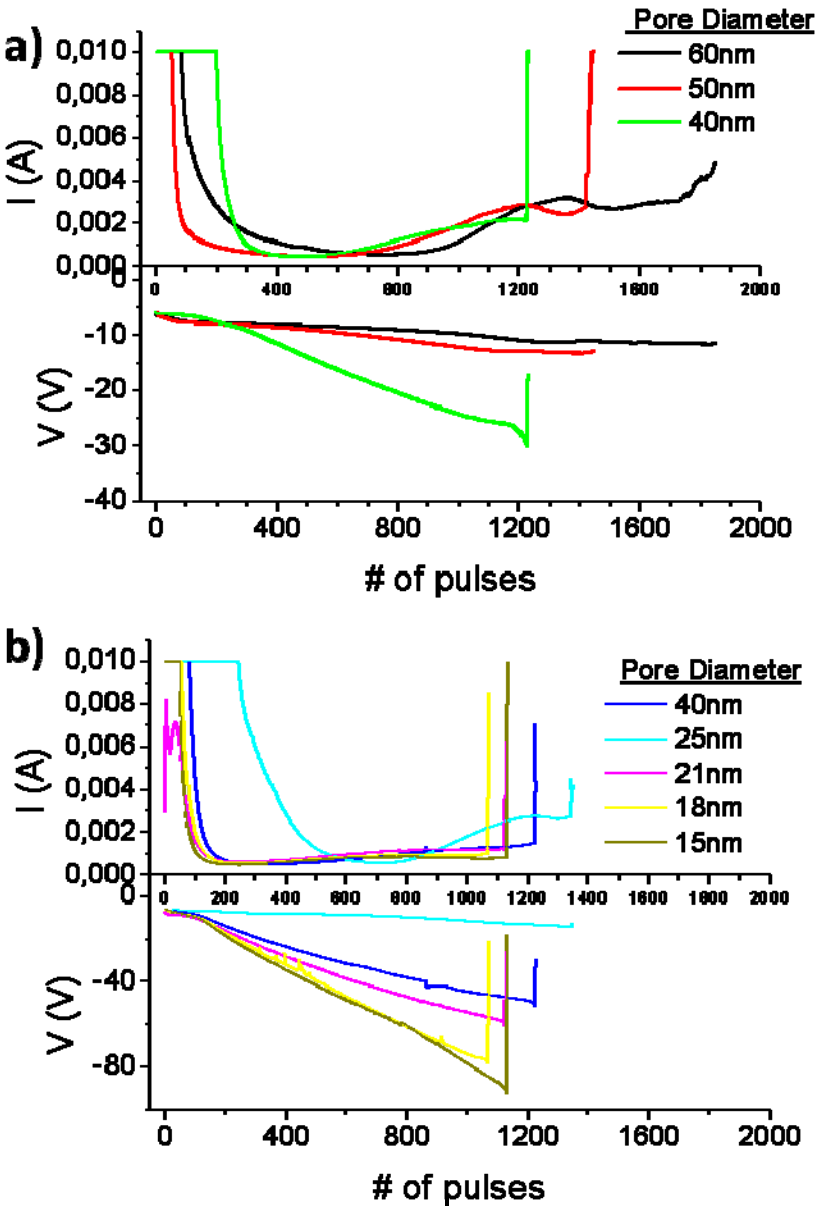

Figure 4.8: Current and voltage evolution with the potentiostatic and galvanostatic pulses. A) Oxalic acid based NAAF with pore widening, b) A25 (pore widening), A25, B23, C20 and C17.

The registered voltages from the galvanostatic pulses show a dependence on the pore diameter of the NAAFs. The wider the pore, the lesser the slope of the electrodeposition voltage.

After SEM characterization we could not observe ZnO nanowires. On the other hand, a thick continuous layer was formed at the top of all the samples, as shown in *Figure 4.9*

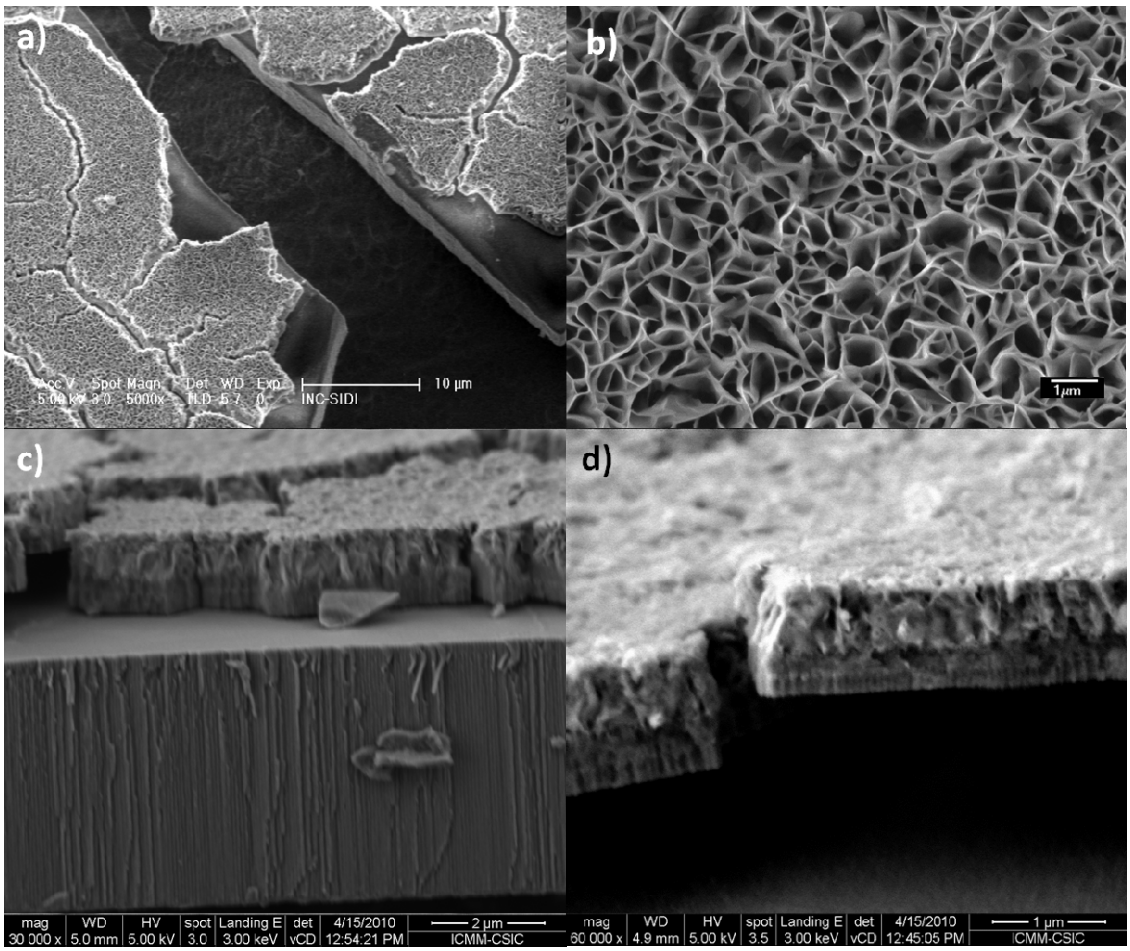

Figure 4.9: SEM micrographs a) and b) shows top view of the surface of the NAAF after electrochemical process. c) and d) cross section SEM micrographs of the layer covering the surface of the NAAF.

The deposited layer is very homogeneous with thickness of ~1µm, and it is formed by very thin sheets or flakes. In *Figure 4.9*c) and d) we can appreciate that the layer has two regions. The upper part is formed by the thin sheets as can be observed in *Figure 4.9*b) , and the lower part is composed by more solid layer and seems to be nanostrutured, replicating the top surface of the NAAF.

After structure characterization by XRD (*Figure 4.10*), we could confirm that the layer is polycrystalline ZnO in wurtzite phase. In the spectrum Aluminium peaks has been also detected and identified.

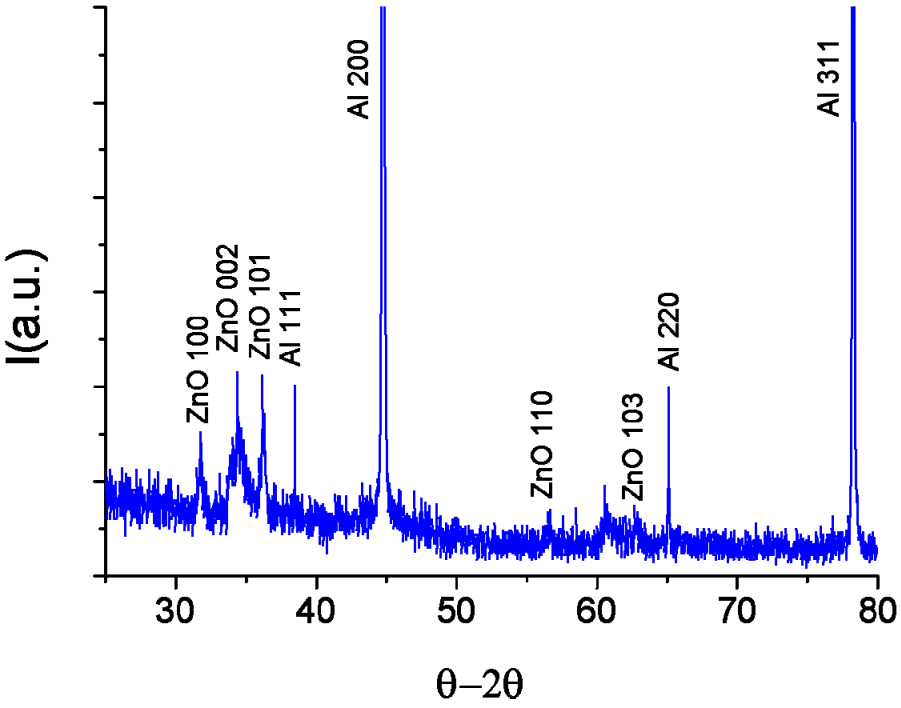

Figure 4.10: XRD spectrum of ZnO layer covering the NAAF surface.

To our opinion, the ZnO layer forming at the top surface impedes the formation of ZnO nanowires from the bottom of the pores. We thought that the layer was formed by precipitation of material during the electrochemical process, so we ideated a system to perform the electrochemical process with the NAAF faced down and avoid possible precipitation on the surface. After some experiments, the ZnO layer still appears. So, we could confirm that it is formed by electrochemical deposition.

Further experiments were carried out. After barrier layer reduction, the dendrites were electroplated with Au expecting to act as a nucleation point for ZnO nanowires, but the layer keeps on forming at the top of the surface.

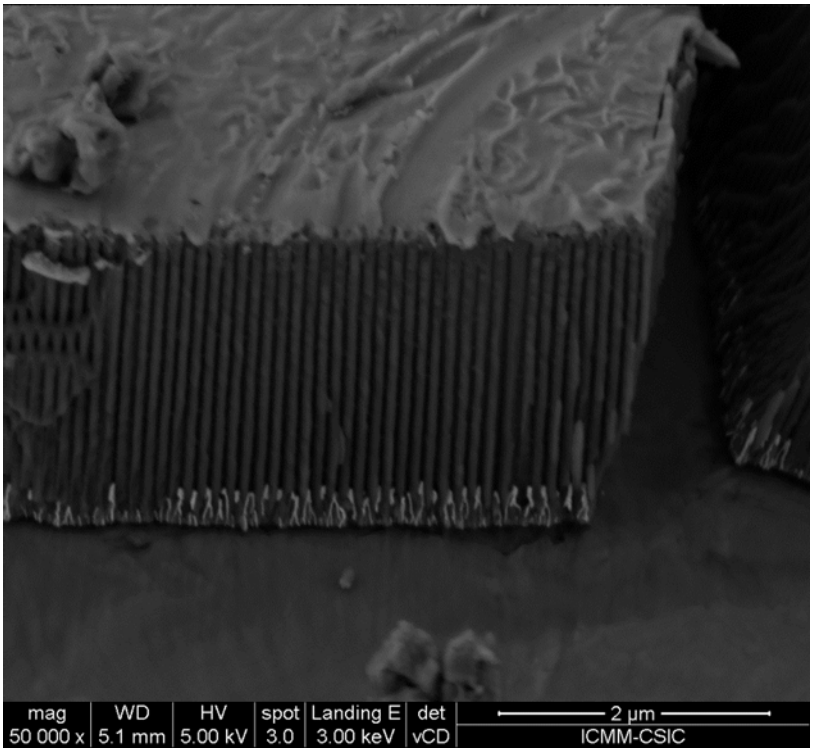

Figure 4.11: Cross section SEM micrograph where the dendrites are electroplated with Au. On the top surface we can observe the incipient ZnO layer.

Other try of ZnO nanowires formation was by potentiostatic electrodeposition. The NAAF was prepared as depicted in section 1.2.2.In this way the electrodeposition requires much less time, so it could be expected that the layer will not be formed, but it was.

However, as previously mentioned, it was found that the lower part of the layer seems to be nanostrutured. So after some characterization, we realize that by removing the layer with an adhesive tape we could find anti-replicating ZnO nanorods, as shown in *Figure 4.12*. As can be appreciated, ZnO nanorods are formed at the top of the NAAF but they do not reach the bottom of the pore, so we can conclude that the ZnO nanorods are not grown as expected, but from the surface of the ZnO layer. In *Figure 4.12*e) and f) we can observe the detached ZnO layer usually covering the surface of the NAAF with the ZnO nanrods.

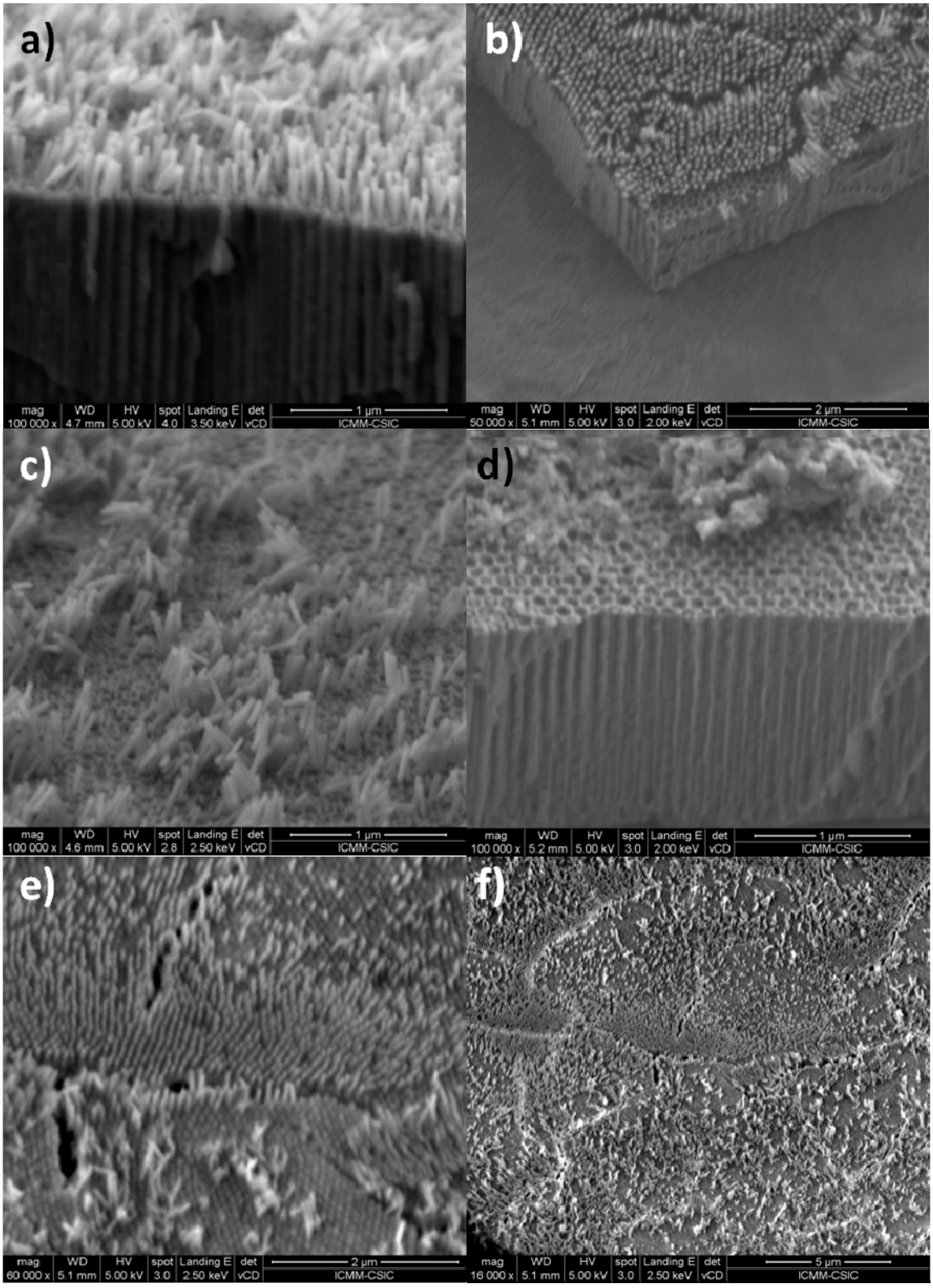

Figure 4.12: SEM micrographs of a), b) and c) ZnO nanorods formed at the top of the NAAF surfaces; d) empty nano-channels; e) and f) ZnO layer detached side surface from the NAAF surface.

4.3. Fabrication and Morphology of ZnO nanorods.

A general description of the hydrothermal growth process is explained in section 1.3.

The reaction of the hydrothermal process is as follows:

$$Zn(NO_3)_2 \rightarrow Zn^{2+} + 2NO_3{}^{-}$$

$$(CH_2)_6N_4 \ + \ 6H_2O \rightarrow 6HCHO \ + \ 4NH_3$$

$$NH_3 + H_2O \rightarrow NH_4{}^{+} \ + OH^{-}$$

$$2OH^{-} \ + \ Zn^{2+} \rightarrow\downarrow Zn(OH)_2 \overset{\Delta}{\rightarrow} ZnO(s) \ + H_2O$$

Although other mechanisms of formation are suggested [11, 28]:

$$Zn^{2+} \ + NH_3 \rightarrow Zn(NH_3)_4{}^{2+}$$

$$Zn(NH_3)_4{}^{2+} + 2OH^{-} \rightarrow\downarrow Zn(OH)_2 \overset{\Delta}{\rightarrow} ZnO(s) \ + NH_3$$

It is clear that the Zinc nitride is the source of Zn ions, but there are some discrepancies about the role of HMT in hydrothermal growth process. On one side, it has been suggested that HMT act mainly as a pH buffer [8]. When the HMT is heated up release hydroxyl ions, OH^-, which reacts with the Zn^{2+} ions to form the ZnO nanorods as shown in the reaction above [29]. But there is other opinion about the contribution of HMT to the ZnO nanorods formation. Sugunan et al. [30] propose that, since HMT is a polymer, their chains will attach to the non polar faces of the ZnO nanorods and leaving free only the polar face [0001]. This implies that the polymer chains would avoid the incorporation of Zn^{2+} ions into the non polar faces, allowing only the growth in the polar face.

Once the experimental process is finished, the solution has turn into a milky liquid with precipitate material on the bottom of the autoclave and on the backside of the template.

After getting the ZnO nanorods, the samples are systematically annealed at 300 °C in air atmosphere during 1 hour in order to improve the stability and remove possible impurities which could prevent the correct CdS coating by SILAR method. A subsequent annealing is carried out in atmosphere composed by Ar (98%) and H_2 (2%) at 400 °C during 1 hour in order to increase the stability and the crystallinity of the CdS coating. The annealing temperature

should not be too much high, since it could affect to the conductive properties of the FTO template.

A schematic diagram is presented in *Figure 4.13*

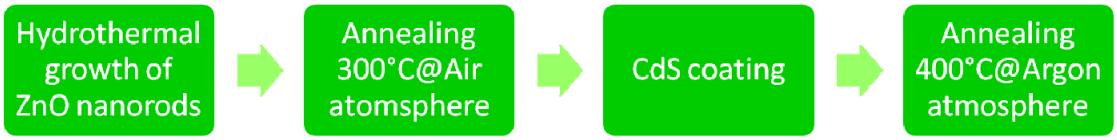

Figure 4.13: Schematic diagram of the process and treatments during fabrication of photoelectrochemical cells.

In *Table 4.1* and are presented the parameters used for the fabrication of these samples and their corresponding micrographs.

Table 4.1: Growth times, precursor concentrations in the promoting growth solution and their respective top-view micrographs after the hydrothermal process carried out at 95 °C. All the micrographs are presented at 50k magnifications.

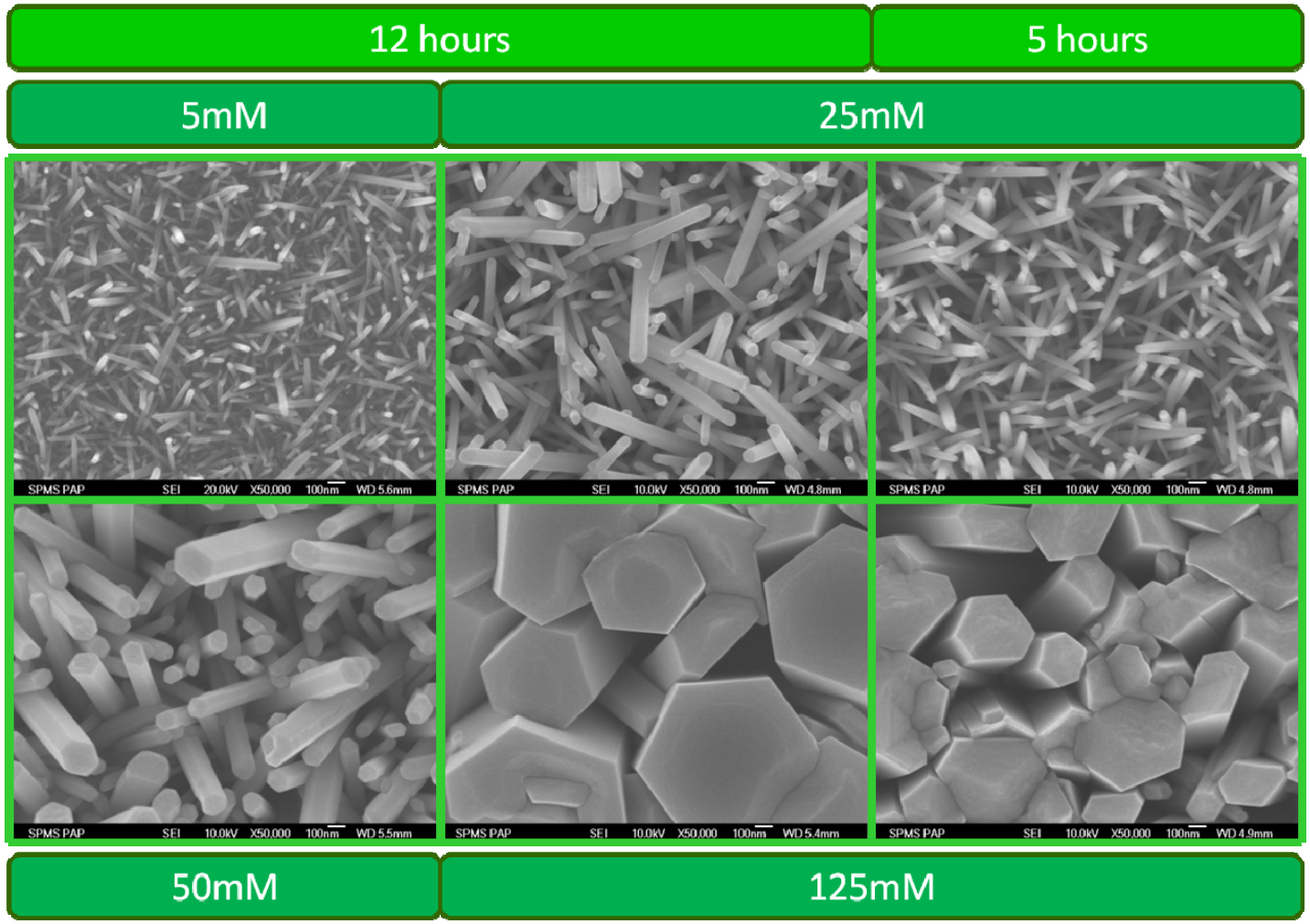

Table 4.2: Cross-section views of ZnO nanorods and the used growth parameters in this section.

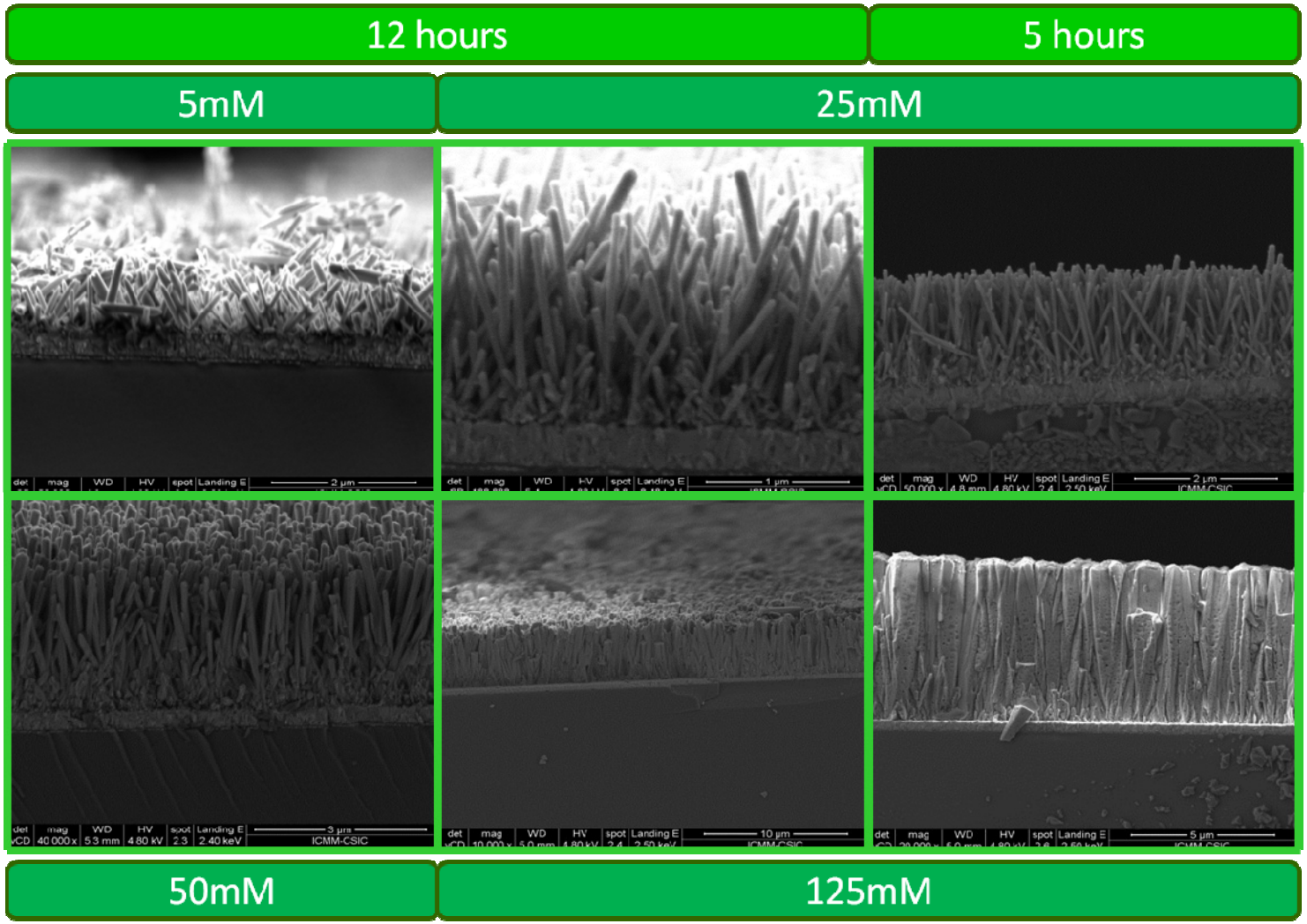

The nanorods were grown in the set-up placed inside the oven at 95 °C in series of 5 and 12 h, by using promoting growth solutions with concentrations of Zinc Nitrate and HMT of 5, 25, 50 and 125 mM. The hexagonal prisms shape of the ZnO nanorods can be observed in the micrographs of *Table 4.1*. It also can be appreciated in *Table 4.2* that as higher is the concentration of the promoting growth solution, the nanorods are more densely packed and as consequence the deviation angle of the nanorods regarding the normal to the surface decrease, i.e. the vertical align gets better. The measured angles in each sample are presented in *Table 4.3*. However, when the used concentration is 125 mM the nanorods are so densely packed that they almost form a continuous film in the bottom part of the growth.

Table 4.3: Angle formed with the normal to the surface of the template, diameter and length of the nanorods grown under these parameters at 95 °C.

	12hours				5 hours	
	5mM	25mM	50mM	125mM	25mM	125mM
Δθ(°)	20±2	14±2	8±1	6±1	14±2	6±1
Average Diameter (nm)	40±10	70±15	150±50	600±250	50±10	450±150
Length (µm)	0.7±0.1	1.6±0.2	2.5±0.2	4.2±0.4	1.5±0.2	4.0±0.4

We also can confirm that the diameters of the nanorods increase with the concentration of the growth promoting solution at a fixed time up to reach a critical diameter where they would form a continuous film of ZnO as showed in *Figure 4.14*.

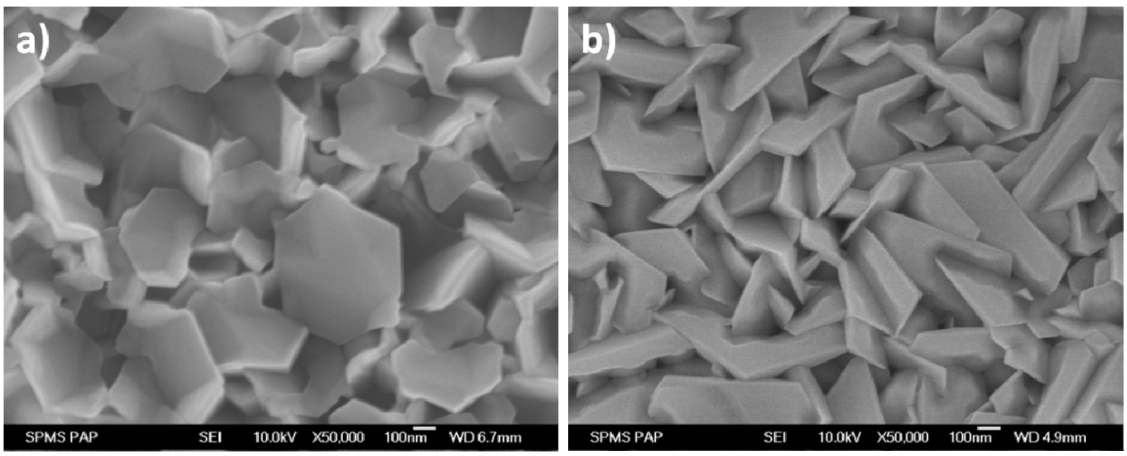

Figure 4.14: Top-view of ZnO grown by hydrothermal method at a) 250 and b) 500 mM concentration of growth promoting solution.

The increase of the diameter reveals an exponential behaviour. However, other publications assume a linear increase with the concentration...

If we compare the samples with same concentration and different times of growth we can observe that there is not much difference between them. Both lengths and formed angle of the nanorods regarding the normal to the surface and are quite similar and it would be almost impossible differentiating between them. However the diameters are slightly narrower for those grown during 5 hours than their counterpart of 12 hours. This reveals that the growth of the nanostructured ZnO mainly takes place within the first 5 hours, and after that, the only geometrical parameter which keeps on growing is the diameter, but very slow rate. During the 8 hours after the first 5, the diameter increase between 35-40%.

From the micrographs presented in *Table 4.1* we can distinguish a wide dispersion of diameters sizes in each sample. It has been observed that the degree of dispersion increase with the concentration of the solution. It can vary from 25% in the case of lower concentration solutions up to 40% for the higher concentration case. On the other hand, the lengths of the nanorods are more or less uniform, but it was also found inhomogeneous thicknesses within the same samples which were grown with the higher concentrated solutions, i.e. 125 mM. In the case of the showed micrograph in *Table 4.2* of sample grown at 125 mM during 5 hours, it presents a variation of 0.5 µm in the thickness and it has been measured thicknesses from 3.8 up to 6 µm. These inhomogeneous thicknesses could be due to the fact that the precipitate material on the bottom of the autoclave prevents homogeneous growth of the ZnO nanorods over the template surface.

We also grew other kind of morphology within the hydrothermal growth method which is the nanotubes formation. After leaving the autoclave cooling down inside the oven during several hours up to reach room temperature, we found the hollow structures as shown in *Figure 4.15*. The formation of this kind of structure is attributed to chemical dissolution in the centre of the nanorod due to an ageing process[31]. The mechanism of formation of ZnO nanorods by hydrothermal growth leads to the polar face will be Zn-terminated, and due to electrostatic interactions the local Zn^{2+}/OH^{-} ratio decrease in the centre of the polar face [0001] leading to a lower growth rate or even localized dissolution in the centre of the nanorod [32], leaving the non-polar faces [01-10] which are more stable [33], as can be observed in the inset of *Figure 4.15*.

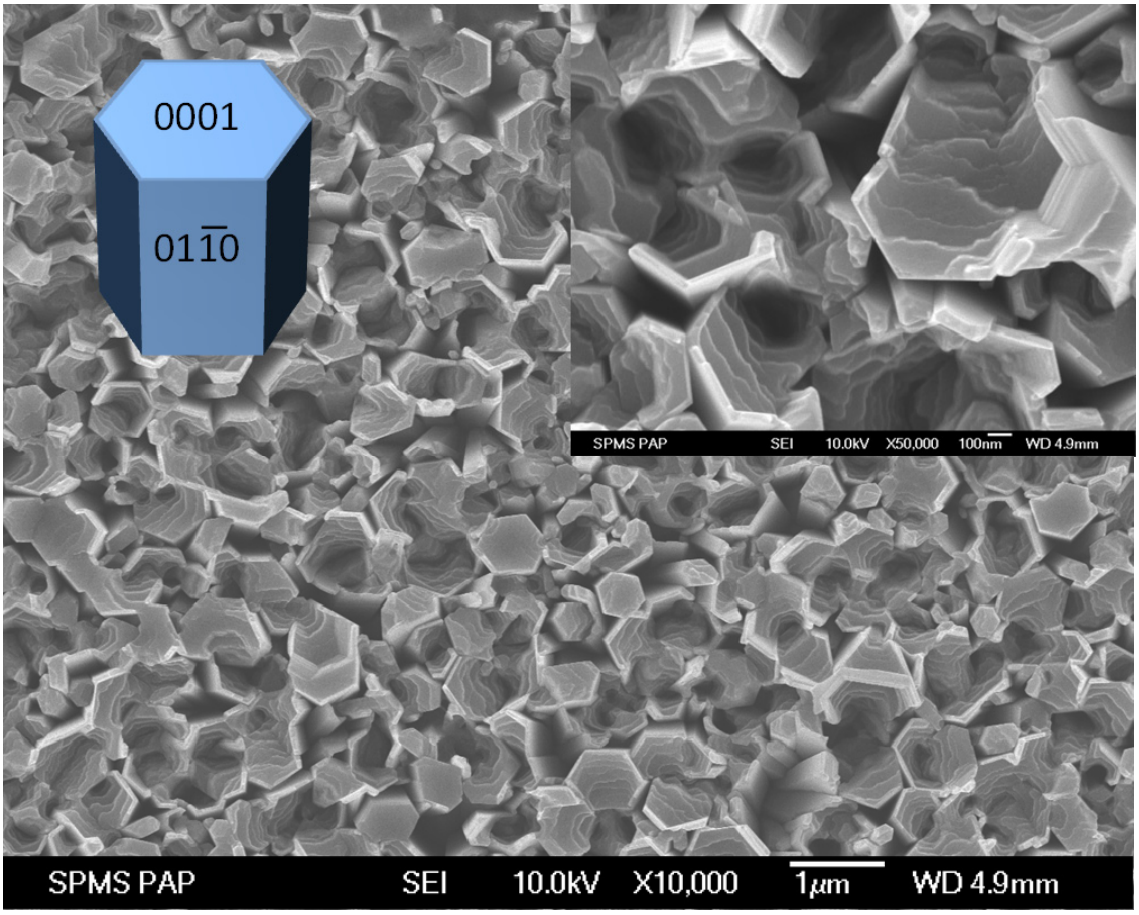

Figure 4.15: SEM micrograph of hollow ZnO nanorods formed after overexposure to the growth promoting solution. In the inset at the right are showed clearly the non-polar planes remaining after the chemical etching. In the left is presented an scheme of the ZnO nanorod morphology with the corresponding facets.

CdS coating.

There are several factors which can affect the deposition of CdS nanoparticles. The immersion time of the substrate with the ZnO nanorods is one of them. The exposure to the precursor solutions should be short but long enough to the reaction takes place. If immersion time is too long the CdS nanoparticles would concentrate at the same positions, forming stack which is a non desirable consequence.

The deposition of CdS nanoparticles can be also influenced by the way we immerse the samples into the different solutions. If we immerse the sample vertically, the penetration depth would be lesser than if we do it horizontally. On the other hand since sediments precipitation of CdS stacks occurs in the solutions after several cycles, the horizontally dip is not recommendable since large CdS aggregates could be attached to the top of the sample.

We performed 10 cycles, as explained in section 1.3.2. by vertically dipping of each sample. Resulting CdS coating is showed in *Figure 4.16*. CdS coating is uniform along the facets of the ZnO nanorods. It could be found nanoparticles accumulation at some points among the nanorods.

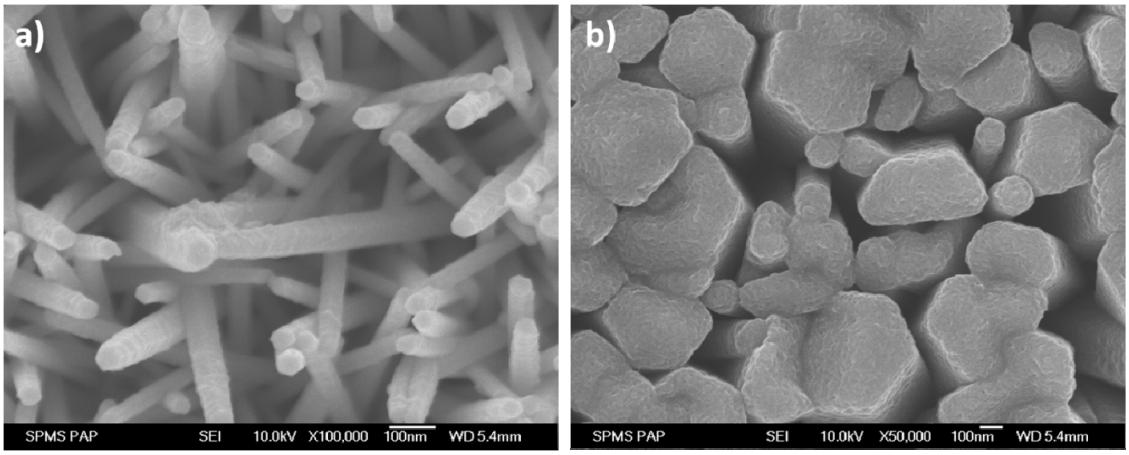

Figure 4.16: SEM micrographs of CdS coating on ZnO nanorods after 10 cycles of SILAR deposition method.

4.4. Structural study of ZnO nanorods and annealing effect.

The X-ray spectra of ZnO nanorods as grown during 12 hours are presented in *Figure 4.14*. From the X-ray diffractogram we can confirm the crystal structure, hexagonal system and typical wurtzite structure of ZnO nanorods grown by hydrothermal method [34] .The peaks which

appear at 31.79° can be ascribed to orientation plane (10-10) , at 34,45° to (0002), at 36,27° to (10-11), at 47,57° to (10.12) and at 62,89° to (10-13). In *Figure 4.17* it is also presented the X-ray pattern coming from the FTO template, which is present in all the spectra of the measured samples, showing tetragonal structure, as was expected. The orientation parameter and the average grain size of the ZnO nanorods are calculated from Scherrer's formulae are presented in *Table 4.4*.

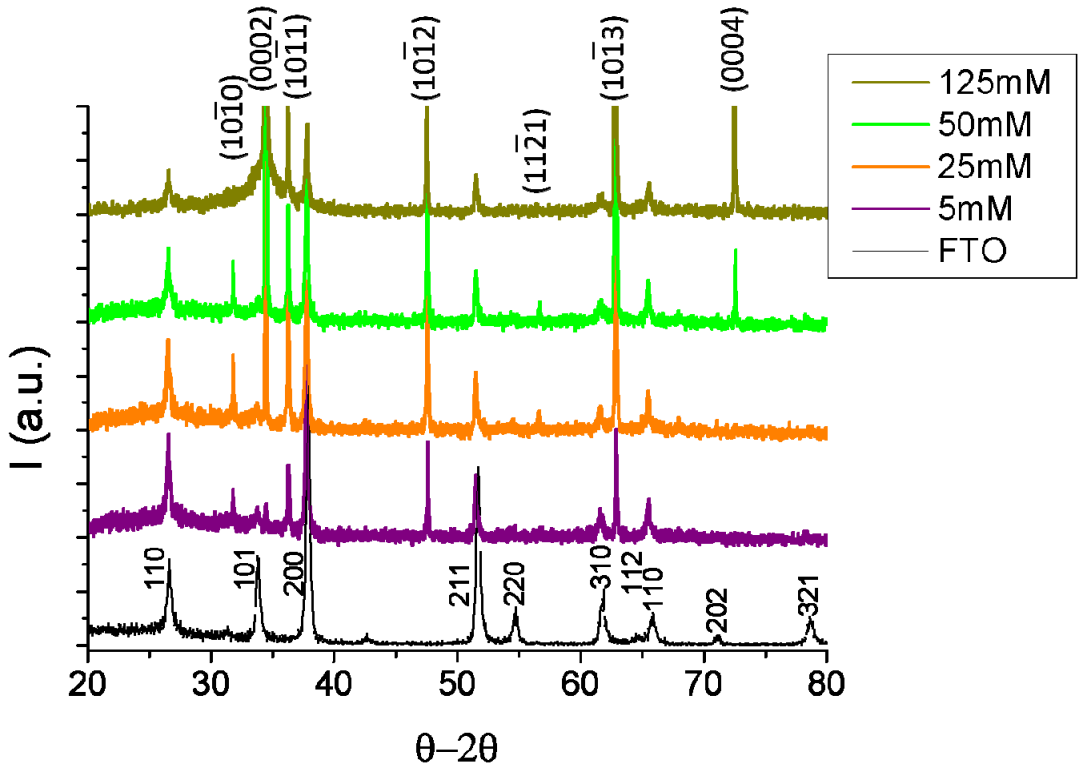

Figure 4.17: X-ray diffractograms of samples as grown with 5, 25, 50 and 125 mM concentration during 12 hours and the spectrum of the FTO template as reference.

Table 4.4: Orientation planes of the analyzed peaks with their orientation parameter and average grain size for samples grown during 12 h.

Orientation Plane	$(10\bar{1}0)$	(0002)	$(10\bar{1}1)$	$(10\bar{1}2)$	$(10\bar{1}3)$	Average Grain Size (nm)
Molar concentration	Orientation Parameter					
5mM	0.048	0.052	0.068	0.463	0.369	61.1
25mM	0.026	0.219	0.034	0.314	0.407	87.0
50mM	0.006	0.704	0.008	0.079	0.203	108.2
125mM	0.0	0.970	0.001	0.006	0.023	135.3

From the analysis presented in *Table 4.4* we can observe that orientation parameter of plane (0002) increase gradually with the concentration of the growth promoting solution in decrement of the other peaks which decrease. For samples grown at lower concentrations, seems to be that the orientation on the c-axes is not preferential, and their spectra are more similar to those typical from nanoparticles or nanoflowers, which are composed by nanorods oriented in different directions [9, 35, 36]. At the contrary, for samples grown with 50 and 125 mM concentrations the orientation on the c-axes is preferential. In micrograph presented in *Figure 4.18* are indicated the planes of the structure. So, the higher the concentration, the larger the crystal size of the plane perpendicular to the normal of the surface. The average grain size also increases with the concentration and together with the perpendicular plane to the c-axes, i.e. .

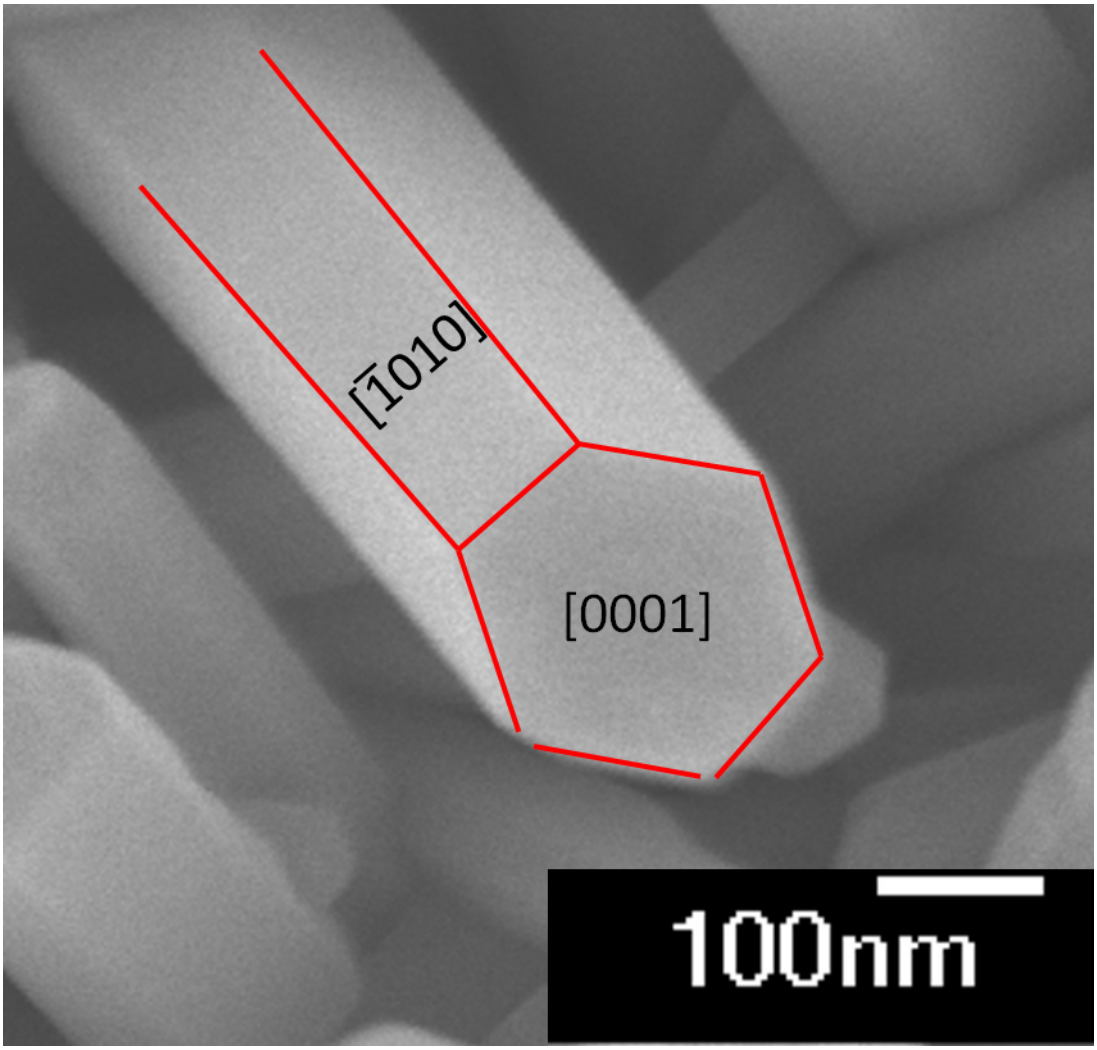

Figure 4.18: SEM micrograph of single ZnO nanorod where it can be appreciated the different planes forming the hexagonal prism.

The samples were characterized again after the last step presented in *Figure 4.13*, i.e. after CdS coating and annealing in Argon atmosphere during 1 hour. The X-ray spectra are presented in *Figure 4.19* and the orientation parameter and the average grain size calculated from Scherrer's formulae are presented in *Table 4.5*.

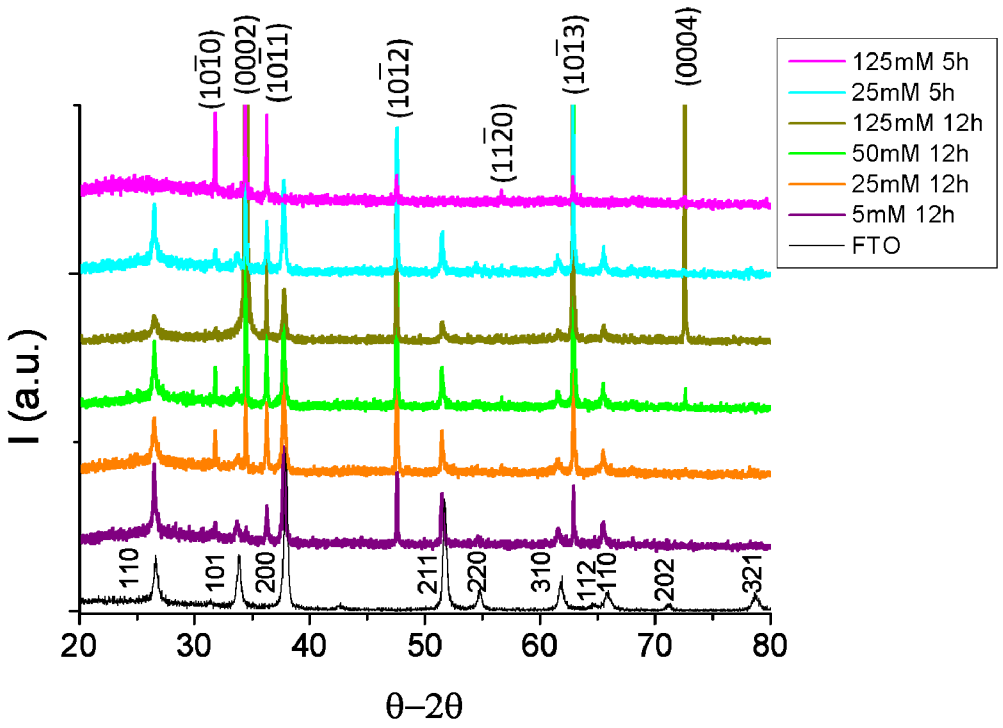

Figure 4.19: X-ray diffractograms of samples grown at 5, 25, 50 and 125 mM concentration during 12 hours and 25 and 125 mM during 5h after CdS coating and annealing at 400 °C in Argon atomosphere. The spectrum of the FTO template is also presented as reference.

Table 4.5: Orientation planes of the analyzed peaks with their orientation parameter and average grain size for samples grown during 12 and 5 hours after CdS coating and annealing at 400 °C in Argon atomosphere.

Orientation Plane		$(10\bar{1}0)$	(0002)	$(10\bar{1}1)$	$(10\bar{1}2)$	$(10\bar{1}3)$	Average Grain Size (nm)
Molar concentration	Growth time	Orientation Parameter					
5mM	12 h	0.043	0.041	0.063	0.597	0.256	71.8
25mM		0.032	0.172	0.038	0.349	0.408	87.0
50mM		0.010	0.465	0.011	0.158	0.356	108.2
125mM		0.0	0.922	0.002	0.016	0.060	135.3
25mM	5 h	0.015	0.197	0.025	0.342	0.421	77.8
125mM		0.131	0.607	0.082	0.104	0.076	85.6

So, after annealing at 400 °C no significant differences appear in the orientation parameters and grain size of the ZnO nanorods. If we compare samples grown at 25 and 125 mM during 5 hours, their grain size is a little smaller than those grown during 12 hours, which could be correlated with the mentioned in section 4.3 about diameters. Moreover, it has not been observed any peak coming from CdS coating, which was expecting since the low quantity of deposited material.

4.5. Photoluminiscence and reflectance characterization.

The PL spectra showed in Figure 4.20 were collected as described in section 1.4.6..The PL spectra of ZnO nanorods present the band gap at 380 nm (3.26 eV) as shown in *Figure 4.20*. The wide band is ascribed to the defects in the energy band of ZnO[37-40] which generally consist of three sub-bands: green band ~2.4 eV (~515 nm), yellow band ~2.1 eV (~590 nm) and orange-red band ~1.9 – 2.0 eV (~620-652 nm) and ~1.8 – 1.9 eV (~652 – 690 nm), respectively.

Oxygen vacancies are the most accepted reason for the appearing of this band [41]. In this kind of nanostructures grown by hydrothermal method, this emission band could also be ascribed to the hydroxyl groups present [42]. The yellow and orange-red luminescence emissions have been mainly associated with Zn deficiency related defects (zinc vacancies, V_{Zn}, oxygen in the positions of Zn, O_{Zn}, or oxygen interstitials, O_i) [43], which seems to agree with the previously conveyed in section 4.3 about the formation of hollow structures due to decrease of the Zn^{2+}/OH^- ratio in the centre of the polar face $[0001]$.

In our case, in *Figure 4.20* the defect emission band appears around 565nm (2.20 eV), which is "green-yellow" emission band, typical for ZnO nanorods structures [42, 44, 45]. Moreover, it also can be appreciated a yellow band shoulder around 620nm, which is visible for samples grown with 5mM concentration.There are three levels emission for oxygen vacancies. The double ionized oxygen vacancy, V_O^{++}, which does not capture any electrons and is double positive charged relative to the ZnO lattice; the single ionized oxygen vacancy, V_O^{+}, which captures one electron; and the neutral oxygen vacancy, V_O^{x}, which captures two electrons and it is neutral relative to the ZnO lattice. The origin of the band present in these samples can be attributed to the recombination of the V_O^{++} centres close to the conduction band and to the transition from V_O^{+} centres to the valence band. The types and relative number of oxygen

vacancies is directly affected by the surface depletion region of the nanorod [46]. The V_O^{++} centres are present close to the surface of the nanorods, in the depletion region.

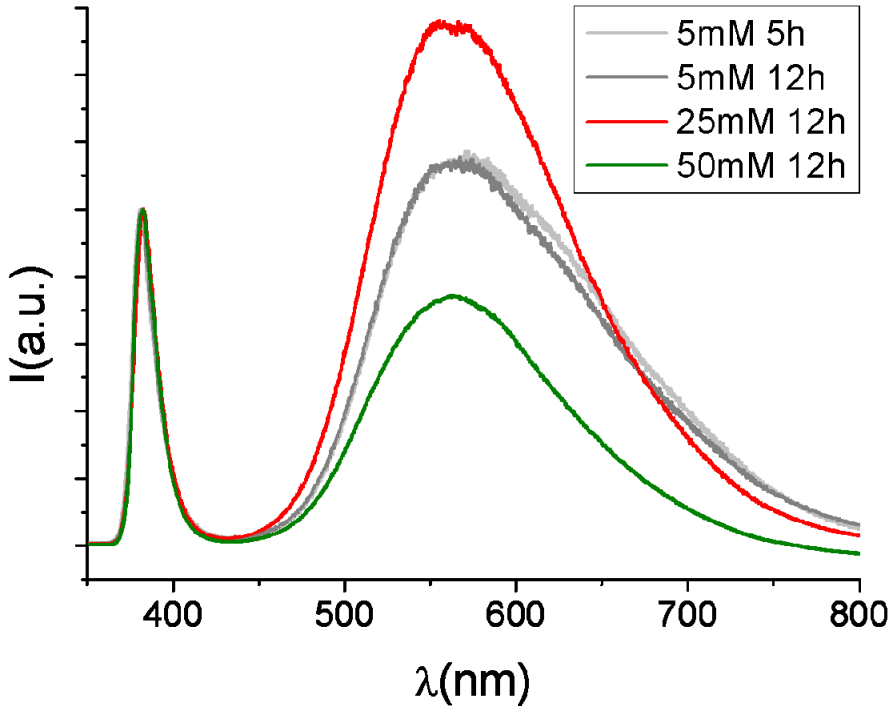

Figure 4.20: Normalized PL spectra of samples grown at 5 mM during 5 hours and 5, 25 and 50 mM during 12 hours.

It can be observed that the intensity of the green-yellow band decrease significantly for the sample with the wider nanorods, which accordingly to the previously conveyed, could imply a decrease of the depletion region near to the surface of the nanorods, and as consequence a decrease of the V_O^{++} centres.

After the annealing at 300 °C in air atmosphere and subsequent CdS coating, we can observe two changes in the visible band (see *Figure 4.21*). The green-yellow band is red shifted to 595 nm (2.08 eV), approximately, which we attribute to the thermal annealing in air atmosphere at 300 °C also observed by other authors [44]. This red-shift could be explained since the annealing in an oxygen-rich atmosphere increases the defect concentration related to oxygen excess in the surface of the ZnO nanorods [47]. On the other hand, the visible band is significantly weakened since the CdS are on the surface and could take place a kind of pasivation reducing the defects concentration and enhancing the charge transfer.

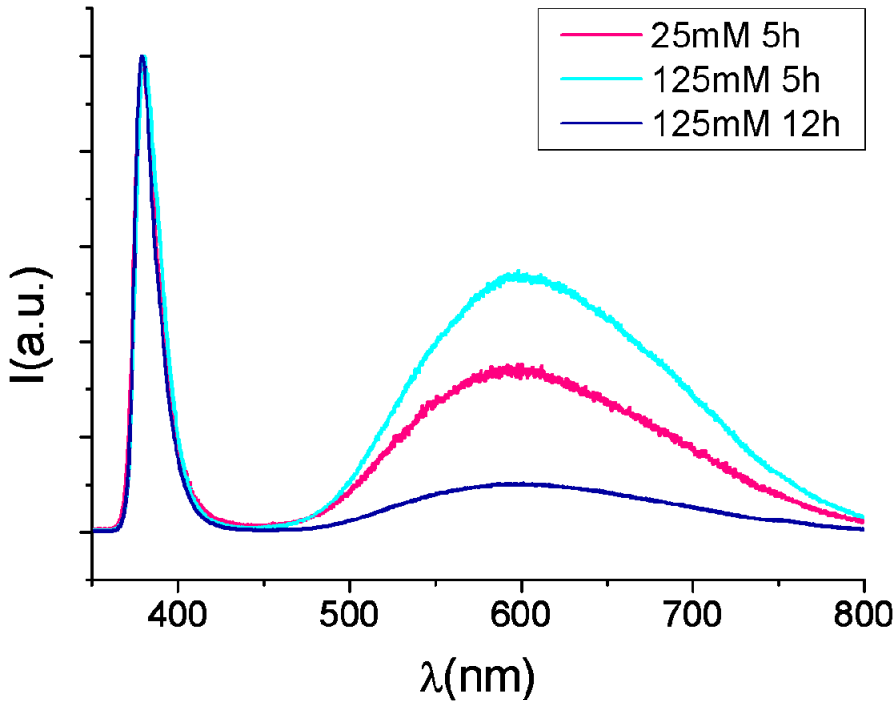

Figure 4.21: Normalized PL spectra of samples grown at 25 and 125 mM, both during 5 and 12 hours, after annealing at 300 °C in air atmosphere and CdS coating.

After thermal annealing at 400 °C in Ar/H_2 atomosphere during one hour, the visible band increase indicating an increase of the of the point defect concentration in the nanostructures (see *Figure 4.22*). However, it could be expected that after annealing an improvement of crystallinity takes place which would decrease the point defect concentration and the visible band intensity. A possible explanation for this behaviour could be the unintentional incorporation of Carbon impurities into the nanostructures. In order to confirm this fact, we performed Raman measurements. In the spectra of the annealed sample presented in *Figure 4.23* appears two band at 1360 cm^{-1} and at 1580 cm^{-1} due to the presence of incorporated Carbon into the PECs.

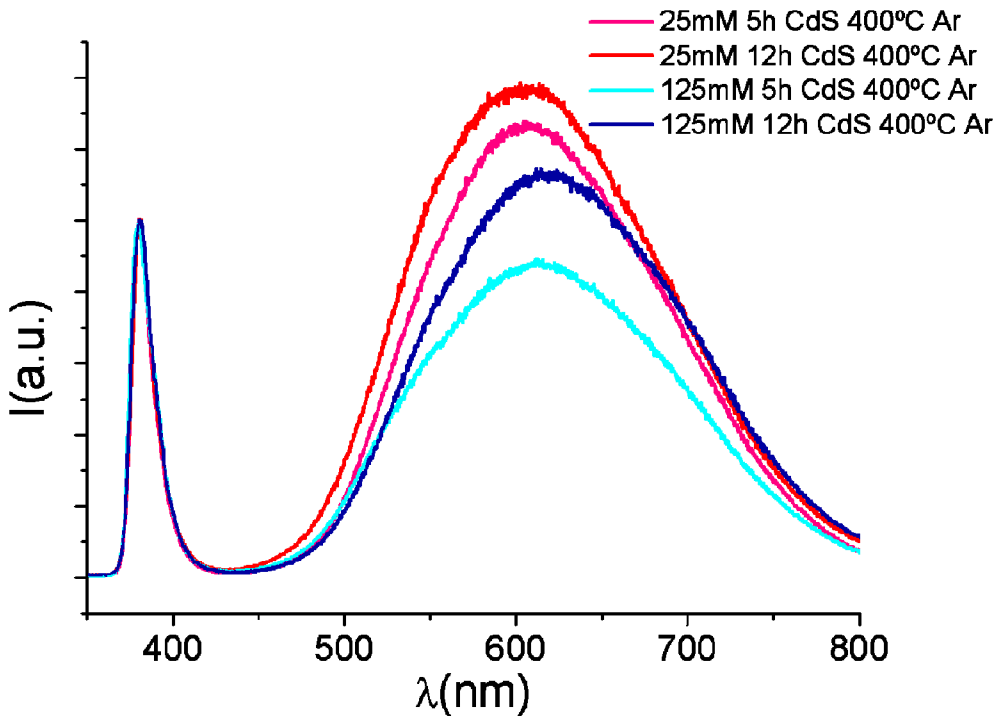

Figure 4.22: Normalized PL spectra of samples grown at 25 and 125 mM, both during 5 and 12 hours, after annealing at 300 °C in air atmosphere, CdS coating and annealing at 400 °C in Argon atmosphere.

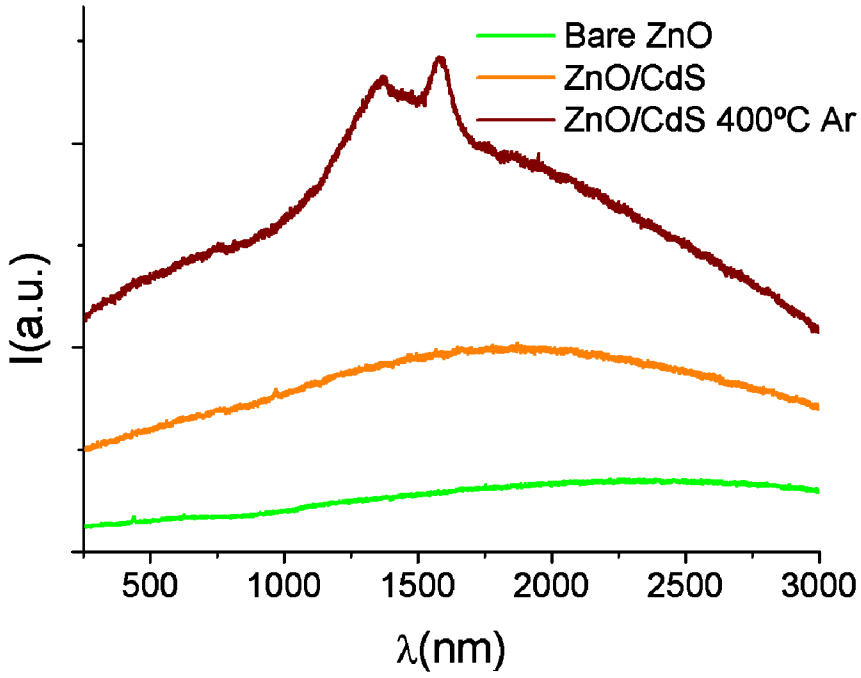

Figure 4.23: Raman spectra of samples grown with 25mM concentration after CdS deposition and thermal annealing at 400°C in Ar atomosphere.

In Figure 4.24 are presented the results from reflectance spectrometry of bare ZnO nanorods as grown and after CdS coating. The absorption edge for bare ZnO nanorods is around 400 nm. However, with the CdS coating the absorption edge can be extended up to 550 nm [48, 49], although depending on the deposited material quantity it could reach up to 600 nm [50, 51]. It is also possible to observe the ZnO absoption edge [52-54] in the coated samples, which is more evident for the samples with ZnO nanorods grown with concentration of 125 mM. This could be attributed to that CdS nanoparticles could not reach the total surface of nanorods or that the surface covered by the CdS nanopartices regarding the volume of ZnO nanorods grown at 125 mM concentration is significantly reduced.

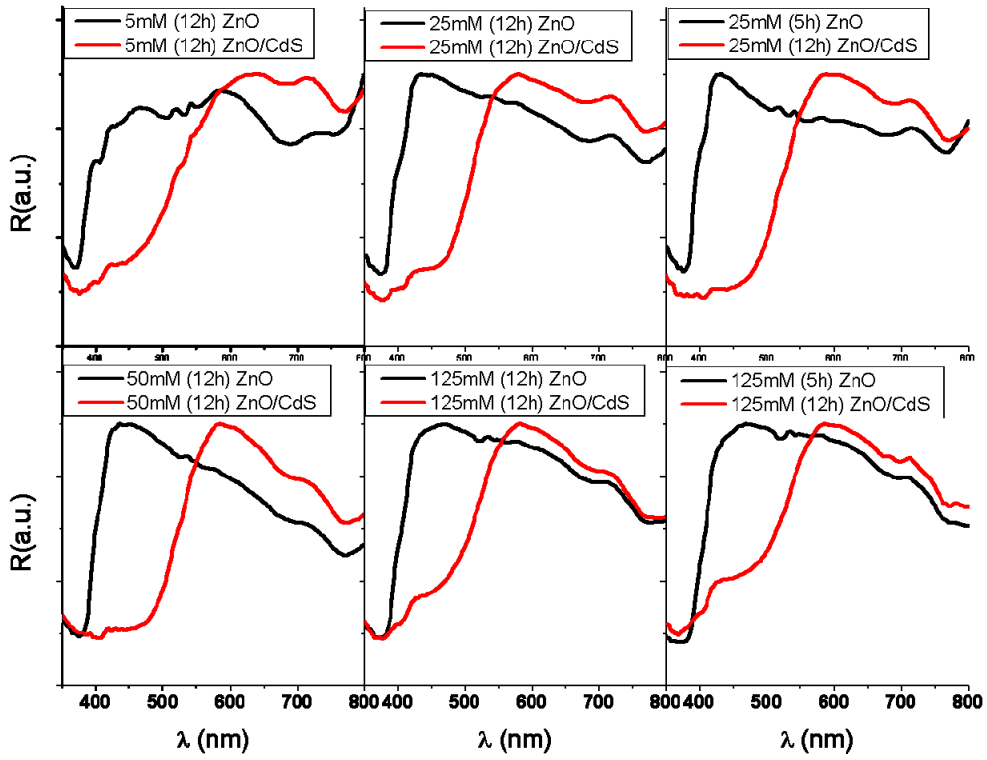

Figure 4.24: UV-Visible reflectance spectra for ZnO nanorods before and afte CdS coating.

4.6. Photoelectrochemical characterization of the ZnO nanostrucutres. Water splitting properties.

The set-up of the photoelectrochemical measurements is presented in section 1.4.7.

The acquired results of linear sweep voltammetry of the devices with bare ZnO nanorods are presented in *Figure 4.25* a) and c). With this characterization it is possible to study how the different morphologies of the nanorods affect the generated photocurrent density. The photocurrent density generated in short circuit, J_{SC}, is below 0.008 mA/cm^2, but as increase the applied bias, the photocurrent density could be 10 time higher. In *Figure 4.25*b) and d) are presented the photocurrent responses of bare ZnO nanorods under V_{bias}=0 V and 0.5 V versus Ag/AgCl reference electrode, for each photoanode.

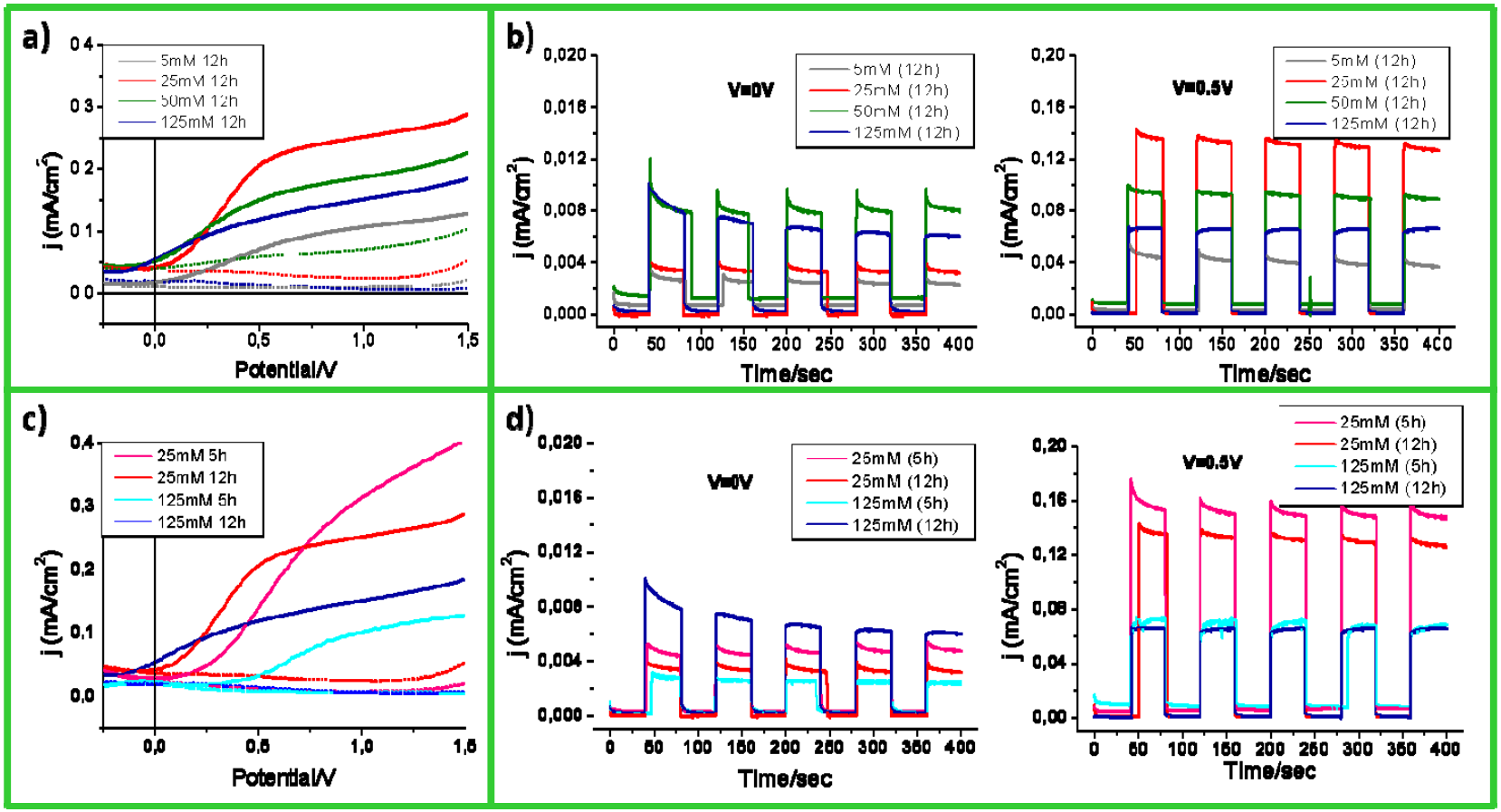

Figure 4.25: a)Linear sweep voltammagrams of photoanodes with bare as grown ZnO nanorods (first step, Figure 4.13) at 5, 25, 50 and 125 mM during 12 hours and c) 25 and 125 mM, both during 5 and 12 hours. The dotted lines correspond to photoanodes in the dark and the solid lines when are exposed to the light source. b) Chronoapmerometric response of photoanodes with bare as grown ZnO nanorods at 5, 25, 50 and 125 mM during 12 hours and d) 25 and 125mM, both during 5 and 12 hours, by applying V_{bias}= 0 and 0.5 V to each one.

The photocurrent response is prompt when the photoanode is exposed to visible light (*Figure 4.25*b and d). When the electrode is illuminated with the Xe lamp each 40 seconds, the photocurrent density increase suddenly and remains almost constant. On the other hand, the photocurrent densities decrease down to 0 mA/cm^2, ideally, or negligible values when it is in dark conditions the photocurrent.

The photoelectrochemical characterization of the CdS sensitized ZnO nanorods are shown in *Figure 4.26*. Sample grown at 125 mM concentration during 12 hours has been excluded from this study since resulted defective. CdS coating enhance significantly the registered photocurrents densities compared with bare ZnO as grown. *Figure 4.26*a) and c) shows the linear sweep voltammagrams. The samples grown during 12 hours present saturation photocurrents which remain constant along the applied voltage range. However, if we compare them with those grown during 5 hours, the later reach higher photocurrent density levels and vary with the applied voltage. In *Figure 4.26*b, the photocurrent responses to exposes each and during 50 seconds to visible light illumination of the photoanodes are quite stable for both applied bias 0 and 0.5V versus Ag/AgCl reference electrode. However, for samples grown during 5 hours (*Figure 4.26*d), the photoresponses are not uniform and decrease with time evolution since the photoanode presents instabilities. For these photoanodes the J_{SC}, vary from 1.5 mA/cm^2, in the case of the samples grown during 5 hours down to 1.0 - 0.5 mA/cm^2 for those grown during 12 hours. The samples which present the highest photoresponse are the 50 mM during 12h and the 25 and 125 mM during 5 hours.

If we compare with bare ZnO, when the V_{bias}=0 V the registered photocurrent densities are in the order of 100 times higher for CdS sensitized ZnO nanorods than those of bare ZnO as grown (*Figure 4.25*b). This increase in the photocurrent densities is due to the increased visible light absorption capability of the photoanode when is coated with CdS nanoparticles, as seen in Figure 4.24.

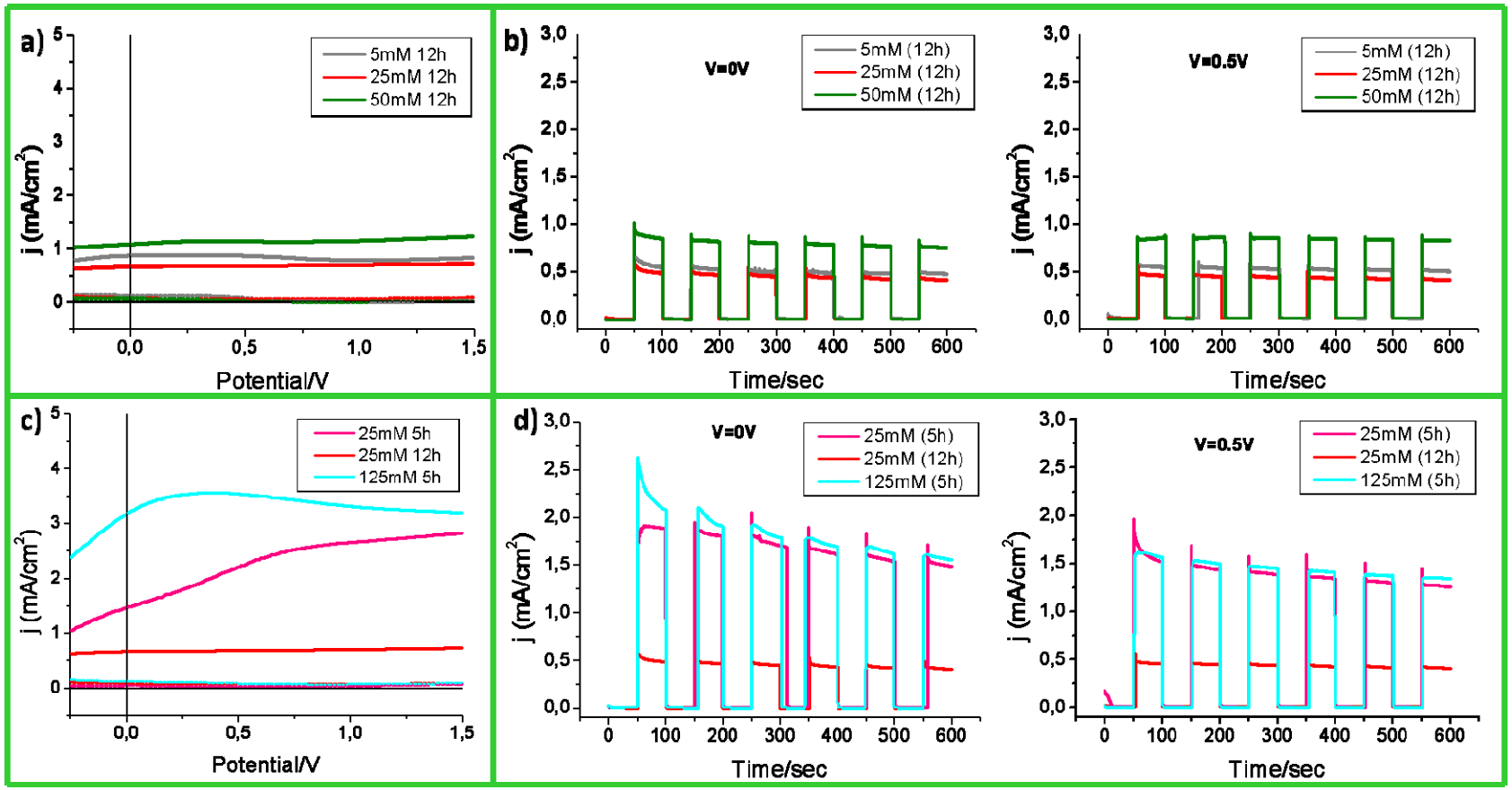

Figure 4.26: a)Linear sweep voltammagrams of photoanodes after annealing at 300 °C in air atomosphere following CdS sensitized ZnO nanorods (third step, Figure 4.13) at 5, 25, 50 and 125 mM during 12 hours and c) 25 and 125 mM, both during 5 and 12 hours. The dotted lines correspond to photoanodes in the dark and the solid lines when are exposed to the light source. b) Chronoapmerometric response of photoanodes with bare as grown ZnO nanorods at 5, 25, 50 and 125 mM during 12 hours and d) 25 and 125 mM, both during 5 and 12 hours, by applying V_{bias}= 0 and 0.5 V to each one.

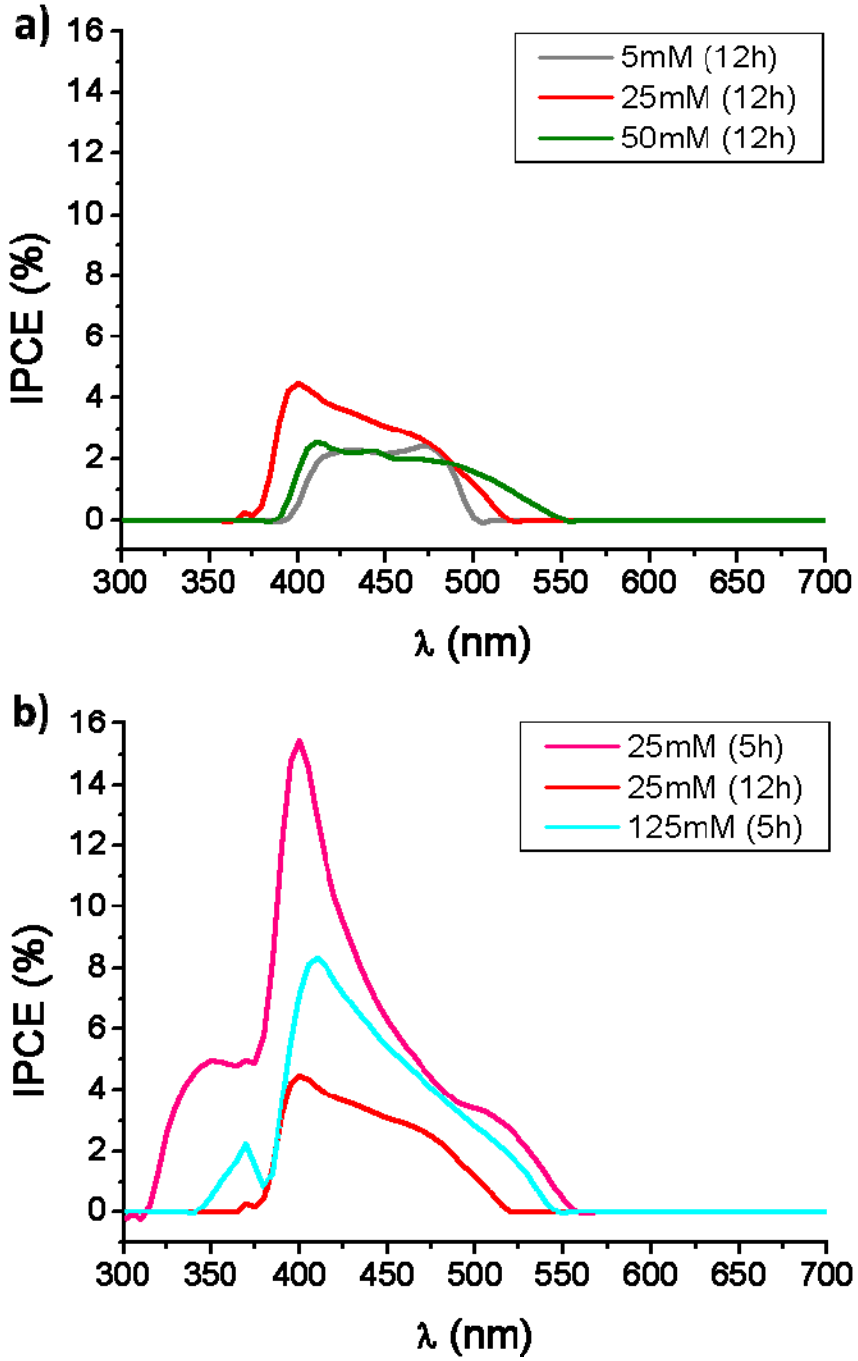

Figure 4.27: Measured IPCE spectra of of photoanodes (at third step, Figure 4.13) grown with 5, 25, 50 and 125 mM concentrations during 12 hours and c) 25 and 12 5mM, both during 5 and 12 hours.

In order to study the photoresponse of the photoanode in function of the incident wavelength we carry out measurements of the incident photon to current conversion efficiency (IPCE). The measured spectra of the samples after the third step indicated in *Figure 4.13* are showed in *Figure 4.27*. The IPCE for the samples grown during 12 hours are below 5% in best case (*Figure 4.27*a), which is the sample with 25 mM concentration. On the other hand, the samples grown during during 5 hours show the best results with IPCE's of ~8 and ~16% for 125 mM and 25

mM concentration respectively (*Figure 4.27*b). In *Figure 4.27*b it can be clearly appreciated two different regions, below and above ~375 nm (~3.31 eV). The contribution of the IPCE up to ~375 nm belongs to the light absorbed by ZnO nanorods, which was expected since it is the absorption edge (*Figure 4.24*). Above this wavelength up to 525-550 nm corresponds to the sensitized CdS nanoparticles, reaching the highest values of IPCE and dropping to the minimum value as approach the absorption edge of CdS.

In Figure 4.28 are presented the photoelectrochemical characterization carried out for the photoanodes after the annealing at 400 °C in Argon atmosphere during 1 hour, i.e. the last step of the experiments. The linear sweep votammograms are shown in Figure 4.28a and c, where we can see the V_{OC} for each photoanode and the J_{SC}. The values of these parameters are presented in Table 4.6 together with the Fill Factor (FF) (Eq. 4.1) and the photon to Hydrogen or Solar to Hydrogen (STH) efficiency (Eq. 4.2).

Eq. 4.1: $$FF = \frac{V_{MPP} \times J_{MPP}}{V_{OC} \times J_{SC}} = \frac{P_{max}}{V_{OC} \times J_{SC}}$$

Eq. 4.2: $$STH\ efficieny = \frac{J_{SC} \times (1.23V - V_{app})}{P_{light}}$$

Where V_{MPP} and J_{MPP} are the voltage and photocurrent density at the maximum power point and P_{max} is the maximum obtainable power, V_{app} is the applied bias and P_{light} is the power density of the illumination.

With difference regarding the previous steps, the photocurrent densities do not reach a saturation value. This suggests a more efficient electron transfer in the post-annealed photoanodes than in the previous ones [55]. The higher values of photocurrent were reached by the samples grown during 12 hours has been found to be the photoanode at 25 mM, which reaches 1.7 mA/cm^2, as we can observe in the chronoamperometric curve *Figure 4.28*b under illumination conditions. However, the best results, again is obtained for the sample grown during 5 hours with concentration of 25 mM, reaching photocurrents near to 2.0 mA/cm^2 at V_{bias}=0 V and above 3 mA/cm^2 at V_{bias}=0.5 V. In general has been observed an increase of the photocurrent density for all the photoanodes after the thermal annealing at 400 °C in Argon atmosphere during 1 hour. This could be attributed to an improvement of the contact at the interface CdS/ZnO and also of the crystallinity of the CdS nanoparticles [17]. The improvement of the contact between CdS nanoparticles and ZnO surface nanorods, not only improves the charge transfer and therefore the separation the excited electron-hole pair, but also restrain the recombination of the charge carriers [17].

Surprisingly the IPCE measurements performed in the photoanodes shows an important decrease *Figure 4.29*. This fact is attributed to the instability of the the CdS nanoparticles and ZnO nanorods immersed into the electrolyte which result having a pH value higher than 13, and the fact of the presence of Carbon impurities which difficult the light absorption and increase the defect points concentration making easy the recombination of the charge carriers.

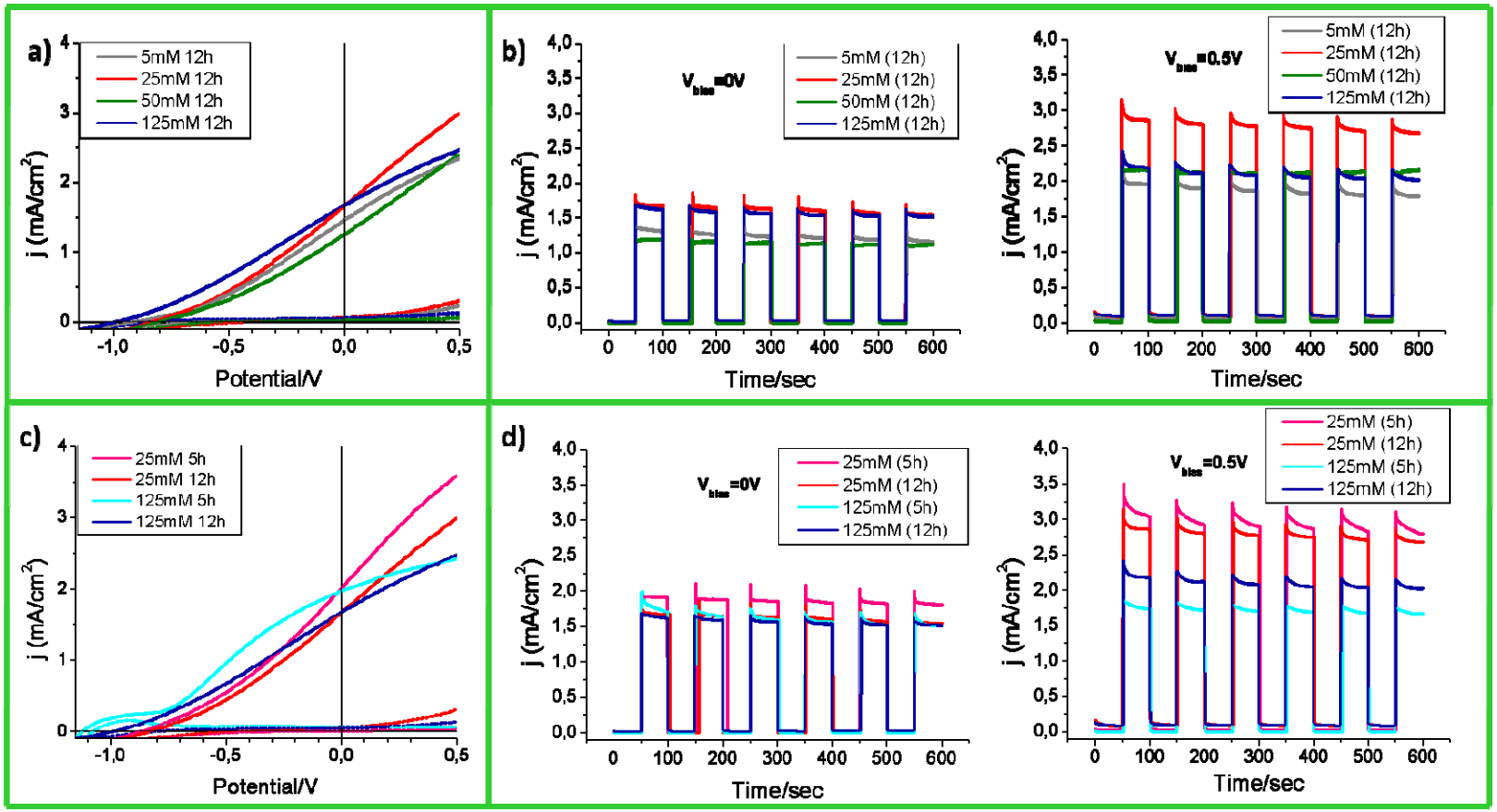

Figure 4.28: a)Linear sweep voltammagrams of photoanodes after annealing at 300°C in air atomosphere following CdS sensitized ZnO nanorods and anneling at 400 °C in Ar atomosphere (last step, Figure 4.13), at 5, 25, 50 and 125 mM during 12 hours and c) 25 and 125 mM, both during 5 and 12 hours. The dotted lines correspond to photoanodes in the dark and the solid lines when are exposed to the light source. b) Chronoapmerometric response of photoanodes with bare as grown ZnO nanorods at 5, 25, 50 and 125 mM during 12 hours and d) 25 and 125 mM, both during 5 and 12 hours, by applying V_{bias}= 0 and 0.5 V to each one.

Table 4.6: Fabrication and geometrical parameters summarized for comparison with the Filling Factor and STH efficiency obtained for each photoanode versus Ag/ClAg.

Growth Time (h)	Concentration $Zn(NO_3)_2$ (mM)	Diameter (nm)	Length (µm)	V_{OC} (V)	J_{SC} (mA/cm^2)	V_{MPP} (V)	J_{MPP} (mA/cm^2)	P_{MAX} (mW)	Filling Factor	STH efficiency (%)
12	5	40±10	0.7±0.1	-0.90	1.45	-0.335	0.714	0.239	0,183	1,62
	25	70±15	1.6±0.2	-0.83	1.67	-0.335	0.798	0.267	0,193	1,87
	50	150±50	2.5±0.2	-0.8	1.25	-0.345	0.564	0.194	0,195	1,40
	125	600±250	4.2±0.4	-0.99	1.67	-0.435	0.813	0.354	0,214	1,87
5	25	50±10	1.5±0.2	-0.86	2.00	-0.355	0.888	0.315	0,183	2,24
	125	450±150	4.0±0.4	-1.12	1.96	-0.425	1.164	0.495	0,225	2,19

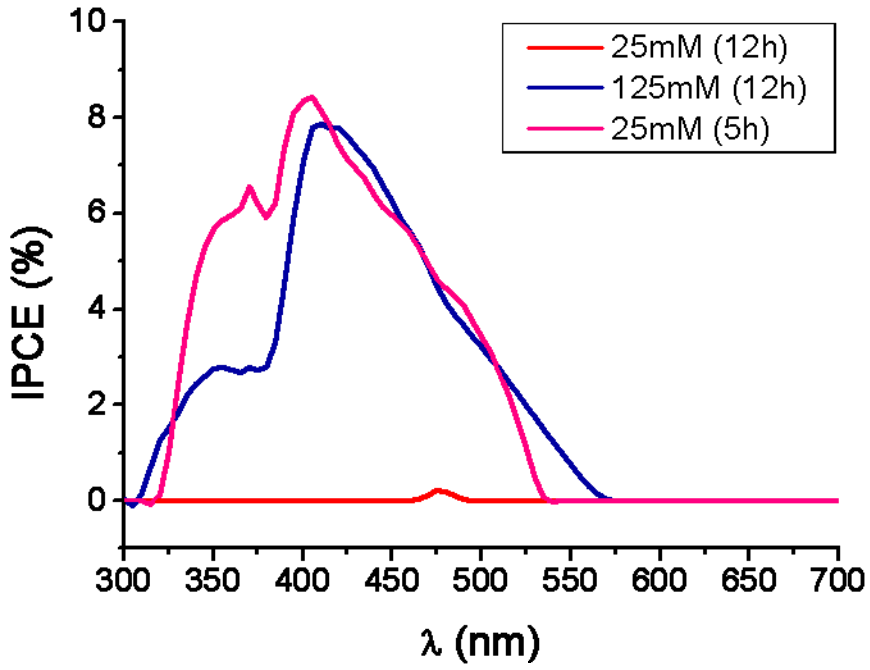

Figure 4.29: Measured IPCE spectra of of photoanodes (at forth step, Figure 4.13) grown with 5, 25, 50 and 125 mM concentrations during 12 hours and c) 25 and 125 mM, both during 5 and 12 hours.

4.7. Summary.

In this chapter we have shown several methods fo obtaining ZnO nanostructures. These methods are based on electrochemical deposition and solution growth fabrication procedures.

Hydrothermal growth has been shown to be the easiest and fastest way to obtain ZnO nanorods in a wide range of diameters between 50 up to 600nm. Also, it has been possible to obtain tubular or hollow nanostructures by local dissolution in the centre of the nanorod.We have take advance of their photocatalytic properties enhanced with the deposition of CdS nanoparticles, which enlarges the absorption light band. We have fabricated photoelectrochemical cells in order to achieve Hydrogen generation starting from solar light energy.

References

1. Wang, Z.L., *Zinc oxide nanostructures: growth, properties and applications.* Journal of Physics-Condensed Matter, 2004. **16**(25): p. R829-R858.
2. Fan, H.J., et al., *Vapour-transport-deposition growth of ZnO nanostructures: switch between c-axial wires and a-axial belts by indium doping.* Nanotechnology, 2006. **17**(11): p. S231-S239.
3. Banerjee, D., *Synthesis and photoluminescence studies on ZnO nanowires.* Nanotechnology, 2004. **15**(3): p. 404.
4. Li, Y., et al., *Ordered semiconductor ZnO nanowire arrays and their photoluminescence properties.* Applied Physics Letters, 2000. **76**(15): p. 2011-2013.
5. Zheng, M.J., et al., *Fabrication and optical properties of large-scale uniform zinc oxide nanowire arrays by one-step electrochemical deposition technique.* Chemical Physics Letters, 2002. **363**(1-2): p. 123-128.
6. Liu, B. and H.C. Zeng, *Hydrothermal synthesis of ZnO nanorods in the diameter regime of 50 nm.* Journal of the American Chemical Society, 2003. **125**(15): p. 4430-4431.
7. Zhang, H., et al., *Low temperature synthesis of flowerlike ZnO nanostructures by cetyltrimethylammonium bromide-assisted hydrothermal process.* Journal of Physical Chemistry B, 2004. **108**(13): p. 3955-3958.
8. Govender, K., et al., *Understanding the factors that govern the deposition and morphology of thin films of ZnO from aqueous solution.* Journal of Materials Chemistry, 2004. **14**(16): p. 2575-2591.
9. Baruah, S. and J. Dutta, *Hydrothermal growth of ZnO nanostructures.* Science and Technology of Advanced Materials, 2009. **10**(1).
10. Barbe, C.J., et al., *Nanocrystalline titanium oxide electrodes for photovoltaic applications.* Journal of the American Ceramic Society, 1997. **80**(12): p. 3157-3171.
11. Li, W.-J., et al., *Growth mechanism and growth habit of oxide crystals.* Journal of Crystal Growth, 1999. **203**(1–2): p. 186-196.
12. Gratzel, M., *Photoelectrochemical cells.* Nature, 2001. **414**(6861): p. 338-344.
13. van de Krol, R., Y. Liang, and J. Schoonman, *Solar hydrogen production with nanostructured metal oxides.* Journal of Materials Chemistry, 2008. **18**(20): p. 2311-2320.
14. http://rredc.nrel.gov/solar/spectra/am1.5/.
15. Cho, S., et al., *Three-Dimensional Type II ZnO/ZnSe Heterostructures and Their Visible Light Photocatalytic Activities.* Langmuir, 2011. **27**(16): p. 10243-10250.
16. Xu, F., et al., *Synthesis of ZnO/CdS hierarchical heterostructure with enhanced photocatalytic efficiency under nature sunlight.* CrystEngComm, 2012. **14**(10): p. 3615-3622.
17. Qi, X.P., et al., *Electrochemical synthesis of CdS/ZnO nanotube arrays with excellent photoelectrochemical properties.* Chemical Communications, 2012. **48**(2): p. 242-244.
18. Barpuzary, D., et al., *Hierarchically Grown Urchinlike CdS@ZnO and CdS@Al2O3 Heteroarrays for Efficient Visible-Light-Driven Photocatalytic Hydrogen Generation.* Journal of Physical Chemistry C, 2012. **116**(1): p. 150-156.
19. Gonzalez-Valls, I. and M. Lira-Cantu, *Vertically-aligned nanostructures of ZnO for excitonic solar cells: a review.* Energy & Environmental Science, 2009. **2**(1): p. 19-34.
20. Masuda, H. and M. Satoh, *Fabrication of gold nanodot array using anodic porous alumina as an evaporation mask.* Japanese Journal of Applied Physics Part 2-Letters, 1996. **35**(1B): p. L126-L129.

21. Masuda, H., F. Hasegwa, and S. Ono, *Self-ordering of cell arrangement of anodic porous alumina formed in sulfuric acid solution.* Journal of the Electrochemical Society, 1997. **144**(5): p. L127-L130.
22. Jessensky, O., F. Muller, and U. Gosele, *Self-organized formation of hexagonal pore arrays in anodic alumina.* Applied Physics Letters, 1998. **72**(10): p. 1173-1175.
23. Li, A.P., et al., *Hexagonal pore arrays with a 50-420 nm interpore distance formed by self-organization in anodic alumina.* Journal of Applied Physics, 1998. **84**(11): p. 6023-6026.
24. Somogyi, A., et al., *ID18F: a new micro-x-ray fluorescence end-station at the European Synchrotron Radiation Facility (ESRF): preliminary results.* X-Ray Spectrometry, 2001. **30**(4): p. 242-252.
25. Somogyi, A., et al., *ID22: a multitechnique hard X-ray microprobe beamline at the European Synchrotron Radiation Facility.* Journal of Synchrotron Radiation, 2005. **12**(2): p. 208-215.
26. Ursaki, V.V., et al., *Multiphonon resonant Raman scattering in ZnO crystals and nanostructured layers.* Physical Review B, 2004. **70**(15).
27. Kumar, B., et al., *Photoluminescence and multiphonon resonant Raman scattering in low-temperature grown ZnO nanostructures.* Applied Physics Letters, 2006. **89**(7).
28. Zhang, J., et al., *Control of ZnO Morphology via a Simple Solution Route.* Chemistry of Materials, 2002. **14**(10): p. 4172-4177.
29. Schmidt-Mende, L. and J.L. MacManus-Driscoll, *ZnO – nanostructures, defects, and devices.* Materials Today, 2007. **10**(5): p. 40-48.
30. Sugunan, A., et al., *Zinc oxide nanowires in chemical bath on seeded substrates: Role of hexamine.* Journal of Sol-Gel Science and Technology, 2006. **39**(1): p. 49-56.
31. Wei, A., et al., *Growth mechanism of tubular ZnO formed in aqueous solution.* Nanotechnology, 2006. **17**(6): p. 1740-1744.
32. Sun, Y., D.J. Riley, and M.N.R. Ashfold, *Mechanism of ZnO nanotube growth by hydrothermal methods on ZnO film-coated Si substrates.* Journal of Physical Chemistry B, 2006. **110**(31): p. 15186-15192.
33. Vayssieres, L., et al., *Three-dimensional array of highly oriented crystalline ZnO microtubes.* Chemistry of Materials, 2001. **13**(12): p. 4395-+.
34. He, Y., et al., *Vertically well-aligned ZnO nanowires generated with self-assembling polymers.* Materials Chemistry and Physics, 2005. **94**(1): p. 29-33.
35. Baruwati, B., D.K. Kumar, and S.V. Manorama, *Hydrothermal synthesis of highly crystalline ZnO nanoparticles: A competitive sensor for LPG and EtOH.* Sensors and Actuators B: Chemical, 2006. **119**(2): p. 676-682.
36. Shao, S., et al., *Stable field emission from rose-like zinc oxide nanostructures synthesized through a hydrothermal route.* Materials letters, 2008. **62**(8–9): p. 1200-1203.
37. Vlasenko, L.S. and G.D. Watkins, *Optical detection of electron paramagnetic resonance in room-temperature electron-irradiated ZnO.* Physical Review B, 2005. **71**(12).
38. Shan, F.K., et al., *The role of oxygen vacancies in epitaxial-deposited ZnO thin films.* Journal of Applied Physics, 2007. **101**(5).
39. Liu, M., A.H. Kitai, and P. Mascher, *POINT-DEFECTS AND LUMINESCENCE-CENTERS IN ZINC-OXIDE AND ZINC-OXIDE DOPED WITH MANGANESE.* Journal of Luminescence, 1992. **54**(1): p. 35-42.
40. Korsunska, N.O., et al., *The influence of defect drift in external electric field on green luminescence of ZnO single crystals.* Journal of Luminescence, 2003. **102**: p. 733-736.
41. Li, D., et al., *Different origins of visible luminescence in ZnO nanostructures fabricated by the chemical and evaporation methods.* Applied Physics Letters, 2004. **85**(9): p. 1601-1603.

42. Djurisic, A.B., et al., *Defect emissions in ZnO nanostructures.* Nanotechnology, 2007. **18**(9).
43. Ong, H.C. and G.T. Du, *The evolution of defect emissions in oxygen-deficient and -surplus ZnO thin films: the implication of different growth modes.* Journal of Crystal Growth, 2004. **265**(3-4): p. 471-475.
44. Qiu, J.J., et al., *Solution-derived 40 mu m vertically aligned ZnO nanowire arrays as photoelectrodes in dye-sensitized solar cells.* Nanotechnology. **21**(19).
45. Li, C., et al., *Wet Chemical Approaches to Patterned Arrays of Well-Aligned ZnO Nanopillars Assisted by Monolayer Colloidal Crystals.* Chemistry of Materials, 2009. **21**(5): p. 891-897.
46. Liao, Z.M., et al., *Surface effects on photoluminescence of single ZnO nanowires.* Physics Letters A, 2008. **372**(24): p. 4505-4509.
47. Kang, H.S., et al., *Annealing effect on the property of ultraviolet and green emissions of ZnO thin films.* Journal of Applied Physics, 2004. **95**(3): p. 1246-1250.
48. Navarro, R.M., F. del Valle, and J.L.G. Fierro, *Photocatalytic hydrogen evolution from CdS-ZnO-CdO systems under visible light irradiation: Effect of thermal treatment and presence of Pt and Ru cocatalysts.* International Journal of Hydrogen Energy, 2008. **33**(16): p. 4265-4273.
49. Tak, Y., et al., *Solution-Based Synthesis of a CdS Nanoparticle/ZnO Nanowire Heterostructure Array.* Crystal Growth & Design, 2009. **9**(6): p. 2627-2632.
50. Wang, X., et al., *Enhanced photocatalytic hydrogen evolution by prolonging the lifetime of carriers in ZnO/CdS heterostructures.* Chemical Communications, 2009(23): p. 3452-3454.
51. Tak, Y., et al., *Fabrication of ZnO/CdS core/shell nanowire arrays for efficient solar energy conversion.* Journal of Materials Chemistry, 2009. **19**(33): p. 5945-5951.
52. Wang, X., et al., *Stable photocatalytic hydrogen evolution from water over ZnO-CdS core-shell nanorods.* International Journal of Hydrogen Energy, 2010. **35**(15): p. 8199-8205.
53. Joo, J., et al., *The fabrication of highly uniform ZnO/CdS core/shell structures using a spin-coating-based successive ion layer adsorption and reaction method.* Nanotechnology, 2010. **21**(32).
54. Wang, X., et al., *Polar interface-induced improvement in high photocatalytic hydrogen evolution over ZnO-CdS heterostructures.* Energy & Environmental Science, 2011. **4**(10): p. 3976-3979.
55. Wang, G.M., et al., *Double-Sided CdS and CdSe Quantum Dot Co-Sensitized ZnO Nanowire Arrays for Photoelectrochemical Hydrogen Generation.* Nano Letters, 2010. **10**(3): p. 1088-1092.

General conclusions.

From the work developed and main results presented in this Thesis it can be drawn the following general conclusions:

1.- Self-Correlation Function (SCF) is a tool that allows for processing micrographs of ordered systems, obtaining statistical images, Self-Correlation Images (SCI) which can be studied in a global way the geometric parameters and the order degree in a qualitative and quantitative way, presenting one alternative over other similar such as Fast Fourier Transform or Pair Distribution Function.

2.- It is possible to reduce the interpore distance by 15 nm and the pore diameter by 6nm within self-ordering regimes, by increasing the concentration of sulphuric acid of the electrolyte from 3 up to 20wt% and by decreasing the applied voltage from 25 down to 20V, complying also with the 10% porosity rule.

3.- From the compositional and structural analysis by RBS, TG and IR on the NAAF grown for the study presented in chapter 1, it has been observed that the incorporation of sulphate ions increase with the applied voltage during the anodization process as well as with the acid concentration of the electrolyte. This fact implies larger impurity incorporation during alumina formation process when increases the electric field through the barrier layer.

4.- The volume expansion of alumina increases for the same quantity of charge flowing through the electrodes in the electrochemical cell. Moreover, from the results obtained in the calculus of the volume expansion factor , it has been noticed that this values also increase with the applied voltage and the sulphuric acid concentration, obtaining values which range between 1.5 and 1.7 for the best self-ordered samples, indicating that the mechanical stress generated in the metal/oxide interface for these conditions is optimal for achieve self-ordering under these experimental parameters, but obtaining these values for one sample do not implies self-ordering conditions.

5.- The efficiency of the anodization process is dependent on the anodization voltage and on the acid concentration. From the analyzed samples it can be observed a tendency to increase the efficiency together with these two parameters reaching values between 60 and 70%.

6.- The effective medium model by Maxwell-Garnett is valid for calculating NAAF thickness within a range of 0.5 and 10μm simply by taking into account the cylindrical porosity

of the anodic alumina matrix. This method presents the advantage of being non-destructive, without the necessity of having to manipulate NAAF detached from the AI substrate and in this case has resulted in being quite precise.

7.- Despite the fact that the hard anodization conditions in an electrolyte based on sulphuric acid are quite different than the ones presented in traditional anodizations in the same electrolyte, the self-ordering generated in the NAAF grown by hard anodization is at least the same presented in the best NAAF self-ordering degree grown by the traditional method.

8.- The structure of anodic alumina grown under hard anodization conditions has a tubular-like growth unlike under mild anodization, where the alumina grows as a porous film. This reveals two different types of growth, which we suggest they could be related to a field-assisted flow of alumina at the barrier layer in case of hard anodization and field-assisted dissolution in case of mild anodization.

9.- A difference between mild anodization and hard anodization is revealed by observing the difference between the ratio interpore distance and voltage applied. It has been observed experimentally that in self-ordered systems of anodic alumina cells that this ratio is about 2.5nm/V in the case of mild anodization, and in the case of hard anodization it varies in between 1,6 and 2,0nm/V.

10.- It is possible to obtain self-ordered systems at reduced anodization times by mean of the HA in Aluminium by anodization on sulphuric acid based aqueous electrolytes. In addition, the interpore distance can be controlled by mean of HA time it is “hard anodized” without losing self-ordering, leading us to our case of interpore distances obtained by the traditional oxalic mode.

11.- As a result of the pulsed anodization mode it has been possible to modulate periodically, and in a controlled way, the diameters of the pores between 25 to 40nm without varying the distance from centre to centre between them, as well as the composition of the aluminium along the channels. The inconvenience of these NAAF is that they present considerable mechanical instabilities due to the high current densities that exist during its growth, which could affect its homogeneity. However, these new geometries open many new possibilities in the creation of new 1D and 3D nanostructures.

12.- The NAAF presented in this dissertation can be used as templates for the production of magnetic materials like Co, and given its particular geometries, it can obtain

magnetic properties of great interest, even though a further study in this field is required apart from the aforementioned.

13.- It has been found extraordinary difficulties during the experiments for obtaining ZnO nanowires by use of NAAF as templates; firstly with the oxidation of the previously electrodeposited metallic Zn after thermal annealing; secondly with formation of a ZnO layer on the top of the NAAF while direct electrodeposition of ZnO inside the nanopores was sought.

14.- It is possible to grow ZnO nanorods in a wide range of diameters ranging from 40nm up to 600nm on average through hydrothermal growth. It has been observed that the rate of increase of the nanorods diameters after the first 5 hours decreases by around 70% of its original rate. Also, it has been possible to obtain tubular or hollow nanostructures by local dissolution in the centre of the nanorod.

15.- The photocatalytic properties of ZnO nanorods have allowed for their utilization in the creation of devices like photoelectrochemical cells, PEC, for the production of H_2, starting from solar light simulator. It also has been observed that ZnO is not a stable material and easily etched by immersing into the electrolyte adequate for the study of photocatalytic properties of these types of semiconductive materials. Despite the results obtained from the research carried out are not entirely satisfactory, it opens up a new dialogue for the improvement of such devices.

Conclusiones generales.

Del trabajo desarrollado y los resultados principales presentados en esta tesis se pueden extraer las siguientes conclusiones:

1.- Función de autocorrelación es una herramienta que permite procesar micrografías de sistemas ordenados, obteniendo imágenes estadísticas, imágenes de autocorrelación a partir de las cuales se puede estudiar de forma global parámetros geométricos y grado de ordenamiento de forma cualitativa y cuantitativa, presentando una alternativa a otros métodos similares como Fast Fourier Transform o Función de Distribución Par.

2.- Ha sido posible reducir 15nm la distancia interporo y 6nm el diámetro de poro dentro del régimen de auto-ordenamiento, mediante el aumento de la concentración de ácido sulfúrico en el electrolito entre 3 y 20% en peso y disminuyendo el voltaje aplicado desde 25 hasta 20V, cumpliendo con la regla de la porosidad del 10%.

3.- Del análisis composicional y estructural mediante RBS, TG e IR de las NAAF crecidas para el estudio realizado en el primer capítulo, se ha observado que la incorporación de iones sulfato aumenta con el voltaje aplicado durante la anodización así como con la concentración de ácido en el electrolito. Esto implica una mayor incorporación de impurezas durante la formación de la alúmina cuando también aumenta el campo eléctrico a través de la capa barrera.

4.- El volumen de expansión de la alúmina anódica aumenta para la misma cantidad de carga que pasa a través de los electrodos en la celda electroquímica. Además, de los resultados obtenidos en los cálculos del volumen de expansión, se ha observado que estos valores también aumentan con el voltaje aplicado y la concentración de ácido sulfúrico en el electrolito, obteniéndose valores que varían entre 1.5 y 1.7 para las muestras que presentan mejor auto-orden, indicando que el estrés mecánico generado en la intercara metal/óxido en estas condiciones son óptimas para conseguir autoordenamiento bajo estos parámetros experimentales. Sin embargo, obtener estos valores no implica condiciones de autordenamiento.

5.- La eficiencia del proceso de anodización también es dependiente del voltaje aplicado y de la concentración del ácido. En las muestras analizadas se ha podido observar una tendencia a aumentar la eficiencia alcanzando valores entre 60 y 70% junto con estos dos parámetros mencionados.

6.- El modelo de medio efectivo de Maxwell-Garnett es válido para calcular los espesores de NAAF dentro de un rango entre 0.5 y 10µm simplemente teniendo en cuenta la porosidad cilíndrica de la matriz de alúmina anódica. Este método presenta la ventaja de ser no destructivo, sin necesidad de tener que manipular la NAAF separada del substrato de Al y ha resultado ser bastante preciso.

7.- A pesar de que las condiciones de anodización dura en electrolito basado en ácido sulfúrico sean muy distintas a las presentadas en las anodizaciones tradicionales en ese mismo electrolito, el auto-ordenamiento generado en las NAAF crecidas mediante anodización dura es al menos igual al presentado en la NAAF con mayor grado de autoorden crecida por el método tradicional.

8.- La estructura de la alúmina crecida bajo condiciones de anodización dura es un crecimiento tubular, no como en condiciones de anodización moderada, donde la alumina crece como una película porosa. Esto revela dos tipos distintos de crecimiento, que nosotros sugerimos está relacionado con el flujo de alúmina asistido por el campo eléctrico en la capa barrera en el caso de anodización dura, y disolución de alúmina asistida por campo eléctrico para el caso de la anodización moderada.

9.- La diferencia entre anodización moderada o blanda y anodización dura se pone de manifiesto al observar la diferencia entre el ratio distancia interporo y voltaje aplicado. Se ha observado experimentalmente que en sistemas auto-ordenados de celdas de alúmina anódica que este ratio es de 2,5nm/V en el caso de anodización moderada y que varía entre 1,6 y 2.0nm/V en el caso de anodización dura.

10.- Es posible obtener sistemas autordenados en tiempos de anodización muy reducidos por medio de la HA en Aluminio mediante anodización basada en electrolitos aquosos de ácido sulfúrico. Además, la distancia interporo se puede controlar mediante el tiempo de anodización dura sin perder el auto-ordenamiento, llegando en nuestro caso a distancias interporo obtenidas por el modo tradicional en oxálico.

11.- Mediante el método de anodización pulsada ha sido posible modular periódicamente y de forma controlada los diámetros de los `poros sin variar la distancia centro a centro entre ellos, así como la composición de la alúmina a lo largo de los canales. El inconveniente de estas NAAF es que presentan considerables intestabilidades mecánicas debido a las altas densidades de corriente que tienen lugar durante su crecimiento, y que

pueden afectar a su homogeneidad. Sin embargo, estas novedosas geometrías abren muchas posibilidades en la fabricación de nuevas nanoestrucutras 1D y 3D.

12.- Las NAAF presentadas en este trabajo se pueden utilizar como plantillas para el crecimiento de materiales magnéticos como el Co, y dada sus particulares geometrías se pueden obtener propiedades magnéticas de gran interés, aunque sea necesario un estudio más profundo que el llevado a cabo en el trabajo presentado.

13.- Se han encontrado extraordinarias dificultades durante los experimentos para la obtención de nanohilos de ZnO en NAAF utilizadas como plantillas. Primero con la oxidación después del tratamiento térmico de Zn metálico electrodepositado previamente y Segundo con la formación de una capa de ZnO en la superficie de la NAAF, mientras se pretendía la electrodeposición directa de ZnO dentro de los nanoporos.

14.- Es posible el crecimiento de nanorods de ZnO en un amplio rango de diámetros que abarca entre 40nm hasta 600nm de media, mediante crecimiento hidrotermal. Se ha observado que la tasa de aumento de diámetro de los nanorods, después de las 5 primeras horas, disminuye en torno a un 70% de su tasa inicial. También ha sido posible la obtención de nanoestruturas tubulares o huecas por disolución local en el centro del nanorod.

15.- Las propiedades fotocatalizadoras de los nanorods de ZnO han permitido su utilización en la fabricación de dispositivos como células fotoelectroquímicas para la generación de H_2 a partir de un simulador de luz solar. A pesar de que las eficiencias de trabajo obtenidas en los experimentos realizados no son plenamente satisfactorias, hay un camino abierto a la mejora de estos dispositivos.